Commande de convertisseurs pour un système électrique à forte intégration d'énergies renouvelables

Rayane Mourouvin

THÈSE

Pour obtenir le grade de

DOCTEUR DE L'UNIVERSITE GRENOBLE ALPES

Spécialité : **Automatique et Productique (AP)**

Arrêté ministériel : 25 mai 2016

Présentée par

Rayane MOUROUVIN

Thèse dirigée par **Didier GEORGES,** et
codirigée par **Seddik BACHA**

préparée au sein du **SuperGrid Institute** et **GIPSA-Lab**
dans **l'École Doctorale Electronique, Electrotechnique, Automatique et Traitement du Signal (EEATS)**

Converter control in a power system with high penetration of renewable energy

Thèse soutenue publiquement le **03 novembre 2021**,
devant le jury composé de :

M. Gildas BESANCON
Professeur, Université Grenoble Alpes / Grenoble INP, France.
Président de Jury.

Mme Houria SIGUERDIDJANE
Professeur, CentraleSupélec, France. Rapporteur.

M. Mauro CARPITA
Professeur, Haute école d'Ingénierie et de Gestion du Canton de Vaud, Suisse. Rapporteur.

M. Germain GARCIA
Professeur, INSA Toulouse, France. Examinateur.

M. Zhe CHEN
Professeur, Aalborg University, Danemark. Examinateur.

M. Didier GEORGES
Professeur, Université Grenoble Alpes / Grenoble INP, France. Directeur de thèse.

M. Seddik BACHA
Professeur, Université Grenoble Alpes, France. Directeur de thèse.

M. Abdelkrim BENCHAIB
Manager R&D, SuperGrid Institute, France. Encadrant de thèse.

M. Jing DAI
Maître de Conférences, CentraleSupélec, France. Encadrant de thèse.
Invité.

Acknowledgments

Before jumping into the main content of this PhD thesis manuscript, I believe it is essential to thank all the people who have been part of this experience and helped me through this journey up to the defense of my PhD. I have had the chance to defend my thesis in the city of Lyon where I had started to go to engineering school seven years ago, so we can say that the cycle is complete. In addition, half of my thesis happened during the Covid-19 pandemic and the support that I received from my loved ones, friends and colleagues was even more meaningful to me and is a significant part of my PhD.

First, I would like to thank Prof. Houria Siguerdidjane and Prof. Mauro Carpita for having spent a lot of time in reading and reviewing my PhD thesis. I want also to express my sincere gratitude to Prof. Zhe Chen and Prof. Germain Garcia for their constructive feedback and taking part in my PhD thesis committee and Prof. Gildas Besançon for having chaired my PhD thesis committee.

Also, I would like to thank SuperGrid Institute and its management board for having funded my research project and having believed in me. Furthermore, I am grateful for the support I received from University of Grenoble Alpes, going from the administrative staff to the skilled researchers from G2Elab and GIPSA-lab whom I had the chance to discuss with.

Then, my thoughts go to my PhD thesis directors Prof. Didier Georges and Prof. Seddik Bacha. Didier, thank you for your diligence and your friendliness, you have always been consensual and gave me great feedback all along the thesis. Seddik, I really enjoyed all the discussions we had during these three years ranging from history and geopolitics to the control of MMCs, you always managed to make yourself available when needed. Also, I had the chance during my PhD to join Dr. Abdelkrim Benchaib's team, who was also one of my thesis supervisors. Thank you Abdelkrim, for having built such a great working environment and to believe in our work everyday, it was truly supportive to work with you. Finally, I would like to thank Dr. Jing Dai for supervising my work as well. All your remarks and feedback you gave me when I was writing papers or my PhD manuscript were

always constructive. Thank you Jing, for all the discussions we had, your kindness and humility. I can say that it was an honor to work with the four of you.

But a thesis is not only about a supervising team, and in my case, I had the chance to join an incredible research group to pursue my work. I would like to thank this team, the "control and stability" group, a.k.a the control guys, a.k.a the late risers: Juan Carlos, Kosei, Mathieu, Paul, Miguel, Lucas, Hind and Gianni and the past members of the group: Sjoerd, Roman, Laila, Jose, Abdelhak and Christopher. Thank you for all the laughs, the coffee-break discussions, the afterwork drinks and the Matlab talks. It was a pleasure to work with such talented and humble people. All of you sincerely made this PhD an unforgettable experience and I am glad to have had you as colleagues and to count you now as friends.

Also, I want to thank Antoine and Louis for having helped me with the real-time platform to achieve the experimental validation of my work. It was at the same time truly instructive and really fun to work with you at the platform and this will remain one of my best memories from my PhD work. Thanks a lot!

But, during these years of work at SuperGrid Institute, I also had the privilege to meet amazing people out of my working group. To Nicolas M., Pascal, Domagoj, Helena, Raga, Nicolas B., Shafie, Léo and all the other people I met there: thank you! You all contributed to make my stay a great experience. Also, to the people from the soccer and basketball teams of SuperGrid, thank you for your constant smiles and your friendliness. It was really nice to meet you over sports during our lunch breaks.

I think it is also important to express my gratitude to Prof. Jeffrey T. Glass and his team who welcomed me during my M.Sc as an intern into their lab at Duke University, NC, USA for five months. You gave the 22-year old student I was one of his best life experiences. In particular, I want to thank Jimmy and Edgard for sparking my passion for research. I do not think that I would have started a PhD without meeting you guys, you were and still are a true source of inspiration.

Then, from a more personal point of view, by coming back to Lyon for my PhD, I knew that I was in familiar territory since I already had some friends living there who I could count on during this thesis. To my group of "engineering" friends in Lyon: Arthur, Paul, Chloé, Antoine, Lisa, Elise, Louis, Maud, Valentin, Elodie, Gaultier, Sébastien, Théophile and Carlota, I would like to say "Merci beaucoup!". It was great to have such a nice group of people to hang out after work or to have a cool dinner with. I am glad that I have shared these three years with you. Moreover,

I also had the chance to meet outstanding people during my PhD, including my colleagues Juan Carlos (yes, you are cited twice), William, Guilherme, Diego and Gustavo. To you and to the rest of the "Montpellier" team (weird name, I know): Coline, Lara, Jorge, Anaïs, Cécile and Simon, thank you for your serenity, your kindness and your craziness. I knew that this PhD will make me learn a lot, but I could not expect to find such a group of close friends while working on my thesis! You are awesome and the only regret I have is that I don't speak Spanish yet!

Nevertheless, I could also count on the support of my friends I had met during my studies and who are now living all around the world. To my former roommates from engineering school: Antoine, Juliette, Noémi, Erlé, David (of course you're in) and Jolan, thank you for your support and patience all along our studies, your friendship means a lot to me. To my friends from high school: Arthur, Berouke, Aina and Sangsong, thank you for our unfailing bond. It is great to see that we are still in sync even after all these years.

On a more personal note, I would like to thank my parents and my brother, who, as always, have given me their continuous support during this PhD. I cannot tell you how important your support means to me. I am really proud of you and I could not have gone so far in my studies without your love and dedication for the past 27 years. Thank you for being by my side, no matter what. Moreover, I would like to thank Christine, Louis, Marie and Lucie whom I have known since kindergarten. Thank you for your support and being like a second family to us. I would also like to thank my girlfriend Sirine's family. Thank you for your encouragement, your kindness and your hospitality everytime I have come over.

As it comes to an end, I would like to finish by thanking you, Sirine. You have been here all along my PhD, regardless of the obstacles, and had more patience than anyone would have had. But, you are so much more than that: you are my roommate and my best friend, and all the moments we have spent together such as the endless board games we play, the four-handed cooking, the hiking trips (without camping) and travels are priceless to me. We endured several quarantines together, and still I have never been happier to spend my time with you. Thank you for everything, I can't wait to live our next adventures, and, of course, to attend your PhD defense!

Abstract

The recent engagements of many national governments backed by the United Nations push for introducing more and more renewable energy in the power systems in an attempt to mitigate global warming. Most of the renewable sources other than hydro power, such as wind turbines (except directly connected) or solar PV systems, depend on Power Electronics (PE) converters for their interconnection with the grid. Thus, the PE-based sources are becoming more and more prevalent in the current power systems and bring brand-new features in the grid. We observe this tendency both at the distribution level where the decentralized production units such as residential solar PV are gaining popularity, and at the transmission level as well where large energy sources such as Offshore Wind Farms (OWF) start to be interconnected with the grid using High-Voltage Direct Current (HVDC) technology.

This PhD thesis addresses some of the future grid challenges of replacing existing Synchronous Generators (SG) by PE-based interfaces and focuses more specifically on Voltage Source Converters (VSC) and their associate control strategies. This work focuses on the transmission grid level and investigates the control of VSCs interfacing renewable sources in hybrid power systems where PE and SG coexist.

In the first part of the work, the different ancillary services provided by SGs are listed and an overview of the existing VSC-based solutions is given, including the so-called grid-following and grid-forming controls. These two approaches are compared in terms of performances and constraints. Next, these types of controls are studied regarding the maximum allowable limit of PE and their interactions with nearby SGs in hybrid systems. It was shown that switching the VSC control mode from grid-following to grid-forming mode can allow a higher penetration rate of PE-based sources, even though some interactions with the remaining SGs must be taken care of.

In the second part of this work, we focus on the application of grid-forming control to Modular Multilevel Converters (MMC) for the integration of OWF in AC grids. The impacts of the DC-grid dynamics on the behavior of the grid-forming controlled MMC are assessed when the station must ensure the stability of the DC grid at the same time. In this context, a method is also proposed to estimate the

energy requirements of the MMC submodules to provide AC-grid related synthetic inertia. The corresponding control proposed is compatible with the state-of-the-art grid-forming control and is validated by simulations in a multi-machine system. To complement, a control solution that enhances the AC/DC support of such stations based on a MIMO-oriented Model Predictive Control (MPC) is proposed. It shows a better handling of the MMC internal energy as well as robustness against parameter uncertainties when compared to the existing SISO-based dual PI structure that relies on a theoretical decoupling between the AC and DC dynamics.

Finally, the proposed MPC-based control is applied to a real MMC. It is validated using an experimental setup which involves a mockup of an MMC of 6 kVA and 60 submodules. The grid-forming control and the proposed MPC are implemented into an Opal RT target and tested with success in real-time conditions to validate the approach developed in this thesis.

Résumé court en français

La plupart des sources renouvelables, telles que le solaire photovoltaïque ou l'éolien, dépendent de convertisseurs à base d'Electronique de Puissance (EP) pour leur raccordement au réseau électrique. Par conséquence, ces interfaces à base d'EP deviennent de plus en plus dominantes dans les réseaux actuels et font évoluer les caractéristiques des réseaux existants. Cette tendance s'observe au niveau des réseaux de distribution, où la production décentralisée telle que les panneaux solaires photovoltaïques résidentiels se développe rapidement. C'est également le cas au niveau du réseau de transport où d'importantes sources d'énergie telles que les Fermes Eoliennes Offshore (FEO) commencent à être interconnectées au réseau grâce à la technologie de Haute Tension à Courant Continu (HVDC).

Cette thèse de doctorat s'adresse à certains des futurs défis du réseau dans lequel les Générateurs Synchrones (GS) des centrales thermiques traditionnelles sont remplacés par des sources à base d'EP. Ce travail se concentre plus spécifiquement sur la technologie des Convertisseurs Source de Tension (VSC) et de leurs commandes associées. En outre, le contrôle de ces convertisseurs et leurs impacts au niveau de réseaux hybrides, où l'EP et les GS coexistent, sont étudiés.

Dans la première partie de ce manuscrit, les différents services systèmes fournis par les GS sont listés et un état de l'art des stratégies de contrôle du VSC existantes est donné, en incluant les notions de suiveurs (*grid-following*) et de formeurs (*grid-forming*) du réseau. Ces deux types de contrôles sont comparés du point de vue de leur capacité à apporter au réseau des services similaires à ce que les GS pouvaient apporter. Ensuite, le rôle de ces deux contrôles est étudié afin de déterminer le taux de pénétration maximal en EP tel que le réseau reste stable ainsi que les problèmes d'interactions potentielles avec les GS dans le cas d'un réseau hybride de référence. Il a pu être démontré que passer d'un contrôle type *grid-following* au *grid-forming* permet d'améliorer le taux de pénétration maximal des VSC dans le réseau, même si dans ce dernier cas des interactions avec les GS existent et devront être prises en compte pour permettre l'intégration massive d'EP dans le réseau.

Dans la seconde partie de ce manuscrit, l'accent est mis sur l'application du *grid-forming* aux Convertisseurs Modulaires Multi-niveaux (MMC) dédiés à l'intégration

de FEO dans les réseaux AC et l'impact des dynamiques du réseau DC sur la réponse de la station MMC contrôlée en *grid-forming*, quand le convertisseur doit également assurer la stabilité de la tension DC. Dans ce contexte, une méthode est proposée pour estimer les besoins en énergie des sous-modules du MMC pour fournir au réseau AC un support inertiel. Un contrôle associé à cet usage est proposé. Sa compatibilité avec le *grid-forming* issu de l'état de l'art est également validée dans un grand réseau multi-machines et multi-convertisseurs. Dans un second temps, une solution de contrôle basée sur une approche multivariable est finalement proposée pour améliorer le support des réseaux AC et DC qu'interconnecte le MMC. Cette solution, basée sur la synthèse d'une Commande Prédictive à base de Modèle (MPC), montre une meilleure gestion de l'énergie interne du MMC que la structure classique qui utilise des correcteurs PI et qui repose sur des hypothèses de découplages entre les grandeurs AC et DC. La robustesse du MPC face aux variations paramétriques du système est également démontrée par simulation.

Enfin, dans un dernier temps, la stratégie basée sur le MPC proposée pour opérer le MMC est validée en utilisant un banc expérimental qui inclut une maquette physique de 6 kVA d'un MMC de 60 sous-modules. Le contrôle *grid-forming* ainsi que le MPC proposé sont implémentés dans une cible Opal RT et testés avec les contraintes temps réel et permettent de valider l'approche développée dans ces travaux de thèse.

Résumé de la thèse en français

Chapitre 1: Introduction générale

Depuis quelques décennies, de plus en plus de projets visant à introduire du renouvelable dans le mix de la production d'électricité voient le jour. C'est le cas notamment au sein de l'Union européenne où les estimations d'évolution du taux de renouvelables prévoient une augmentation significative de ces ressources. Ces sources de production reposant sur les énergies renouvelables ont de nombreuses caractéristiques qui les distinguent des centrales de production conventionnelles:

- *distributivité*: contrairement aux grandes infrastructures que sont les centrales de production, ces systèmes renouvelables peuvent être installés à l'échelle du réseau de distribution et même à l'intérieur des centres urbains.
- *intermittence*: là où la puissance produite par une centrale thermique peut être facilement contrôlée en jouant sur la quantité de combustible brûlé, l'énergie produite par les systèmes photovoltaïques et éoliens dépend des conditions météorologiques. Par conséquence, parvenir à faire correspondre la consommation à la production en temps réel représente un véritable défi dans ce type de configurations.
- *interface au réseau*: une centrale thermique conventionnelle est couplée au réseau électrique par le biais d'une interface électromécanique appelée le Générateur Synchrone (GS), qui convertit une puissance mécanique de rotation en électricité. Pour la plupart des systèmes éoliens et photovoltaïques cependant, le couplage au réseau est assuré par des convertisseurs à base d'Electronique de Puissance (EP) qui convertissent un type de tension donné (généralement une tension continue, dite DC en anglais) en une tension alternative (AC) triphasée.

Aujourd'hui, cette intégration rapide de sources renouvelables conduit à une augmentation significative du nombre d'interface à base d'EP dans le réseau électrique. Leur présence s'illustre au niveau des réseaux de distribution avec notamment de nouvelles charges conçues à base d'EP mais également à l'échelle de la très haute tension où de nouvelles installations Haute Tension à Courant

Continu (HVDC en anglais) voient le jour, comme illustré sur la carte donnée dans la figure 1. L'objectif de ces projets HVDC est de permettre d'améliorer le maillage du réseau AC existant et ainsi d'augmenter les échanges de puissance entre les pays. Cela serait d'autant plus utile dans les réseaux à forte proportion d'énergie renouvelable où l'intermittence de ces sources pourrait être partiellement compensée par une augmentation des échanges. Egalement, ces liaisons HVDC permettraient d'intégrer plus de sources renouvelables et notamment les fermes éoliennes offshore dans le réseau.

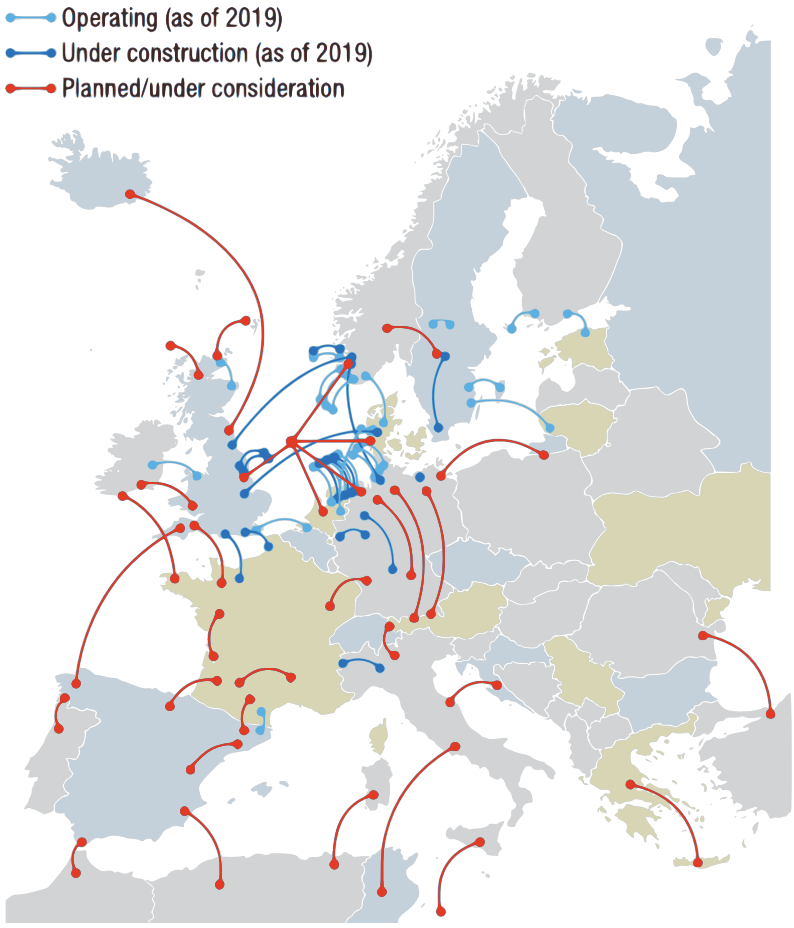

Figure 1: Carte de l'Europe incluant les projets VSC-HVDC existants et futurs [1].

Par conséquence, il est prévu d'assister dans les années à venir à une évolution des réseaux électriques, allant de systèmes dominés par les générateurs synchrones à des systèmes où l'EP et ces générateurs cohabitent voire où l'EP serait dominante.

L'objectif de cette thèse de doctorat est d'étudier le contrôle et l'opération de convertisseurs de puissance de type VSC avec un focus porté sur les Convertisseurs

[1]Source: `https://www.hitachi.com/rev/archive/2020/r2020_04/gir/index.html`.

Modulaires Multi-niveaux (MMCs en anglais) intégrant des sources d'énergie renouvelables. Ce travail s'intéresse à la stabilité du réseau AC/DC quand le convertisseur est opéré en mode de contrôle formeur (grid-forming en anglais) et se focalise donc sur le contrôle à l'échelle du convertisseur

Ce manuscrit de thèse est organisée de la façon suivante:

- Dans le chapitre 2, un état de l'art des stratégies de contrôle du convertisseur existantes est présenté. En particulier, les différents modes de contrôle sont comparés et leur pertinence est évaluée vis-à-vis de leur capacité à fournir les principaux services systèmes que peuvent fournir les machines synchrones.
- Dans le chapitre 3, une analyse de stabilité de ces principaux modes de contrôle (plus précisément les modes grid-following et grid-forming) est proposée dans le but de déterminer le taux de pénétration maximal en EP dans des réseaux hybrides où les convertisseurs et générateurs synchrones cohabitent.
- Dans le chapitre 4, l'accent est mis sur le rôle de la technologie HVDC, et plus particulièrement l'application des MMCs à l'interconnection de Fermes Éoliennes Offshores (OWF en anglais) avec le réseau continental. L'originalité de ce travail consiste à prendre en compte les dynamiques du réseau DC et de proposer une nouvelles manière de définir les besoins en énergie du MMC pour fournir un support inertiel au réseau AC et de l'utiliser avec une nouvelle loi de commande.
- Dans le chapitre 5, une Commande Prédictive à base de Model (MPC en anglais) est appliquée pour contrôler de manière optimale l'énergie interne du MMC ainsi que la tension du réseau DC. Cette solution de commande est synthétisée en utilisant un modèle identifié du réseau AC et ses performances vis-à-vis du rejet de perturbations sont comparées au contrôle reposant sur deux correcteurs Proportionnel Intégral (PI) en parallèle. Le comportement du MPC et sa robustesse vis-à-vis des incertitudes de paramètres et des changements de points de fonctionnement sont établis dans un second temps.
- Dans le chapitre 6, le contrôle grid-forming ainsi que la couche de contrôle MPC présentée au chapitre 6 sont validés en utilisant un correcteur temps réel et appliqués à une maquette de MMC de 6 kVA. Plus particulièrement, le concept de grid-forming appliqué à la maquette de MMC permet au convertisseur de se synchroniser au réseau AC sans la Boucle à Vérouillage de Phase (PLL en anglais). Deuxièmement, le MPC proposé au chapitre 6 est implementé en C de manière à être compatible avec le reste de la structure de commande implémentée en Matlab/Simulink.

- Dans le chapitre 7, une conclusion sur les principales contributions de cette thèse de doctorat est dressée et les hypothèses de départ considérées pour établir ces travaux sont discutées. Dans un second temps, d'éventuels nouveaux axes de recherche sont présentés afin de pouvoir étendre les résultats de cette thèse.

Une synthèse des différents chapitres est proposée dans la suite de ce résumé.

Chapitre 2: État de l'art des solutions existantes

Pour assurer la stabilité de réseaux hybrides où GS et EP cohabitent, les convertisseurs vont devoir intégrer petit à petit les fonctions de soutien au réseau que proposent les GS de telle sorte que les réseaux restent opérables dans des conditions similaires, puisque les charges et les machines restantes sur le réseau imposent toujours des contraintes en fréquence, tension et angle sur le réseau AC.

L'objectif de ce chapitre est de présenter les commandes développées dans la littérature scientifique afin de fournir ces fonctions de soutien à l'aide de convertisseurs AC/DC de type VSCs, décrits dans la figure 2. Il s'agit d'un sujet vraiment d'actualité au niveau de la communauté scientifique et qui attire même l'attention de la presse généraliste.

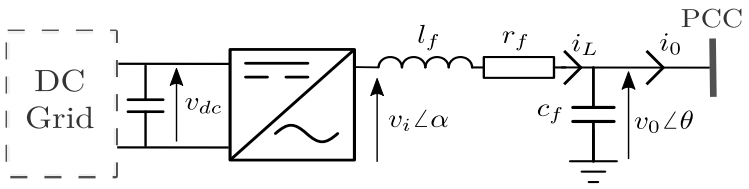

Figure 2: Circuit électrique équivalent d'un VSC interfaçant un réseau AC et DC.

Ce chapitre propose une comparaison des différents modes de contrôle, et notamment les deux principales familles que sont les modes source de courant et source de tension, dont les schémas de contrôles les plus communs sont donnés dans les figures 3 et 4 respectivement. Il est important de noter que là où la structure de commande dite source de courant, donnée dans la figure 3, permet de contrôler parfaitement le courant sortant du VSC, elle nécessite un estimateur d'état de type Boucle à Vérouillage de Phase (PLL en anglais) pour se synchroniser au réseau AC. De son côté, la structure de commande dite source de tension, donnée dans la figure 4 permet quand à elle de se synchroniser directement au réseau en se basant sur la puissance active calculée à partir des mesures de courant et tension et donc de ne

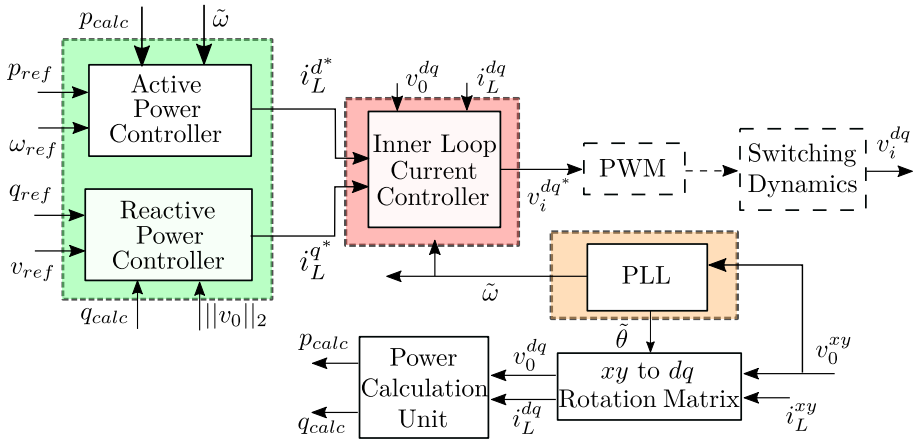

Figure 3: Commande cascadée du VSC en mode source de courant.

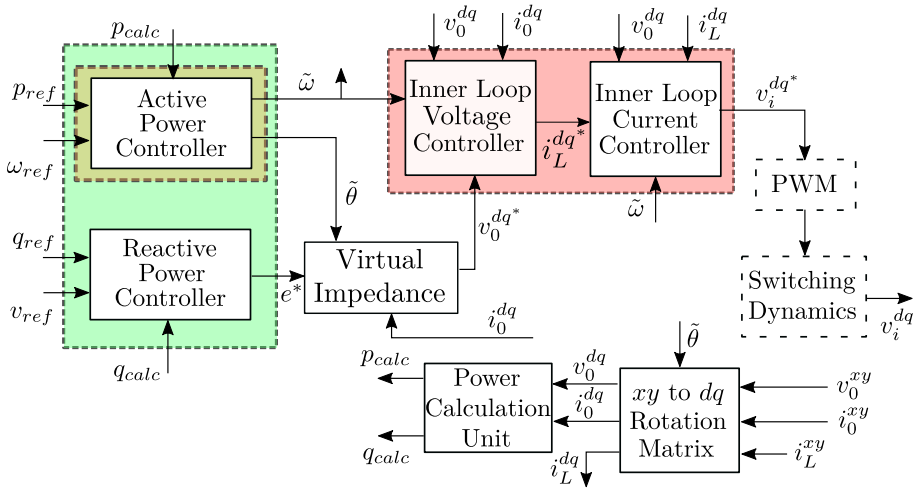

Figure 4: Commande cascadée du VSC en mode source de tension.

pas passer par une PLL. Cela permet notamment aux convertisseurs opérés avec ce schéma de commande de se connecter aux réseaux faibles, voire aux réseaux passifs.

Du fait du changement de paradigme entre ces deux modes de contrôles, ce chapitre comprend une analyse comparative de ces deux modes, à la fois du point de vue de leur impact sur le comportement du convertisseur, tels que la méthode de synchronisation, le suivi de références de puissance et les actions pour limiter le courant, mais également sur les fonctionnalités qu'ils peuvent fournir au réseau AC, tels que l'inertie synthétique, le partage de charge, le support en puissance réactive, la contribution à la force du réseau, la contribution aux courants de court-circuit et l'amortissement des oscillations de puissance.

Chapitre 3: Analyse modale sur les limites d'intégration de l'EP dans les réseaux AC

Une fois que les différents modes de contrôle ont été présentés, une analyse sur le rôle que peuvent jouer ces différents modes de contrôle sur les limites d'intégration de l'EP dans les réseaux AC est proposée. Cette analyse repose sur l'analyse modale d'un réseau de référence élémentaire composé d'un GS et d'un VSC interconnectés par une ligne de transmission de longueur variable et séparées par une charge. Ce réseau de référence est présenté dans la figure 5.

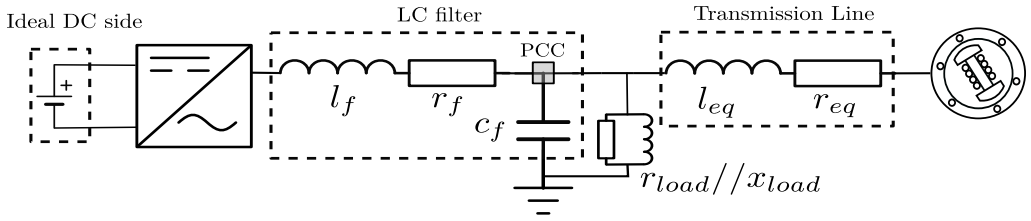

Figure 5: Réseau de référence élémentaire considéré pour l'étude.

Afin d'étudier l'évolution de la pénétration en électronique de puissance dans le réseau, une métrique dénommée ici le ratio de puissance et notée P_R est utilisée. Il y a dans la littérature plusieurs manières de définir ce ratio de puissance. Dans cette étude, la formulation retenue est:

$$P_R = \frac{S_{vsc}}{S_{sg} + S_{vsc}} = \frac{S_{vsc}}{S_{base}} \tag{1}$$

où S_{vsc} and S_{sg} sont respectivement les puissances de base du VSC et du GS et S_{base} la puissance de base du système, maintenue constante. Ce P_R permet de comparer le ratio de la puissance installée du VSC avec la puissance du système total. Par conséquence, en faisant varier ce P_R, il est possible de simuler des cas où le rapport entre convertisseur et générateur synchrone est différent, et donc d'analyser le rôle de ce rapport sur la limite de stabilité petit signal.

Les résultats obtenus à partir de l'analyse modale sont donnés dans la figure 6. Il a ainsi été montré que les dynamiques de la ligne de transport généraient des interactions négatives avec la PLL du VSC lorsque celui-ci est en mode source de courant, confirmant une tendance observée dans la littérature. En revanche, pour ce qui est du VSC en mode grid-forming, la longueur de ligne semble avoir peu d'impacts sur le ratio de puissance maximal admissible.

Cependant, cette analyse a permis de mettre en évidence une interaction négative qui correspond aux modes instables entre le Régulateur Automatique de Tension

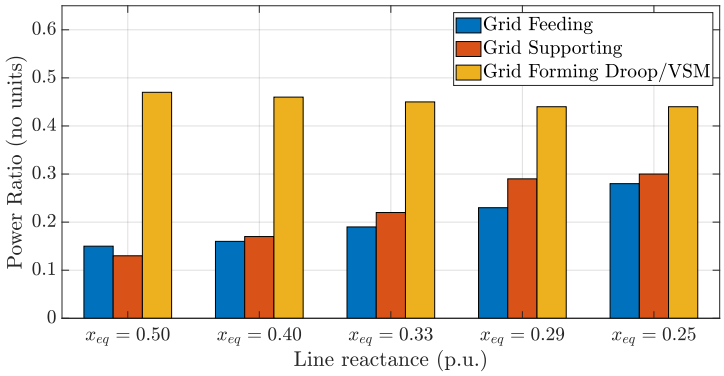

Figure 6: Ratio de puissance maximal admissible pour différentes valeurs de x_{eq}.

(AVR en anglais) du GS et la boucle de contrôle externe du VSC lorsque celui-ci est en grid-forming. À notre connaissance, ce résultat n'avait pas été souligné jusqu'à présent et est très important dans le sens où il confirme que les interactions entre les VSCs et les GS restantes dans ces futurs réseaux hybrides rendront un tel système plus difficilement opérable que les réseaux comprenant uniquement 100% d'EP. Enfin, une analyse sur un réseau multi-machines inspirée du réseau deux zones de Kundur est également présentée dans ce chapitre et confirme les tendances obtenues avec le réseau de référence élémentaire et illustrées figure 6.

Chapitre 4: Application du grid-forming aux convertisseurs modulaires multi-niveaux

Après avoir mis en évidence les bénéfices de piloter d'avantage de convertisseurs en grid-forming, l'accent est mis sur l'application de la commande grid-forming aux convertisseurs utilisés dans les systèmes VSC-HVDC et plus particulièrement sur la nouvelle technologie de convertisseurs que sont les MMCs.

Dans un premier temps, l'étude se focalise sur les interactions entre les réseaux AC et DC d'un MMC connecté au réseau continental et servant à l'intégration de fermes offshores dans le réseau électrique. Dans ces conditions, le MMC reçoit une puissance qu'il ne contrôle pas depuis le réseau DC et doit donc assurer la stabilité de la tension DC tout en étant piloté en grid-forming côté AC. Du fait des temps de réponse relativement longs qu'amènent le grid-forming, un compromis doit être trouvé entre la stabilité AC et la stabilité DC, d'autant que ces interactions affectent directement l'énergie interne du MMC, comme cela a également été montré récemment dans d'autres études.

Dans un second temps, la ressource que représente l'énergie interne du MMC, qui permet de jouer un véritable rôle de tampon entre les réseaux AC et DC, est étudiée plus en détail. Plus particulièrement, une méthodologie est proposée pour calculer l'énergie que devrait fournir un MMC pour apporter une réponse inertielle synthétique similaire à un générateur synchrone de même puissance sur les plages de fréquences opérationnelles d'un réseau typique définies dans leur code de réseau. Une fois cette méthodologie appliquée, une loi de commande basée sur la structure actuelle de contrôle du MMC est proposée. Cette loi de commande, dénommée "commande du rotor virtuel", agit sur la référence d'énergie envoyée au contrôle du MMC. Elle permet de faire varier l'énergie stockée dans les sous-modules du MMC proportionnellement à la déviation du carré de la fréquence estimée du réseau AC. Elle s'exprime de la manière suivante:

$$W^*_{mmc} = W^*_{mmc,0} + k_{vr} \cdot ({\omega_1}^2 - {\omega^*}^2) \tag{2}$$

$$W^{min}_{mmc} \leq W^*_{mmc} \leq W^{max}_{mmc} \tag{3}$$

où $W^*_{mmc,0} = 1$ p.u. est la référence d'énergie correspondant à la fréquence de référence (50 Hz), ω^* est la fréquence de référence normalisée et k_{vr} est un coefficient réglable qui permet d'émuler la réponse d'une machine tournante. W^{min}_{mmc} et W^{max}_{mmc} sont utilisées afin de s'assurer que le correcteur de l'énergie interne respecte les limites physiques du MMC.

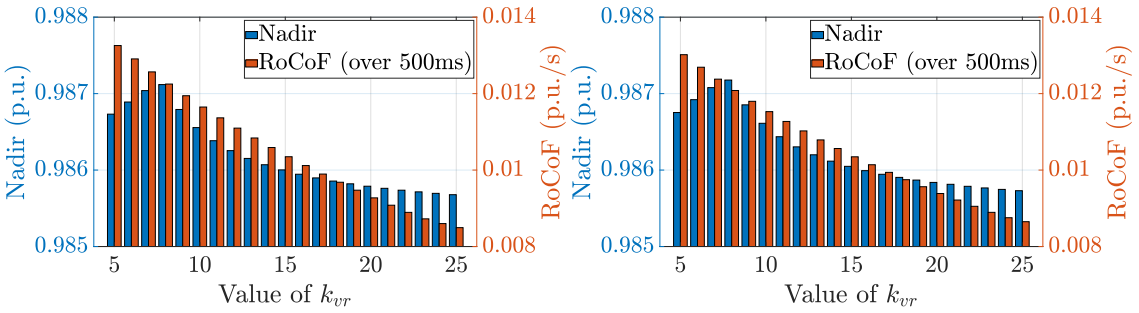

(a) AC power disturbance (b) DC power disturbance

Figure 7: Influence de k_{vr} sur le nadir et le RoCoF à la suite d'une perturbation de charge de 250 MW.

Même s'il existe une valeur de gain k_{vr} basée sur des calculs en régime permanent qui permet d'utiliser au mieux l'énergie disponible du MMC sur une plage de fréquence donnée, une analyse est conduite dans ce chapitre afin d'étudier le rôle que peut jouer le choix de ce gain sur les métriques de fréquence AC et notamment le taux de change de la fréquence (RoCoF en anglais) et la valeur minimale de cette

fréquence (nadir en anglais). Les résultats pour des perturbations côté AC et DC sont donnés dans la figure 7. Ils sont obtenus avec un modèle simplifié de réseau AC et de MMC et montrent que là où le RoCoF est toujours amélioré lorsque la valeur du gain k_{vr} augmente, étant donnés les problèmes que causent les interactions entre GS et MMC, le choix d'un k_{vr} élevé doit être évité car ce dernier peut s'avérer contre-productif pour améliorer le nadir.

Afin de valider la loi de commande proposée ci-dessus, des simulations multi-machines ont été réalisées sur le réseau nordique (Nordic 44-bus) décrit figure 8.

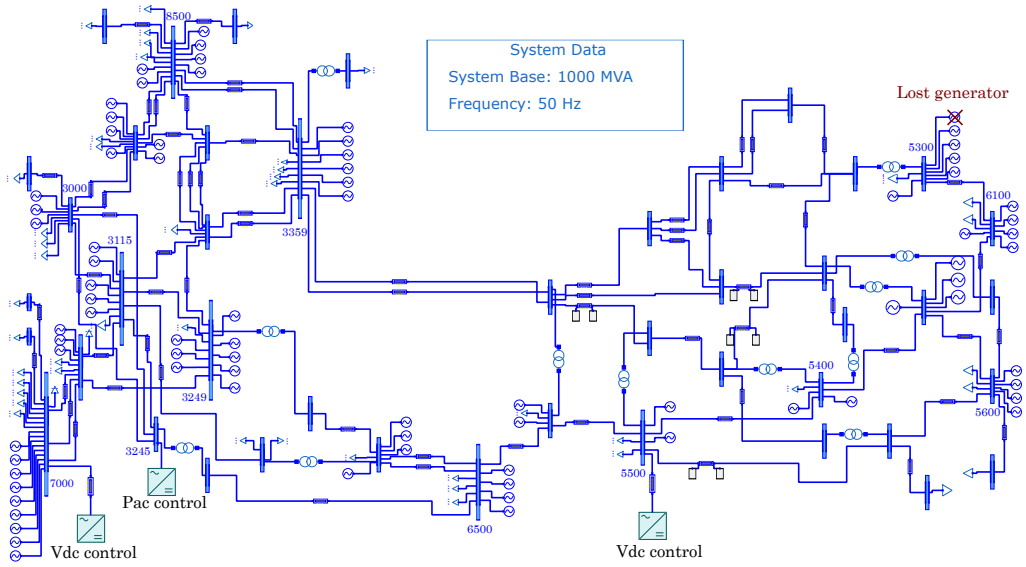

Figure 8: Modèle modifié du réseau nordique européen (Nordic 44-bus).

Dans ce réseau modifié, trois GS sont remplacés par des MMCs en grid-forming. Les deux MMCs contrôlés en mode source de tension (v_{dc}-mode en anglais) embarquent d'avantage d'énergie dans leurs sous-modules afin de pouvoir tester la loi de commande du rotor virtuel. Les résultats de simulation obtenus confirment la faisabilité d'une telle solution et le soutien effectif au RoCoF du réseau mais montrent que des oscillations inter-zones subsistent dans un tel réseau et ne sont pas résolus avec la solution proposée.

Chapitre 5: Synthèse du MPC pour améliorer la réponse du MMC en grid-forming

Une des limites de la solution de commande proposée dans le chapitre précédent est qu'elle ne permet que d'apporter du soutien au réseau AC, là où il serait bénéfique que le MMC apporte également un soutien au réseau DC. En effet, la structure de contrôle du MMC est telle qu'elle permet de piloter indépendemment la puissance extraite côté DC et la puissance injectée côté AC (et vice-versa). Le problème consiste donc à un problème à trois reservoirs et deux robinets, présenté dans la figure 9.

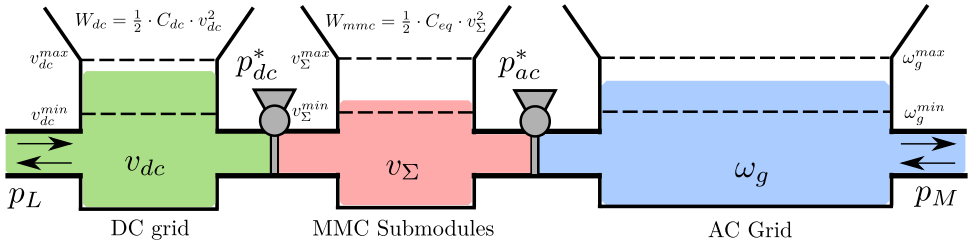

Figure 9: Trois réservoirs interconnectés illustrant les échanges d'énergie entre le MMC et les réseaux AC et DC.

Dans ce cas de figure, agir sur les références de puissance, respectivement p_{dc}^* et p_{ac}^*, permet de contrôler les échanges d'énergie entre le réseau DC caractérisé par sa tension DC notée v_{dc}, les sous-modules du MMC caractérisée par l'énergie interne totale du MMC notée W_{mmc}, et le réseau AC caractérisé par sa fréquence AC notée ω_g. Le problème est ainsi formulé sous forme d'un système Multi-Entrées/Multi-Sorties (MIMO en anglais) avec 2 entrées de commande et 3 sorties.

Ce chapitre consiste à présenter une commande optimale permettant de répondre à ce problème en tenant en compte les contraintes physiques du réseau DC et du MMC. Puisqu'il s'agit d'un problème d'optimisation sous contraintes, la solution retenue est la Commande à base de Modèle (MPC en anglais). Cette commande vient comme une surcouche par rapport aux commandes de courant DC et grid-forming côté AC, et est représenté dans la figure 10.

Ici, le MPC envoie des consignes de puissance optimale DC et AC, respectivement notées p_{dc}^* et p_{ac}^*, en prenant en compte les métriques décrites précédemment. Comme la commande agit sur un système AC/DC non linéaire, noté Σ, il est nécessaire d'avoir un modèle fiable permettant de réaliser la prédiction et l'estimation des états du systèmes. Dans ces conditions, une méthode d'identification est présentée dans ce chapitre pour obtenir un modèle identifié linéaire du réseau AC. En considérant

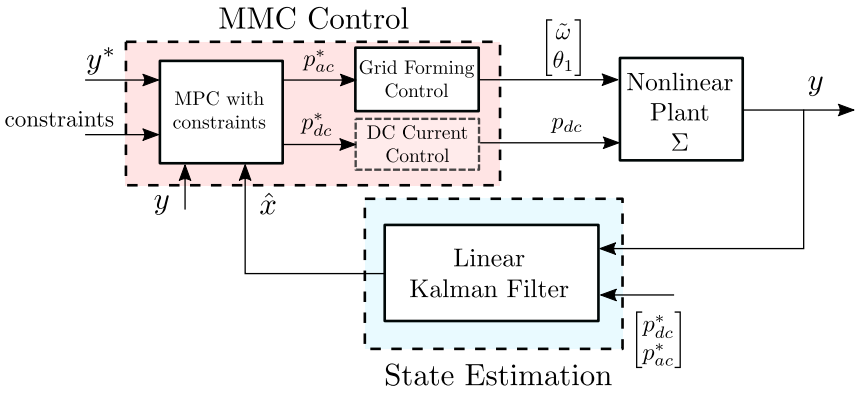

Figure 10: Structure générale de la commande MPC et estimation d'état.

des modèles connus et simples (linéaires du premier ordre) pour les dynamiques de l'énergie interne du MMC et du réseau DC, il est possible de construire un modèle du réseau AC/DC qui peut être utilisée par le MPC et l'estimateur d'état, qui est ici un filtre de Kalman.

Finalement le MPC est implémenté en utilisant la librairie YALMIP qui permet de développer ce type de commandes dans l'environnement Matlab. Le MPC est comparé à la structure de contrôle classique reposant sur deux correcteurs PI en parallèle (dual PI en anglais) qui gèrent la tension DC et l'énergie interne indépendamment et sans tenir compte par défaut de la fréquence AC. Cette comparaison est effectuée dans l'environnement Matlab/Simulink et les résultats sont donnés dans la figure 11.

Ces résultats montrent une meilleure gestion de l'énergie interne du MMC pour supporter le réseau AC/DC à la suite de perturbations venant à la fois du côté DC et du côté AC. En effet, W_{mmc} est déchargée de manière à fournir un support inertiel au réseau AC, que cela soit à la suite d'une perturbation AC ou DC. De plus, la réponse de la puissance AC est moins oscillante que celle obtenue avec le dual PI.

Dans un second temps, la robustesse de la commande face à des variations de points de fonctionnement ou de paramètres est établie.

Chapitre 6: Validation expérimentale

Un des verrous majeurs qui bloquent aujourd'hui le déploiement de solutions de commande type MPC dans les systèmes industriels est les performances de calcul. En effet, le MPC repose sur la synthèse d'une commande optimale qui est calculée à partir de la projection d'un modèle défini dans le MPC sur un horizon de temps défini dans le correcteur. Cela nécessite donc à chaque pas de temps de réitérer

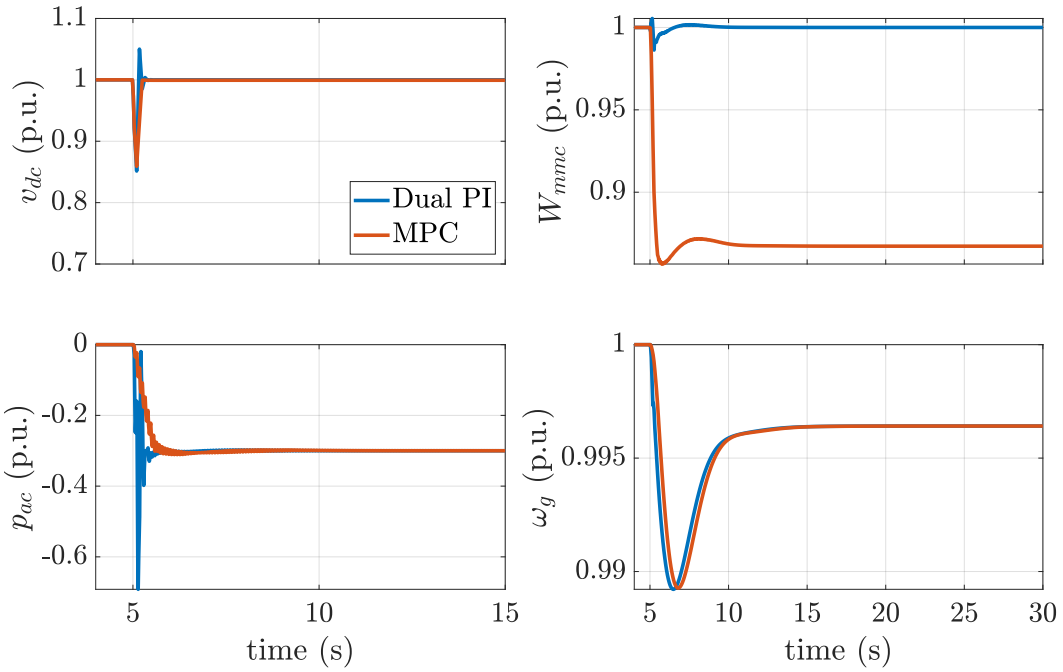

(a) Résultats de simulation à la suite d'une perturbation de puissance de -0.3 p.u. côté DC.

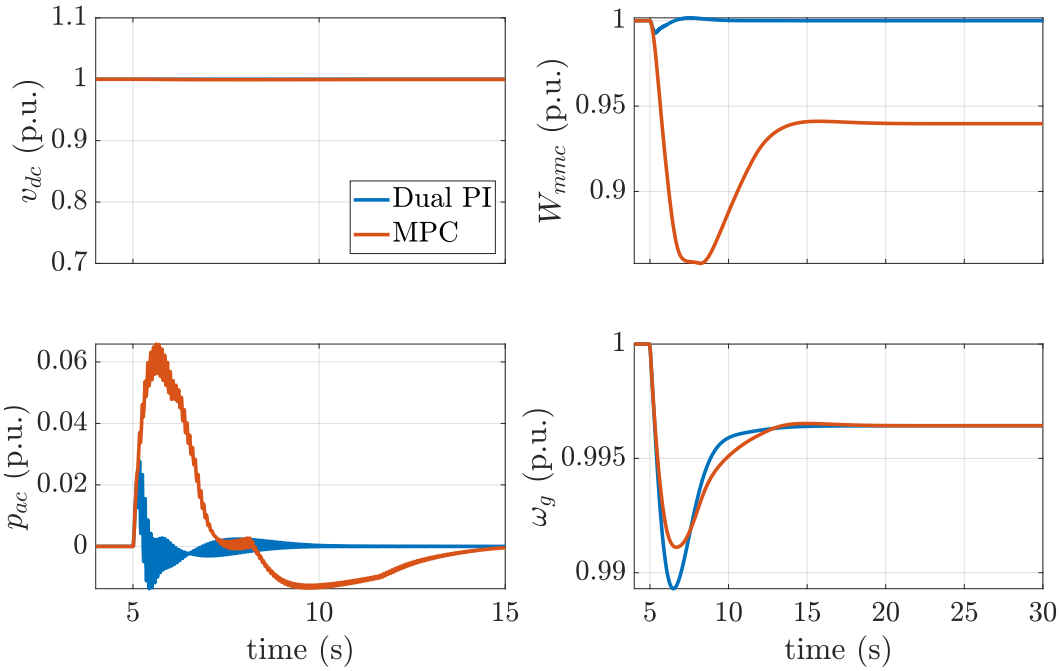

(b) Résultats de simulation à la suite d'une perturbation de puissance de -0.3 p.u. côté AC.

Figure 11: Comparaison des structures dual PI et MPC à la suite de deux types de perturbation.

cette opération pour connaître le comportement du modèle sur cet horizon, puis de résoudre le problème d'optimisation qui minimise la fonction de coût du MPC.

Un des enjeux de ce chapitre est de démontrer la faisabilité d'une telle solution de contrôle sur un système physique lorsque le correcteur est compilée sur une cible qui fonctionne en temps réel. Dans ce chapitre, la solution de contrôle proposée au chapitre 5 est implémentée sur une cible Opal RT (OP4510) afin de contrôler une vraie maquette de MMC décrite dans la figure 12.

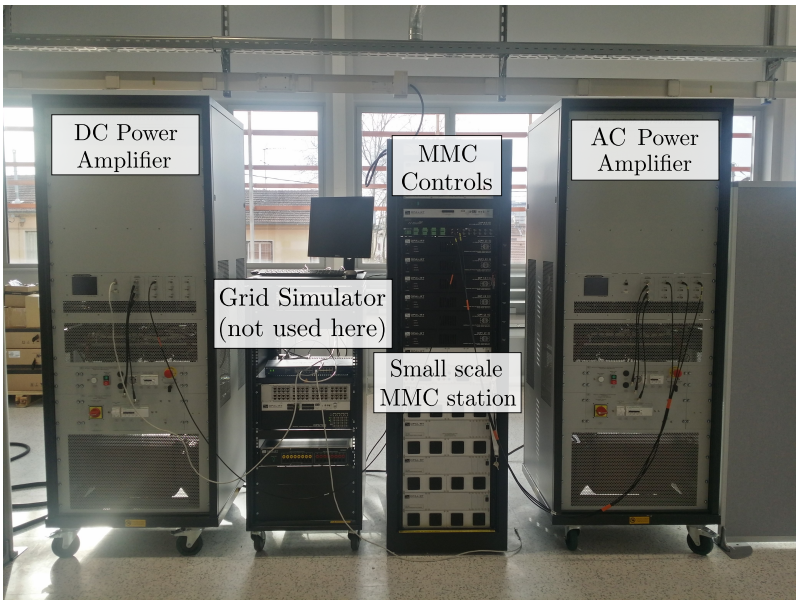

(a) Photographie de la maquette.

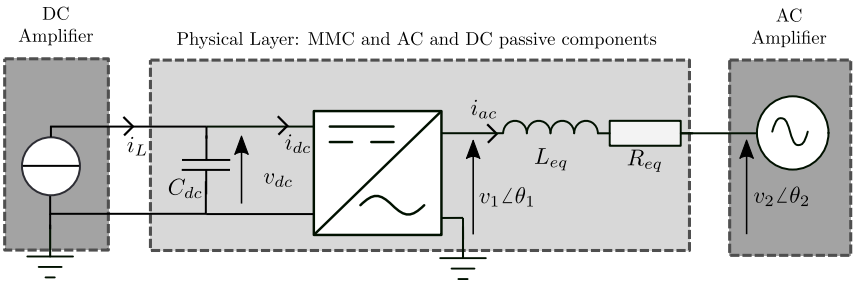

(b) Schéma electrique de la maquette de MMC avec ses amplificateurs AC et DC.

Figure 12: Installation expérimentale "Power-Hardware-In-the-Loop" (PHIL) à SuperGrid Institute à Villeurbanne, France.

Les réseaux AC et DC sont décrits par des modèles simplifiés, ce qui ne permet pas de tester tous les types de perturbation et notamment les pertes de génération ou les sauts de charge côté AC. De plus, le MMC étant dimensionné pour émuler une station HVDC conventionnelle, ses sous-modules ne sont pas conçus pour fournir un support inertiel tel que défini dans le chapitre 4. Par conséquence, il n'est pas

possible de tester le support au réseau AC que peut aider à fournir le MPC. Ici, l'enjeu est d'avantage de valider la structure de commande proposée dans cette thèse avec les contraintes temps réel et notamment d'étudier l'intérêt en termes de temps de réponse et de rejet des perturbations que peut représenter le MPC dans ce cas.

Après avoir implémenté la commande grid-forming issue de travaux récents de la littérature, la couche MPC est implémentée directement en langage C à partir de l'outil μao-MPC qui permet de générer le code avec un solutionneur (solver en anglais) adapté au temps réel. Une fois le contrôle développé en Matlab/Simulink et embarqué sur la cible OP4510, différents cas d'étude sont étudiés pour comparer les performances du dual PI et du MPC. Ces cas d'étude sont présentés dans le tableau 1.

Cas #	**Caractéristique**	**Description**
Cas 1	suivi de tension DC	Changement de référence de 1 à 0.95 p.u. sur v_{dc}^*
Cas 2	suivi de l'énergie interne	Changement de référence de 1 à 0.9 p.u. sur W_g^*
Cas 3	perturbation côté DC	Créneau de courant DC de 0 à 0.1 p.u. sur i_L
Cas 4	perturbation côté AC	Créneau de tension AC de 1 à 0.9 p.u. sur v_2
Cas 5	perturbation côté AC	Créneau d'angle AC de 0 à 10^o sur θ_2

Table 1: Cas d'étude pour la validation expérimentale en PHIL.

Les résultats concernant les performances en termes de suivi de référence (Cas 1 et 2) des correcteurs dual PI et MPC sont donnés dans la figure 13.

À l'exception de l'erreur en régime permanent concernant le MPC, qui demeure inférieure à 1%, les deux correcteurs offrent des performances similaires. La solution MPC est légèrement plus rapide que la solution PI mais également plus oscillante.

Les résultats concernant les performances en termes de rejet de perturbation (Cas 3 à 5) sont donnés dans la figure 14. Si pour les Cas 3 et 4 les réponses des correcteurs se rapprochent à nouveau, pour le Cas 5, il est clair que le MPC fournit une meilleure solution de contrôle puisqu'il permet au MMC de rester connecté là où le MMC se bloque suite à la perturbation avec le dual PI.

Finalement, ce chapitre a permis de valider l'implémentation temps réel d'un MPC appliqué au contrôle d'un convertisseur type MMC. Cependant, beaucoup de temps a été passé sur le réglage du correcteur MPC et notamment le compromis entre l'horizon de prédiction, la période d'échantillonnage et les performances finales. Consacrer un système hardware dédié au MPC pourrait permettre d'améliorer les performances de calcul. Cependant, cela nécessiterait d'établir un protocole de

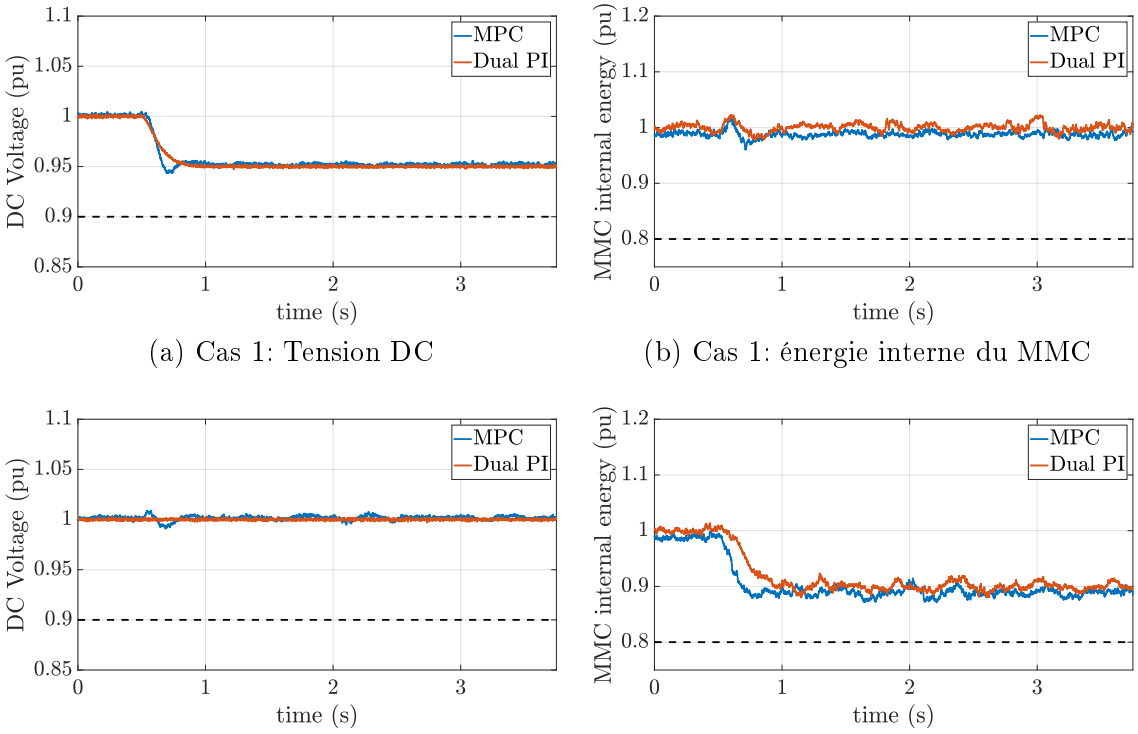

(a) Cas 1: Tension DC

(b) Cas 1: énergie interne du MMC

(c) Cas 2: Tension DC

(d) Cas 2: énergie interne du MMC

Figure 13: Comparaison des solutions dual PI et MPC en PHIL en termes de suivi de référence (Cas 1 et 2).

communication entre le système OP4510 et ce nouveau système. D'un point de vue modélisation, il serait possible d'intégrer des modèles de réseaux AC multi-machines ou des réseaux DC multi-terminaux dans l'expérimentation PHIL afin de pouvoir valider la structure de contrôle dans un système plus complexe.

Chapitre 7: Conclusion générale

Pour résumer les contributions principales de cette thèse de doctorat, le travail présenté a démontré l'intérêt d'avoir d'avantage de VSCs commandés en grid-forming. En effet, cette fonctionnalité de grid-forming permet d'éviter les problèmes de réseaux faibles et permet même de supporter un îlotage par rapport au réseau principal. Cependant, la principale fonction d'un convertisseur étant malgré tout d'injecter de la puissance dans le réseau, ce nouveau mode de contrôle amène plusieurs problèmes tels que: le maintien de la tension DC, le contrôle de l'énergie interne des MMCs, les interactions AC/DC, etc. Cela est notamment dû au fait que son temps de réponse est relativement long et que ses performances en termes de suivi de consigne sont faibles. Après avoir discuté du besoin de ralentir la

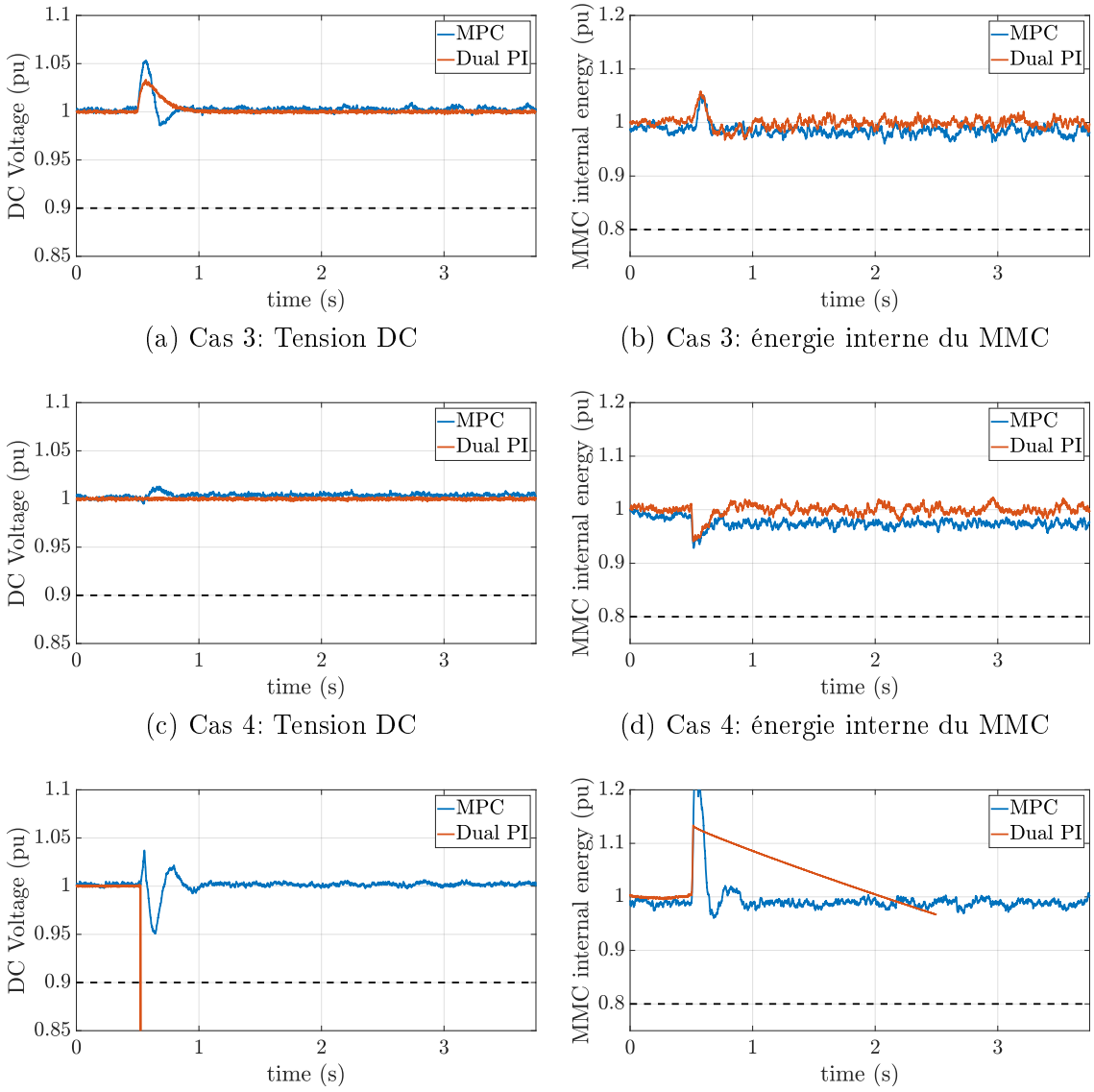

(a) Cas 3: Tension DC

(b) Cas 3: énergie interne du MMC

(c) Cas 4: Tension DC

(d) Cas 4: énergie interne du MMC

(e) Cas 5: Tension DC

(f) Cas 5: énergie interne du MMC

Figure 14: Comparaison des solutions dual PI et MPC en PHIL en termes de réjection de perturbation (Cas 3 à 5).

boucle de tension DC pour résoudre ce problème, ce manuscrit de thèse investigue l'application du grid-forming aux MMCs et developpe une méthodologie basée sur la Commande Prédictive à base de Modèle (MPC en anglais) pour résoudre ce problème. L'application du MPC à l'échelle de la commande de MMC est démontrée à l'aide d'une maquette physique de MMC. Ceci constitue une contribution vis-à-vis de l'application de ce type de solutions de contrôle avancées pour des systèmes industriels à base d'électronique de puissance.

Dans un second temps, les perspectives de recherche suivantes ont été identifiées et sont discutées:

- **Intégration des dynamiques de sources DC**: Dans les premiers chapitres de la thèse, le réseau DC est considéré comme étant un réseau parfait, c'est-à-dire modélisé par une source de tension continue. Bien que cette hypothèse de modélisation est très répandue dans la littérature, elle ne permet pas d'étudier les interactions entre les réseaux AC et DC lorsque le convertisseur est piloté en grid-forming. C'est notamment pourquoi dans les chapitres 4 à 6, le réseau DC est modélisé par un condensateur et une source de courant constante, permettant au moins d'intégrer les dynamiques de tension DC dans les études. Cependant, l'intégration de modèles plus complexes, intégrant les dynamiques des sources d'énergie renouvelable ou des systèmes de stockage constitue une perspective intéressante afin d'étendre l'analyse et la simulation de convertisseurs à base d'EP.
- **Utilisation des techniques d'Intelligence Artificielle (AI en anglais) pour le MPC**: Dans le chapitre 6, les limites en termes de temps de calcul d'une implémentation classique de la commande MPC a été discutée. Avec l'émergence actuelle des techniques d'AI dans le domaine de l'électronique de puissance, une des solutions pour résoudre ces problèmes pourrait être d'avoir recours à des techniques de machine learning pour synthétiser la commande offline à partir de grands jeux de données. Cette technique permettrait entre autres de s'affranchir du coût de calcul d'un solutionneur temps réel.
- **Analyse de stabilité transitoire des MMCs**: Dans le chapitre 3, une analyse de stabilité petit signal a été proposée en étudiant un réseau hybride composé d'un VSC et d'un GS. Les conclusions de cette étude n'étant valables que pour de petites perturbations, il serait intéressant d'étendre ce type d'études à des analyses large signal (aussi appelées analyses transitoires). Ce type d'études a déjà été conduit dans le cas de réseaux hybrides multi-machines et multi-convertisseurs, où les VSCs étaient pilotés en grid-following. Cependant, ce type d'analyses n'ont pour le moment que très rarement été appliquées au MMC et au rôle qu'il peut jouer dans la stabilité transitoire de réseaux hybrides. Une telle étude serait d'autant plus pertinente qu'elle nécessiterait de s'intéresser aux manières de limiter le courant dans les bras du MMC lorsque celui-ci est piloté en grid-forming, un sujet d'actualité.
- **Commande coordonnée de plusieurs convertisseurs**: Dans l'ensemble de ce manuscrit de thèse, l'accent a été mis sur la manière de contrôler un

convertisseur pour supporter un réseau hybride où EP et GS cohabitent. Cependant, il serait possible de proposer une réponse coordonnée de différents convertisseurs connectés au même réseau AC avec des sources DC découplées et variées ou d'utiliser un réseau MTDC intégré dans un même réseau synchrone. Ce type de solutions nécessiterait cependant d'établir une communication entre les stations.

Contents

List of Tables

List of Figures

Acronyms

ALM Augmented Lagrangian Method.
AVR Automatic Voltage Regulator.
COI Center of Inertia.
DAE Differential and Algebraic Equations.
EMT Electro-magnetic Transient.
EU European Union.
FACTS Flexible AC Transmission Systems.
FFR Fast Frequency Response.
FGM Fast Gradient's Method.
FRT Fault Ride Through.
HVAC High Voltage Alternative Current.
HVDC High-Voltage Direct Current.
LCC Line-commutated Converter.
MMC Modular Multi-level Converter.
MPC Model Predictive Control.
MTDC Multi-terminal Direct Current.
ODE Ordinary Differential Equation.
OE Output Error.
OWF Offshore Wind Farm.
PCC Point of Common Coupling.
PE Power Electronics.
POD Power Oscillation Damping.
PSS Power System Stabilizer.
PV Photovoltaic.
RMS Root mean square.
SG Synchronous Generator.
SM Submodules.
TSO Transmission System Operator.
UK United Kingdom.
VRC Virtual Rotor Control.
VSC Voltage Source Converter.
VSM Virtual Synchronous Machine.

Chapter 1

General Introduction

1.1. Context

1.1.1. A brief history of fossil fuels

The Industrial Revolution started in the mid-XVIIIth century in Europe and more precisely in the British countryside, where famines were a recurring problem [1]. While in the early 1800's the mechanical machines were driven by hydro power and were installed alongside rivers, the emergence of steam engines have been a game changer in the development of the first mass production factories in the United Kingdom (UK). Indeed, these machines were powered with a fuel, such as coal or oil, that could be stored and exchanged between communities and countries. This fuel was burnt in order to heat some water and turn it into steam. This relatively high-pressure steam was used to drive a wheel in mills or factories. Back then, these types of steam-powered machines were only used in the agricultural and industrial sectors to pump water, to mill grains and later to produce manufactured goods such as pieces of clothing or furniture.

Subsequently, a novel era began with the invention of the first electrical machines, capable of converting a mechanical effort into electricity. Thanks to the numerous

research works of Nicolas Tesla on Alternative Current (AC) systems [2], the development of the first AC electrical networks began in the last decades of the XIXth century. Fossil fuels then became increasingly more used in the production of electricity in power plants and the electrical network made it possible to transport this energy to the consumers connected to the grid. At the same time, thermal motors turned out to be more and more used in embedded applications, e.g. cars, buses, ferries and then airplanes. Thereafter, in the post-WWII era, the electrification of industrial, agricultural and tertiary sectors in most of the countries around the world led to a drastic increase of the consumption of fossil fuels in the world which became dependent on those resources for its economic development and for essential sectors. Because the oil reserves are not infinite, there is a real risk of fuel shortage, causing many geopolitical conflicts around the world and affecting the international relations.

1.1.2. Climate change and necessary energy transition

In addition to the problems related to the existing resources of fossil fuels, the quantity of fossil fuels that has been consumed since the beginning of the Industrial Revolution is tremendous and is now the main cause for the average rise of temperature of +0.87 °C in the atmosphere compared to the pre-industrial data [3]. Climate change has already been said to be responsible for several natural disasters such as the 2020 Australian wildfires [4], or the cold storm that hit Texas in February 2021 causing week-long power shortages [5] and whose cause can be linked to the heating of the Arctic [6]. In the future, climate change could provoke greater natural disasters, such as flooding causing many human casualties and massive infrastructure damages [7].

In consequence, the Intergovernmental Panel on Climate Change (IPCC) considers that 70-85% of electricity should be produced by renewable energy sources [3] in 2050 to limit global warming to +1.5 °C. In order to carry out this energy transition, there is a need for a change of paradigm and an update of the current energy infrastructure. From now on, if we use the existing infrastructure until the end of its lifetime, it will emit 658 gigatonnes of CO_2. If we add the proposed power plants using fossil fuel (planned, permitted or under construction), approximately 188 gigatonnes of CO_2 emitted in their liftetime will be added [8]. The data regarding these emissions per industrial sector and per country are detailed in Figs. 1.1 (a) and 1.1 (b) respectively. On the other hand, if we want to respect the limit of +1.5 °C above the pre-industrial level fixed by the Paris Agreement [9], we have to emit

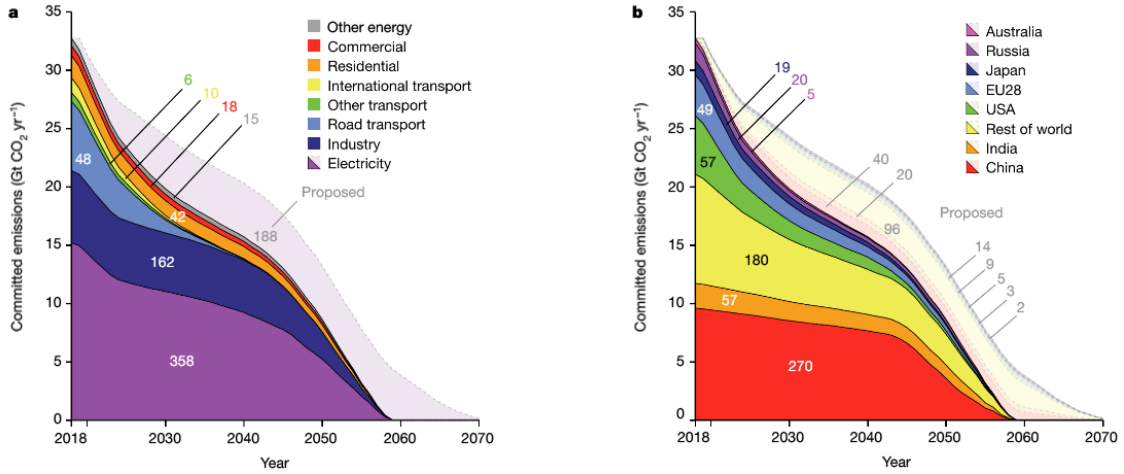

(a) Estimated emissions of CO_2 per industry.

(b) Estimated emissions of CO_2 per country.

Figure 1.1: Annual CO_2 emissions from the existing and under-construction/under-consideration energy infrastructure in 2019 [8].

less than 580 gigatonnes of CO_2. This means that all the planned fossil-fuel-based infrastructure projects have to be stopped, while some of the existing infrastructures will have to be decommissioned. This incurs a huge responsibility to the electricity sector, since the energy transition depends on, among others:

- the replacement of the current fossil fuel power plants by renewable energy sources, which must be controlled adequately;
- an electrification of some sectors that used to be dependent on fossil fuels, such as transport systems;
- the development of energy storage systems to compensate for the intermittency of wind and solar power in order to ensure the reliability of electricity.

1.1.3. A transition reliant on resources

The transformations previously mentioned require massive investments and new materials to develop those technologies. The problems related to the materials to build this type of infrastructure are discussed in this paragraph.

Most of the renewable energy systems, such as the photovoltaic panels and the wind turbines, require particular materials, even in small amounts: the rare earth metals. These minerals are elements of the periodic table that have really specific electronic and magnetic properties that make them key players of these systems [10].

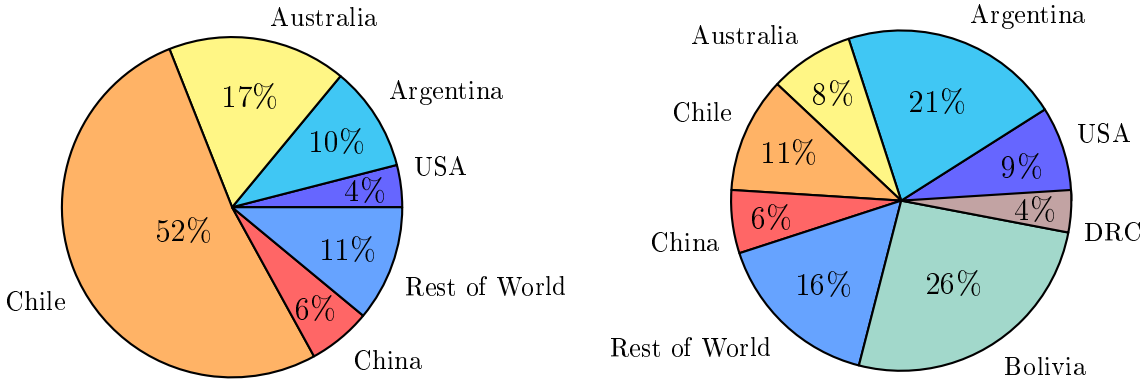

(a) World reserves

(b) World resources

Figure 1.2: Lithium reserves and resources in the world in 2020. "Reserves" corresponds to the economically exploitable part and "resources" include all the available minerals in the subsoil. Data from [13].

However, their scarcity poses problems of shortages in the future of the energy transition.

In addition, the electrification of many economic sectors requires many lines and cables to transport and distribute electricity from the producers to the consumers. The main conductor used in these cases is copper, whose demand should explode in the upcoming decades, creating concerns over the capacity of supply. Indeed, the cumulative primary copper demand between 2010 and 2050 is found to be 89.4% of the copper resources known in 2010, and in 2018, 34% of consumed copper was used in power network projects [11].

Finally, the necessity of developing storage systems will increase the consumption of lithium material, with Li/ion batteries being nowadays one of the most mature solutions to store electricity. In addition to the multiple embedded applications, e.g. computers, cell phones, electric vehicles, stationary storage of electricity with big batteries is now being more and more considered, as illustrated by the 100 MW/129 MWh storage system in service in the state of Victoria in Australia [12]. This is boosting the lithium mining industry, which is currently dominated by Chile, as shown in Fig. 1.2 (a). At the same time, more and more countries investigate their potential lithium resources, as shown in Fig. 1.2 (b), which appears to be an economic accelerator in the present context for some countries like Bolivia. However, this rush for lithium could generate problems of supply and would make the energy transition dependent on mining, which brings the well-known socio-environmental problems of this sector [14]. Some solutions to limit the recourse to mining exist,

such as the use of second-hand batteries from electric vehicles to provide grid-scale storage systems [15].

Last but not least, such renewable energy systems need a lot of ground surface for their installation. In the UK for instance, there are some concerns about converting agricultural fields into solar farms, which reduces the food self-sufficiency of the country in terms of crop production [16].

To conclude, it is clear that there is yet no silver bullet to tackle climate change and to significantly boost the energy transition from a technological perspective. However, a wise combination of the existing solutions of clean production of electricity and storage could provide significant advances in the evolution of the electricity sector. Nevertheless, introducing these new technologies into the power systems brings major issues in terms of the operation of the transmission grid which interconnects the producers with the consumers. These changes are developed in the next section.

1.2. Upcoming changes for the transmission grid

1.2.1. More renewable energy

Renewable energy shares in the European Union (EU) is expected to increase drastically in the next decades [17]. In addition to the mature hydro power plants, which are already well developed in some parts of Europe, the EU is pushing for introducing more and more renewable energy sources, at the distribution level with rooftop PV, as illustrated in Fig. 1.3 (a), and at the transmission level, with solar farms or offshore wind farms, as illustrated in Fig. 1.3 (b).

These renewable energy sources have many features that make them truly different from the conventional power plants:

- *distribution*: contrary to the huge power plants, these systems can be installed at the distribution level and incorporated in cities, solar PV panels being much more acceptable than tall smoky pipes;
- *intermittency*: while a thermal power plant's output power can be easily controlled by acting on the amount of fuel to be burnt, wind and solar powers are dependent on weather conditions. In consequence, matching the demand with this type of production at any time is a true challenge;
- *grid interface*: a thermal power plant is coupled with the grid using an electromechanical interface called a Synchronous Generators (SG), which

(a) Installed rooftop PV in Freiburg im Breisgau, Germany.

(b) Offshore wind farm.

Figure 1.3: Examples of renewable energy sources that use power electronics converters.

converts the mechanical power into electricity. For most wind and solar Photovoltaic (PV) systems, the interface with the grid is ensured by Power Electronics (PE) converters, which convert one type of voltage (usually DC) into the desired level of 3-phase AC voltage.

In particular, the role that PE-based interfaces play in the introduction of renewable energy is the focus of this thesis and is developed in the next section.

1.2.2. More power electronics

As explained in Section 1.2.1, more renewable energy means more power electronics in the grid. This increasing share of PE is observed at the distribution level with the distributed generation units [18] and PE-based loads [19] but also at the transmission level, where the development High Voltage Direct Current (HVDC) projects increases [20, 21]. The main functions of HVDC are:

- to enhance the meshing of the grid so that there are more exchanged power capacity between countries. This is even more useful in the case of grids with a large proportion of renewable energy where the intermittancy can be partially compensated for by power exchange;
- to interconnect renewable energy sources such as offshore wind farms with the main grid.

A map of Europe with the present and future VSC-HVDC projects is given in Fig. 1.4. This map shows that even though VSC-HVDC projects were mainly developed in Northern countries in the first place, they are now gaining popularity among public institutions over the entire continent.

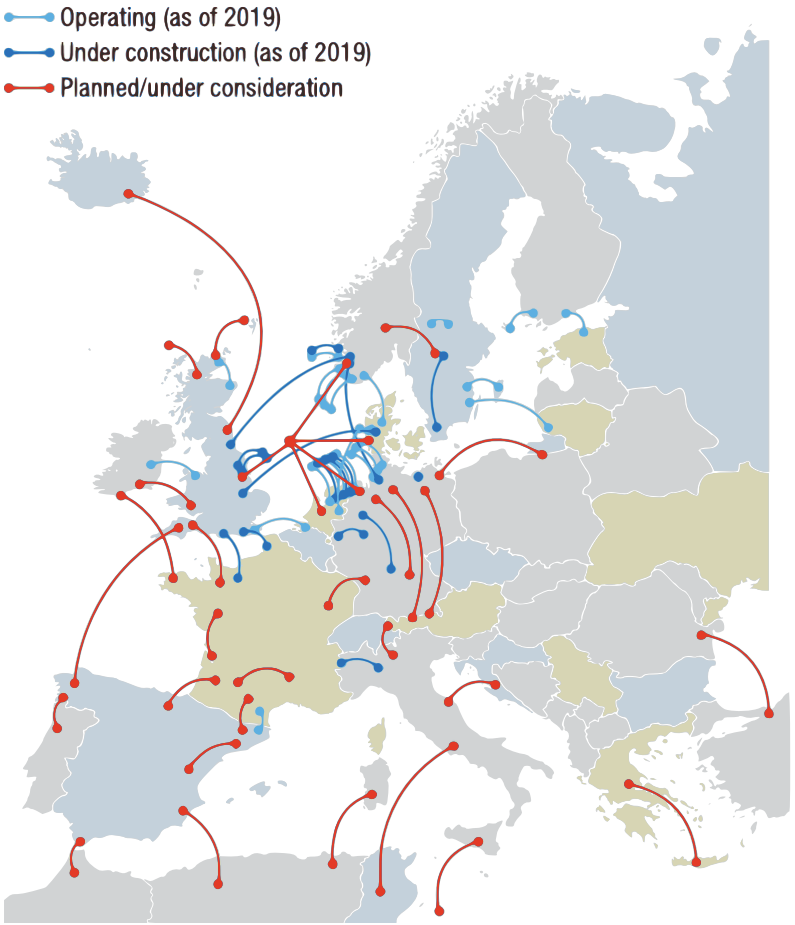

Figure 1.4: Map of Europe including the existing and expected future VSC-HVDC projects to interconnect synchronous and asynchronous areas [20].

In addition, there are also more and more stability-dedicated systems that are installed in the grids: the Flexible AC Transmission Systems (FACTS). Their function is not to inject active power but rather to improve the stability margins and the power transfer capacity of the grid [22]. These devices, such as Static Var Compensators (SVC) or STATCOM, are mainly based on PE as well.

In consequence, it is expected to see in the near future the emergence of PE-dominated systems that will replace the traditional SG-dominated grids. An illustration of such a network is given in Fig. 1.5. The current tendencies are: *a*) the increased share of renewable energy, *b*) the decommissioning of existing power plants and *c*) the interconnection of more areas, in AC or DC. Therefore, the control of such grids is about to be more complex and the operation of such systems must take into account the capacity and limits of PE-based sources.

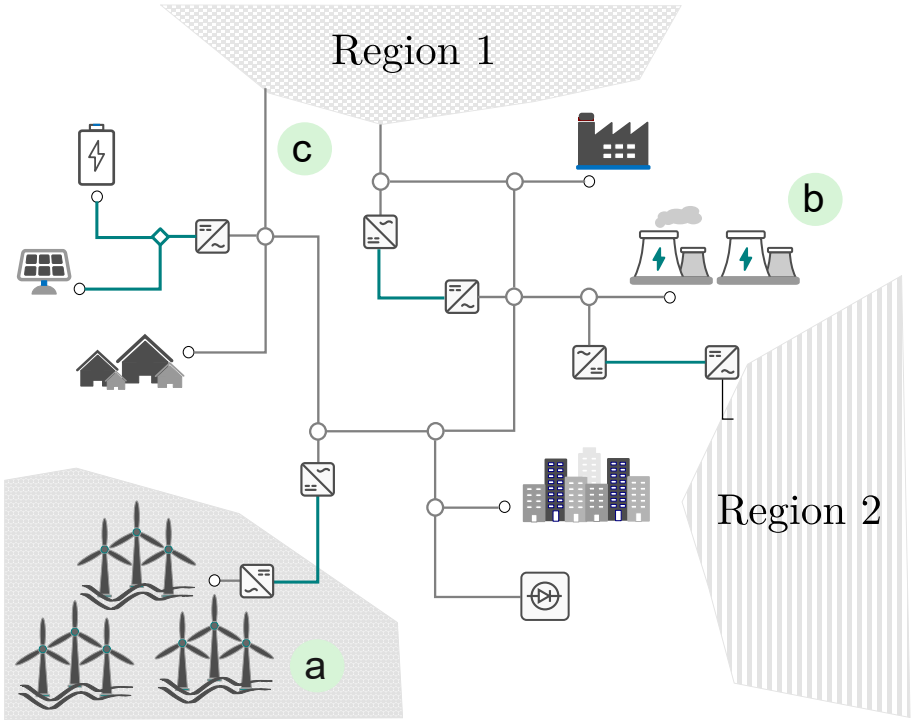

Figure 1.5: Illustrative example of a hybrid power system incorporating synchronous generation and power electronics based sources [18].

In the near future, the reliability of such grids requires the proper operation of the AC and DC grids where the PE-based interfaced will be prevalent. The coordinated control of such grids is one of the main challenges in the power system community.

1.3. Scope and objectives of the thesis

The main objective of this PhD thesis focuses on the control of power converters in the transmission grid, when this grid contains a high proportion of renewable energy. In particular, studying the concept of *grid-forming* control that makes it possible to operate a Voltage Source Converter (VSC) like a Virtual Synchronous Machine (VSM) was one of the objectives of this thesis. This concept had been widely known in the microgrid community to operate 100% grids where all the power could come from PE-based sources [23]. However, there was no consensus regarding its aspects in the power system community, leading to several EU-funded projects to investigate this type of solution, as the MIGRATE project [24].

This PhD thesis deals with the integration of power electronics in the transmission grid and the associated issues with the dismantlement of traditional power plants happening at the same time. It first presents the limits of the classical

converter control mode, i.e. the *grid-following* or *grid-feeding* control, in terms of dynamic behavior and expected support functions. Then, a comparison with the new *grid-forming* control is made and this latter class of control is considered for all the rest of the thesis. Its role in the integration of more VSC-based sources in the grid is studied, regardless of the VSC topology (two-level, three-level or multilevel) nor the DC-side dynamics.

In the second part of the thesis, the focus is placed on MMCs interconnecting offshore wind farms using HVDC links. In consequence, the DC-grid dynamics are integrated in the study and the specificities of MMC technology are considered to operate the converter in grid-forming mode. The control of the MMC is studied in terms of the stability of the AC/DC grid and more specifically the DC voltage and the AC frequency. Most of the disturbances studied in this work are power disturbances such as load steps or loss of parts of the DC-grid power. However, more serious disturbances such as line tripping or generator losses were also considered in this work to study the robustness of the proposed methods. On the contrary, the behavior of grid-forming controlled VSCs under AC faults [25] remains out of the scope of this PhD thesis.

To summarize, this thesis is about the control and operation of VSCs, with a focus on MMCs in HVDC systems integrating renewable energy sources. This work deals with the stability of the AC/DC system when operating a converter in grid-forming mode and thus is about the control of the conversion unit. There is no considerations about the internal dynamics of the renewable sources, even though such considerations could extend the results of this work.

1.4. Main contributions

The main contributions of this thesis are summarized below:

- An overview of the existing control strategies has been given. In addition to the existing literature, a comparative analysis of the main grid-following and grid-forming controls has been performed regarding their potential from the converter and the grid perspectives;
- In Chapters 4 to 6, a simple constant power source model has been considered to take into account the DC-side dynamics when operating a converter in grid-forming mode. This was novel compared to similar work in the literature. The combination of the DC-voltage controller with the grid-forming control was another contribution;

- When the DC grid is considered as a constant power source, the power cannot be adjusted, which is a problem when AC frequency-related services are considered. In this case, we proposed a methodology to calculate the necessary internal energy from an MMC to provide similar inertial response as SGs. To complement, a control law has been designed and tuned to use this energy accordingly.
- In order to optimize the use of the MMC internal energy, an optimal control solution based on Model Predictive Control (MPC) has been proposed to control the MMC internal energy using an online optimization tool. This approach makes it possible to use the MMC internal energy to support the AC frequency and DC voltage in transient depending on the type of disturbance to the system;
- The main problem of sophisticated solutions such as MPC is that there are many technical and computing issues related to their usage in fast industrial systems such as power electronics. Another contribution of this thesis is to prove the feasibility of this kind of controller in a real-time target. This controller was synthetized in C and tested upon a physical mockup of an MMC in real-time conditions.

1.5. List of publications

During the three years of work on this project, several publications have been submitted, peer-reviewed and published in scientific journals and international conferences. Some of them were still in the peer-reviewing process when the manuscript was sent to the PhD thesis committee. The list of the publications can be found below:

Journal papers

- **Journal I** [26]: Rayane Mourouvin, Juan-Carlos Gonzalez Torres, Jing Dai, Abdelkrim Benchaib, Didier Georges, Seddik Bacha. Understanding the role of VSC control strategies in the limits of power electronics integration in AC grids using modal analysis, *Electric Power Systems Research*, March 2021.
- **Journal II** [27]: Rayane Mourouvin, Jing Dai, Seddik Bacha, Didier Georges, Abdelkrim Benchaib. An Overview on the Recent Advances of the Voltage Source Converter Control Modes in Terms of their Roles in Transmission Grid Ancillary Services (under review).

- **Journal III** [28]: Rayane Mourouvin, Louis Filliot, Antoine Ghyselinck, Jing Dai, Seddik Bacha, Didier Georges, Abdelkrim Benchaib. Real-time Hierarchical MPC Applied to an MMC in Grid-Forming Mode: Implementation and Validation in Power Hardware-in-the-Loop (in submission process).

Conference papers

- **Conference I** [29]: Rayane Mourouvin, Kosei Shinoda, Jing Dai, Abdelkrim Benchaib, Seddik Bacha, Didier Georges. AC/DC Dynamic Interactions of MMC-HVDC in Grid-Forming for Wind-Farm Integration in AC Systems, *Proceedings of the 2020 22nd European Conference on Power Electronics and Applications (EPE'20 ECCE Europe)*, Lyon, France, September 2020.
- **Conference II** [30]: Rayane Mourouvin, Jing Dai, Sjoerd Boersma, Seddik Bacha, Didier Georges, Abdelkrim Benchaib. Model Predictive Control for AC/DC Energy Management of a Modular Multilevel Converter Operated in Grid-Forming Mode, *Proceedings of the 2021 European Control Conference (ECC)*, Rotterdam, Netherlands, June 2021.
- **Conference III** [31]: Rayane Mourouvin, Jing Dai, Seddik Bacha, Didier Georges, Abdelkrim Benchaib. Energy Requirements of Modular Multilevel Converter Submodules and High-level Control Design for Synthetic Inertia Function, *Proceedings of the 2021 23rd European Conference on Power Electronics and Applications (EPE'21 ECCE Europe)*, Ghent, Belgium, September 2021.
- **Conference IV** [32]: Juan-Carlos Gonzalez Torres, Rayane Mourouvin, Kosei Shinoda, Ahmed Zama, Abdelkrim Benchaib. A Simplified Approach to Model Grid-Forming Controlled MMCs in Power System Stability Studies, *Proceedings of the 2021 IEEE PES Innovative Smart Grid Technologies Europe (ISGT-Europe)*, Espoo, Finland, October 2021.

Interdisciplinary report

- **Credited as contributing author in** [18]: Irina Oleinikova, Emil Hillberg. micro vs MEGA: trends influencing the development of the power system, *ISGAN report*, 2020.

1.6. Organization of the manuscript

The manuscript is organized as follows:

- In Chapter 2, a state of the art of the existing converter control modes is presented. In particular, the different control modes are compared and their relevancy is assessed regarding the main ancillary services that used to be provided by synchronous generators;
- In Chapter 3, a stability analysis of the main converter control modes, namely *grid-following* and *grid-forming*, is presented in order to assess the power electronics penetration limits in hybrid grids with remaining synchronous generators.
- In Chapter 4, we focus on the role of HVDC technology, especially the applications of the high-voltage Modular Multilevel Converters to Offshore Wind Farm (OWF) interconnection with AC grids. The originality of this work is to take into account the DC grid dynamics and to propose a novel way to calculate the energy requirements of the MMC to provide inertial support to the AC grid;
- In Chapter 5, Model Predictive Control (MPC) is applied to optimally control the MMC internal energy and the DC grid voltage. This control solution is implemented using an identified model of the AC grid and its performances regarding disturbance rejections are compared to the state-of-the-art control structure which relies on two PI controllers. Its behavior and robustness with respect to parameter uncertainties and setpoint changes are assessed in a second time;
- In Chapter 6, the application of grid-forming control to MMCs as well as the MPC layer developed in Chapter 4 and Chapter 5 are validated using a real-time controller which is applied to a physical mockup of an MMC. In particular, the concept of grid-forming is applied to the MMC mockup which makes it possible to synchronize with the grid without any PLL. Second, the hierarchical MPC approach developed in Chapter 5 is implemented in C and made compatible with the rest of the control structure developed in Matlab/Simulink.
- In Chapter 7, a conclusion of the main contributions of this PhD thesis is drawn and the assumptions considered in this work are discussed. In a second time, potential novel lines of research are presented to extend the results of this thesis.

Chapter 2

State-of-the-art of existing control solutions for Voltage Source Converters to support the Transmission Grid

This chapter is based on the journal publication (under review) ***Journal II****.*

2.1. Context and literature review

2.1.1. Context

Power systems now encounter massive changes in terms of generation, transmission and distribution of electricity. In the European Union, the share of renewable energy in electricity generation is expected to rise constantly for the next decades [17], in a worldwide attempt to tackle climate change [9]. In particular, at the transmission-grid level, especially in Europe, many HVDC systems have been built to exchange energy across long distances and interconnect Offshore Wind Farms (OWF) to the

mainland [33]. At the distribution-grid level, Power Electronics (PE) converters are used to integrate renewable power sources [34] and new types of loads, such as islanded systems [35, 36] and electric vehicles [36]. These changes will lead to an evolution of the operation of power systems, where a large number of Synchronous Generators (SG) will be replaced by PE-interfaced sources and loads [18].

2.1.2. Literature review

To ensure stability of such power systems in the future, the PE converters will have to play the roles of traditional SG. This topic has been discussed for years in the scientific community [37] and draws public attention [38]. In particular, the current methods we know to operate and secure the power systems will have to evolve. In order to understand the necessary conditions to operate these PE-dominated grids, we need to analyze the elementary functions that are brought by synchronous generators. Traditionally, the grid stability and reliability is ensured by implicit actions from generators themselves and by specific actions which require additional controls, such as primary frequency support or Power System Stabilizers (PSS) or dedicated equipment such as synchronous condensers or FACTS. In various regions of the world, some of these functions are allocated using ancillary services market [39–41]. In parallel, with the growing role of PE-based converters, more and more studies now focus on the potential contributions of VSCs to the operation of 100% PE-based grids, such as microgrids [23], offshore networks [42] and HVDC transmission grids [43, 44]. However, these papers only deal with the control options, instead of addressing the needs of the grid. In the last decades, a consistent classification of the power system stability issues has been used as a reference for transmission grid operability and stability [45]. But it is only recently that this classification has been adapted to take into account the increasing role of VSCs in the grid [46], but no classification of the existing control solutions for any of those issues is achieved.

More recently, the impacts of VSC control to provide specific support functions to the common system stability issues was discussed in [47], which only focuses on vector-controlled, also named current-source controlled, VSCs and only briefly mentions the role of grid-forming. On the other hand, some recent studies [48, 49] did compare the role of different grid-forming implementations in multi-machine systems but did not compare them to the most commonly used current-source mode. Indeed, even though there has been some research conducted on classifying those different grid forming controls [50, 51], there is still a missing piece between

what can be achieved in terms of ancillary services, i.e. from the grid point-of-view, by the different VSC control modes. In [52], the authors study the evolution of power systems and how it will affect the existing ancillary services. Although it provides insightful review of the implementation of new ancillary services, it does not focus on the control aspects of the VSCs. In [53], the authors present a review of the support functions of VSC for microgrids, but this work is specific to low-voltage systems and do not discuss wide-area issues such as frequency support or power oscillation damping for instance. Some papers proposed a review of specific support functions of VSCs for transmission grids, such as inertia [54], short-circuit contribution for unbalanced faults [55] and power sharing options, both active and reactive, hence integrating grid-forming controls [56]. In addition, more recent reports were published about the role of grid-forming controlled VSCs in grid support functions [36, 57]. However, no comparison is clearly drawn with the most commonly-used current-source controls. In parallel, the role of the grid-forming controlled VSCs in enhancing the PE-based sources penetration limits using modal analysis have been the topic of several studies [26,58,59] but these papers are mainly based on simplified systems and it is hard to extract the precise role of each support function when applied to more complex systems. To the authors' best knowledge, there is no review in the literature which focuses on the different VSC control options for the needed support functions from the transmission grid perspective.

2.1.3. Chapter summary and contents

In this chapter, we gather information about the existing grid services that are currently provided by synchronous machines and that will be needed from the VSCs to ensure a smooth transition to hybrid grids with remaining synchronous units and a high proportion of PE-based converters. The novelty of this chapter is to propose a comprehensive comparison of the converter control modes, i.e. current-source and voltage source modes, not only in terms of converter-level control performances, but also in terms of the potential ancillary services they can provide to the grid.

The chapter is organized as follows. In Section 2.2, we describe the ongoing evolution of power system production and transmission structures and the role of SGs in power system stability. In Section 2.3, the VSC control modes are introduced and an updated classification is defined for the transmission grid. In Section 2.4, the role of the VSC in both current-source and voltage-source modes are explored in terms of the grid support functions. Finally, an overview of the differences is drawn in Table 2.3 and discussed in Section 2.5.

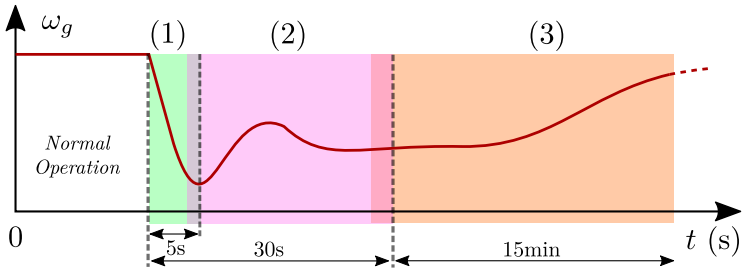

Figure 2.1: Different mechanisms with distinctive time scales of the grid frequency when encountering an active power disturbance. (1) is for inertial response, (2) is for primary frequency control and (3) is for secondary frequency control.

2.2. Impacts of the replacement of SGs by Power Electronics-based Stations

The role of the SGs in power systems has been studied for decades [60,61], and their services to the grid are summarized in this section, in particular, frequency support, reactive power support, contribution to system strength, short circuit contributions and power oscillation damping.

2.2.1. Frequency support

Traditionally, the grid frequency is mainly supported by the synchronous generators which provide a frequency response following a contingency in the form of an unbalance between the generation and the load. A typical frequency profile of such response is given in Fig. 2.1, where the different mechanisms are highlighted in terms of the time constant:

- *Inertial response*: The physical law imposes that, in case of a frequency deviation, the SG instantaneously releases the kinetic energy in its rotor, which reduces the Rate of Change of Frequency (RoCoF).
- *Primary frequency control*: The speed governor, usually in form of a droop, adjusts the mechanical power from the prime mover in the time scale of 30 seconds, in order to stabilize the frequency.
- *Secondary frequency control*: The secondary frequency regulator, with a time constant of 15 minutes, adjusts the mechanical power of the synchronous generators of the control area where the disturbance originates, in order to bring back the grid frequency to 50 Hz and restore the power exchange between the control areas.

2.2.2. Reactive power support

The reactive power support refers to the capacity of a given system to provide some reactive power which is used to maintain the grid voltage. For this, the SG are equipped with an Automatic Voltage Regulator (AVR), which observes the voltage magnitude and adjusts the reactive power accordingly. Indeed the reactive power compensation is used to maintain the grid voltage within acceptable limits. This support is often seen as an ancillary service from the TSO point of view [62]. It can be separated in two types [62, 63] according to the time scales:

- *dynamic support*: it refers to the capability to control the bus voltage magnitude following a disturbance. The Belgian TSO Elia defines it as a voltage control that *"is activated automatically by the user's production units"* [63]. This is provided by the SGs' AVRs for instance;
- *static support*: it refers to changes of reactive power references in a given grid in order to support the AC grid voltage at all nodes. This corresponds to a centralized action dictated by the regional TSO. It is triggered *"either automatically or manually depending on the situation"* [63].

To illustrate the role of reactive power in voltage control, a simple case system is given in Fig. 2.2 (a). The reactive power received at the bus 1, denoted by Q_R can be calculated, with phasor assumptions [64], as:

$$Q_R = \frac{V_1}{X}(V_2 \cos\delta - V_1) \tag{2.1}$$

$$Q_R \approx \frac{V_1}{X}(V_2 - V_1) \tag{2.2}$$

Fig. 2.2 (b) gives the evolution of Q_R using (2.2) and shows the importance of acting on the reactive power to control the AC voltage magnitude. In practice in traditional power systems, the operating points of SGs are determined in power flow studies in order to avoid line congestions and have acceptable voltage magnitude levels [65] but the TSOs also rely on automatic voltage control actions to maintain the bus voltages following unexpected disturbances.

2.2.3. System Strength

The system strength, or voltage stiffness, is a metric that quantifies the capability of a given AC bus to maintain the bus voltage around its nominal setpoint, in terms of both voltage magnitude and phase angle. In its 2016 System Operability Framework [66], the British TSO National Grid gives the following definition in the voltage management section:

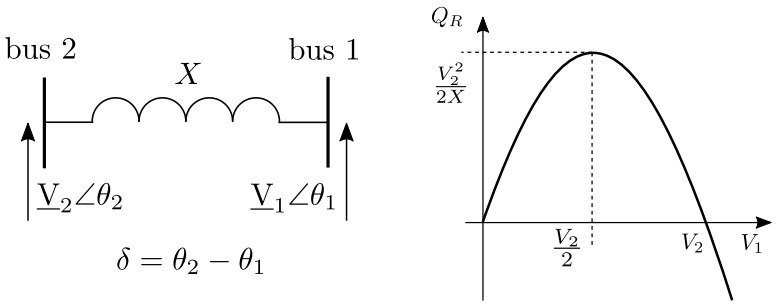

(a) Simplified view of a two-bus system interconnected with a purely inductive line.

(b) Reactive power evolution around small disturbances ($\delta = 0$).

Figure 2.2: Approximation of the reactive power steady-state value depending on the voltage magnitude [64].

"System strength is a regional characteristic which can be expressed as short circuit level (SCL), measured in kA. It provides an indication of the local dynamic performance of the system and behaviours in response to a disturbance."

With this definition, it is clear that a bus connected to a voltage source, such as an SG, has a stiff voltage since the generator controls its voltage magnitude thanks to its AVR. To quantify the system strength of a grid dominated by SG, the power system community has used for decades the notion of Short-Circuit Level (SCL) or Short-Circuit Ratio (SCR) [67], defined as the amount of fault current that will be injected to the bus in case of a fault normalized with the bus base power. This means that for a given voltage, the higher the SCR is, the closer it is to SGs since the equivalent impedance to the faulty bus is smaller. Nowadays, the system strength is considered as a rising issue because a low value of SCR can create stability problems due to the PE-based source controllers [46].

Although the SCR is a single notion to study the system strength, it actually contains two different power system issues: the system strength at the given bus discussed in this subsection, and the contribution to the short-circuit current, discussed in the next subsection.

2.2.4. Short-circuit contributions

The voltage-source behavior of the machine and its large overcurrent capacity make it possible to inject a high short-circuit current in case of a fault, which is essential for the proper operation of the protective relays. The SGs inherently provide a Short-Circuit Contribution (SCC) when a fault occurs. Indeed, during the first instants

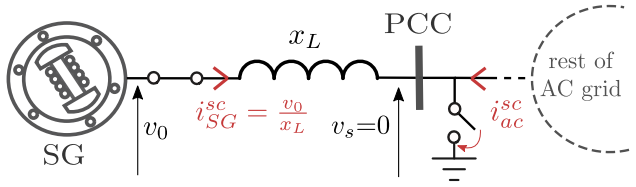

Figure 2.3: Grid-connected synchronous generator response when encountering a fault at its point of coupling.

following the fault, the machine remains connected and injects a fault current which can be as high as 500% of the nominal current [68]. This behavior is illustrated in Fig. 2.3. As shown in this figure, from the point of view of the faulty bus, all the fault currents from the SG and the other AC grid fault currents converge to it. These fault currents are valuable because they are used to detect and locate the fault in the AC grid. Note that, similar to the inertial response, the short-circuit contribution is also a natural behavior of the SG, i.e. no additional control is needed to realize this. However, this feature is based on the voltage-source behavior of the SG which still relies on the AVR performances during the fault.

2.2.5. Power oscillation damping

Power oscillations refer to low-frequency oscillations, in the range of 0.1 to 1 Hz, which are due to structural limits of the system when certain large-scale disturbances (synchronous generator loss, line tripping, ect) occur. They are mainly due to the poor damping of low-frequency modes which exist in power systems where the loads and production units are not regularly distributed or where the transmission lines are relatively long [69]. These oscillations must be taken care of because they provoke power oscillations which generate more losses and can cause the tripping of lines. To solve this problem, the Power System Stabilizer (PSS) [64] can be added to the AVR to improve the damping of power oscillations.

However, this problem is still an up-to-date topic because the locations of the SGs equipped with PSSs plays a major role on the damping factor of the whole system. An illustrative case of inter-area oscillations which occured in Europe in 2017 [70] is given in Fig. 2.4. In this example, 0.3Hz oscillations were noticed by European TSOs in December 2017 between the Northern and Southern parts of Europe. The root cause was not a single large-scale event but rather a sum of different low-risk factors in South Italy.

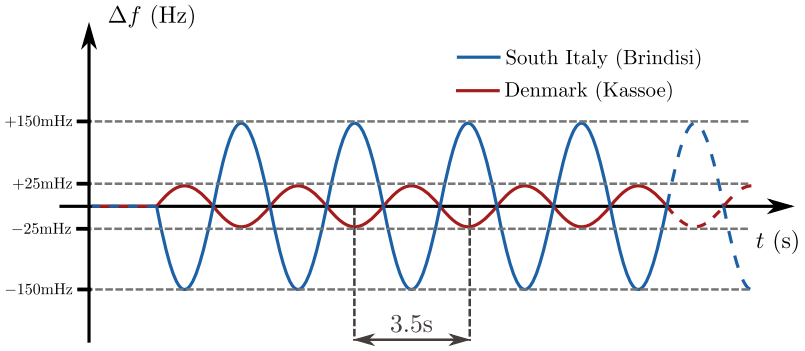

Figure 2.4: Illustration of the inter-area oscillation event of the 3rd of Dec. 2017 in the European grid. Based on [70].

This event shows the importance of the PSSs allocation, since the disturbance severity can be drastically different depending on the grid node, as described in Fig. 2.4.

2.2.6. Consequences of the SG dismantlement on system stability

As synchronous generators are being progressively replaced by PE converters, all the functions described earlier in this section will have to be fulfilled in transitional grids with high proportion of PE and the remaining SGs. This issue is gaining more and more attention from academia [71] and industry [24] across the world.

In 2017, a list main challenges on power system stability were highlighted by European TSOs [24], of which the following items are related to the replacement of SGs by PE-based generation units:

1. Decrease of inertia;
2. Reduction of transient stability margins;
3. Wrong participation of PE-based generators in frequency containment;
4. Loss of devices in the context of Fault-Ride-Through (FRT) capability;
5. Lack/excess of reactive power;
6. Voltage dip-induced frequency dip;
7. Introduction of new power oscillations and loss of existing power oscillation dampers (such as PSS of SGs).

Taking the first one for instance, the inertia of most of the European countries is expected to decrease due to the increasing of renewable generation in the electricity mix. The expected equivalent inertia constants of different European countries by 2030 is given in Table 2.1.

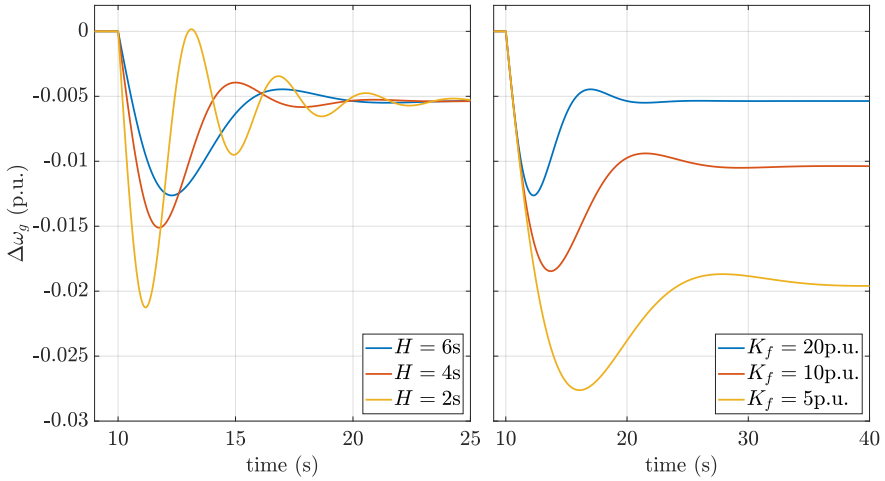

Figure 2.5: Effects of decreasing inertia and primary frequency reserves in AC grid frequency ω_g. H is the inertia constant and K_f the primary frequency droop gain. The nominal case (blue line) is $H = 6$s and $K_f = 20$ p.u.

Inertia (s)	**Countries**
H $<$ 2s	Germany, Italy, Ireland, Spain, UK.
2s $\leq$ H $<$ 3s	Austria, Switzerland.
3s $\leq$ H $<$ 4s	Finland, France, Norway, Sweden.
H $\geq$ 4s	Hungary, Poland, Serbia.

Table 2.1: Inertia contributions of different countries in Europe following ENTSO-E 2030 scenario [36].

This table shows that countries which would rely on massive renewable sources such as Southern European countries with solar power or Northern Sea countries with wind power, would have a low inertia contribution. On the other hand, Central European countries which still rely on coal-powered plants would have a much higher inertia. Finally, countries that have started to introduce renewables in their electrical systems but still rely on low-carbon power plants, either hydro or nuclear, would be in-between.

In consequence, there is a need to counterbalance the impacts of dismantling current power plants in order to maintain the system operable. In Fig. 2.5 we illustrate the consequences of decreasing inertia and the deployment of primary frequency reserves following an active power load step in the frequency deviation of a two-bus system with one SG and one load. The lack of inertia may cause the tripping of certain components due to an excessive value of RoCoF.

2.2.7. Opportunity of the use of power electronics in transmission grids

Even if many challenges arise due to this grid transition, PE-based sources may offer innovative solutions since these interfaces are much more controllable and faster than typical SGs. In addition, as illustrated in Table 2.2, the integration of renewable energy sources such as OWF, here denoted as wind power plants, the grid-side converter rarely works at its maximum rated power due to wind intermittency mostly. The average active power setpoint can be derived as follows. The maximum active and reactive power headroom from this average setpoint are then calculated while assuming the initial reactive power setpoint is $q^* = 0$:

Features	**symbol**	**Wind Power Plant**	**Thermal Power Plant**
Installed capacity, from [72]	S_b	2500 MVA	1000 MVA
Operating hours, from [72]	t_{op}	2000 h	5000 h
Yearly produced energy, from [72]	W_y	5000 GW.h	5000 GW.h
Overcurrent capability, from [73]	i_{max}	110%	500%
Average power setpoint	p^*_{avg}	0.23 p.u.	0.57 p.u.
Max. active power headroom	P_{hr}	0.77 p.u.	0.43 p.u.
Max. reactive power headroom	Q_{hr}	0.97 p.u.	0.82 p.u.

Table 2.2: Comparison of the characteristics of a SG and a VSC in terms of available power headroom and energy for support function provisions.

$$p^*_{avg} = \frac{t_{op}}{t_{year}} = \frac{t_{op}(h)}{8670} \tag{2.3}$$

$$P_{hr} = S_b \times (1 - p^*_{avg}) \tag{2.4}$$

$$Q_{hr} = S_b \times \sqrt{1 - {p^*_{avg}}^2} \tag{2.5}$$

It appears that the active power at the operating point of the converter is quite low, here assumed to be at $p^*_{avg} = 0.23$ p.u.. In consequence, there would be a lot of power headroom, both active and reactive, available in average, to counterbalance the progressive dismantlement of SGs and the upcoming challenges listed above. This will still require to implement additional control options, which are summarized in Sections 2.3 and 2.4.

2.3. Converter-level control modes

This section presents the existing converter control modes classified into two main categories: current-source mode and voltage-source mode. The state variables we use in the control schemes are based on the equivalent VSC with its LC filter described in Fig. 2.6.

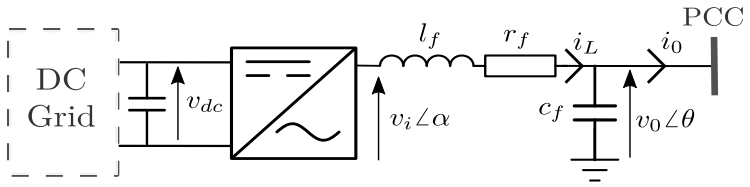

Figure 2.6: Equivalent electrical circuit of a Voltage Source Converter (VSC) between its AC and DC interfaces.

2.3.1. Current-source mode

The current-source control, also known as grid-following or grid-feeding control, is the most commonly used method, where the converter imposes both the active and the reactive power, independent of the grid frequency and voltage. The controller receives the power setpoints and yields the reference for the current to be injected into the grid. Thus, the converter works as a current source, i.e. the current (and hence the active and reactive power) is controlled while the voltage magnitude and the frequency is free to change. Note that the power reference itself can be varying due to other factors, e.g. the intermittency of renewable energy sources, or an over-layer controller providing some grid service.

A classical implementation of the grid-following control is shown in Fig. 2.7. The voltage at the point of common coupling (PCC) is denoted as v_0, while the voltage synthesized by the converter as v_i. A reactor l_f is placed between the two voltages. With a properly synthesized v_i, the power exchanged between the converter and the AC grid across the reactor l_f follows its reference.

In Fig. 2.7, the current and the voltage in the natural *abc* frame are transformed in the synchronous *dq* frame, and a cascaded control is used. The control is composed of four blocks:

- *Phase-Locked Loop (PLL)*: it observes the three-phase voltage at the PCC located between the converter and the AC grid, and estimates its angle θ, as illustrated in Fig. 2.8. This information will be used by the other blocks.

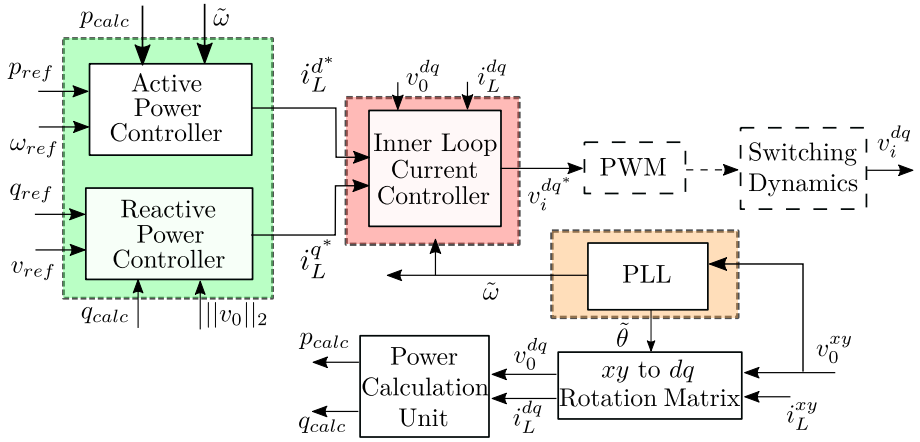

Figure 2.7: VSC cascaded structure control scheme in current-source mode.

- *Outer power loop*: based on p_{ref} and q_{ref}, the reference values of active and reactive power, the outer power loop calculates the current references, denoted by $i_L^{d^*}$ and $i_L^{q^*}$, which are then sent to the inner current loop. By aligning the grid voltage to the d axis, p and q can be decoupled and thus controlled independently. In particular, p depends only on i_L^d while q only on i_L^q. To calculate $i_L^{d^*}$ and $i_L^{q^*}$ based on p_{ref} and q_{ref} respectively, the control structure in Fig. 2.7 uses the measurement of the PCC voltage to generate the current references, where p_{ref} and q_{ref} are simply divided by the grid voltage to obtain $i_L^{d^*}$ and $i_L^{q^*}$. An alternative way to calculate the current references is to use closed-loop control, where PI controllers compare the power references with the measured and filtered power, and then adjusts the current references.
- *Inner current loop*: based on the current references $i_L^{d^*}$ and $i_L^{q^*}$ sent by the outer power loop, the inner current loop calculates $v_i^{d^*}$ and $v_i^{q^*}$, the desired voltage to be synthesized by the converter, which are then sent to the PWM block. The PI controllers compare the current references with the measured currents, and then adjusts the voltage references. This inner loop is used to control the current flowing through the converter and limit potential overcurrents. More information about the tuning can be found in [2].
- *Pulse-Width Modulation (PWM)*: based on the $v_i^{d^*}$ and $v_i^{q^*}$ given by the inner current loop, the PWM generates the gate control signals, which are sent to the switches of the 2-level VSC so that the fundamental component of the obtained voltage is the desire voltage. In case of the other types of VSC, such as Modular Multilevel Converters (MMC), adequate control should be implemented to synthesize the desired voltage [74].

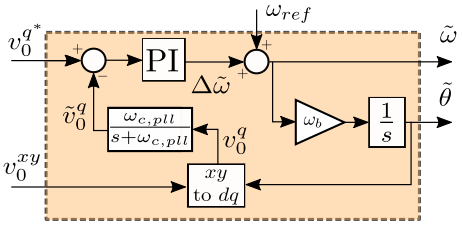

Figure 2.8: Detailed control scheme of a classical PLL [75].

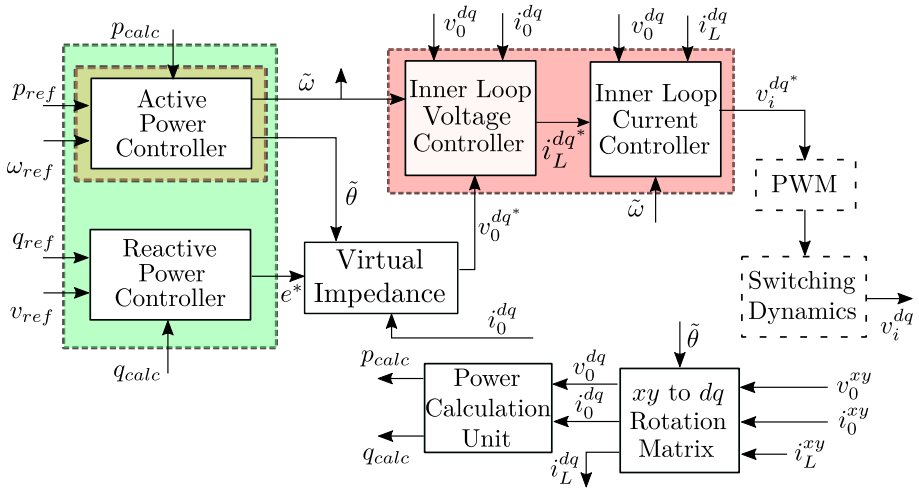

Figure 2.9: VSC cascaded structure control scheme in voltage-source mode.

The grid-following control is not capable of feeding a passive network, because it always needs a grid voltage to follow, whose frequency and magnitude should be regulated by synchronous machines or converters working in other control modes. When left unregulated, the grid voltage and frequency may deteriorate and result in a voltage collapse, which is unacceptable from the demand-side point of view.

2.3.2. Voltage-source mode

This control mode, which is also referred to as grid-forming control, has emerged in islanded microgrids first [23]. In this mode, the VSC operates as a voltage source and, in consequence, generates a voltage of desired magnitude and frequency at the connecting bus.

The general scheme is given in Fig. 2.9. The voltage at the PCC, denoted by v_0, is also the voltage of the capacitance c_f. This capacitance can be the physical capacitance of an LC filter [76] or the capacitance of an AC component such as an overhead line or underground cable [77] if there is no filter. The control scheme is composed of the following blocks:

- *Outer power loop*: based on the voltage and current measurements at the PCC, the control loop calculates the active and reactive powers which are compared with the references. The control errors of active and reactive power are used to adjust, respectively, its frequency $\tilde{\omega}$ and voltage magnitude e^*. This function reflects the principles of grid-forming which will be detailed in Section 2.3.3.
- *Virtual impedance*: when several VSCs are working in voltage-source mode in parallel, this block can be used to eliminate the circulating currents between them. In fact, it changes the voltage reference e^* sent by the outer power loop to emulate an additional impedance between the controlled voltage v_0 and the PCC to generate the voltage reference $v_0^{dq^*}$ which is used for the inner control loops, as described in [76].
- *Inner control loops*: in addition to the inner current control similar to the one in Section III-A for the grid-following control, there is also an inner voltage control law that controls v_0^{dq} using PI controllers and generates current references $i_L^{d^*}$ and $i_L^{q^*}$ for the current controller. More information about the tuning can be found in [78].
- *Pulse-Width Modulation (PWM)*: similar to the one in Section 2.3.1.

There are in the literature different variants of grid-forming control, which depends on the way the power variations and the voltage references are coupled in the outer power loop. In particular, in Fig. 2.10 (c), the droop-based grid-forming control [78–81] couples the active power deviation with that of the VSC estimated frequency $\tilde{\omega}$. The virtual inertia and load sharing of the grid-forming control can be tuned by acting on the low-pass filter cutoff frequency ω_{pq} and the droop gain $m_{p\omega}$ given in Fig. 2.10 (c).

It is important to note that the vf control, also known as voltage and frequency control [51], which basically imposes a constant voltage magnitude e^*, usually 1 p.u., and a constant frequency $\tilde{\omega} = \omega_{ref}$, usually 50 Hz or 60 Hz, may also be referred to as grid-forming control in microgrid literature [23]. In fact, vf mode can be seen as a particular case of the scheme given in Fig. 2.9 where the outer loops are bypassed and the references are fixed values of e^* and $\tilde{\omega}$.

2.3.3. Classification in the context of transmission grids

Thanks to the small size of a microgrid, a grid-forming converter is able to impose by itself the frequency to the whole system. However, in the context of a transmission grid, one single converter, which is of much smaller rating than the whole synchronous area, would become incapable of imposing the frequency

on its own. Therefore, compared to its original definition in the microgrid where the converter behaves as a voltage source with imposed frequency and voltage magnitude, the grid-forming control in the transmission system is slightly different, and the following classification can be used instead:

- *Grid-following*: the converter works as a current source that injects power without consideration on the grid conditions.
- *Grid-supporting*: the converter works as a current source and modulates its power references with respect to the initial load flow conditions to provide voltage, frequency or angle support. In other words, the grid-supporting combines the current-source working mode with an external control modulating the power references. A commonly-used method for controlling the active and reactive powers using a PI control is given in Figs. 2.10 (a) 2.10 (b);
- *Grid-forming*: the converter works as a voltage source and provides voltage and frequency support. However, the frequency imposed by the converter will not be the nominal frequency, but such that the resulting power and the frequency are coupled to emulate the behavior of SM. The differences between existing grid-forming controls lie in the different control designs of their active and reactive outer power loop and the coupling between them. In addition to the droop-based control given in Figs. 2.10 (c) 2.10 (d), other options exist, such as emulation of Synchronous Machines (SM) [82–87] and more advanced control-oriented strategies [88,89]. Besides, some comparisons were drawn between different grid-forming options in microgrids [90] and in transmission grids [91,92] and showed similar small-signal behaviors and compatible control laws between each other. However, the transient stability analysis showed different behaviors of the grid-forming options [93].

Note that the above classification, borrowed from [23], is somewhat an abuse of language, because the classification criterion is a mixture of the control method and control objective. On the one hand, in terms of the control method, the grid-supporting control resembles the grid-following since both have the converter working as a current source; on the other hand, in terms of the control objective, the grid-support control seems closer to the grid-forming control, since both make the converter to contribute to the voltage and frequency regulation. In other words, to support the frequency, one can either use the grid-supporting control where a Δp^* term is added in the active power controller of the converter working as a current source, as described in Fig. 2.10 (a), or alternatively, use the grid-forming

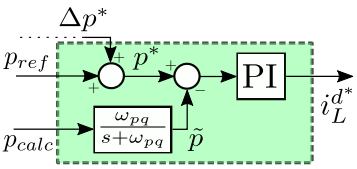

(a) Active power control loop with PI controller in current-source mode

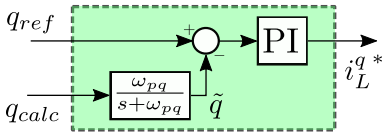

(b) Reactive power control loop with PI controller in current-source mode

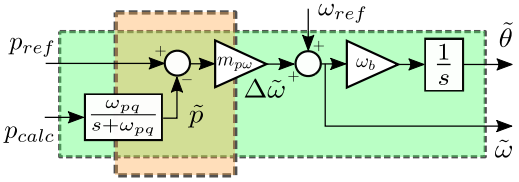

(c) Droop-based active power control loop in voltage-source mode

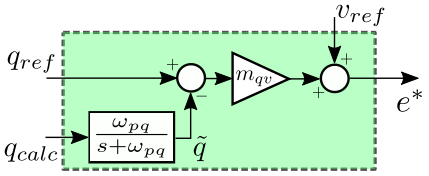

(d) Droop-based reactive power control loop in voltage-source mode

Figure 2.10: Examples of the outer power control loops of the VSC in current and voltage source modes respectively.

control as described in Fig. 2.10 (c). In addition, the active power controller of the grid-forming scheme from Fig. 2.9 plays a double role as described in Fig. 2.10 (c). Indeed, it provides a PLL-free synchronizing unit [79] and makes the VSC contribute to frequency support as SGs do, i.e. by providing both synthetic inertia and primary frequency response [76].

In terms of performances, grid-following control is designed to ensure a good power tracking of the power references p_{ref} and q_{ref} using a dedicated controller as in Figs. 2.10 (a),2.10 (b). However, the behavior of the VSC relies on strong grid assumptions, i.e. with a high SCR and the VSC can even become unstable if connected to a weak grid (SCR<3). On the other hand, the grid-forming control has a power tracking capability thanks to its power controller shown in Figs. 2.10 (c),2.10 (d) but since it behaves as a voltage source, its AC power response depends on the SCR. However, it is capable of working in weak grid conditions as well, on the contrary to grid-following controlled VSCs. These conclusions are shown in Fig. 2.11 where simulations were carried out using a simple benchmark containing a VSC model based on Fig. 2.6 which is connected to an infinite bus through a transformer and a line modeled with a dynamic phasor model.

2.4. Grid-level control modes

With the current-source and voltage-source modes described at the converter level in Section 2.3, this section presents their services from a grid point of view.

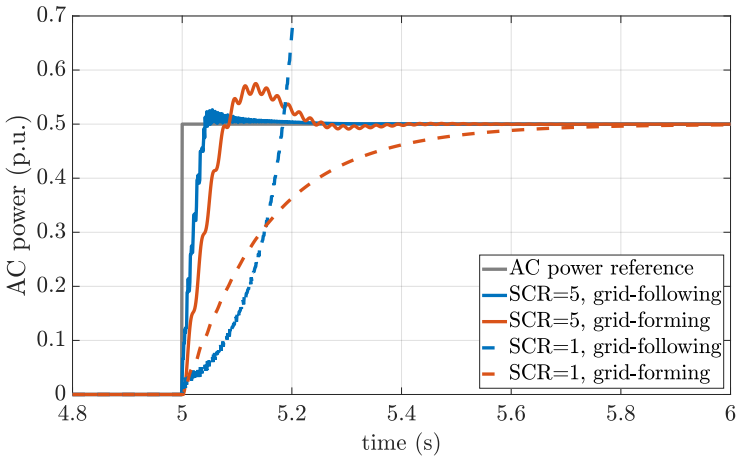

Figure 2.11: Influence of the SCR on the performances of the VSC in terms of power tracking, following a 0.5 p.u step of p_{ref}. The test-case is based on [94] with PLL gains taken from [95].

2.4.1. Frequency support

Contrary to SGs whose frequency response is a combination of the physical behavior and explicit control, the VSC output power is entirely decoupled from the grid frequency behavior in grid-following mode. However, there are different active power profiles that can be provided by the VSC to support the grid frequency:

- *Active power / frequency droop*: developed in [96–99], its aim is to provide an active power response that is proportional to the measured frequency deviation as described in Fig. 2.12 (a). This control scheme is inspired by the primary frequency control of traditional SGs given in Fig. 2.1. In consequence, the VSC takes part in the load sharing with the SGs.
- *Virtual inertia*: as in [100, 101], with this control, almost instantenously after the disturbance, the converter changes the active power reference proportionally to the RoCoF in order to emulate the kinetic energy delivered by the SG's rotor. It is known as the inertial response, and is illustrated in Fig. 2.12 (b). It is important to note that the implementation of a derivative term $\frac{d\Delta\omega}{dt}$ would require an additional notch filter in practical conditions.
- *Fast Frequency Response (FFR)*: this type of response has started to spread in islanded transmission grids [52] and provides an active power contribution deployed with a latency of less than 1s [102–104]. In consequence, it can be seen as a trade-off between the inertial response and the primary frequency control, and the power profile of the FFR can be customized instead of following a certain pattern, as illustrated in Fig. 2.12 (c).

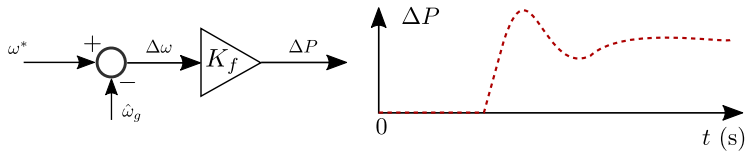

(a) Active power / frequency droop response

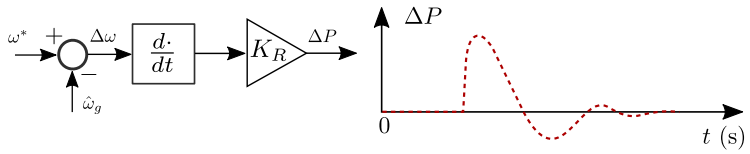

(b) Virtual inertia response

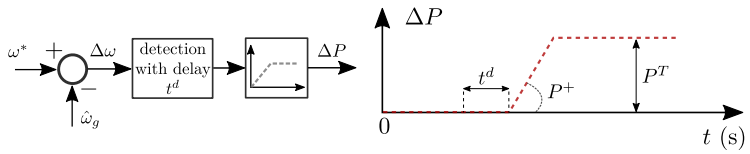

(c) Fast Frequency Response (FFR)

Figure 2.12: Illustration of different potential supporting actions using a variation of power reference provided by a power converter.

As to a grid-forming converter, it provides inherent frequency support since it emulates the SG dynamic response, i.e. with virtual inertia and load sharing capability. Concerning this last item, the current-source controlled and voltage-source controlled VSCs provide similar responses if sized and tuned accordingly [105]. However, if the DC-side of the converter is not adapted to provide this load sharing capability, this contribution may not be desired. This inherent frequency droop action of the grid-forming controller can thus be cancelled by using a high-pass filter or a frequency estimation $\tilde{\omega}$ from a PLL [106] instead of the nominal frequency ω_{ref} in the active power control loop given in Fig. 2.10 (c). Another option is to replace the droop gain $m_{p\omega}$ by an IP controller [107].

About the inertia then, since the grid-forming controlled VSC is operated as a SG during the first instants following any kind of disturbances, it does provide some inertia to the grid. On the other hand, the inertia provided by the virtual inertia controller in current source mode from Fig. 2.12 (b) is slightly different because it is an extra control loop that relies on the PLL speed, accuracy and the notch filter to deliver such inertia, meaning it will not be delivered at the very first instants following the disturbance.

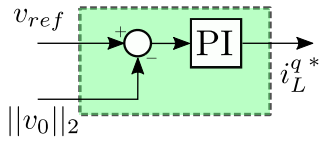

(a) AC voltage magnitude control [109].

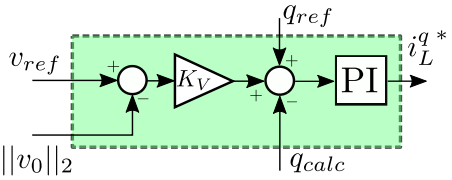

(b) AC voltage droop control [23].

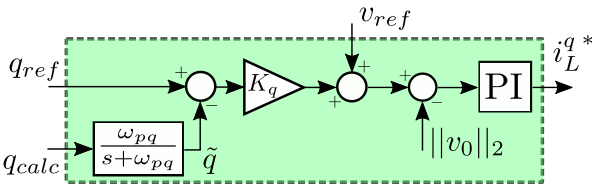

(c) AC voltage magnitude control with reactive power droop [99].

Figure 2.13: Different implementations of AC voltage support using reactive power modulation in current-source mode.

2.4.2. Reactive Power Support

PE-based systems have been used for decades to provide AC voltage / reactive power support. One of the most famous examples are STATCOM systems [108], which are also based on VSC technology. Indeed, by controlling the reactive current of a converter, wether it is an HVDC grid, a FACTS or a system connected to an energy source, the VSC is capable of adjusting its reactive power to support the PCC voltage as described in Section 2.2.2. In the literature, there are different ways the VSC can control its reactive power to support the AC voltage. In addition to the reactive power loop from Fig. 2.10 (b), there are other options which are given in Fig. 2.13. In Fig. 2.13 (a), another implementation of the reactive power loop is proposed to control the PCC bus voltage using PI control. In Fig. 2.13 (b), the support is a power droop similar to the active power frequency droop in Fig. 2.12 (a), which is used to provide a support proportional to the voltage magnitude deviation. In Fig. 2.13 (c), the controller regulates the voltage magnitude at the PCC but the reference is changed dynamically with respects to the reactive power deviation. However, the two implementations from Figs. 2.13 (a), 2.13 (c) can be a problem if multiple VSCs with this type of control are connected to the same bus because the PI controllers will compete against each other, creating undesired oscillations.

For the grid-forming control, the behavior of the VSC is based on controlling the PCC voltage magnitude as shown earlier in Fig. 2.10 (d). However, as for the options given in Figs. 2.13 (a), 2.13 (c), there is a problem if multiple converters are connected in parallel at the same bus. In practice, this is one of the advantages of

implementing a virtual impedance as in Fig. 2.9. Also, it is important to note that the grid-forming control is not only about maintaining the AC voltage magnitude but also its phase, as it is described in the next section.

2.4.3. Contribution to system strength

In the literature, it has been shown that PE-based converters controlled in current-source mode can be unstable when connected to a weak grid, i.e. where the SCR at the PCC is inferior to 3, due to the interactions between the line dynamics and the PLL [110]. To illustrate these interactions, a frequency analysis of the open-loop PLL given in Fig. 2.8 is performed for different PLL gains. The analysis is carried out considering $k^{\alpha}_{p,pll} = \alpha \cdot k_{p,pll}$ and $k^{\alpha}_{i,pll} = \alpha \cdot k_{i,pll}$ for different values of $\alpha = \{1, 2, 3, ..., 20\}$, where $k_{p,pll} = -0.05$ p.u., $k_{i,pll} = -2.53$ p.u., and $\omega_{c,pll} = 200$ rad/s, based on values from [95].

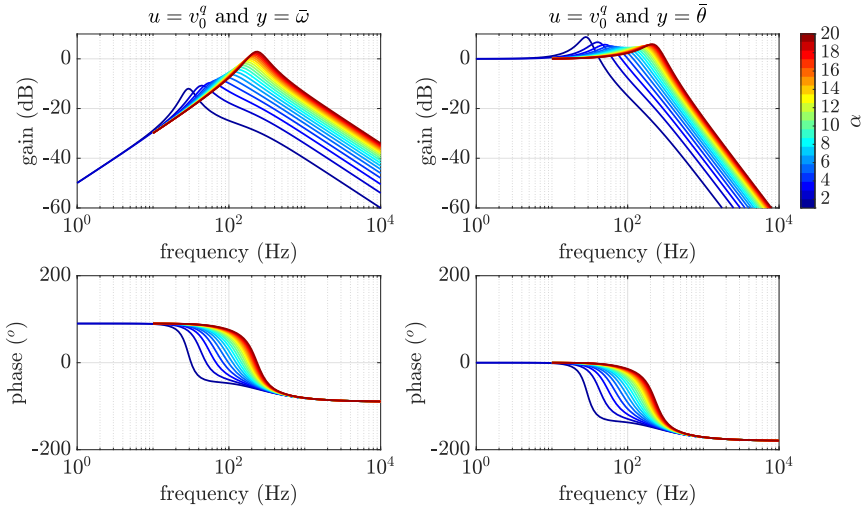

Figure 2.14: Bode plots of the linearized PLL for different values of gain $k^{\alpha}_{p,pll}$ and $k^{\alpha}_{i,pll}$ with respect to the two outputs $\bar{\omega}$ (left-side) and $\bar{\theta}$ (right-side).

As shown in the Bode plots given in Fig. 2.14, there is a trade-off between the speed of the tracking capability of the PLL and its robustness: if the PLL is fast enough to track any frequency changes, it is also more sensitive to disturbances. The resonance frequency of the PLL is found to be around 100 Hz, which is the order of magnitude of the transmission line dynamics [59], hence the negative interactions with the lines causing instability when the lines are too long, which correspond to weak grid conditions.

Nowadays, this weak grid issue is responsible for renewable energy curtailments in some power systems [111]. In the literature, there are three main solutions to allow more VSCs to be connected to weak grids:

- Introduce synchronous condensers to provide system strength to the weak regions [112]. However, this solution does not include any VSC-related function;
- Reinforce the weak grids, for example by grid-forming control in Fig. 2.9. This is different from the services by FACTS that improve the long-term voltage stability by reactive power compensation [45]. However, it is possible to control STATCOMs using grid-forming control [113] to make them contribute to the system strength;
- Develop novel PLL algorithms for weak and very weak grids, i.e with a SCR$\leq$2 [95, 114] and keep the current-source control structure presented in Fig. 2.7. Today, this current-source control has better performances than classical voltage-source controls in terms of power tracking for strong grid situations [94,115], as illustrated in Fig. 2.11. Therefore, the VSC owners and TSOs should reach an agreement on whether most, if not all, of the VSC should participate to some extent in this voltage control, as the SG used to do, or only some specific VSC should be required to ensure minimum service in this aspect.

Even though the notion of SCR was a consistent metric for short-circuit contributions and voltage stiffness in SG-based systems, it is not sufficient enough in PE-dominated systems since the fault-transient behavior and the system strength in normal operation are no longer coupled. Developing novel metrics to assess the system strength levels in PE-dominated grids is still an open-topic. Indeed, contrary to SGs, a VSC in grid forming does not maintain its voltage-source behavior at all time because of its limited overcurrent capability. Indeed, its contribution to the voltage stiffness strongly depends on the nature of the disturbance and its operating point, in particular its active and reactive power references. In that way, dynamic analysis are required to assess the voltage stiffness of a PE-dominated grid, while it was possible for SG-dominated grids to use only static analysis [112].

2.4.4. Short-circuit contributions

Unlike SGs whose high overcurrent capability makes it possible to contribute to short-circuits during AC faults, as described in Section 2.2.4, VSCs are highly sensitive to overcurrents due to their semiconductor devices. If no current limit

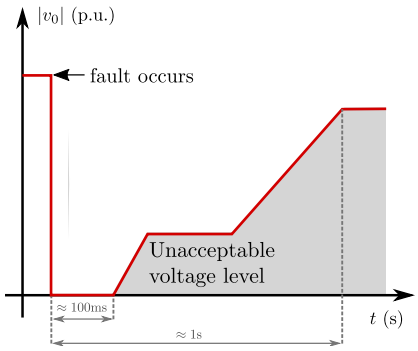

(a) Typical Low Voltage Fault-Ride-Through (LVFRT) profile imposed by a grid operator.

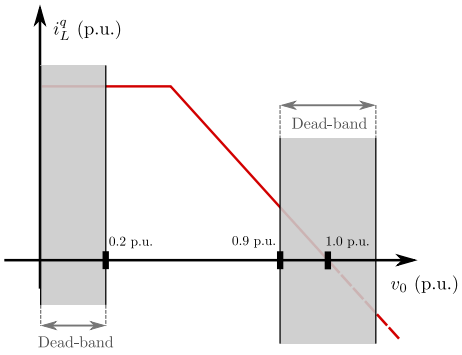

(b) Reactive fault current requirements depending on the voltage level. Based on [68] and [25].

Figure 2.15: Synthesis of the expected voltage and current responses of a VSC following an AC-side fault.

is imposed, the conversion valves will be blocked and the VSC will be disconnected from the grid, hence interrupting its power conversion and making it unable to contribute to the short-circuit currents.

In consequence, we may require in the future that VSCs have a Fault-Ride Through (FRT) capability where they remain connected when encountering large disturbances, such as a fault or a generation unit loss. The FRT capability is usually assessed by TSOs using a FRT profile which corresponds to the minimum voltage response of the equipment following a given fault to remain connected to the grid. There are many profiles which depend on the TSO grid codes [116]. A typical FRT is given in Fig. 2.15 (a). In addition to the voltage deviations, the VSC can still lose synchronism even though the voltage magnitude remains within the FRT profile. This transient stability needs to be assessed and is currently a topic of great concern by academia [25, 117].

Second, in addition to remaining connected, the VSC may also be asked to contribute to the short-circuit currents in order to help detecting the fault. In the literature, there have been some studies about developping strategies to make the VSCs in current-source mode remain connected and provide 1 p.u. of reactive current when the voltage drops below a certain level [118, 119], 90% of nominal voltage in [25]. However, in several grid codes, these contributions are not mandatory anymore if the PCC voltage, v_0 in Fig. 2.15 (b), drops below 20% of its nominal value [68] as it is illustrated in Fig. 2.15 (b).

In the voltage-source mode, as in Fig. 2.9, the FRT capability is more complex to achieve, because the branch current results directly from the voltage the VSC

imposes at its terminal. In consequence, the VSC control must act quickly to avoid a fault current which would damage the conversion devices or force the interruption [73]. In the recent literature, two main ways of achieving FRT with a VSC controlled in voltage-source mode have emerged:

- *Use of a backup PLL*: When the control detects a current rise, it switches to an emergency current-source mode and keeps the synchronization through a backup PLL. The new power references are chosen in order to inject a fault current of 1 p.u. [79].
- *Limitation of the voltage magnitude*: The control keeps running in voltage source mode but the voltage reference is decreased to limit the branch current. One solution could be the implementation of a fault detector with a virtual impedance control as in [120, 121].

For both the current-source mode and the voltage-source mode, the short-circuit contribution of a VSC is physically limited by the semiconductor devices. In consequence, the current way the TSOs detect and clear AC faults has to be re-defined for large penetration of PE-based sources scenarii [73]. There are two tendencies that have emerged in the literature for AC fault detection:

- *Enhance the fault response of PE-based sources*: According to this conservative strategy based on the assumption that power grids will still rely on SGs, the fault detection algorithms are unlikely to change. On the other hand, the very limited overcurrent capability of VSCs, currently at approximately 110% as shown in Table 2.2, must be enhanced. One solution is to upgrade the thermal management system of the converter. There are examples in the literature of PE-based systems where the current is able to go up to 200% for less than 200μs [118]. Another solution is to integrate synchronous condensers in parallel with the VSC to enhance the fault response at the point of coupling [122].
- *Change the AC grid fault detection strategy*: Today the AC fault detection algorithm is based on differential functions, relying only on measurements of currents and Kirshoff's current law. However, with the recent advances in system identifications, new methods based on Dynamic State Estimation (DSE) make it possible to monitor a given protection zone without requiring large overcurrents or coordination between the zones [123].

However the choice of relevant solutions requires the coordination of the different actors (TSOs, converter manufacturers, etc...) and is more a design problem rather than a control problem.

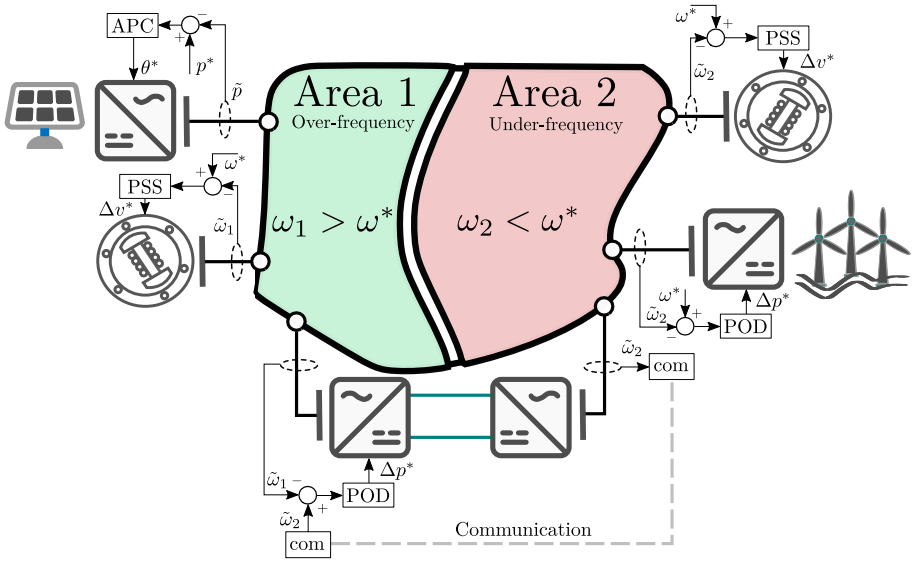

Figure 2.16: Different manners of damping inter-area power oscillations in a single synchronized power system using synchronous generators, VSC-interfaced power sources and VSC-HVDC links.

2.4.5. Power oscillation damping

Following the development of several embedded HVDC links in some interconnected systems, several studies have shown that VSC-interfaced power sources and VSC-HVDC links operating in current-source mode can provide a Power Oscillation Damping (POD) function if the active power reference are adjusted accordingly [124–127]. These power references can be changed according to the difference of the two-area frequencies $\Delta p^* = f(\omega_2 - \omega_1)$ or the difference between the reference and the local frequency $\Delta p^* = f(\omega^* - \omega_2)$ for instance, as illustrated in Fig. 2.17 (a). In the former case, the system needs communication devices whereas the latter option only relies on local measurements. Both cases are illustrated in Fig. 2.16. The POD function can also be achieved using reactive power reference modulation [128] or be applied to Multi-terminal HVDC (MTDC) embedded systems [129].

For grid-forming VSCs, also given in Fig. 2.16, since they have a SG-like behavior, they add supplementary electromechanical-like modes in the system. However, these modes can still be damped by adding an additional damping controller though. In this case, to damp the power oscillations, the power references p_{ref} and q_{ref}, defined in Fig. 2.9, can be adjusted similar to a VSC working in current-source mode. In this way, the power-tracking capability of the grid-forming mode [94] is used to provide POD. Another option is to adapt the active power control loop to add a notch filter which eliminates the undesirable oscillations, as in [130, 131] and illustrated in Fig. 2.17 (b).

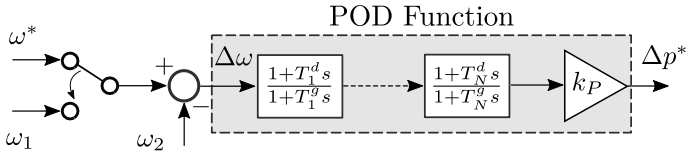

(a) POD control structure using active power modulation [126].

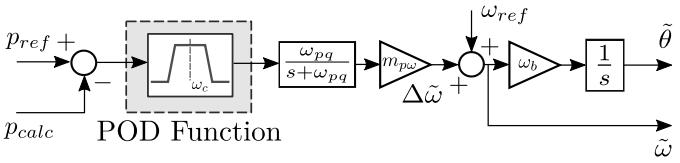

(b) POD control structure using modified droop-based grid-forming control [130].

Figure 2.17: Options for POD functions depending on the VSC control mode.

Nevertheless, all these types of POD impose some constraints on the VSC:

- Some power headroom must be dedicated to POD at all time to be capable of acting on the power references. In consequence, the VSC cannot operate at its maximum apparent power.
- It impacts the transferred power of the VSC, which can generate market-related and operational issues if the HVDC system is between two distinct areas/countries.

2.5. Discussions & Conclusions

The two VSC control modes, namely, the current-source control and the voltage-source control, were presented in Section 2.3, while the converter services to the grid were discussed in Section 2.4. As described in this last section, most of the grid support functions can be added to the grid-following scheme by slightly modifying the control, i.e. by adding current limitations or $\Delta p^*/\Delta q^*$ power references. As a consequence, the supporting action can be tuned accordingly to the available reserves from the DC side. On the other hand, voltage-source mode can provide most of the grid services since it is capable of emulating SG behavior. However, because of its voltage source behavior, the extracted power is a consequence of the imposed voltage. Thus, it requires a large energy source to provide functions such as frequency support, system strength contribution or POD. The short-circuit contribution is however limited by the semiconductor device overcurrents. Traditional SGs can

provide the short-circuit current thanks to their large overcucrrent capability, as shown in Section 2.2. These functions are included in the definition of grid-forming in some references [57] though, which can be misleading from a control point of view. To be properly integrated in the grid, the VSC control must consider the energy management algorithms of the power sources on the DC side that deliver this supplementary energy, which could be brought directly in DC or through another AC/DC converter. This extra energy can be provided by deloading PV arrays [102], wind power plants [132–134] or by storing it in an Energy Storage System (ESS) through Li/ion batteries [105, 135] or supercapacitors [136]. On the other hand, it is possible to control a VSC in grid-forming even though there is no dedicated storage unit, as for HVDC links interfacing two AC grids [137] or interconnecting offshore wind farms [29]. As a summary, the compatibility of the two control modes with the grid services is given in Table 2.3, where frequency support is split into *virtual inertia* and *load sharing capability* to highlight this.

This distinction between the different objectives of a grid-forming controlled VSC are an up-to-date topic. In [138], several categories of "grid-forming" were drawn such as:

- **grid-forming**: refers to VSCs controlled as constant voltage sources, which is equivalent to the vf control described in Section 2.3.2;
- **synchronous grid-forming**: refers to VSCs in grid-forming which are capable of synchronizing with other parallel-connected voltage sources (grid-forming VSCs, SGs or SCs);
- **Virtual Synchronous Machine (VSM)**: refers to synchronous grid-forming VSCs which are capable of providing power from an extra source of energy and a short-circuit current during faults.

In this classification, *grid-forming* and *synchronous grid-forming* refer to control aspects: the VSC is seen as a voltage source from the grid perspective and the outer loop control inputs are a voltage magnitude and angle, as in Fig. 2.9. On the other hand, *Virtual Synchronous Machine* refers to the grid aspects because it includes some of the support functions described in Section 2.2. This terminology is compatible with Table 2.3 and shows the need to distinguish in the "grid-forming" related literature the *control aspects* which makes it possible to have a PLL-free synchronization from the *grid aspects* which replaces the functions of the SGs with VSCs. This understanding makes us realize that some inherent functions of SGs, such as inertia, whose shortage in future power systems was considered as the worst issue for European TSOs in 2017 [24], are less important than others, such as

	Current-source mode		**Voltage-source mode (Grid forming)**	
	Grid-Following	*Grid-Supporting*	*with extra energy*	*w/o extra energy*
Converter-level				
synchronization	Uses an external PLL to capture the grid frequency and phase angle.		Observes the variations of active power to estimate the grid frequency and phase angle. The converter and the grid are naturally coupled by the synchronizing torque.	
power-tracking	Relies on strong grid assumptions. Quite good performances in power tracking when these conditions are met. See Fig. 2.11		Not as good as current-source mode for power tracking in terms of both time response and static error [94, 115].	
current-limiting action	Current limiters can be implemented in the current controller.		No inherent current controller at first place. But cascaded structure with current controller is now widely used [76, 78].	
Grid-level				
virtual inertia	No. The VSC tracks power references.	Possible with virtual inertia control as in Fig. 2.12 (b). Not as well adapted as grid forming option [101].	Yes, due to the dynamics of the Low-Pass Filter (LPF) in the active power controller shown in Fig. 2.10 (c).	Yes, due to the LPF dynamics. Support is however limited by the quantity of available DC power.
load sharing capability	No. The VSC tracks power references.	Possible with active power / frequency droop control as in Fig. 2.12 (a).	Yes, as shown in [78, 91].	Impossible if there is no dedicated storage system [29].
reactive power support	No. The VSC tracks power references.	Possible with the supporting actions described in Fig. 2.13	Yes, the VSC controls the PCC voltage magnitude and adjusts its reactive power accordingly as long as it respects its overcurrent limitations.	
system strength contribution	Impossible. The VSC is operated as a current-source and the PCC voltage is seen as an external disturbance.		Yes. The VSC is operated as a voltage source and the PCC voltage magnitude and phase angle are seen as control variables [23].	
short-circuit contribution	Can be implemented as in [55]. The contribution is limited by the thermal limits [73].		FRT must be taken care of because of the voltage source behavior. See [79] or [120, 121] for control options.	
power oscillation damping	No. The VSC tracks power references.	Possible using active or reactive power reference modulation as described in Fig. 2.17 (a). See [124–127].	Inherent damping based on SG emulation but can disturb the system as well. Compatible with SG's PSS.	POD actions can be added as in Figs. 2.17 (a) ([124–127]) - 2.17 (b) ([130]). Needs some available energy for active power damping.

Table 2.3: Compatibility of the two main VSC control modes with the different grid support functions.

system strength reinforcement. In fact, it is clear now that weak grids is a significant challenge right now for islanded power systems such as Texas [111] or Australia [139] where weak grid issues were recently reported. In conclusion, the desired behavior of VSCs in the future might not be to emulate SGs but could be less restrictive since those PE-based sources are much more controllable.

The contributions of this chapter can be listed as follows:

- a comprehensive introduction to the upcoming challenges of AC transmission grids due to the increasing amount of renewables and the ongoing dismantlement of synchronous generators;
- an overview of the main VSC control modes and a front-to-front comparison of the current-source and voltage-source modes, respectively the grid-following and grid-forming controls;
- a presentation of the main ancillary services that used to be realized by SGs and how the two types of VSC control modes can be adjusted and modified to provide some of these functions to the grid.

In future work, it should be primordial to investigate the compatibility of all the controllers with each other and how to dispatch the different control modes within a given grid. In particular, in the next chapters of the thesis, we will investigate the role of the main VSC control modes in the power penetration limits in AC grids and the specificities related to HVDC and Modular Multilevel Converters (MMC) technology.

Chapter 3

Impacts of VSC control on the limits of Power Electronics Converters integration in AC grids

The contents of this chapter is based on the peer-reviewed publication ***Journal I****.*

3.1. Introduction

3.1.1. Context

In the introduction of this thesis, the evolution of the power system stability issues were discussed. In Chapter 2, a literature review was provided to identifiy the role that VSC controls can play in providing the response to some of these issues such as frequency support, reactive power compensation or power oscillation damping. These functions become more and more expected of the VSC. Indeed, by 2050, renewable energy is expected to produce 70-85% of electricity in an attempt to limit

global warming to 1.5°C [3]. On the one hand, the conventional renewable energy sources, i.e. hydro power, which covered 14.4% of the annual power consumption in France in 2018 [140], would still be highly solicited. On the other hand, most of the other renewable energy sources, especially solar PV and wind, are interfaced with the grid through PE-based technology. In consequence, 100% PE-based grid scenarii will unlikely occur, but instead, hybrid systems with a high penetration of PE and the remaining SG including hydro power plants and synchronous condensers could be the future tendency. For such systems, it is essential to study the interactions between large PE-based stations and SGs. Hence, this chapter is about studying the interactions between the VSC in common control modes and the SG. A limit of power penetration is assessed using modal analysis tools.

3.1.2. Literature review

In the literature, some studies have been published to tackle the interactions between the VSC in the grid-feeding mode and SG and show penetration limit through modal analysis, with different notions of power ratio [75,97,141,142]. The notion of power penetration ratio has also been introduced in experimental setups recently [143]. The impacts of critical dynamics such as the Phase-Locked-Loop (PLL) and transmission lines (characterized by the Short-Circuit Ratio, or SCR) have been highlighted for grid-feeding VSCs [110]. The impact of the transmission lines was also pointed out recently for grid-supporting strategies using frequency and voltage droop controllers [99].

Following the development of grid-forming control strategies for transmission systems [79,82], the grid-forming control has become an accepted solution for weak grids, i.e. high-impedance grids and low-inertia systems [71]. The impact of the converter's electrical distance on the main grid [76] and its interactions with existing machines when controlled as a voltage source [59] or operating in grid-forming mode [58] have been recently studied using the notion of power ratio. Among different grid-forming strategies, droop [76] and Virtual Synchronous Machine (VSM) [**?**] controls are now the most commonly used in literature [87]. In addition, a comparison of existing grid-forming control strategies such as dispatchable virtual oscillator (dVOC) [88] and matching synchronous machines [89] was conducted using time-domain simulations of multiple-bus systems [92]. However, to our best knowledge, there are no studies that compare current-source modes and voltage-source modes of VSC at the same operating conditions for assessing the stability limits of the system.

3.1.3. Chapter summary and contents

In this chapter, the interactions between AC grid and existing VSC control modes are analyzed. In particular, three VSC control modes, namely grid-feeding, grid-supporting and grid-forming, are compared with each other in order to assess VSC/grid coupling level at the same grid conditions and power setpoints. In order to underscore the growing role of VSCs in transmission systems, an elementary benchmark network is considered. It includes an equivalent SG, a VSC, a load and a transmission line with a varying electrical distance. On this model, a modal analysis is conducted to study the interactions between the different VSC controls and the SG dynamics using a Matlab/Simulink environment. The converter penetration rate is represented by a variable power ratio between the converter and the machine, while the electrical distance by an RL dynamic impedance. This approach makes it possible to assess the stability limits on the VSC share imposed by the system strength. Negative interactions are identified and recommendations for novel converter control strategies proposed. Besides, the influence of the AVR with the VSC in grid-forming as well as PLL-related stability issues with the VSC in grid-feeding or grid-supporting are shown to be the key limiting factors for increasing the penetration of PE-based sources. Last but not least, different scenarii are studied by simulations with a multi-machine system in order to deepen the modal analysis results.

This chapter is organized as follows: in Section 3.2, the test system and its nonlinear differential equations are presented. In Section 3.3, the modal analysis method and results are presented, which are validated using a Matlab/Simulink state-space model and a multi-machine system developed in Modelica language in different scenarii in Section 3.4. Finally, the conclusions and future work are discussed in Section 3.5.

3.2. System modeling

3.2.1. Test system

For the study, an elementary benchmark is considered, which is composed of one VSC with its LC filter, one synchronous generator, the two connected by an AC line, and a load at the point of common coupling (PCC) located on the VSC side, as given in Fig. 3.1.

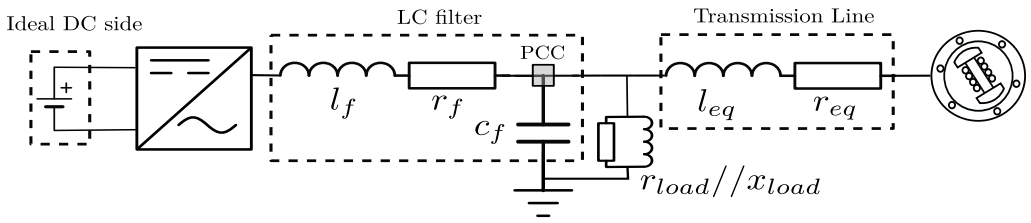

Figure 3.1: Considered benchmark for the study.

In order to assess the system stability, the system is linearized around an operating point. A modal analysis is performed for different PE penetration levels and AC grid strengths, i.e. for different values of the line impedance. The penetration of PE is modeled by the *Power Ratio*, denoted by P_R and defined as:

$$P_R = \frac{S_{vsc}}{S_{sg} + S_{vsc}} = \frac{S_{vsc}}{S_{base}} \tag{3.1}$$

where S_{vsc} and S_{sg} are respectively the VSC and SG rated powers and S_{base} is the system base power.

3.2.2. Synchronous machine model and control

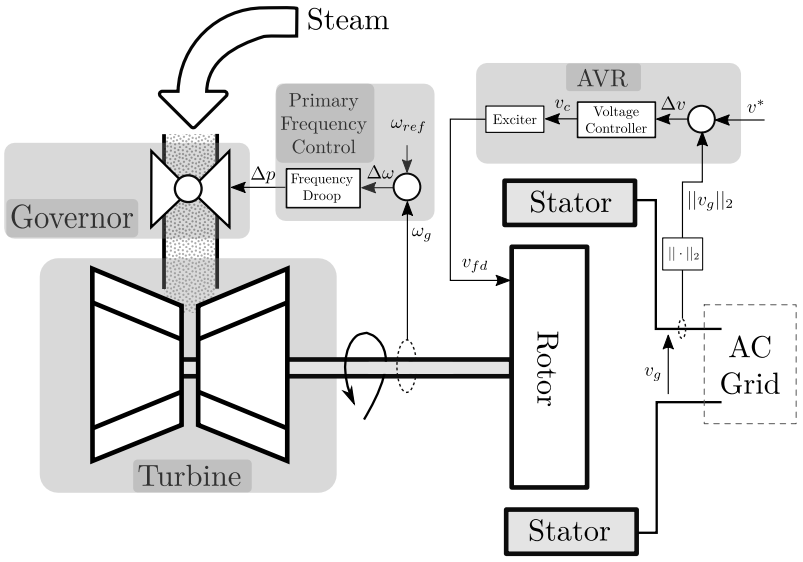

Figure 3.2: Synchronous Generator (SG) with its voltage and frequency controls.

As the SGs are currently the most commonly used for power generation, their dynamics need to be taken into account to highlight possible negative interactions [141], [142]. These interactions could not be tackled with the grid modeled as an equivalent voltage source [76] or with only electromechanical models [99]. Indeed, SG have several controllers among which the voltage regulator, or AVR, can have a

negative impact on the system. A conceptual scheme of the SG control model is given in Fig. 3.2. The SG model considered in this study is a reduced-order 1-axis model of a steam-powered SG that captures both electromechanical and electromagnetic dynamics. This model was developed in details in [60] and the considered equations are given in Appendix A.

3.2.3. Converter modeling & control

This section describes the converter model and their control schemes, which can be classified into two categories [23] and are adapted here for transmission grids. The details of this classification for transmission grids can be found in Chapter 2:

- **Current source control**: the VSC follows power references and injects a current in phase with the network thanks to the PLL synchronizing unit. It corresponds to the *grid-feeding*, also called *grid-following* mode. In the *grid-supporting* mode, the power references are adjusted to provide grid services;
- **Voltage source control**: the VSC works as a voltage source and is thus able to operate in islanded mode. It uses the power variations to synchronize with the grid so that no PLL is needed anymore. It corresponds to the *grid-forming* mode.

Both classes use cascaded loops including a current control loop with potential current limiting actions to protect the semiconductor devices. Indeed, the over-current capability of VSCs is only 110%, which is much smaller than traditional SGs [73]. Nevertheless, the impact of current limiting control on stability is not considered in this study. In both classes, the inner loop control uses PI controllers whose gains are tuned using pole placement methods [2], [78] and whose method is described in Appendix B.

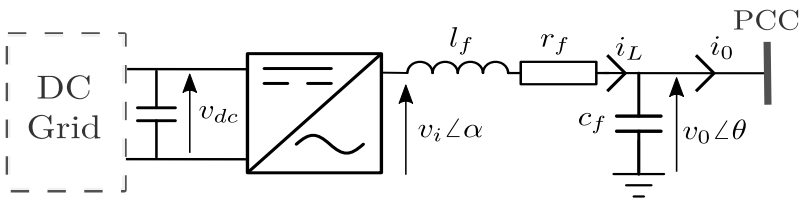

Figure 3.3: Equivalent electrical scheme of VSC with LC filter.

The VSC is considered with an LC filter, as described in Fig. 3.3. In the current source mode, the control scheme regulates the line current i_L by acting on the output voltage v_i. To synchronize with the grid voltage v_0, the scheme needs a PLL to capture the grid-frequency and the PCC electrical angle.

In the next paragraphs, the implemented VSC controls are described. These controls present some differences with the general control schemes presented in Chapter 2. Also, each control block is explicited in order to ensure the repeatability of the presented method.

3.2.3.1. Physical model of VSC

The VSC model considered here is an ideal voltage source where the dynamics of the switches are neglected. In addition, the PWM control dynamics are neglected and thus the actual output voltage is considered to be equal to the reference voltage given by the control law:

$$v_i^{dq} = v_{i,ref}^{dq} \tag{3.2}$$

Even though some recent works focus on the stability analysis of grid-connected converters taking into account the states of the switches [144], the use of averaged models, as in (3.2), is relevant to assess the small-signal stability of the grid [59, 75, 85]. Indeed, the switching dynamics of the VSC are much faster than the grid and SG dynamics that we focus on in this chapter.

3.2.3.2. Outer loop for current-source control

Current source control refers to the scheme that uses the VSC voltage output as the control variable to regulate the branch current passing through the LC filter. The general scheme of this type of control is given in Fig. 3.4 and covers grid-feeding [75, 110, 141] and grid-supporting [99] strategies.

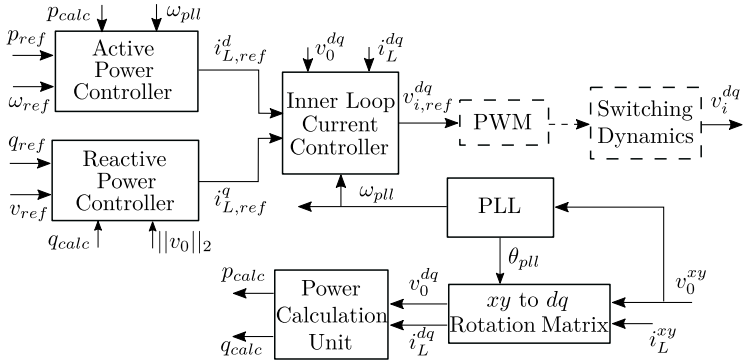

Figure 3.4: VSC control in current source mode: grid-feeding and grid-supporting.

With the grid-feeding control, the outer power loops use pure integral controllers, with k_{ip} as the control gain, to regulate the filtered active and reactive powers to their references. In grid-supporting, an additional droop is added to change the

active and reactive power references to contribute respectively to frequency and voltage stability, which are given by:

$$p'_{ref} = p_{ref} + K_{p\omega} \cdot (\omega_{ref} - \omega_{pll}) \tag{3.3}$$

$$q'_{ref} = q_{ref} + K_{qv} \cdot (v_{ref} - ||v_0^{dq}||_2) \tag{3.4}$$

where p_{ref}, q_{ref}, ω_{ref} and v_{ref} are respectively the references of active power, reactive power, frequency and voltage in per unit obtained from the load flow solution. The droop gains $K_{p\omega}$ and K_{qv} are used to provide support to the grid, hence the name grid-supporting. As presented in Chapter 2, there are other ways to provide frequency and voltage support to the grid in current-source mode, but these other strategies are not studied here since the two droop methods are the most commonly used controls. In grid feeding mode, $K_{p\omega} = K_{qv} = 0$.

The power control loop which generates the current reference in dq-frame for the inner current controller is:

$$i_{L,ref}^{dq} = k_{ip} \cdot [\epsilon_p, \epsilon_q]^T \tag{3.5}$$

where $\dot{\epsilon}_p = p'_{ref} - p_{avg}$ and $\dot{\epsilon}_q = q'_{ref} - q_{avg}$ are respectively the active and reactive power control errors. The filtered measured powers are calculated as:

$$\begin{bmatrix} \dot{p}_{avg} \\ \dot{q}_{avg} \end{bmatrix} = \omega_{c,power} \cdot \begin{bmatrix} p_{calc} - p_{avg} \\ q_{calc} - q_{avg} \end{bmatrix} \tag{3.6}$$

where $p_{calc} = v_0^d \cdot i_L^d + v_0^q \cdot i_L^q$ and $q_{calc} = v_0^q \cdot i_L^d - v_0^d \cdot i_L^q$ are the calculated output powers for the current-source mode. Finally, the PLL is modeled by a PI controller with a low-pass filter, as described in [75, 95]:

$$\dot{\hat{v}}_0^{dq,pll} = \omega_{c,pll} \cdot (v_0^{dq,pll} - \hat{v}_0^{dq,pll}) \tag{3.7}$$

$$\omega_{pll} = k_{i,pll} \cdot \epsilon_{pll} + k_{p,pll} \cdot \dot{\epsilon}_{pll} \tag{3.8}$$

$$\dot{\theta}_{pll} = \omega_{base} \cdot \omega_{pll} \tag{3.9}$$

with $k_{i,pll}$ and $k_{p,pll}$ as the PI gains of the controller and $\dot{\epsilon}_{pll} = 0 - \hat{v}_0^{dq,pll}$, $\hat{v}_0$ the filtered signal of v_0 and $\omega_{c,pll}$ the low-pass filter cutoff frequency.

3.2.3.3. Outer loop for voltage-source control

In voltage-source mode, the control scheme regulates the PCC voltage v_0, which is no longer an external disturbance from the control point of view. The scheme relies on cascaded loops, described in Fig. 3.5, where it uses the branch current i_L

to act on v_0 and uses the VSC output voltage v_i to control i_L. The synchronization with the grid is insured by the outer-loop control, i.e. grid-forming, thus no PLL is needed any more. This control scheme for grid-forming is the most commonly spread in literature even though it requires a good enough estimation of both the filter inductance and capacitance to control the PCC voltage and a physical LC filter at the VSC output. To address this issue, some other grid-forming control schemes have emerged recently to avoid the voltage control loop and act as current sources [86]. However, they remain out of the scope of this chapter.

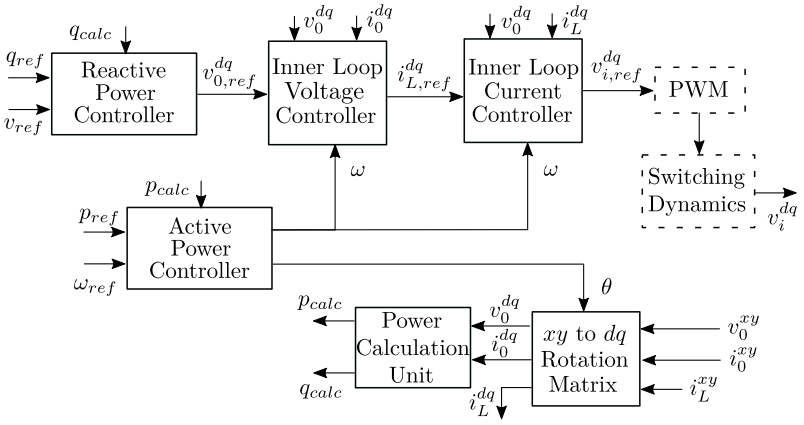

Figure 3.5: VSC control in voltage source mode: grid-forming.

The outer loop controls use the variations of active power and reactive power to respectively synchronize with the grid and maintain a certain voltage amplitude.

The active power control for the droop and the VSM schemes are, respectively:

$$\omega = \omega_{ref} + m_{p\omega} \cdot (p_{ref} - p_{avg}) \tag{3.10}$$

$$\dot{\omega} = \frac{1}{2 \cdot H_c} \cdot (p_{ref} - p_{calc} - D_c \cdot \omega) \tag{3.11}$$

Then, the corresponding angle is calculated as

$$\dot{\theta} = \omega_{base} \cdot \omega \tag{3.12}$$

The output powers of the VSC in voltage-source mode are $p_{calc} = v_0^d \cdot i_0^d + v_0^q \cdot i_0^q$ and $q_{calc} = v_0^q \cdot i_0^d - v_0^d \cdot i_0^q$.

It is important to note that the gains of the VSM control are chosen to give the same steady-state response as grid-forming droop control [76].

The reactive power control is a droop controller and is similar for the droop (3.10) and VSM (3.11) controls, as in [76]. The option of using the electromagnetic

state-space model of the SG [82,86] is discarded in this study. The control law is:

$$e^* = v_{ref} + m_{qv} \cdot (q_{ref} - q_{avg}) \tag{3.13}$$

$$ev_{0,ref}^{dq} = [e^*, 0]^T \tag{3.14}$$

3.2.3.4. Inner control loops

In grid-forming mode, as in Fig. 3.5, the output terminal voltage and the line current are regulated using two cascaded loops. PI controllers are implemented for these loops and are tuned with pole placement method [2]. The voltage loop is designed to be ten times slower than the current loop to avoid potential interference [78]. The inner voltage control law is:

$$i_{L,ref}^{dq} = k_{iv} \cdot \epsilon_v^{dq} + k_{pv} \cdot \dot{\epsilon}_v^{dq} + \omega c_f \cdot \begin{bmatrix} 0 & -1 \\ 1 & 0 \end{bmatrix} \cdot v_0^{dq} + \alpha_i \cdot i_0^{dq} \tag{3.15}$$

with $\dot{\epsilon}_v^{dq} = v_{0,ref}^{dq} - v_0^{dq}$. The current reference generated from the voltage controller is then used in the current control law as:

$$v_{i,ref}^{dq} = k_{ii} \cdot \epsilon_i^{dq} + k_{pi} \cdot \dot{\epsilon}_i^{dq} + \omega l_f \cdot \begin{bmatrix} 0 & -1 \\ 1 & 0 \end{bmatrix} \cdot i_l^{dq} + \alpha_v \cdot v_0^{dq} \tag{3.16}$$

with $\dot{\epsilon}_i^{dq} = i_{L,ref}^{dq} - i_L^{dq}$. The output signal of the current control loop, $v_{i,ref}^{dq}$, refers to the desired voltage in dq-frame to be generated by the VSC internal actuators, which are not considered here.

The same current controller is used in all the grid-feeding, grid-supporting and grid-forming schemes. The inner current controllers based on PR (Proportional Resonant) control to regulate the VSC current in the stationary frame ($\alpha\beta$) [23,145] are gaining more interest compared to the classical PI control [146,147]. However, it remains out of this study where the most prevalent VSC control schemes are considered to assess the stability limits.

3.2.4. Network modeling & interfaces

3.2.4.1. Interconnecting line model

The network is modeled as a dynamic RL line which connects the SG bus with voltage v_g to the load and VSC output filter bus with voltage v_0, as described by:

$$\frac{di_{eq}^d}{dt} = \frac{\omega_{base}}{l_{eq}} \cdot (v_g^d - v_0^d - r_{eq} \cdot i_L^d + \omega_g \cdot l_{eq} \cdot i_{eq}^q) \tag{3.17}$$

$$\frac{di_{eq}^q}{dt} = \frac{\omega_{base}}{l_{eq}} \cdot (v_g^q - v_0^q - r_{eq} \cdot i_{eq}^q - \omega_g \cdot l_{eq} \cdot i_{eq}^d) \tag{3.18}$$

The line impedance is defined in per unit, to take into account the changes of the SG power ratings when acting on the power ratio. Indeed, an electrical line of 100 km will not have the same influence when connected to a 100 MVA machine or a 1000 MVA one. Then, considering a constant ratio $X_{eq}/R_{eq} = 10$, which is common in power system studies, the equivalent resistance can be calculated.

3.2.4.2. Load model

The load is modeled as a static $R_{load}//X_{load}$ load connected at the PCC. The impedances are calculated using the expected load setpoints in S.I.:

$$R_{load} = \frac{U_{base}^2}{P_{load}} \;\; ; \;\; X_{load} = \frac{U_{base}^2}{Q_{load}} \tag{3.19}$$

3.2.4.3. Global system & interfaces

From its description, the whole system appears to be a combination of several subsystems with their own dq-frames. To associate the equations at the load bus, an interface is needed between:

- {SG + line} in the SG's dq-frame, denoted by DQ;
- {VSC + LC filter} aligned with the load bus voltage's dq-frame, denoted by dq.

This association can be achieved using rotation matrices between the two different frames as:

$$\begin{bmatrix} x^D \\ x^Q \end{bmatrix} = \begin{bmatrix} \sin(\delta - \theta) & -\cos(\delta - \theta) \\ \cos(\delta - \theta) & \sin(\delta - \theta) \end{bmatrix} \cdot \begin{bmatrix} x^d \\ x^q \end{bmatrix} \tag{3.20}$$

3.3. Modal analysis

3.3.1. Parameters and operating points

For the modal analysis, the parameters and input data of the system are given in Table C.1 in Appendix C. The VSC reactive power reference q_{ref} and the SG active power reference P_m^* are not fixed but are adjusted in order to have $||v_0|| = v^*$ and $\omega_g = \omega_{ref}$. The tuning of the grid-forming outer loops (active and reactive power controllers) is based on [78, 148]. For the grid-feeding and grid-supporting schemes, the values of the power filter, PI power control and droop gains are based on [99]. The feedforward gains α_v and α_i from (3.15) and (3.16) are boolean and

their values depend on the activation of the feedforward action for each controller. For the current-source controlled strategies, $\alpha_v = 1$ as there is no voltage control loop. For grid-forming strategies, we choose $\alpha_v = 1$ and $\alpha_i = 0$ because the voltage controller's feedforward action proves to cause instability [78].

3.3.2. Method for modal analysis

The system model gathers the state variables of the different components and can be rewritten in general form as:

$$\dot{x} = f(x, u) \tag{3.21}$$

with $x = \left[x_{1,SG}, \ldots, x_{n,SG}, x_{1,VSC}, \ldots, x_{m,VSC}, i_{eq}^{d}, i_{eq}^{q}\right]^T$ as the state variable vector of the system, n the order of the SG subsystem with $x_{i,SG}$ as its state variables and m the order of the VSC subsystem with $x_{i,VSC}$ as its state variables. The vertical vector $u = \left[p_{ref}, q_{ref}, v_{ref}, P_m^*, v^*, \omega_{ref}\right]^T$ is the system input vector. Using this state-space model, we define the setpoints of all the state variables corresponding to the load flow solution and we linearize the system around the operating point $\{u_0, x_0\}$ as:

$$\Delta\dot{x} = A \cdot \Delta x + B \cdot \Delta u \tag{3.22}$$

$$A := \left.\frac{\partial f}{\partial x}\right|_{u_0, x_0} \in \mathbb{R}^{(n+m+2)\times(n+m+2)} \tag{3.23}$$

$$B := \left.\frac{\partial f}{\partial u}\right|_{u_0, x_0} \in \mathbb{R}^{(n+m+2)\times 6} \tag{3.24}$$

where A is the state matrix and corresponds to the structural properties of the system since it does not depend on the input/output signals. The matrix B is the input matrix. By extracting the eigenvalues of the A-matrix, we can analyze the stability of the system around the nominal point. The participation factors of some specific critical modes will also be used to enrich the results. The method for calculating the normalized participation factors is detailed in [61].

A study over some selected dynamics is also carried out to highlight harmful interactions between the SG and the VSC modes. The impact of the AVR dynamics (both lead-lag filter and AC exciter) on the system stability is studied. We compare the modal analysis results of two cases: the system with the AVR dynamics considered or neglected, as illustrated in Fig. 3.6 (a). For PLL-based controls, i.e. grid-feeding and grid-supporting, we compare two cases: one with the PLL dynamics, the other with an ideal PLL that captures the exact angle and exact frequency with no time-delay, as in Fig. 3.6 (b).

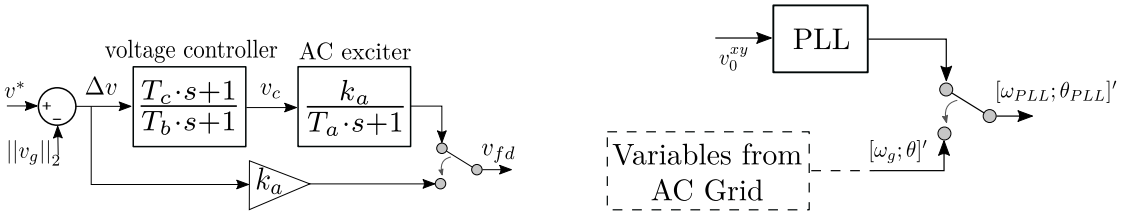

(a) Transfer function of the AVR and the switch when neglecting the AVR dynamics.

(b) Equivalent scheme of the PLL and the switch when neglecting the PLL dynamics.

Figure 3.6: Illustrative scheme of the selection of AVR and PLL specific dynamics for studies.

3.3.3. Results for PLL-based controls: grid-feeding and grid-supporting schemes

3.3.3.1. Influence of the power ratio

The results of the modal analyses for a given grid scenario with $x_{eq} = 0.33$ p.u. are displayed in Fig. 3.7 for the grid-feeding and grid-supporting cases. In these results, we observe that the AVR has little impact on the system stability when the VSC is controlled in current-source mode. Indeed, the critical modes in Figs. 3.7 (a)-3.7 (c) and in Figs. 3.7 (b)-3.7 (d) are similar. On the other hand, the PLL appears to act as a limiting factor because the modes with an ideal PLL are all stable for $P_R \leq 0.8$ as described in Figs. 3.7 (e)-3.7 (f). In addition, the grid-supporting control results in a higher penetration limit compared to grid-feeding.

For further investigation, we calculate the participation factors of the critical mode, which is denoted by $\lambda_{4,5}$ in Fig. 3.7 (a), to show the potential destabilizing role of the PLL. The results are given in Fig. 3.8. It is clear that the PLL is responsible for the observed instability due to high participation factors when the power ratio is low. However, the larger the P_R, the smaller the PLL-variable participation. Indeed, as P_R increases, the share of the PLL is gradually replaced by the state variables of the passive components, namely the RL dynamics of the line and the LC filter, which implies that we can reach the structural limits of the current-source controlled VSCs regardless of the tuning of the PLL. This result confirms the limits of controlling VSCs in current sources when increasing their number in the AC grid, a phenomenon that cannot be observed when modeling the lines using static models [97]. The role of the PLL in destabilizing the system with PE-based sources attracts more and more attention from TSOs [149]. However, the nature of the oscillations appears to

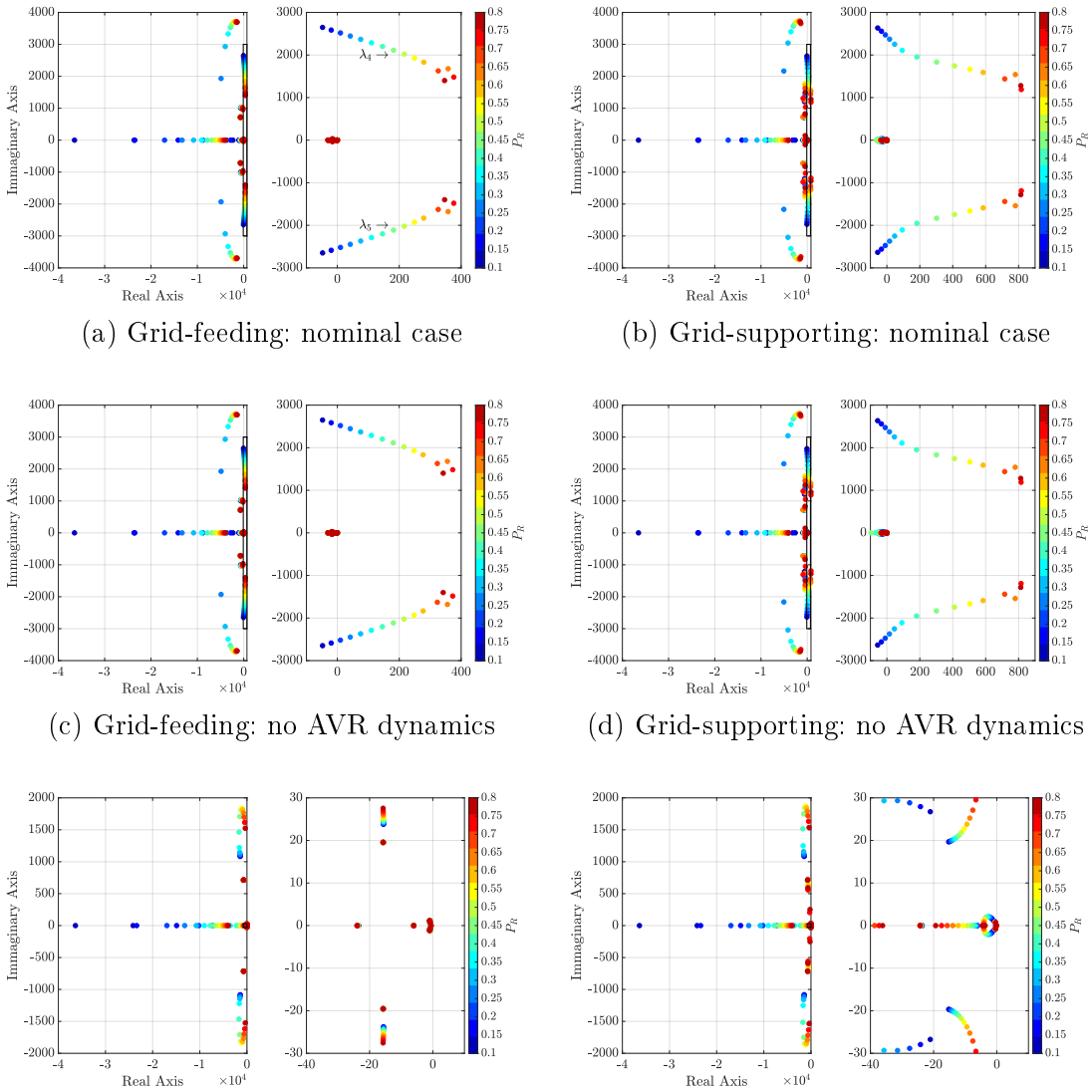

(a) Grid-feeding: nominal case

(b) Grid-supporting: nominal case

(c) Grid-feeding: no AVR dynamics

(d) Grid-supporting: no AVR dynamics

(e) Grid-feeding: "ideal" PLL

(f) Grid-supporting: "ideal" PLL

Figure 3.7: Modal analysis results for different values of P_R with the VSC in grid-feeding (left-side) and grid-supporting (right-side) modes and $x_{eq} = 0.33$ p.u.

depend on the grid conditions [150] and the PLL structure [151] and needs further investigation in the future.

3.3.3.2. Influence of the electrical distance

In this paragraph, we perform a modal analysis on the PLL-based controlled VSCs for a given power ratio $P_R = 0.2$ and we change the line impedance. The results for the grid-feeding and grid-supporting are given in Fig. 3.9. As in the previous paragraph, it is clear that the AVR dynamics play no role on the small-signal

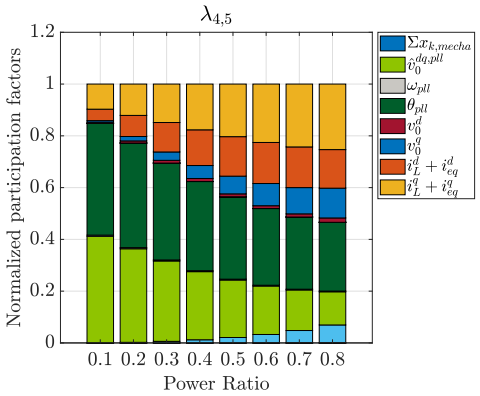

Figure 3.8: Participation factors of the $\lambda_{4,5}$ mode for different values of the power ratio P_R whith the VSC in grid-feeding mode and $x_{eq} = 0.33$ p.u.

stability of the system when the VSC is controlled either in grid-feeding or in grid-supporting. The system stability is still too sensitive to the power ratio and does not allow us to increase the penetration of PE above 30%. Nevertheless, the use of different grid-feeding control structures based on PR controllers could enhance the stability limits, since PR controllers exhibit better performances in weak grid conditions compared to PI controllers [152]. In the next section, we study the role that the grid-forming control can play in increasing those limits.

3.3.4. Results for PLL-free controls: grid-forming schemes

3.3.4.1. Influence of the power ratio

Since the grid-forming droop and VSM exhibit the same small-signal behavior [91], we only plot the results for the droop control with respect to the power ratio in Fig. 3.10. For the case $x_{eq} = 0.33$ p.u., we observe that the system is stable until around 45%, whereas it is stable for all the values of P_R when neglecting the AVR dynamics. To understand the critical mode evolution, we take a look at the critical modes $\lambda_{12,13}$ and $\lambda_{18,19}$ defined in Fig. 3.10 (a).

We calculate the participation factors of each mode for different values of P_R. The results, given in Fig. 3.11, show that both modes are low-frequency modes, since the participation factors of the SG mechanical variables, denoted by $x_{k,mecha}$, is high. Even if the role of the AVR dynamics is clear for modes $\lambda_{18,19}$, its impact on modes $\lambda_{12,13}$ is less evident using the participation factors. From Fig. 3.10, it is clear that the influence is weak but causes instability since the conjugate modes just slightly move beyond the imaginary axis, compared to the case where the AVR is neglected. In addition, compared to the electromagnetic dynamics, the time constants of the

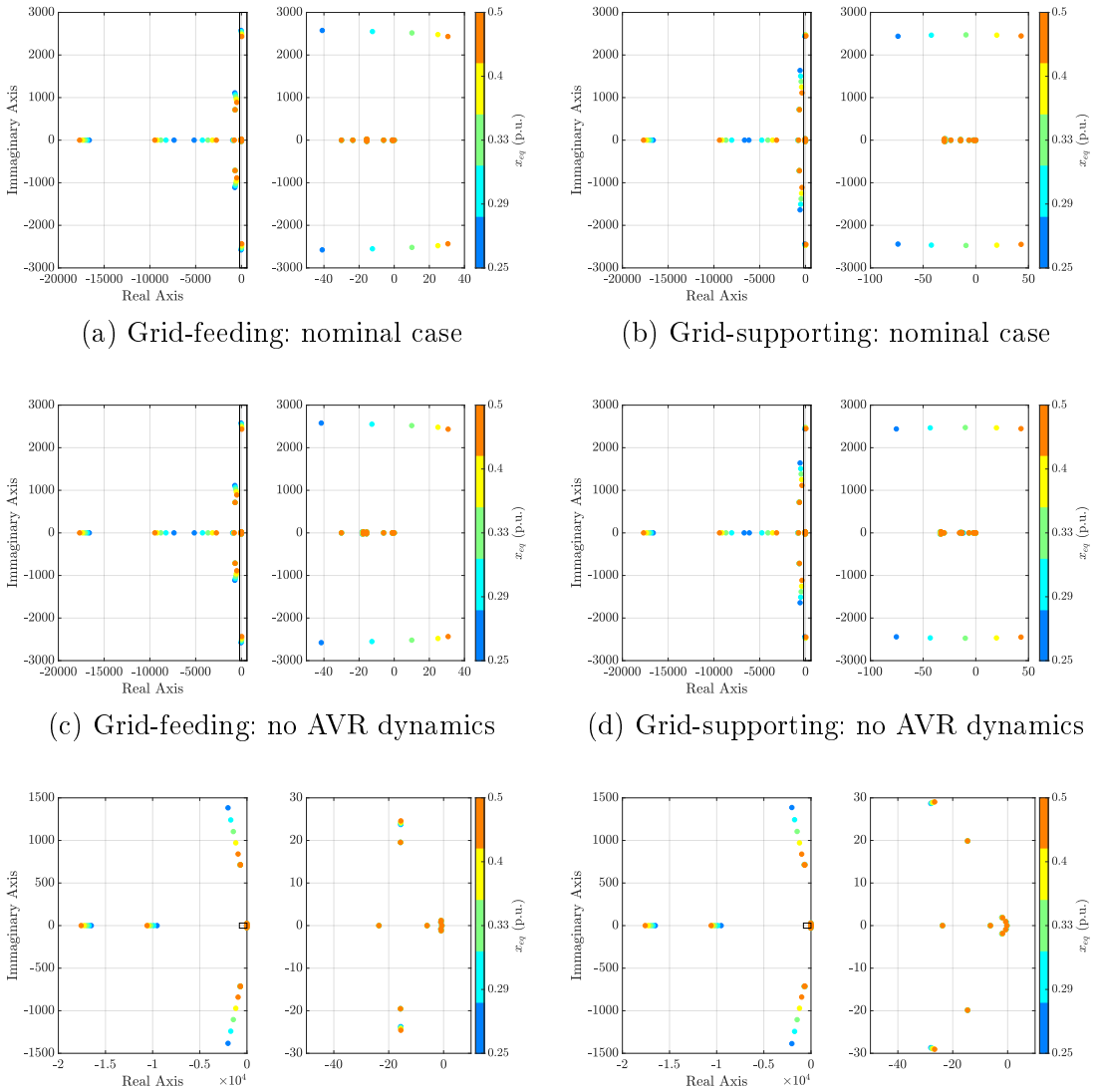

(a) Grid-feeding: nominal case

(b) Grid-supporting: nominal case

(c) Grid-feeding: no AVR dynamics

(d) Grid-supporting: no AVR dynamics

(e) Grid-feeding: "ideal" PLL

(f) Grid-supporting: "ideal" PLL

Figure 3.9: Modal analysis results for different values of $x_{eq}$with the VSC in grid-feeding (left-side) and grid-supporting (right-side) modes and $P_R = 0.2$.

AVR lead-lag filter are rather slow, which fall in the range of electromechanical dynamics. This can explain why the undamped oscillatory modes $\lambda_{12,13}$ interact with the electromechanical variables. This result may seem counter-intuitive since 100% PE-based generation with VSCs in grid-forming has been proved to be stable [78]. In fact, the transition to 100% will go through a hybrid system where a high proportion of PE generators coexist with the remaining SGs. Because of their interactions, even with all converters working in grid-forming, this transition of the power systems should be more challenging than the 100% PE scenario [59].

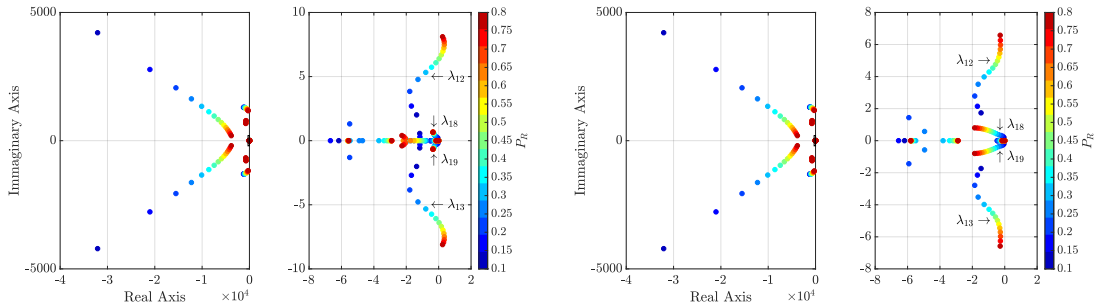

(a) Nominal state-space model

(b) State-space model with no AVR dynamics

Figure 3.10: Modal analysis results for different values of P_R with the VSC in grid-forming (droop or VSM) mode and $x_{eq} = 0.33$ p.u.

3.3.4.2. Influence of the electrical distance

In this part, we perform a modal analysis for a given grid scenario with $P_R = 0.45$ for different values of the line reactance x_{eq}. The results in Fig. 3.12 show the AVR dynamics move the modes to the right semi-plane. Even if the dependency of the modes on the electrical distance is small, bringing the SG closer to the VSC makes the system unstable. On the one hand, this result is counter-intuitive when compared to the PLL-controlled VSC. On the other hand, this result confirms the local interaction between the AVR and the synchronizing scheme of the grid-forming VSC.

Finally, for grid-forming controls (both droop and VSM), the interactions with AVR dynamics appear to act as a limiting factor for the penetration limit which cannot be observed when modeling the network using an infinite bus.

3.3.4.3. Influence of the active power droop gain

As described in Section 3.3.4.1, the maximum allowable power ratio is around 45% with $x_{eq} = 0.33$ p.u. This value is similar to the 50% that was found in a previous study on the interactions between a similar SG and a VSC in grid-forming mode in a microgrid directly connected to the machine [58]. In order to understand the role of the grid-forming control gains in the stability limit, we perform a parametric study with the $m_{p\omega}$ varying from 1% to 5%. The results are presented in Fig. 3.13.

It is clear that the droop gain has little influence on the maximum allowable power ratio, because even though it moves the critical eigenvalues in the complex plan, the intersection between the imaginary axis and the rightmost eigenvalues is

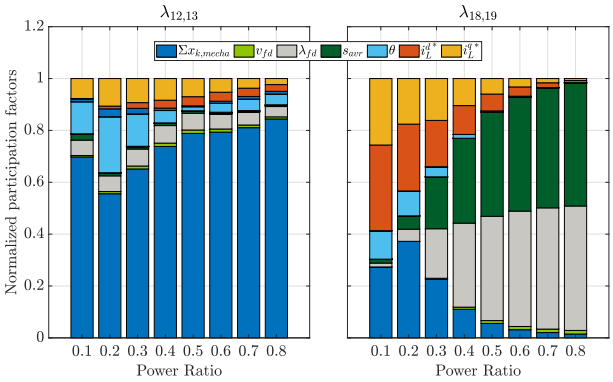

(a) Nominal state-space model

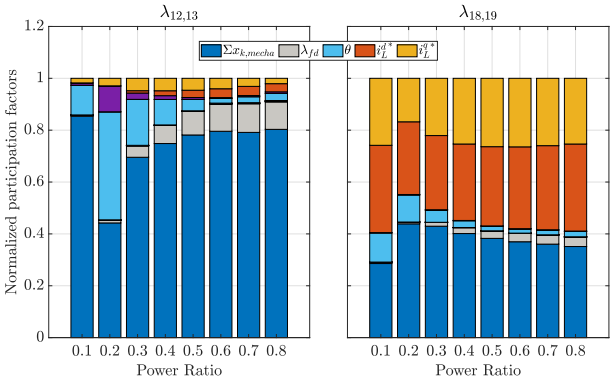

(b) State-space model with no AVR dynamics

Figure 3.11: Participation factors of the $\lambda_{12,13}$ and $\lambda_{18,19}$ modes for different values of P_R with the VSC in grid-forming droop mode and $x_{eq} = 0.33$ p.u.

reached for $P_R \approx 45\%$. On the other hand, when the AVR dynamics are neglected, the system remains stable for all the values of $m_{p\omega}$ we considered.

This result confirms the conclusions drawn in Sections 3.3.4.1 and 3.3.4.2 on the influence of the outer power control loop and the AVR of the SG on the critical modes of the system. In addition, we also studied the impacts of the low-pass filter cutoff frequency $\omega_{c,power}$. Since this parameter has no impacts on the eigenvalues, the results were not displayed in this study.

3.3.5. Penetration limit assessment

In order to summarize all the results we obtained for the different VSC control strategies, for different values of the line reactance on the SG and the power ratio, we plot in Fig. 3.14 the maximum allowable, i.e. stable, power ratio. This gives an indication about the influence of x_{eq} on the system stability. For PLL-based strategies (grid-feeding and grid-supporting), the longer the line, the lower the

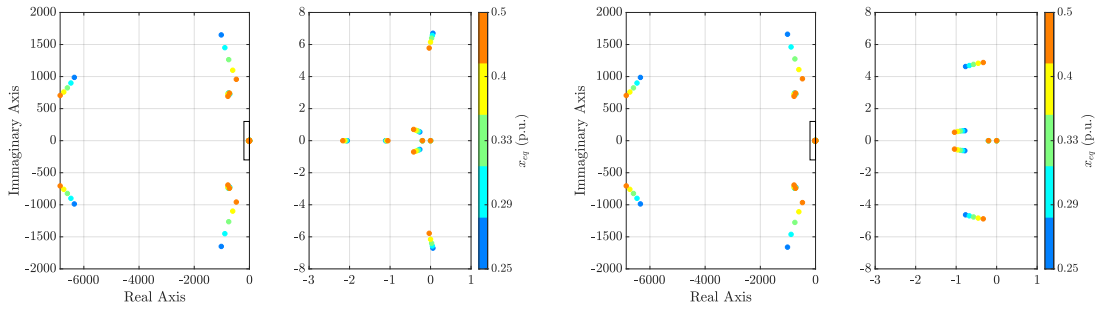

(a) Nominal state-space model (b) State-space model with no AVR dynamics

Figure 3.12: Modal analysis results for different values of x_{eq} with the VSC in grid-forming (droop or VSM) mode and $P_R = 0.45$.

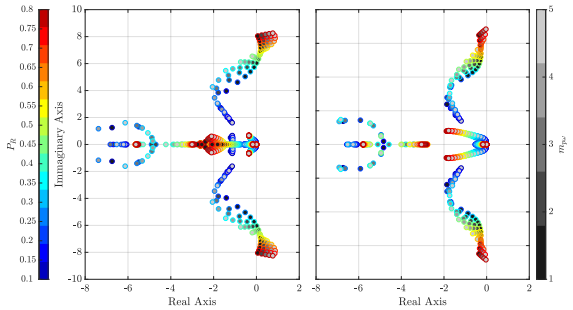

Figure 3.13: Modal analysis results for different values of P_R and different droop gains $m_{p\omega}$ with the VSC in grid-forming droop mode and $x_{eq} = 0.33$ p.u. The left-side figure is the nominal state-space model whereas the right-side figure is the state-space model with no AVR dynamics.

maximum allowable power ratio. This is an intuitive result since the system stability relies on the PLL algorithm, which is sensitive to the electrical distance to the voltage sources [110]. For grid-forming controls, the impact of the electrical distance is such that the closer the PE is to the SG, the less stable the system becomes. To the authors' best knowledge, this result has not been shown in the literature so far and which could drive future research on grid-forming algorithms for improving their penetration limits in power systems. One solution could be introducing a virtual impedance control, as in [59], to electrically "move away" the VSC. However, this control would weaken the PCC voltage stiffness because it would bring farther the voltage source connected to it. Besides, since the electrical distance plays a small role in the stability limit, as described in Fig. 3.14, it may weaken the grid while bringing no real improvements in terms of small-signal stability.

In addition, for longer lines with $x_{eq} > 0.45$ p.u., the grid-supporting strategy tends

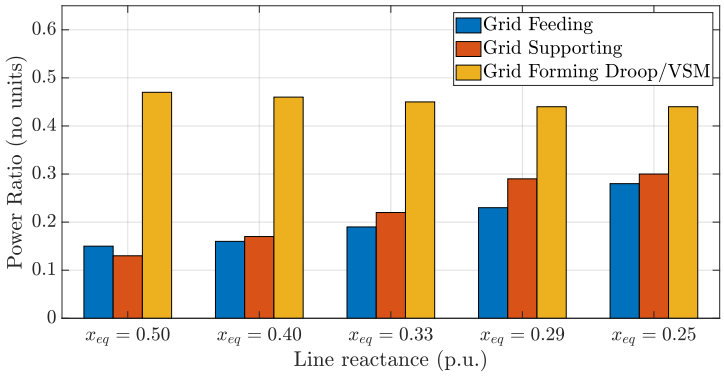

Figure 3.14: Maximum allowable power ratio with respect to the line reactance of the system.

to be less stable than the grid-feeding one. As the equivalent voltage source becomes farther, the PLL synchronizes to the grid with difficulty. In fact, the droop actions from (3.3) is responsible for destabilizing the system.

3.4. Validation by simulations

In Sections 3.4.1 and 3.4.2, we run time-domain simulations using the nonlinear state-space model developed in Section 3.2 to verify the modal analysis results given in the previous section. In Section 3.4.3, we study the stability limit assessments in the case of a multi-machine grid.

3.4.1. Influence of the power ratio and the electrical distance

Fig. 3.15 shows the time-domain simulation results on the system when the VSC is controlled in grid-feeding for $P_R = 0.1$ and $P_R = 0.3$ with $x_{eq} = 0.25$ p.u., following a 5% step of active power load. They show that the higher value of P_R results in unacceptable high-frequency voltage oscillations, as predicted by the modal analysis on the stability limits in Fig. 3.7. Next, we focus on the dependency of the maximum allowable P_R on x_{eq} to quantitatively confirm the results of the modal analysis. We launch a simulation for $P_R = 0.25$ and $x_{eq} = 0.25$ p.u. and introduce a line disturbance such that the line inductance increases up to $x_{eq} = 0.3$ p.u. The evolution of PCC voltage and frequency following this contingency is given in Fig 3.16. It shows that only the system with the VSC in grid-feeding becomes unstable, which confirms the modal analysis results in Fig. 3.14. In addition, a large

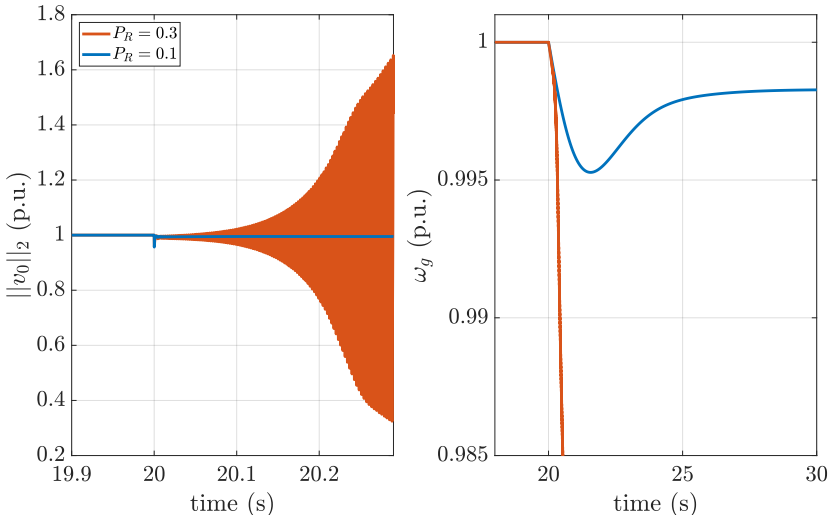

Figure 3.15: Evolution of the PCC voltage magnitude and grid frequency following an active power load step at $t = 20$ s when the VSC is controlled in grid-feeding mode for different P_R and $x_{eq} = 0.25$ p.u.

overshoot and a longer settling time can be observed when the VSC is controlled in grid-forming than in grid-supporting. This can result from the self-synchronizing capability of grid-forming techniques. Indeed, with grid-forming, we observe two equivalent oscillators, i.e. the machine and the converter that oscillate together to reach a consensus, whereas in the grid-supporting case, the two oscillators show a leading-following relation: the VSC "follows" the SG oscillations, hence much less interferences. On the other hand, regarding voltage stability, thanks to its explicit inner voltage control loop, the grid-forming ensures better performances than the grid-supporting, which uses the reactive power/voltage droop given in (3.4).

3.4.2. Influence of the AVR dynamics

To clarify the relationship between the AVR dynamics and the instability of the system when the VSC is in grid-forming mode, we perform two time-domain simulations for $P_R = 0.5$ and $x_{eq} = 0.33$ p.u., with a 5% step in the load's active power as the disturbance. The simulation results given in Fig. 3.17 show that the system is unstable when the AVR is taken into account, whereas it remains stable when the AVR dynamics are neglected.

This confirms the modal analysis in Fig. 3.10. Besides, the frequency of the oscillations is rather slow and may correspond to the undamped low-frequency modes in Fig. 3.10 in the range of electromechanical dynamics. If such oscillations are caused by the AVR interactions with the grid-forming control, then the use of

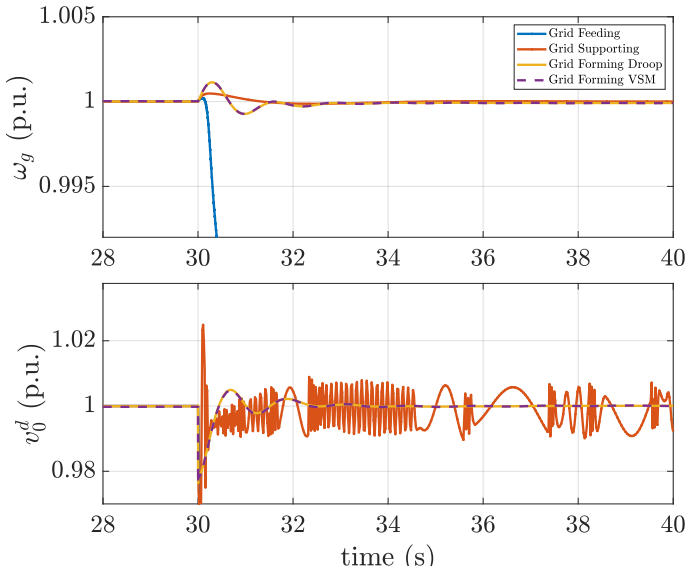

Figure 3.16: Evolution of the PCC voltage and grid frequency following a line impedance step at $t = 30$ s with $P_R = 0.25$ and $x_{eq} = 0.25$ p.u.

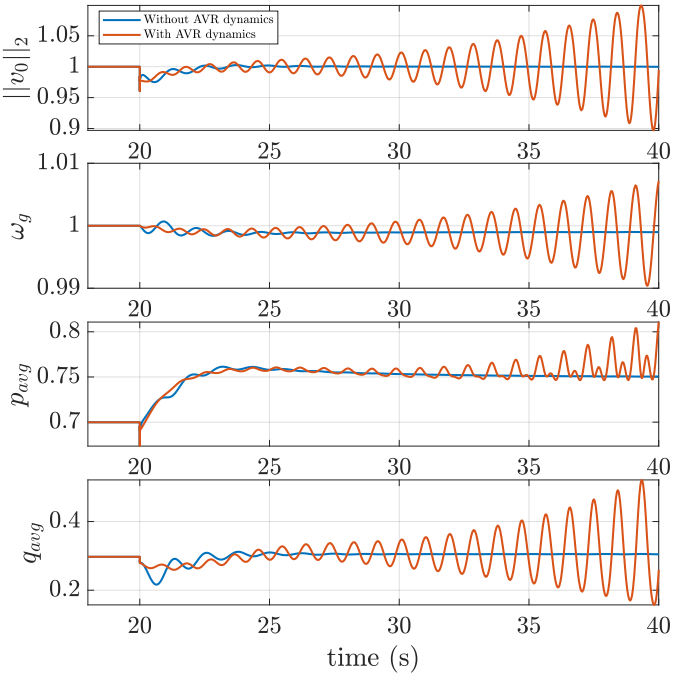

Figure 3.17: Evolution of the system state-variables when the VSC is in grid-forming droop mode following an active power load step at $t = 20$ s, with $x_{eq} = 0.33$ p.u and $P_R = 0.5$.

Power System Stabilizers (PSS) could enhance the compatibility of VSC with the remaining SG. The recent works on penetration limit assessment where the SG is considered with a PSS back this assumption [59].

Table 3.1: Different scenarii using the 4-machine, 2-area system

	VSC control mode	Line reactance x_{eq}
Case 1	grid-feeding	0.005 p.u.
Case 2	grid-feeding	0.5 p.u.
Case 3	grid-forming	0.5 p.u.

3.4.3. Influence of the power system topology

In order to check if the results about the penetration limit assessment given in Fig. 3.14 can be generalized to more complex systems, we simulate different scenarii with a multi-machine system. For the validation purpose, we choose to consider the much more complicated system shown in Fig. 3.18, obtained by replacing the SG in Fig. 3.1 by the 2-area Kundur system defined in [60].

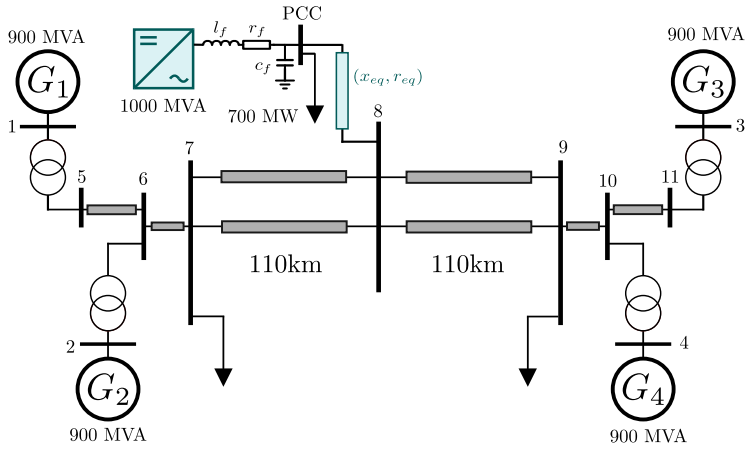

Figure 3.18: Modified Kundur's 4-machine, 2-area system, based on [60].

The Kundur's 4-machine system is a 3-phase balanced system of symmetric topology with four 900 MVA SG which was used recently for studying the impacts of power electronics integration in power systems [153]. For the multi-machine system, the VSC model was developed in Modelica language and the Kundur system is based on the iPSL library [154]. The whole system was simulated using Open Modelica software. The initial power flow data and the system bases are given in Appendix D. We considered a 1000 MVA VSC which corresponds to $P_R = 21.7\%$ based on (3.1). The VSC control mode and the line reactance of the three cases simulated are summarized in Table 3.1, in the Kundur system base in order to assess the limits of stability of grid-feeding controlled VSCs when connected to a high impedance grid. The line resistance r_{eq} is calculated accordingly as in Section 3.2.4.1.

For the simulation cases, the VSC operates at $p^* = 0.7$ p.u. to match the active power setpoint used so far. The load connected to the PCC is modeled as a constant-

current source load to consume 700 MW at the initial voltage. For the grid-feeding cases, the reactive power reference is adjusted to $q^* = -0.065$ p.u. in order to match the absorbed reactive power of Case 3. For the VSC control gains in grid feeding, the control gains are similar to the values from the previous sections. For Case 3 in grid-forming mode, the only differences from Table C.1 are the inner voltage controller gains which correspond to a 1000 MVA VSC [94] and $m_{qv} = 0$ in this case study. The VSC in grid-forming mode is operated with a voltage reference $v_{ref} = v_8^0$ where v_8^0 is the initial value of Bus 8 voltage given in Appendix D. At $t = 30$s, we introduce a 400 MW load step at Bus 9. The corresponding results for the 3 cases are given in Fig. 3.19. v_i corresponds to the i^{th} bus voltage magnitude and $\Delta\omega_{COI} = \omega_{COI} - \omega_{ref}$ is the frequency deviation at the Center of Inertia (COI) which is defined as:

$$\omega_{COI} = \frac{1}{\sum_{i=1}^{4} H_{g_i} S_{g_i}} \cdot \sum_{i=1}^{4} H_{g_i} S_{g_i} \cdot \omega_i \tag{3.25}$$

where $S_{g_i} = 900$ MVA, H_{g_i} and ω_i are respectively the rated power, the inertia constant and the rotor speed of the i^{th} SG. The slight differences between the voltage setpoints in Figs. 3.19 (a) to 3.19 (d) in grid-feeding and grid-forming modes are due to the changes between the line impedance (x_{eq},r_{eq}).

With grid-feeding, we observe that the bus voltages settle at their steady-state values when $x_{eq} = 0.005$ p.u., but show a limit cycle with oscillations at a high frequency when $x_{eq} = 0.5$ p.u. Even though the disturbance was introduced at Bus 9 (see Fig. 3.19 (c)) which has the largest voltage dip, its voltage does not have the largest oscillation magnitude. In particular, the magnitude of voltage oscillations gets larger when the bus is located closer to the VSC (see Bus 8 voltage in Fig. 3.19 (b)) which suggests they are caused by the VSC operating in grid-feeding mode. In addition, these oscillations become less significant near the SGs (see Bus 2 and Bus 11 voltages in Figs. 3.19 (a) and 3.19 (d)). This is in accordance with the claims in Section 3.5 for the case where the P_R is around 20%. In grid-forming, all the bus voltages are brought back to stable operating points when $x_{eq} = 0.5$ p.u., which shows the robustness of the control with respect to high-impedance grids.

For the frequency response given in Fig. 3.19 (e), we observe a smaller frequency dip for Case 2 than Case 1, which is due to the voltage-dependent nature of the load at the PCC. However, we still observe low frequency modes in the first two cases, with the frequency of Case 2 less damped than Case 1. In Case 3, the grid frequency deviation exhibits a better response with a smaller frequency dip and a smaller steady-state error, thanks to the frequency support of the grid-forming

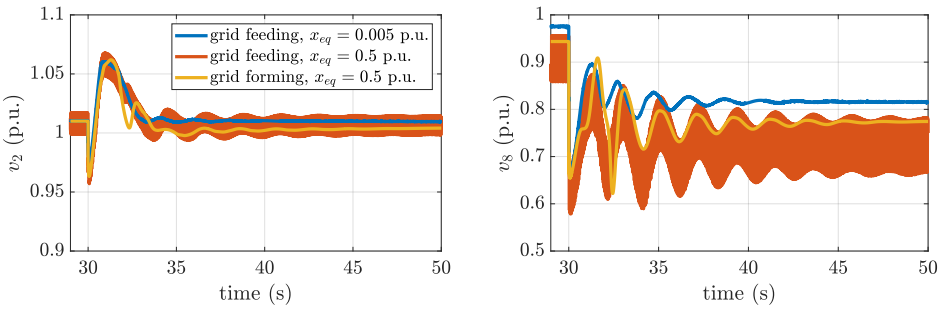

(a) Bus 2 voltage

(b) Bus 8 voltage

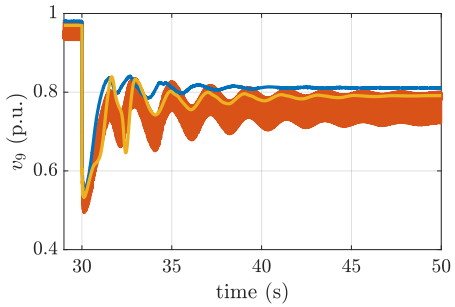

(c) Bus 9 voltage

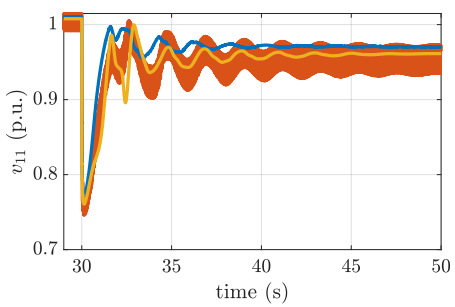

(d) Bus 11 voltage

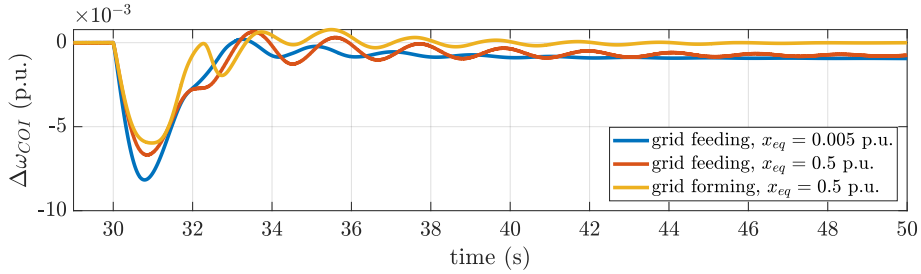

(e) COI frequency

Figure 3.19: Evolution of selected bus voltage magnitudes and COI frequency following an 400 MW active power load step at $t = 30$s at Bus 9 for different VSC control modes and x_{eq}.

controlled VSC, while in the grid-feeding cases, the VSC keeps injecting the same power despite the contingency.

3.5. Conclusions

In this chapter, stability issues of AC power network with PE based VSC converters using different control strategies have been highlighted. Rather than using an AC power system solely based on PE, a simplified network with both VSC and SG has been considered in order to show the impact of PE on power system stability.

Three VSC control strategies and AVR dynamics of the SG are considered against different values of the power ratio (VSC power rating over SG) and the transmission line length. The following concluding remarks can be pointed out:

- For grid-feeding control, it has been shown that, due to the PLL, stability is lost when the PE penetration ratio becomes too high. This issue can be partially mitigated when using the grid-supporting control, which tolerates a higher PE penetration ratio than the grid-feeding control. In future work, a complementary study could be pursued to take into account the impacts of the control gains, especially the PLL, in the stability limits. Additionally, the influence of the electrical distance between the VSC and SG which has been studied using participation factors has also shown stability issues when the electrical distance is increased. For real power systems, this problem exists but with less impact since the grid buses are reinforced through redundant lines.
- For grid forming controls, i.e. droop and VSM, it has been highlighted that the interactions between the AVR and the VSC control seem to be almost independent of the electrical distance, where stability issues may be caused by the electromechanical resonance with VSC outer-loop controls. In this case, it would be desirable to extend the use of the PSS as a potential solution. This could be done in future work knowing that the interactions between VSCs and SGs may change when considering multiple-bus AC power systems with different types of SGs.

In Section 3.4.3, time domain simulations were carried out in a multi-machine system. However, the conclusions of this study could be tested in the future with even more realistic power systems where the distribution of the SGs and VSCs corresponds to the energy needs and resources. In future work, stability analysis methods based on attraction regions tools [127, 155] could provide complementary results for understanding the limits of power electronics penetration in AC grids. Moreover, it will be essential to consider the DC-side dynamics of the VSC when studying the overall dynamics of the AC network with the constraints from these new power sources with the role of grid-forming, an aspect that has been up to now rarely addressed in literature.

Chapter 4

Operation of Modular Multilevel Converters in Grid-Forming Mode: High-level Control Constraints and Enhancements

The contents of this chapter is based on the peer-reviewed publications ***Conference I*** *and* ***Conference III****.*

4.1. Introduction

4.1.1. Context

In Chapter 2, a state of the art of the main VSC control solutions to provide grid support functions was presented. In particular, the grid-forming and grid-following principles were introduced. Then, in Chapter 3, the need to use grid-

forming strategies to relax the power electronics penetration limits in AC grids was highlighted. Similarly to distributed PE-based sources, High Voltage Direct Current (HVDC) stations have to fulfill some additional requirements to make the grid operable and reliable, such as contributing to forming the grid voltage: the *grid-forming* capability [36]. Such requirements concern especially islanded transmission grids such as the UK, where the TSOs experience at the same time a fast decommissioning of fossil-fuel power plants and their associated Synchronous Generators (SG). The remaining SGs will be more unevenly distributed geographically as shown in Fig. 4.1, thus creating weak regions in the grid. In Europe, a lot of research has been conducted so far on grid-forming control [57], where the VSC controlled in grid-forming is often studied with an ideal DC grid [25] and the interactions between AC and DC grids are still a topic that requires further investigation [47].

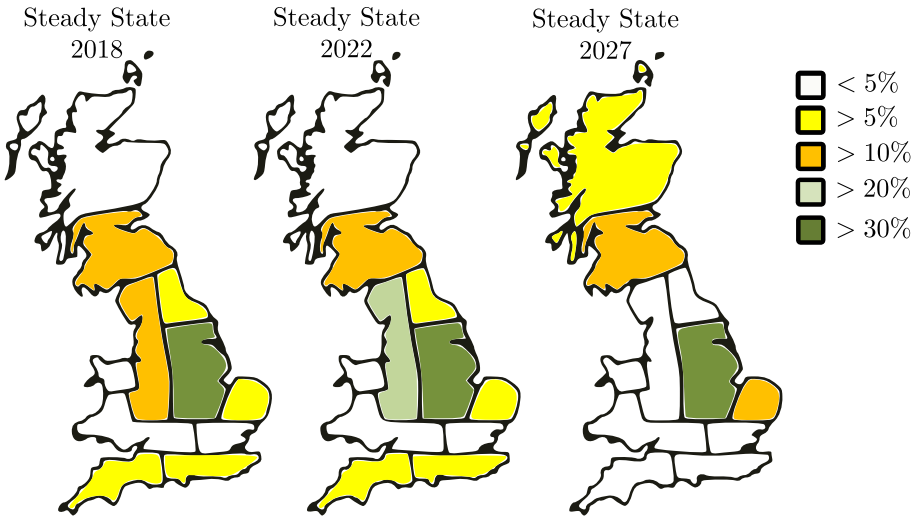

Figure 4.1: Distribution of synchronous generation at the maximal inequality moment in Great Britain [156].

This chapter focuses on the integration of Offshore Wind Farms (OWF) to the AC grid by a DC collector and a HVDC link with the onshore MMC working in DC voltage control mode, as described in [157, 158] and illustrated in Fig. 4.2. The impacts of the interactions between DC-voltage control and grid-forming control on the system are discussed in the particular case of the MMC, which is able to decouple AC and DC in transient by acting on its internal energy. We highlight the problems related to the DC voltage and internal energy and propose possible solutions to these issues. Subsequently, we develop a method to calculate the energy requirements for MMC stations to provide AC-grid ancillary services. Then, an additional high-level control is proposed to ensure the proper use of the MMC enhanced internal

energy. Its performance is assessed using a benchmark representing the case of the high-voltage OWF interconnection described below. The method developed in this chapter is applied to the UK National Grid scenario. Finally the controller is tested upon a multi-machine system to assess its compatibility with a hybrid grid where power electronics and SGs coexist.

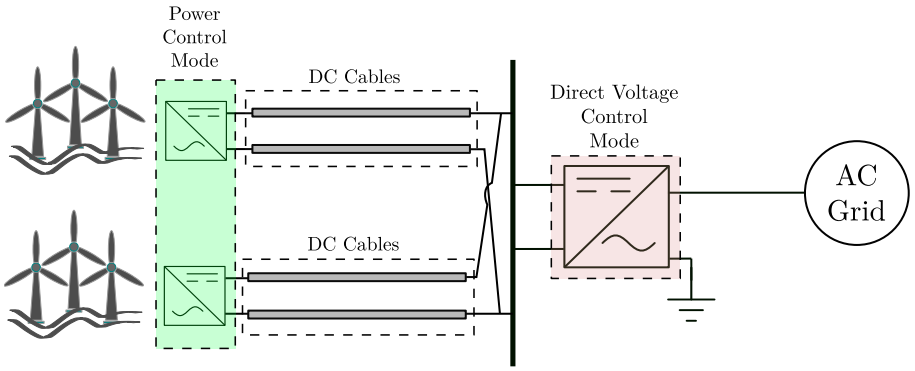

Figure 4.2: Studied architecture for the integration of offshore wind farms in AC grids.

4.1.2. Literature review

In the literature, many studies have been conducted on the control and operation of MMCs for OWF integration. In most of them, the onshore converter is in charge of regulating the DC voltage for the DC side while, on the AC side, it works as a current source converter which uses a classical Phase Locked-Loop (PLL) to synchronize with the AC grid. However, since coastal areas are often the weak parts of a power system, the synchronization through a PLL could be compromised, as highlighted in Chapter 3. One solution is to let the onshore converter work in the grid-forming mode, whereby it behaves like a self-synchronized converter controlled as a voltage source. The interferences between grid-forming control on the AC side with the DC voltage control were discussed for standard 2-level VSCs in [137]. On the other hand, a lot of studies have been carried out on low-inertia systems with more and more power-electronics (PE) converters connected to the grid [58, 59, 76], but many of them do not take into account the DC dynamics and the impacts of the AC power fluctuations on the DC voltage.

In addition, while some studies focus on designing storage systems for VSCs dedicated to grid-forming function [135], the impacts of the grid-forming control on the behavior of HVDC systems, including Modular Multilevel Converter (MMC) internal energy [77] and DC-grid voltage [29], have only been the focus of a few recent studies. However, the change in the high-level control from commonly used

grid-following control to grid-forming control may have consequences on the energy management of the HVDC stations. It could even represent an advantage as the MMC submodules can act as a buffer between AC and DC grids [159] and thus avoid the propagation of disturbances. Moreover, there have been some studies that propose novel control solutions to use the MMC internal energy to support the AC grid frequency: in [160], the MMC energy is discharged using an energy reference profile, while in [161] the MMC energy is discharged using a classical frequency droop. However, to our best knowledge, there are no studies that propose to couple the MMC internal energy with the AC grid frequency similarly to the SG's rotating mass kinetic energy as it is proposed in this chapter.

4.1.3. Chapter summary and contents

In this chapter, the operation of an MMC in grid-forming control is assessed with the DC-grid constraints taken into consideration. In particular, the high-level dynamics of a typical grid-forming droop control are studied. A trade-off is highlighted between supporting the AC grid through grid-forming control and ensuring the security of the DC grid due to the additional delays in power tracking brought by the grid-forming control. Subsequently, a method is presented to calculate the energy requirements of the MMC submodules to provide inertial response to the AC grid as SGs do. This method is combined with a novel control law that makes it possible to use this internal energy to support the AC grid and that is compatible with the state-of-the-art grid-forming control. This control is then analyzed for different types of disturbances and different tuning parameters to show its efficiency. The validation of this control and its compatibility with the grid-forming control is also another contribution of this work.

The structure of this chapter is as follows: In Section 4.2, the MMC technology is presented and the test system used in this chapter is introduced. In Section 4.3, the control structure of an MMC is presented, with a focus on the high-level structure. In Section 4.4, the AC/DC dynamic interactions caused by the operation of the MMC in grid-forming are discussed. Then, the additional energy requirements to provide synthetic inertia to the grid are presented in Section 4.5. In Section 4.6, the proposed control law to use this extra energy is introduced and validated by simulations in Section 4.7. These results are extended to multi-machine systems in Section 4.8. Finally, Section 4.9 concludes and discusses future work.

4.2. Modeling of the system

4.2.1. MMC technology

The Modular Multilevel Converter or MMC is a topology of HVDC converter which is gaining more and more interest to develop point-to-point HVDC links and Multi-terminal DC (MTDC) systems [162]. Contrary to two-level VSCs which use many IGBTs directly connected in series to generate a square voltage which is then filtered using a LC filter, as presented in Chapter 2, the MMC is made of a large number of elementary conversion units: the *submodules*, which can be up to 2000 per station.

The most known topology of MMC-HVDC system is given in Fig. 4.3. the MMC is operated by either activating or deactivating the submodules of the different arms to generate a three-phase AC voltage while maintaining a constant DC voltage on the other side of the converter.

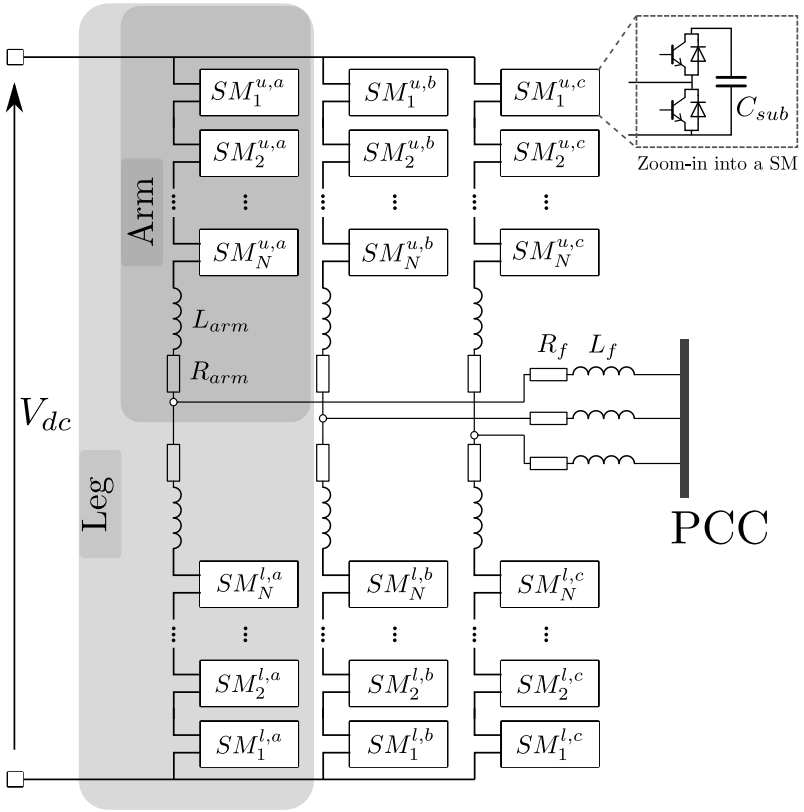

Figure 4.3: Conventional topology of a Modular Multilevel Converter. Figure based on [163, 164].

The voltage generated at the AC point of coupling is the sum of the submodule voltages connected at that moment. Thus, by acting on the gate signals sent to the submodules, it is possible to generate a stepped square sinusoidal waveform [165] as

described in Fig. 4.4. This voltage waveform is much closer to the ideal sine wave compared to the two-level VSCs. In consequence, there is no need of the LC filter in the case of MMC. Thus, the physical AC capacitance is no longer available for implementing the cascaded control structure in Chapter 2 used in the grid-forming control. In the literature, while some works still assume the capacitive effects of AC grid in order to use this cascaded structure [77,166], some other works highlight the necessary changes due to the absence of the physical LC filter in MMC [167].

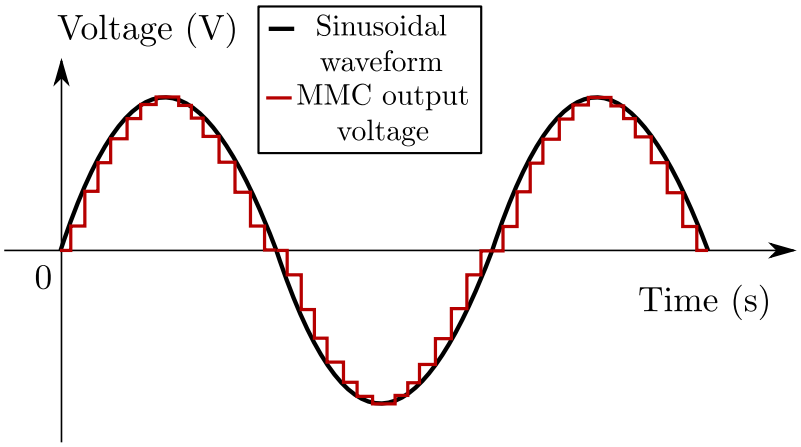

Figure 4.4: AC voltage generation using the MMC submodules to generate a stepped square sinusoidal waveform.

Thanks to its modular nature, the MMC technology becomes a more interesting option for future offhsore wind farm interconnection projects [33]. The main advantages of MMCs compared to classical two-level VSCs are summarized below:

- The conversion equipment generates smaller losses than the conventional VSCs;
- The MMC modular nature makes it possible to easily change the rating, if a higher voltage is needed for instance, without having to replace the entire arm/valve;
- Some extra energy is embedded in the capacitances of the submodules, which gives an extra degree of freedom from a control aspect. In particular, this last item is detailed in Section 4.2.2.

The MMC technology is still emerging and remains a more expensive solution when compared to commoner solutions, such as Line Commutated Converters (LCCs) or two-level VSCs [168]. As an example, the price of a 1000 MW MMC station is higher than a similar two-level VSC: 125 ($\pm$20%) million euros versus 90 ($\pm$20%) million euros [2].

4.2.2. Modeling of the test system

We use an average MMC model which integrates the DC-side dynamics and the AC-side active power control to highlight the interactions that may arise from their coupling. The study is based on the benchmark given in Fig. 4.5 that represents the system of Fig. 4.2.

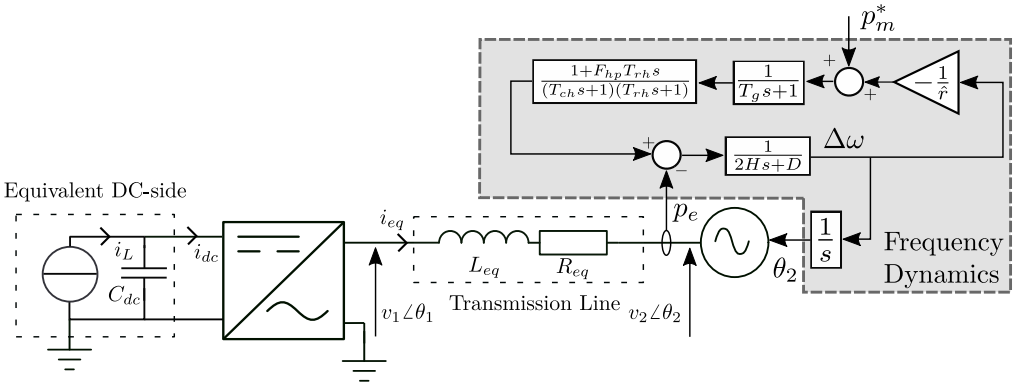

Figure 4.5: Studied equivalent system.

The power from the OWF is modeled by an ideal power source with a delivered power P_L. The DC-voltage dynamics are:

$$\frac{dv_{dc}^2}{dt} = \frac{2}{C_{dc}} \cdot (P_L - P_{dc}) \tag{4.1}$$

where C_{dc} is the DC-side capacitor, v_{dc} is the DC-grid voltage and P_{dc} is the power received by the converter.

It is important to note that contrary to the classical 2-level VSCs, MMCs have an embedded storage capacity thanks to their large number of submodules which are used for the voltage modulation. As proposed in [159], from a grid point of view, the MMC can be seen as a classical AC/DC converter plus an equivalent DC/DC converter which is the interface with the DC grid, as illustrated in Fig. 4.6. This is possible by assuming that the MMC submodules are well balanced at any time.

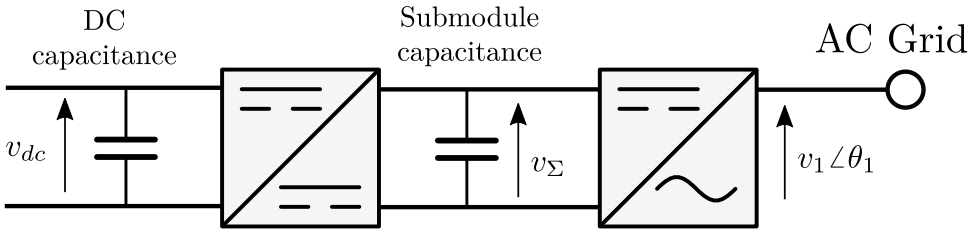

Figure 4.6: System-level view of an MMC, based on [158, 159].

The capacitor between the AC/DC and the DC/DC models the equivalent aggregated submodule capacitance of the converter. In transient, this internal

storage system can act as a buffer to the system by decoupling the power extracted from the DC grid and the power injected in the AC grid. The internal energy dynamics of the MMC can be described by:

$$\frac{dW_{mmc}}{dt} = (P_{dc} - P_{ac}) \tag{4.2}$$

$$W_{mmc} = \frac{1}{2} \cdot C_{eq} \cdot v_{\Sigma}^2 \tag{4.3}$$

where P_{ac} is the AC output power, v_{Σ} is the voltage of the MMC equivalent capacitor, W_{mmc} is the the MMC internal energy, and C_{eq} is the equivalent capacitance of the MMC, which represents all the submodules in the three phases. C_{eq} can be expressed as:

$$C_{eq} = \frac{6}{N_{arm}} \cdot C_{sub} \tag{4.4}$$

where N_{arm} is the number of the submodules in each of the 6 arms of the MMC and C_{sub} is the capacitance of one submodule.

The dynamics of the AC line between the equivalent AC grid and the MMC are given by:

$$\frac{di_{eq}^d}{dt} = \frac{\omega_{base}}{l_{eq}} \cdot (v_2^d - v_1^d - r_{eq} \cdot i_{eq}^d + \omega_{sys} \cdot l_{eq} \cdot i_{eq}^q) \tag{4.5}$$

$$\frac{di_{eq}^q}{dt} = \frac{\omega_{base}}{l_{eq}} \cdot (v_2^q - v_1^q - r_{eq} \cdot i_{eq}^q - \omega_{sys} \cdot l_{eq} \cdot i_{eq}^d) \tag{4.6}$$

where ω_{sys} is the grid frequency and ω_{base} the system fundamental angular frequency, and l_{eq} and r_{eq} are respectively the line inductance and resistance in per unit.

The numerical values of the parameters are given in Table 4.1.

For the equivalent AC grid, as described in Fig. 4.5, a perfect voltage source is considered: $v_2 = 1$ p.u. For the frequency dynamics, a steam-powered synchronous generator described in [58] and based on models from [60] is used.

4.3. Control of the MMC

The general MMC control structure is adapted from the one used in grid-following [164]. For the control of the MMC, as described in Fig. 4.7 (a), the considered MMC is controlled in grid-forming mode on the AC side and in DC-voltage mode on the DC side. In this figure, the considered control dynamics are as follows:

- DC voltage controller which uses a PI control to regulate the DC voltage to its reference. Usually we choose $v_{dc}^* = 1$ p.u.;

- Energy controller, which uses a PI control to maintain the MMC total internal energy within an acceptable level;
- Active power controller, also known as power synchronization loop [79], which uses the variations of active power to synchronize with the grid.

Quantity	**Notation**	**Value**
Base frequency	ω_b	50 Hz
voltage reference setpoints	v_1, v_2	1 p.u.
MMC rated power	S_{MMC}	500 MVA
AC grid rated power	S_{grid}	2500 MVA
AC line-to-line base voltage	V_b^{ac}	320 kV
DC base voltage	V_b^{dc}	640 kV
# of submodules per arm	N_{arm}	400
DC-side capacitance	C_{dc}	140 µF
Line resistance	r_L	0.03 Ω/km
Line reactance	x_L	0.3 Ω/km
Line length	d_L	100 km

Table 4.1: Parameters of the test system.

In this chapter, the AC voltage control dynamics of a reactive power controller are neglected because the focus of the study is the active power related with the interactions between grid-forming synchronization control and DC voltage controller. In addition, the inner-loop controls of the AC and DC sides are not considered, which are, by definition, much faster than the considered outer loop controls [59, 78]. The three considered control loops, with their detailed schemes, are shown in Fig. 4.7 (b). The *Weighting Factors* function allows to distribute the regulation of energy between the AC and DC sides:

$$p_{dc}^* = p^* + \alpha \cdot \Delta p^* \tag{4.7}$$

$$p_{ac}^* = p^* - (1 - \alpha) \cdot \Delta p^* \tag{4.8}$$

where α is the weighting coefficient. In this chapter, we only consider the cases where $\alpha = 0$ and in consequence the MMC energy is only balanced by the AC power modulation. However, the energy control action can also be ensured by the DC power ($\alpha = 1$) [158] or shared between the two ($0 < \alpha < 1$) [169]. The grid-forming control structure is taken from [76]. The design of the DC voltage and energy PI controllers are achieved using pole placement methods as described in [158]. In the next sections, T_{rdc}, ζ_{dc}, T_{rwh} and ζ_{wh} respectively refer to the desired response time/damping ratio of the DC-voltage and energy controllers. The numerical values for the design of each controller are given in Table 4.2 where the damping ratio ζ is

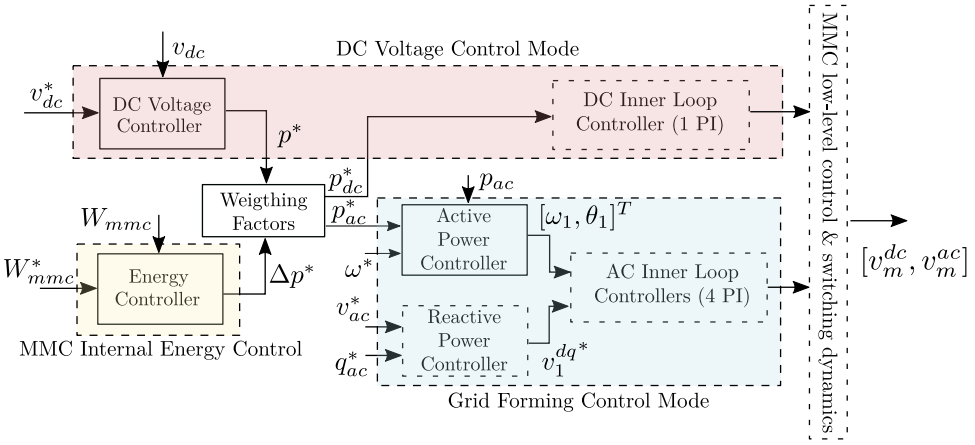

(a) General control structure.

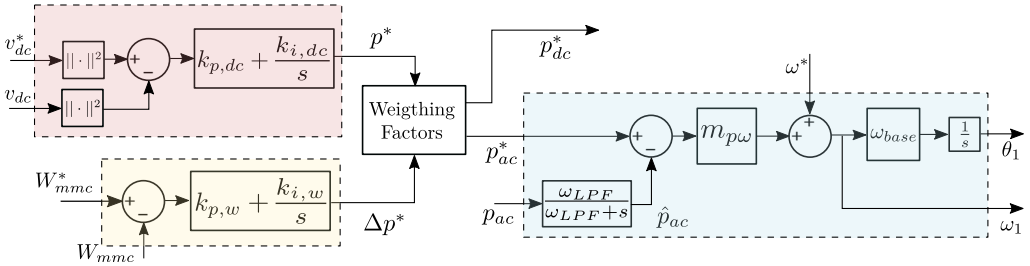

(b) Control scheme of the considered outer-loop control dynamics.

Figure 4.7: Main control scheme of the MMC with the different levels of control.

defined as:

$$\zeta_{dc} = \zeta_{wh} = \zeta \tag{4.9}$$

Quantity	**Notation**	**Value**
Active power droop gain	$m_{p\omega}$	0.1 p.u.
Outer loop filter cut-off frequency	ω_{pq}	31.4 rad/s
Reference frequency	ω^*	1 p.u.
Initial power reference	p^*	0.7 p.u.
Energy control response time	τ_{rwh}	0.5 s
Energy reference	W^*_{mmc}	1 p.u.
Min energy reference	W^{min}_{mmc}	0.8 p.u.
Max. energy reference	W^{max}_{mmc}	1.2 p.u.
v_{dc} response time	τ_{rdc}	0.382 s
DC voltage reference	v^*_{dc}	1 p.u.
Damping ratio of all controls	ζ	0.707

Table 4.2: Control parameters of the test system.

To summarize, the onshore MMC is responsible for controlling the DC voltage by adjusting the extracted power from the DC grid. If there is a disturbance coming

from the wind farm, the chain of action from the control part of Fig. 4.7 (b) is as follows:

1. The wind is blowing more strongly, hence a higher power P_L is injected into the DC grid;
2. The DC voltage increases, due to (4.1);
3. The DC voltage controller adjusts the power reference p^*;
4. p^*_{dc} and p^*_{ac} are adjusted after the weighting factor block from (4.7) and (4.8).

The response time of the DC-voltage controller is not given here because it is used for parametric studies in the following section.

4.4. Impacts of grid-forming control on the DC-voltage loop

4.4.1. Time-domain analysis

As described in Section 4.2.2, the DC-voltage regulator keeps the DC voltage within certain acceptable limits, with a time constant of $T_{V_{dc}}$. Nevertheless, the AC-side active power loop should be chosen fast enough to ensure robust synchronization with the grid and its decoupling from the inner loops, while slow enough to filter the power harmonics [78]. To satisfy these conditions, we chose:

$$\omega_{LPF} = \frac{1}{T_{LPF}} = \frac{\omega_{base}}{10} \tag{4.10}$$

We implement a simulation setup in Matlab/Simulink environment to illustrate the impact of poorly designed AC/DC controls with their time constants close to each other. Two types of simulations are carried out: one with identical time constants: $T_{V_{dc}} = T_{LPF}$, and the other with a slower DC voltage control loop: $T_{V_{dc}} = 4 \cdot T_{LPF}$, where $T_{V_{dc}}$ is the time constant of the PI controller.

It is important to note that $T_{V_{dc}}$ is different from the response time, or the settling time, T_{rdc}. Based on [158], we have:

$$T_{rdc} = 3 \cdot T_{V_{dc}} \tag{4.11}$$

The simulation results in response to a -0.1 p.u. DC power disturbance, which may model the loss of a group of OWF for instance, are given in Figs 4.8. and 4.9. In Fig. 4.8 (a), it is observed that slowing down the DC-voltage loop has a positive impact on the damping of the oscillations in AC due to the DC-side disturbance.

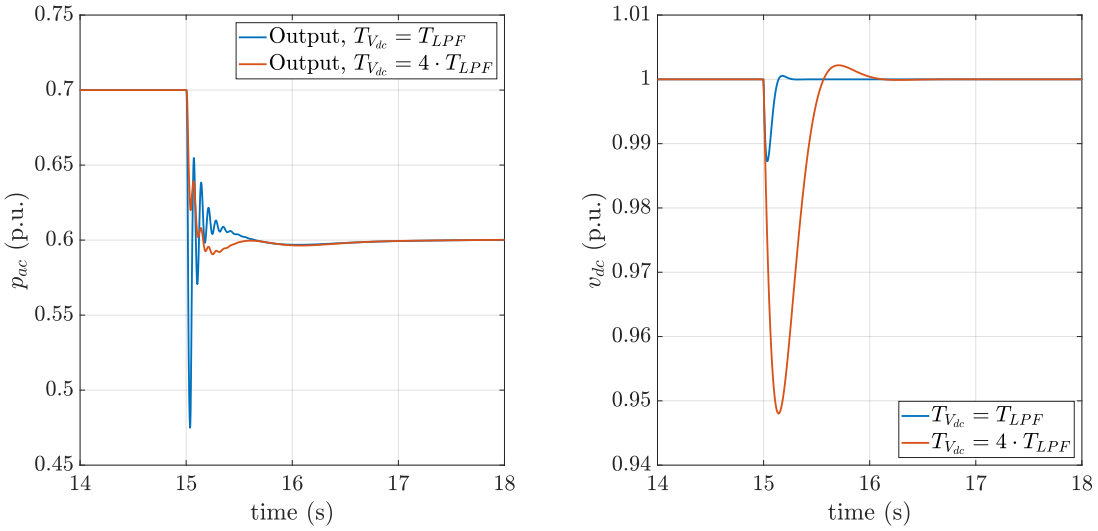

(a) Instantaneous AC power from MMC (b) DC voltage

Figure 4.8: Simulation results of MMC external outputs in response to a disturbance in DC power p_L at $t = 15s$.

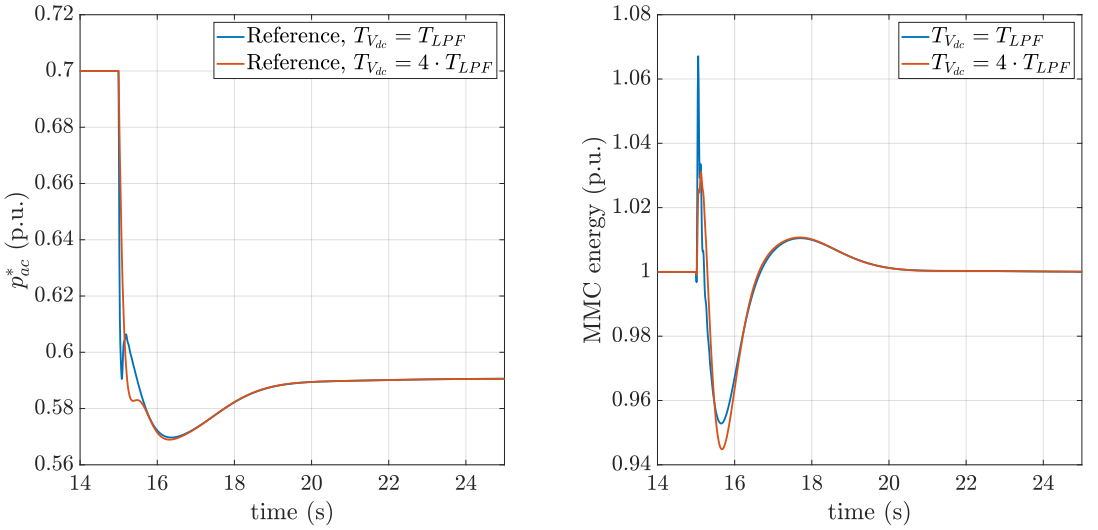

(a) AC power reference (b) MMC internal energy

Figure 4.9: Simulation results of relevant system state variables in response to a disturbance in DC power p_L at $t = 15s$.

However, slowing down the DC-voltage loop makes the DC-voltage less stiff as seen in Fig. 4.8 (b). This would lead to a non-acceptable level in transient when subject to a more severe disturbance.

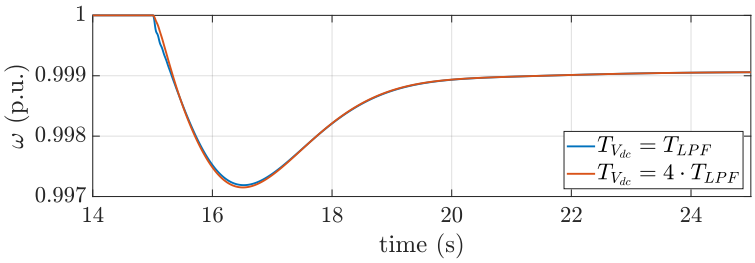

Figure 4.10: Evolution of the AC grid frequency following a disturbance in DC power p_L at $t = 15s$.

It is quite interesting to note that the AC power oscillations in Fig. 4.8 (a) are not visible on the DC voltage. This is due to the decoupling of AC and DC powers in transient, which is made possible by the MMC internal energy. In fact, the DC-side disturbance directly causes variations in the MMC internal energy, as shown in Fig. 4.9 (b), which has an impact on the AC power reference due to the internal energy controller, as illustrated in Fig. 4.9 (a) and thus on the AC power as in Fig. 4.8 (a). Last but not least, it is important to note that all these dynamics are fast compared to the grid frequency dynamics, and represent too little energy to have any significant impact on the AC grid frequency, as given in Fig. 4.10.

4.4.2. Parametric study

In order to understand the cause of the oscillations observed on the AC power, we performed a modal analysis of the system for different values of $T_{V_{dc}}$:

$$\frac{T_{LPF}}{2} < T_{V_{dc}} < 10 \cdot T_{LPF} \tag{4.12}$$

We define a parametric DC-voltage time constant $T_{V_{dc}}(k)$ as:

$$T_{V_{dc}} = \frac{T_{LPF}}{k} \tag{4.13}$$

The eigenvalues are displayed in Fig. 4.11 for $k = \{0.1, 0.2, ..., 2\}$. As expected, slowing down the DC voltage controller results in a better damping on the oscillatory modes related to the controller. Indeed, when $T_{V_{dc}}$ is increased, i.e. when k is reduced, the oscillatory modes have their imaginary part reduced and move towards the real axis, which corresponds to completely damped modes.

The modal analysis confirms the AC/DC interactions between the DC-voltage controller and the AC grid-forming loop. However, it is hard to extract any optimal controller gains from this figure since it does not take into account the constraints

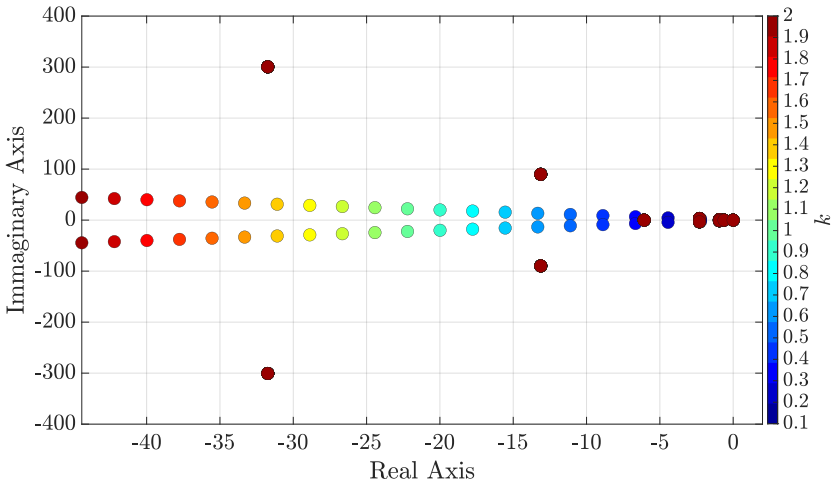

Figure 4.11: Evolution of the eigenvalues of the linearized system when increasing the time-constant of the DC-voltage regulator, denoted by $T_{V_{dc}}$.

on the MMC submodule energy and the DC-voltage limits. To illustrate the trade-off that must be made between the DC voltage and the MMC energy, the squared max deviation following a -0.1 p.u. DC power disturbance is calculated for different values of $T_{V_{dc}}$.

The squared max deviation of the simulation corresponding to a given $T_{V_{dc}}$ is calculated as:

$$\epsilon_{dc}(k) = ({v_{dc}^*}^2 - {v_{dc,min}}^2)^2 \tag{4.14}$$

$$\epsilon_{mmc}(k) = (W_{mmc}^* - W_{mmc,max})^2 \tag{4.15}$$

where $v_{dc,min}$ is the minimum DC voltage following the DC-side disturbance and corresponds to the voltage nadir illustrated in Fig. 4.8 (b) and $W_{mmc,max}$ is the maximum MMC internal energy transient level following the DC-side disturbance and corresponds to the peak observed in Fig. 4.9 (b). The results for the different values of k are given in Fig. 4.12.

As expected, for lower values of k, i.e. slower DC-voltage control, the DC-voltage deviation is relatively significant whereas the MMC energy is kept within acceptable limits. The deviation of the MMC energy becomes greater than that of the DC voltage when $k = 0.6$, for which the sum of the deviations $\epsilon_\Sigma = \epsilon_{dc} + \epsilon_{mmc}$ is also one of the most acceptable. However, if it had been decided to give different weights to the DC voltage and the MMC internal energy deviations, the results could have been different. In the future, it could be reasonable to expect this trade-off between the grid and the converter constraints to be made by the grid operators themselves.

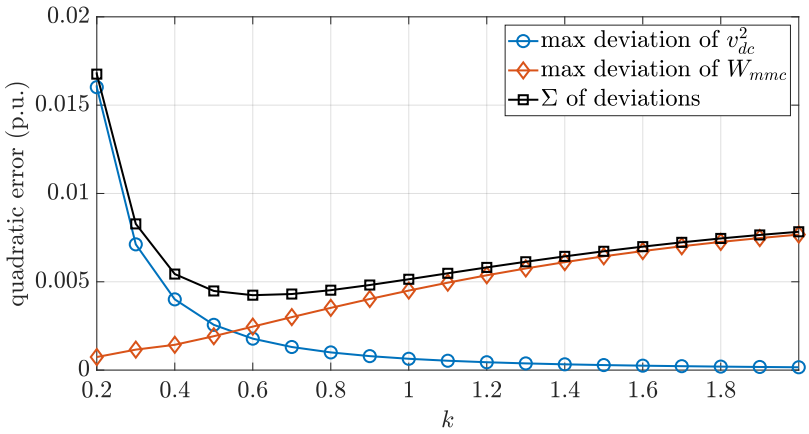

Figure 4.12: Evolution of the squared max deviation of the DC voltage and MMC internal energy when increasing the time constant of the DC-voltage regulator, denoted by $T_{V_{dc}}$.

To summarize, this study analyzes the dynamic behavior of an MMC-HVDC controlled in DC voltage mode in DC and grid-forming in AC, to illustrate negative interactions that may occur when integrating offshore wind farms in the grid. The importance of slowing down the DC voltage control loop is shown to avoid the interactions issues. However, this solution poses problems to the DC stability and some measures should be taken, such as adding a physical DC capacitance. Concurrently, the MMC can also be used to provide additional services to the AC grid, especially frequency-related support. This last part is the focus of the next sections of this chapter.

4.5. Method to define MMC internal energy requirements

4.5.1. Grid code requirements & frequency response

Frequency is one of the key metrics monitored by Transmission System Operators (TSOs) to ensure the stability of the grid, and all the loads and generators have to respect the voltage and frequency requirements imposed by the TSOs. These requirements are described in the grid code. In the rest of this chapter, we focus on the UK grid code, where National Grid imposes the operational frequency ranges given in Table 4.3.

In an SG-dominated system, inertia is the sum of all the SGs inertia connected to the system at a given moment. This inertia is useful because it limits the Rate of Change of Frequency (RoCoF). In particular, a large RoCoF implies a high risk of SG

Frequency Range	Requirements
51.5 Hz to 52 Hz	Operation for a period of at least 15 minutes
51 Hz to 51.5 Hz	Operation for a period of at least 90 minutes
49 Hz to 51 Hz	**Continuous operation is required**
47.5 Hz to 49 Hz	Operation for a period of at least 90 minutes
47 Hz to 47.5 Hz	Operation for a period of at least 20 seconds

Table 4.3: Frequency range requirements in the UK grid code [170].

disconnection or line tripping, while a small RoCoF makes it easy to counterbalance the disturbance within an acceptable amount of time. The UK grid frequency is currently well regulated and, even though its required range of normal operation is ± 1 Hz (see Table 4.3), it is in reality kept within an even narrower range. For example, Fig. 4.13 shows that the frequency remained within the range of ±250 mHz during the whole month of November 2019 in the UK.

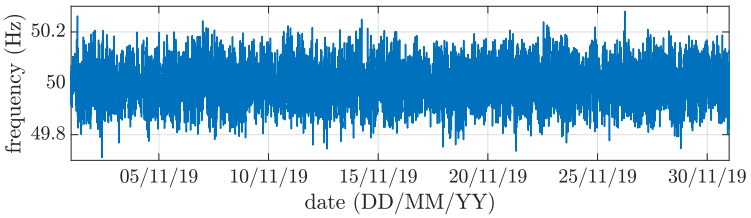

Figure 4.13: Frequency monitoring in the UK transmission system in November 2019 [171].

However, with the ongoing dismantlement of SGs, HVDC stations, such as OWF onshore MMC, could be asked to provide frequency response to support the grid as SGs used to do. If the frequency containment reserves can be managed at the wind-farm level [134], the inertial response of SGs may be too fast to be emulated by the wind farm control. Therefore, this work focuses on the inertial response of SGs using the internal energy of the MMC.

4.5.2. Synthetic inertia needs

The method presented in this chapter makes the MMC emulate the typical inertial response of synchronous generators following an active power disturbance, given in Fig. 4.14. In particular, the MMC submodules are required to provide as much energy as needed in order to emulate this inertial response, for example the first-swing response covered by the green hashed lines in Fig. 4.14. Since the frequency range in Table 4.3 in which any equipment (SG or VSC) is supposed to remain connected is ±1 Hz, only a fraction of the entire equivalent kinetic energy of the rotating mass would be enough to realize the frequency support. In the following,

we determine the MMC required energy that can provide a SG-like inertial response within the frequency range of ±1 Hz.

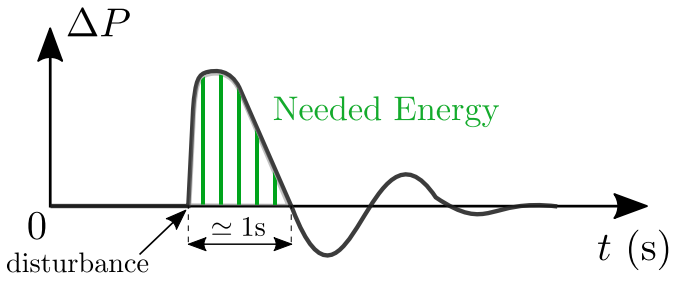

Figure 4.14: Typical inertial response of synchronous generators.

Since an MMC already stores some internal energy in its submodules, a primary comparison is required to see how much extra energy is needed. We assume that the submodules can tolerate a variation of 20% around their nominal energy [163]. Table 4.4 gives a comparison of the available energy between the rotating mass of a typical SG and an MMC of the same power rating, based on the features in [77], where the available energy is calculated as $\Delta W_{SG} = H_0 \cdot (\omega_0^2 - \omega_{min}^2) \cdot S_{nom}$ for the SG and $\Delta W_{MMC} = H_0 \cdot (W_0 - W_{min}) \cdot S_{nom}$ for the MMC.

Quantity	**Synchronous Generator**	**Modular Multilevel Converter [77]**
Rated power S_{nom}	500 MVA	500 MVA
DC grid rated voltage V_b^{DC}	not relevant	640 kV
Submodule capacitance C_{sub}	not relevant	8 mF
# of submodules N_{arm}	not relevant	400 per arm
Inertia constant H_0 (s)	3 s	49.2 ms
Minimum frequency ω_{min}	49.0 Hz	not relevant
Minimum energy W_{min} [163]	/	0.8 p.u.
Available energy ΔW	59.4 MJ	4.915 MJ

Table 4.4: Comparison of standard operational quantities of a synchronous generator and an MMC.

As shown in this table, even though the ratio between SG and MMC stored energy is almost 100 (3s *vs* 49.2ms), their ratio in terms of available energy is only slightly above 10 (59.4 MJ *vs* 4.915 MJ).

4.5.3. Energy requirement calculations

This part presents the method to calculate the energy requirements and the corresponding size of the MMC submodules to provide similar synthetic inertia as SGs. In particular, we seek to increase the size the submodules so that its released

or absorbed energy is of the same amount of what a SG with the same power rating would release or absorb when the frequency changes by a certain level.

First, the kinetic energy variation of an SG when the frequency decreases by 1 Hz can be found as

$$\Delta W_{SG} = H_0 \cdot (\omega_0^2 - \omega_{min}^2) \cdot S_{nom} = 3 \cdot (1 - (49/50)^2) \cdot 500 = 59.4\text{MJ} \tag{4.16}$$

The internal energy of the original (not oversized) MMC, denoted by W_{mmc}, can be expressed as $W_{mmc} = \frac{1}{2} C_{eq} v_{dc}^2$, where $C_{eq} = \frac{6}{N_{arm}} C_{sub}$ is the equivalent capacitor of the original MMC. Using the values in Table 4.4, we have

$$W_{mmc} = \frac{1}{2} C_{eq} v_{dc}^2 = \frac{1}{2} \frac{6}{N_{arm}} C_{sub} v_{dc}^2 = \frac{1}{2} \frac{6}{400} 0.008 * 640^2 = 24.58\text{MJ} \tag{4.17}$$

Denote by C'_{sub} the equivalent capacitance of the oversized MMC submodules and introduce $N_{oversize}$ as the oversizing coefficient of the submodule capacitance defined such that $C'_{sub} = N_{oversize} \cdot C_{sub}$. For simplicity, $N_{oversize}$ is assumed to only take integer values. Obviously, the internal energy of the oversized MMC, denoted by W'_{mmc}, can be expressed as $W'_{mmc} = N_{oversize} \cdot W_{mmc}$. Assuming that W_{mmc} can tolerate a minimum value of 0.8 p.u., the energy variation of the oversized energy can be obtained as

$$\Delta W'_{mmc} = (1 - 0.8) \cdot N_{oversize} \cdot W_{mmc} \tag{4.18}$$

If we require that when the MMC internal energy variation reaches its limit, the energy released or absorbed by the submodules is of the same amount that an SG of the same power rating would release or absorb when the frequency changes by ± 1 Hz, then we must have

$$\Delta W_{SG} = \Delta W'_{mmc} = (1 - 0.8) \cdot N_{oversize} \cdot W_{mmc} \tag{4.19}$$

Numerically,

$$N_{oversize} = \text{round}\left(\frac{\Delta W_{SG}}{(1 - 0.8) \cdot W_{mmc}}\right) = \text{round}\left(\frac{59,4}{(1 - 0.8) \cdot 24,58}\right) = 12 \tag{4.20}$$

Alternatively, instead of using oversized MMC submodules, the same amount of energy for frequency response can be provided by an additional Energy Storage System (ESS) which is interfaced with the MMC submodules by a DC/DC converter [172]. The required energy for such an ESS can be calculated as

$$\Delta W_{ESS} = \Delta W_{SG} - 0.2 \times W_{mmc} = 59.4 - 0.2 \times 24.58 = 54.5\text{MJ} \tag{4.21}$$

Desired features of SG		**Oversized MMC capacitors**		**Additional ESS**
Desired equivalent inertia	Required energy	Oversized submodule capacitance	Available energy ($\pm 20\% W_{mmc}$)	Needed extra energy
H_0 and Δf	ΔW_{SG}	$C'_{sub} (= N_{oversize} \cdot C_{sub})$	$\Delta W'_{mmc}$	ΔW_{ESS}
3s and ±1Hz	59.4 MJ	96 mF (=12×8) mF	59.0 MJ	54 MJ
6s and ±1Hz	119 MJ	192 mF (=24×8) mF	118.0 MJ	112 MJ
3s and ±0.5Hz	29.9 MJ	49 mF (=6×8) mF	29.5 MJ	24.6 MJ

Table 4.5: Comparison of the energy requirements for the MMC to emulate different inertial responses. The requirements are given in terms of an oversized submodule capacitance and in terms of power and energy if an additional ESS is needed.

The above method is used to design oversized MMC submodules or alternative ESS for different values of the inertia constant and the frequency deviation range of the SG, and the results are summarized in Table 4.5.

In fact, the alternative ESS can also be considered as equivalent oversized capacitors because the associated DC/DC converter can be controlled using the control law proposed in [163] which emulates the behavior of an additional parallel-connected capacitor. In consequence, in the rest of the study, only the oversized MMC submodules are considered to provide the extra energy.

4.6. Control design

4.6.1. Proposed control law

To provide frequency support using oversized submodules, we propose to use a dynamic energy reference controller [77, 163], whereby the internal energy reference W^*_{mmc} is changed in proportion to the deviation of the square of the grid frequency ω_g. Since this variable is difficult to compute in real time, we consider rather the local frequency imposed by the grid-forming control and denoted by ω_1. The control law is:

$$W^*_{mmc} = W^*_{mmc,0} + k_{vr} \cdot ({\omega_1}^2 - {\omega^*}^2) \tag{4.22}$$

$$W^{min}_{mmc} \leq W^*_{mmc} \leq W^{max}_{mmc} \tag{4.23}$$

where $W^*_{mmc,0} = 1$ p.u. is the energy reference corresponding to 50 Hz, ω^* is the AC grid reference frequency in per unit, and k_{vr} is a tunable coefficient which emulates the response of a rotating machine. W^{min}_{mmc} and W^{max}_{mmc} are used to ensure that the energy controller respects the physical limits of the MMC and their values will be specified later.

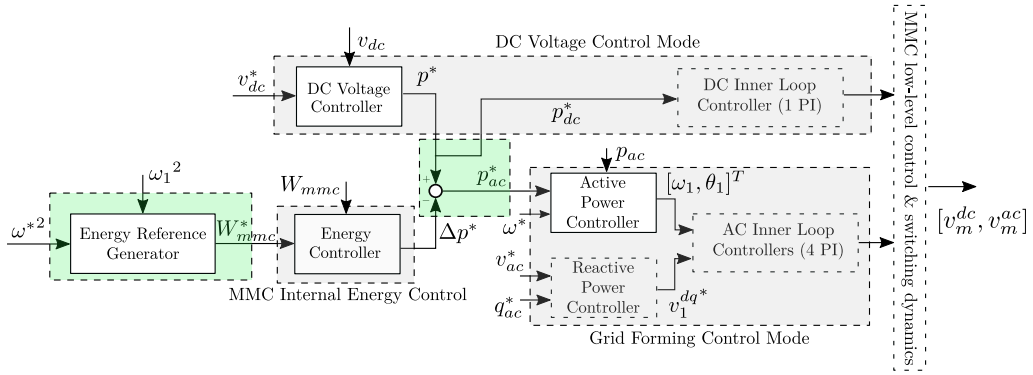

Figure 4.15: General control scheme of the MMC controlled in grid-forming mode, based on [29]. The blocks in *green* are specific to this study.

Since this control law is based on emulating the kinetic energy of the rotating mass of a SG, it is named *Virtual Rotor Control* or VCR in this chapter where k_{vr} is the associated virtual rotor coefficient. In order to provide this energy to the AC grid, the energy controller is coupled to the AC power reference only. This AC power reference p_{ac}^* is used in the grid-forming control as detailed in Fig. 4.15. This control is based on the general control scheme presented in Fig. 4.7. Besides, the MMC also ensures the DC grid voltage control.

4.6.2. Controller tuning

In this subsection, the tuning of the coefficient k_{vr} is discussed. Since the aim of the control law is to use all the available energy in the MMC submodules when the maximum acceptable frequency is reached, $W_{mmc}^{min} = 80\%$ must be reached when the grid frequency reaches $\omega_{min} = 49.0$ Hz based on Table 4.3. Thus, k_{vr} can be calculated as:

$$W_{mmc}^{min} = W_{mmc,0}^* + k_{vr} \cdot ({\omega_{min}}^2 - \omega^{*2}) = 80\% \tag{4.24}$$

$$\implies k_{vr} = \frac{W_{mmc}^{min} - W_{mmc,0}^*}{{\omega_{min}}^2 - \omega^{*2}} = \frac{0.8 - 1}{0.98^2 - 1^2} \approx 5 \tag{4.25}$$

4.7. Validation by simulations

4.7.1. Test case

To show the effectiveness of the virtual rotor control, we conduct simulations on a simple system where an MMC representing an OWF, modeled by an equivalent power source with DC-side voltage dynamics, is connected to an aggregated AC grid by an overhead line. Only the outer-loop control shown in Fig. 4.15 is considered

for MMC, and the grid-forming control used is the droop-based option [94]. More details about this test system can be found in Section 4.2.

The submodule capacitance considered in the simulations is $C_{sub} = 96$ mF, based on the results from Table 4.5, in order to match the response of a SG of $H_0 = 3$ s in a range of ± 1 Hz. The additional physical and control parameters of the test system are given in Tables 4.1 and 4.2. The parameters concerning the frequency dynamics of the aggregated AC grid can be found in [75].

Four types of disturbance are tested. Two of them are an AC power increase by 50 and 250 MW, respectively, which can represent a sudden load increase, while the other two are a DC power drop by the same values, which can represent the loss of some of the energy coming from the OWF for instance.

4.7.2. Results

The results are given in Fig. 4.16. They show that for all the 4 considered disturbances, the virtual rotor control always yields better results than the standard MMC energy controller in terms of the RoCoF and the frequency nadir. In addition, since W_{mmc} never reaches 0.8 p.u., there is still some available energy to further support the frequency, which can be realized by choosing a larger k_{vr}. Lastly, the virtual rotor control neither improves nor deteriorates the DC voltage, which suffers from a severe dip when subject to the 250 MW disturbance from the DC grid.

To investigate the role of k_{vr}, further simulations are conducted with k_{vr} varying between 5 and 25. The time evolution of physical quantities are given in Fig. 4.17, and the dependency of the frequency nadir and the RoCoF upon k_{vr} is given in Fig. 4.18. On the one hand, increasing k_{vr} results in a smaller (or better) RoCoF, while on the other hand, the nadir is the highest (or the most desirable) when $k_{vr} = 9$. These observations are similar for both the DC and AC disturbances. However, as k_{vr} increases, W_{mmc} may violates its lower limit $W_{mmc}^{min} = 80\%$, which is less acceptable than the case where $k_{vr} = 5$. This large overshoot in the evolution of W_{mmc} may be attributed to the relatively poor power tracking performances of the grid-forming control compared to the classical grid-following control [115].

4.8. Extension to multi-machine systems

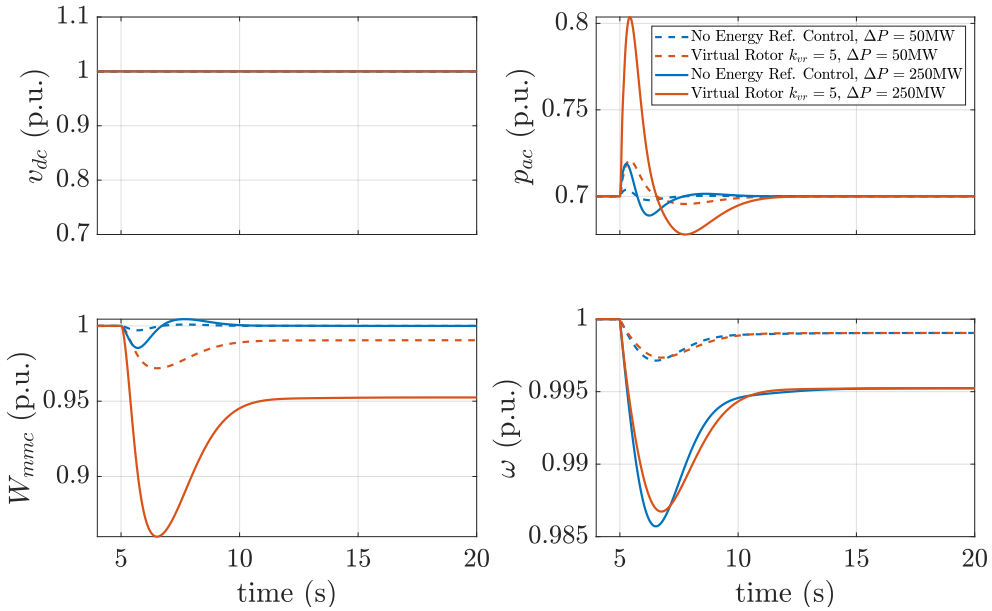

(a) Dynamic response of the system subject to AC power disturbances of 50 and 250 MW.

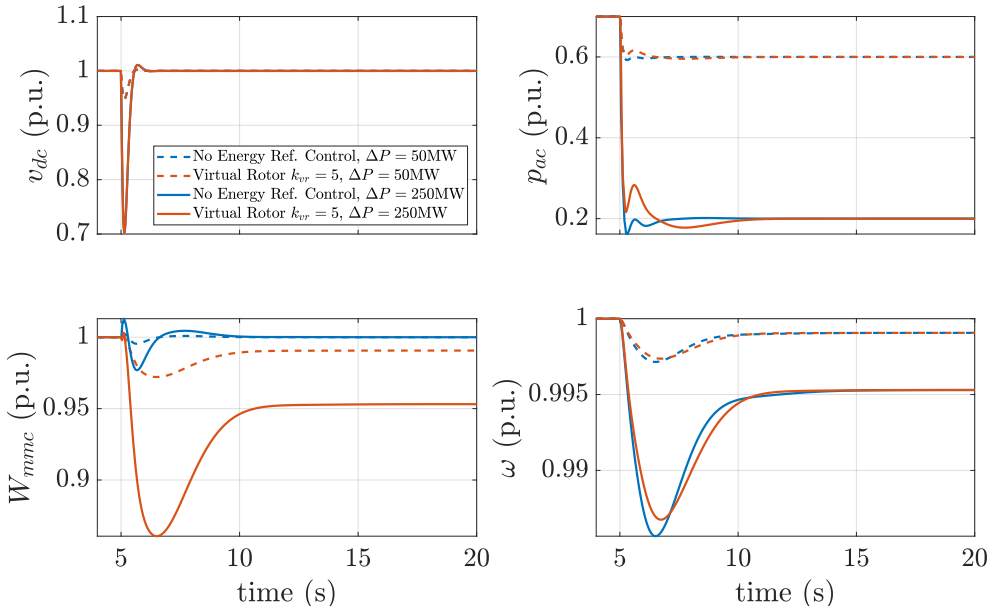

(b) Dynamic response of the system subject to DC power disturbances of 50 and 250 MW.

Figure 4.16: Simulation results for the MMC operated with the proposed control law compared to the standard internal energy controller, under the 4 types of disturbance.

4.8.1. Grid model

So far in this chapter, all the results presented are based on an aggregated model of an AC grid, which is relevant for studying the frequency-related functions of the AC grid and connected converters. However, in a real power system, there are many

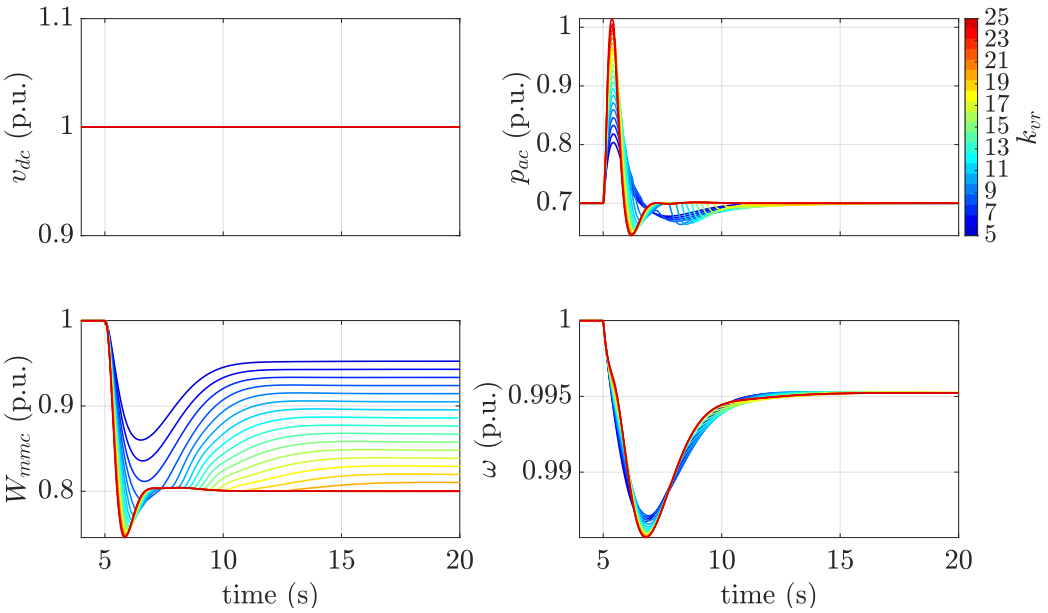

(a) AC power disturbance

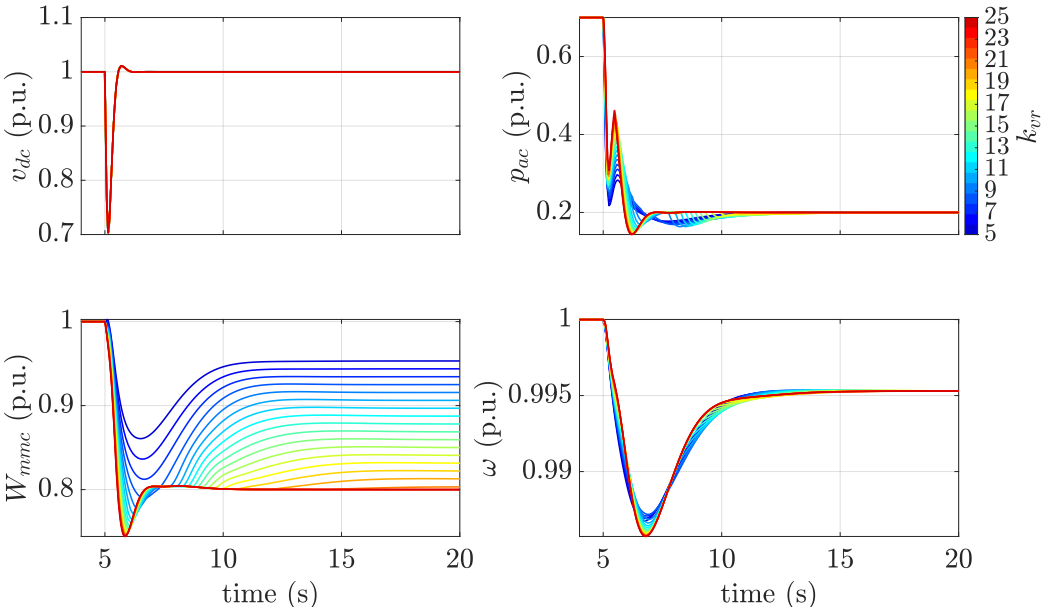

(b) DC power disturbance

Figure 4.17: Simulation results following a power step disturbance of 250 MW for different values of k_{vr}.

generators and loads, which bring their own dynamics to the system and can even interact with each other. The aim of this section is to study the behavior of the "Virtual Rotor Control" when the frequency dynamics are no longer homogeneous but instead when the system can encounter inter-area oscillations.

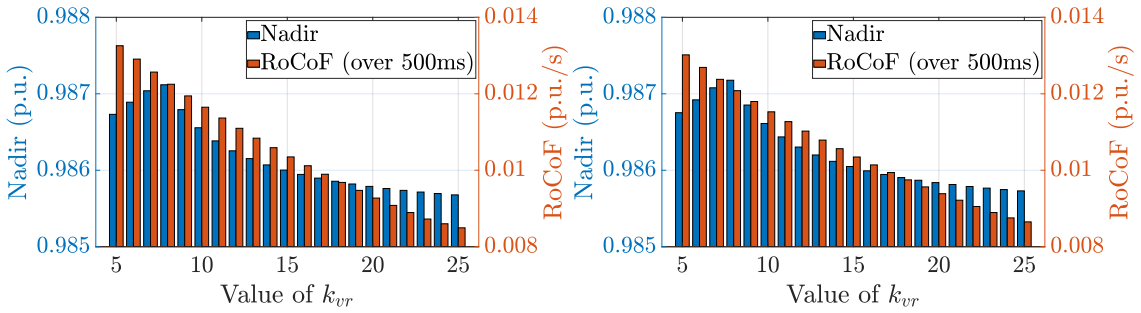

(a) AC power disturbance (b) DC power disturbance

Figure 4.18: Dependency of the frequency nadir and the RoCoF on the value of k_{vr} following a disturbance of 250 MW.

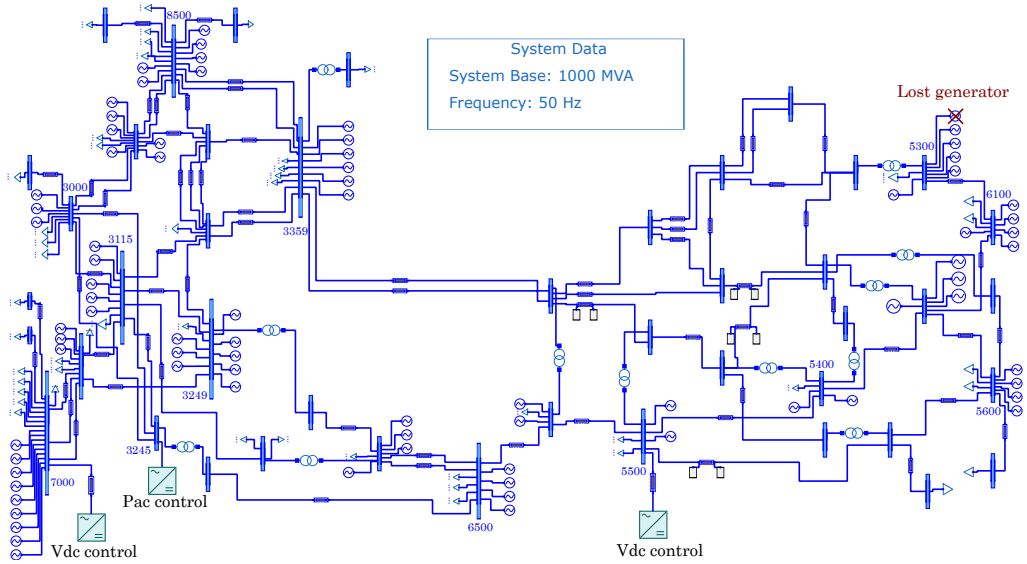

Figure 4.19: Modified transmission grid model of the Nordic 44 system representing the Nordic synchronous area.

In order to have a realistic model, we consider the Nordic 44 system which contains 80 synchronous generators. More details about this model can be found in [173]. We modified the existing power system by introducing three MMCs with different control modes, one in AC power control mode (p_{ac}-mode) and two in DC-voltage mode (v_{dc}-mode).

The modifications with respect to the original case [173] are:

- Two grid-forming MMCs (1000 MVA each) in v_{dc}-mode are connected to buses 7000 and 5500 through transmission lines ($x_l = 0.166$ p.u. and $r_l = 0.0166$ p.u.). On their DC side, an equivalent capacitor and a filtered DC current injector are connected. The initial power set-point of these stations is 0 MW.

- The generator at bus 3245 is replaced by a grid-forming MMC station in p_{ac}-mode. The active power set-point of this station is the same as the replaced synchronous generator (i.e. 205MW).
- The transmission lines connecting the MMCs to the nearest generators are represented by dynamic π-sections (also known as *hybrid network model* [174]).

In the rest of the chapter, each MMC will be referred to by its bus number in order to avoid misunderstandings.

4.8.2. Test cases

In order to test the impacts of the AC grids dynamics on the method proposed in this chapter, we conduct two test cases:

- **Case 1 (without VRC):** the three MMCs are similar in terms of the number of submodules and ratings. Their submodules are not oversized and no VRC is implemented;
- **Case 2 (with VRC):** MMC 3245 is similar to case 1, but MMCs 7000 and 5500 have oversized submodules so that they can provide synthetic inertia to the system. For the latter two MMCs, VRC is implemented with $k_{vr} = 25$.

The numerical values of the MMCs parameters can be found in Table 4.6. In both cases, we simulate the loss of a generator in the bus 5300 which results in a -800MW power unbalance in the system. This event is triggered at $t = 5$s.

MMC #	**Control mode**	**SM capacitance (C_{sub})**	**# of SM per arm (N_{arm})**
MMC 3245	p_{ac}-mode	10mF	200
MMC 5500	v_{dc}-mode	10mF	200
MMC 7000	v_{dc}-mode	10mF	200

(a) Case 1

MMC #	**Control mode**	**SM capacitance (C_{sub})**	**# of SM per arm (N_{arm})**
MMC 3245	p_{ac}-mode	10mF	200
MMC 5500	v_{dc}-mode	96mF	400
MMC 7000	v_{dc}-mode	96mF	400

(b) Case 2

Table 4.6: Parameters of the MMCs incorporated in the Nordic 44 test system.

4.8.3. Modeling and control of the MMCs

The three MMCs are modeled by (4.2) and (4.3), presented in Section 4.2.2. The AC transformer inductance and resistance, L_f and R_f respectively, shown in Fig. 4.3

are taken into account. For the three MMCs, we take $L_f = 0.18$ p.u. and $R_f = 0.001$ p.u.

In terms of control, the grid-forming outer loop control is the same as the one presented in Section 4.3. The MMC inner loop control is based on [115]. The values of the control parameters which differ from Section 4.3 can be found below. In addition to those changes, compared to the numerical values given in Table 4.2, the following control parameters were also considered for the three MMCs:

$$k_{vr} = 25, m_{p\omega} = 0.02 \text{ p.u.}, \tau_{rdc} = 0.15 \text{ s}, \tau_{rwh} = 0.4 \text{ s} \tag{4.26}$$

4.8.4. Results and discussions

The two cases described in Section 4.8.2 are simulated using Dymola software [175] in DAE-mode, with the grid and the MMCs modeled using Modelica language. The results are given in Fig. 4.20.

It is interesting to note that the VRC works well even when we consider a large power system. Indeed, as described in Fig. 4.20 (d) where the internal energy of MMCs 7000 and 5500 is used accordingly to the frequency deviation to support the AC grid. This contribution is also observable in terms of the injected AC power given in Fig. 4.20 (a). However, the VRC appears to have almost no impacts on the AC voltage magnitude or the reactive power, which justifies our choice to use simplified models. Also, it is important to note that, similarly to the results given in Fig. 4.16 with an aggregated model, the AC-side disturbance does not propagate to the DC grid in either case, as expected.

From the grid perspective, we see that in both cases, we have low-frequency oscillations in the active power and the rotor speed of the generators, which are transmitted to the MMC internal energy, but not to the DC grid thanks to the buffering action of the MMC submodules. Indeed, these oscillations are caused by the interactions between all the synchronous generators of the grid, and are transmitted to the MMCs because they are controlled in grid-forming mode and behave in consequence as virtual synchronous generators.

Finally, we observe in Fig. 4.20 (f) that the VRC does provide some inertial support to the neighboring SGs by discharging the MMCs submodules, but this support is relatively small because the Nordic 44 grid is much bigger in terms of the installed power compared to the ratings of the two MMCs controlled with VRC. However, the low-frequency oscillations are still present on the frequency and active power. Additional actions should be considered to damp these oscillations.

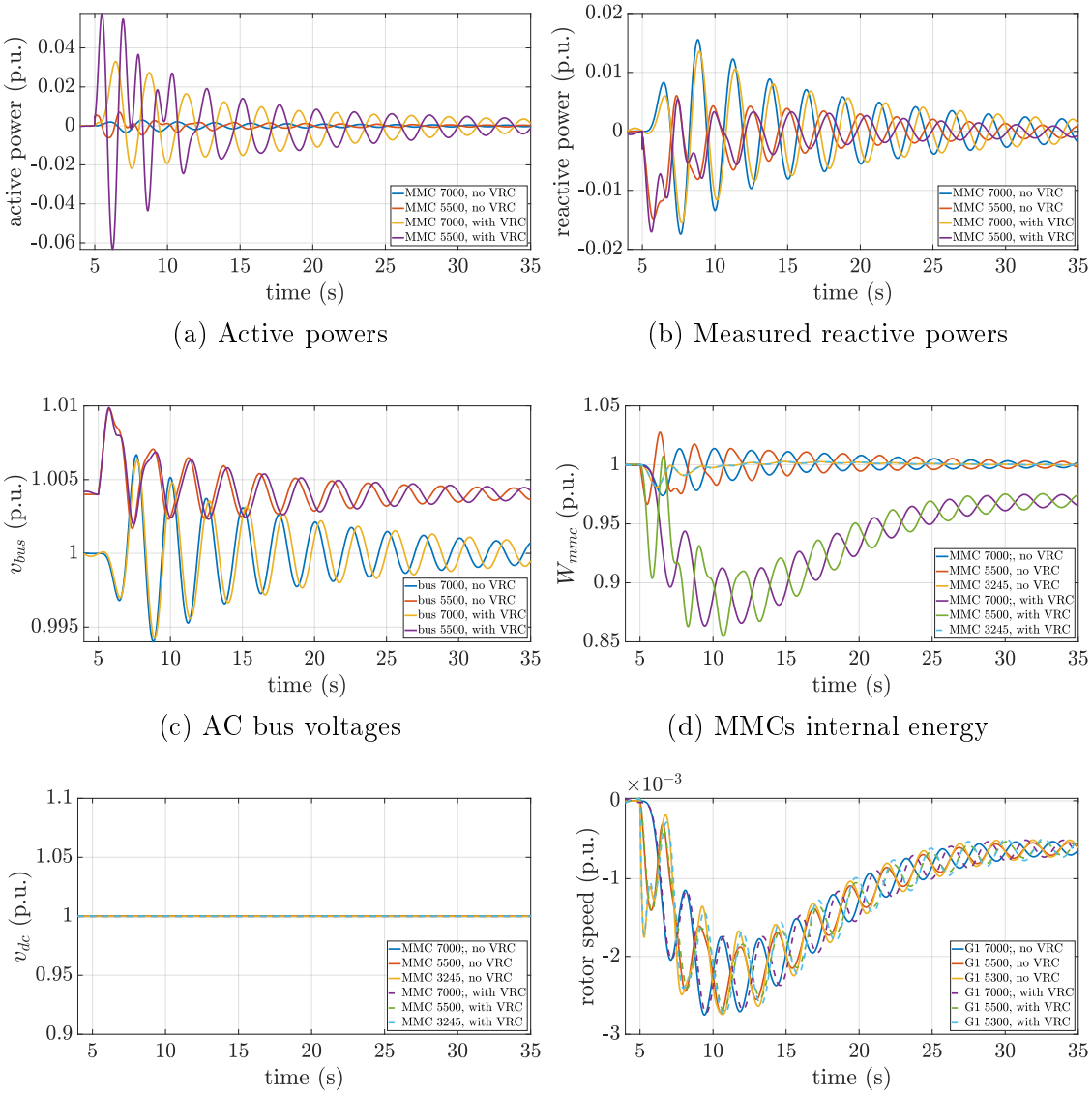

(a) Active powers

(b) Measured reactive powers

(c) AC bus voltages

(d) MMCs internal energy

(e) DC grid voltage

(f) Generator rotor speeds

Figure 4.20: Evolution of relevant grid state variables following a -800MW generation loss at bus 3245 when $t = 5$s and comparison between Cases 1 and 2.

4.9. Conclusions

In this chapter, a method is proposed to quantify the energy requirements when increasing the size of the MMC submodules in order to provide the same AC frequency support as SGs. Then, a control law compatible with the state-of-the-art MMC grid-forming control is proposed to emulate the inertial response of SGs by using the MMC internal energy. Simulations were performed and show a better response of the new controller in terms of the AC frequency response to AC and DC power disturbances.

In the simulation section, we observed that the energy reference limits were not always respected when $k_{vr} > 5$, which can be attributed to the relatively poor tracking capability of the grid-forming control compared to the grid-following control. In Section 4.8, the results obtained with an aggregated grid were extended to the case of the Nordic power system. This analysis showed the compatibility of the proposed control with more complex grids where PE-based sources and SGs coexist. In the future, the novel grid-forming controls with enhanced tracking performances [107, 115] could be combined with the new control proposed in this chapter. In addition, it would be worthwhile investigating the possibility of using the MMC energy in order to provide complementary AC or DC grid services, such as the regulation of the DC voltage, which suffered from a severe dip in the simulations shown in Section 4.7.2.

In future work, the following items should be investigated in order to consolidate the results obtained in this chapter:

- First, the novel grid-forming controls with enhanced tracking performances [107, 115] could be combined with the new control proposed in this chapter;
- The dynamics of the power source, here the offshore wind farm, should be taken into account in order to assess the AC/DC stability of this more detailed system;
- In addition, the low-frequency oscillations observed in Fig. 4.20 for the Nordic 44 grid were not solved with the VRC. It could be worth investigating the use of complementary controllers, such as POD controllers [125, 129], to damp these oscillations;
- Finally, the use of Multi-Input Multi-Output (MIMO-)oriented control represents an interesting opportunity to stabilize the system while taking into account the AC/DC constraints. In particular, this item will be developed in Chapter 5.

Chapter 5

Application of Model Predictive Control to Operate an MMC in Grid-Forming Mode

This chapter is based on the peer-reviewed publication ***Conference II****.*

5.1. Introduction

5.1.1. Context

In Chapter 4, we presented the MMC system, which is more complex than the classical two-level VSC and is dedicated to high-voltage systems. The MMC control is complex and requires the coordination of the *low-level* control, which makes sure that all the submodules are equally sollicitated in the generation of the desired waveform, and the *high-level* control, which focuses on the energy flows between the AC and DC grids. This chapter deals with the high-level control.

The impact of the MMC internal energy dynamics and its control on the grid-level behavior is the topic of some recent studies in the power system community

[29, 77]. Indeed, contrary to the classical 2-level Voltage Source Converters (VSCs), this internal energy acts as a *buffer* between the AC and DC grids and can be seen as a supplementary degree of freedom which can be used to provide additional services such as DC-grid voltage support [163] or AC-grid inter-area oscillations damping [176, 177]. In addition, the MMC submodules can also be designed to store even more energy for potential AC grid frequency support [178]. But these considerations focus on the submodule-level design and control and do not take into account the progress in high-level control such as grid-forming control, where the converter acts as a self-synchronized voltage source with respect to the AC grid. This new paradigm changes the way MMCs are currently operated [166] compared to the classical grid-following control where the converter behaves as a current source, as presented in Chapter 2.

In this chapter, we propose a novel way of designing the upper layer of the high-level MMCs control structure which is compatible with the concept of grid-forming control and ensures the proper operation of the DC grid, the AC grid and the converter submodules at the same time, based on Model Predictive Control (MPC) approach. Contrary to the control law presented in Chapter 4, this MPC relies on a semi-centralized approach to coordinate the AC and DC grids at the same time.

5.1.2. Literature review

Since its early development, MPC has been dedicated to slow dynamic systems such as chemical processes [179] or entire hydro power valleys [180], mainly due to the required computation costs. However, with the constant improvement of the computational systems, it is now possible to apply MPC algorithms to the fields of power electronics and power systems.

Regarding HVDC applications, MPC has been used to enhance the operation of MTDC grids [181] or applied to HVDC links to support the neighbouring AC grids [182]. However, these works are more about the system-level operation of AC/DC grids, meaning the MPC is a centralized solution that coordinates the behavior of several stations. In this chapter, even if we also deal with grid-level support, we focus here on converter-level operation, and especially its compatibility with grid-forming control. This last item was the topic of a recent study which focused on developping a centralized optimal controller which uses Linear Quadratic Regulator (LQR) method to update the grid-forming control gains of distributed VSCs [87]. However, this method is at the grid-level and does not consider any constraints. On the other hand, at the converter-level, while the use of MPC for

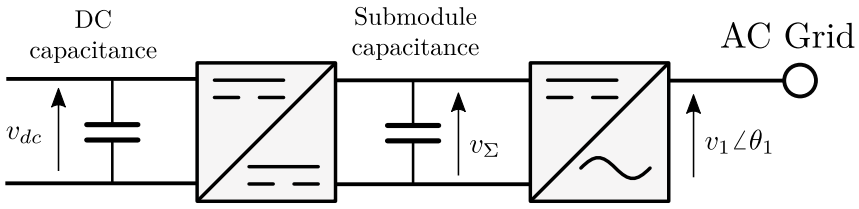

Figure 5.1: Energy exchange between the AC and DC grids via the MMC submodules, from [159].

two-level VSCs controlled in grid-forming was the topic of a recent paper [183], there is no paper, to the best of our knowledge, which focuses on the role that can be played by the MMC in supporting the AC/DC grids under constraints using MPC. The application of the MPC in this case is the main contribution of this work.

5.1.3. Chapter summary and contents

In this chapter, an optimization problem is formulated and a complete control solution is proposed that uses the Model Predictive Control (MPC) for AC/DC energy management of a Modular Multilevel Converter (MMC) controlled in grid-forming mode. First, for the implementation of the MPC, a relevant model of the grid is found by system identification. The identified model is then validated before its usage in the MPC. The simulation results show a better response to disturbances from AC grid and DC grid, as well as a better coordination in the management of the MMC internal energy and DC grid voltage compared to the commonly used dual PI structure.

The structure of this chapter is as follows: In Section 5.2, the problem of controlling the outer loops of the MMC is stated and the need to have a MIMO-oriented control is explained. In Section 5.3, an identification method, namely the prediction error method, is described to obtain an equivalent linear model of the AC grid. In Section 5.4, the MPC algorithm is detailed, and the cost function and constraints are specified. In Section 5.5, the control solution is tested on a simplified system to show its effectiveness compared to the classical PI structure. Section 5.6 concludes.

5.2. Problem formulation

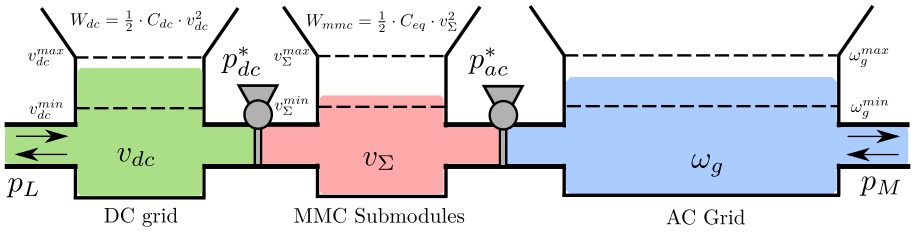

Figure 5.2: Three interconnected reservoirs showing the energy exchange between MMC, AC and DC grids.

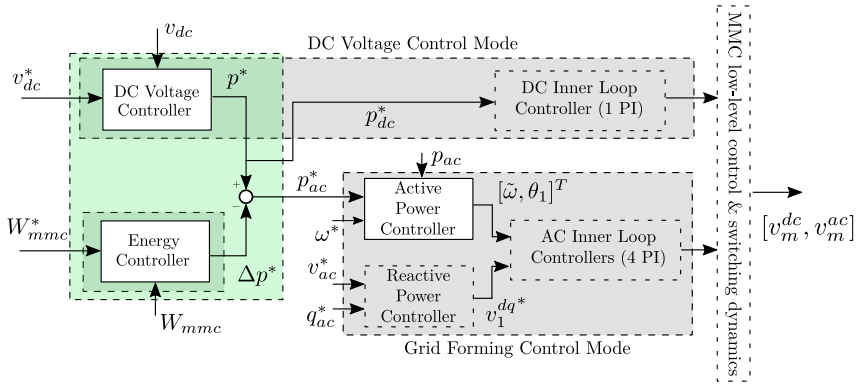

(a) Classical double PI controller using p_{ac}^* to regulate the MMC energy. Adapted from [164].

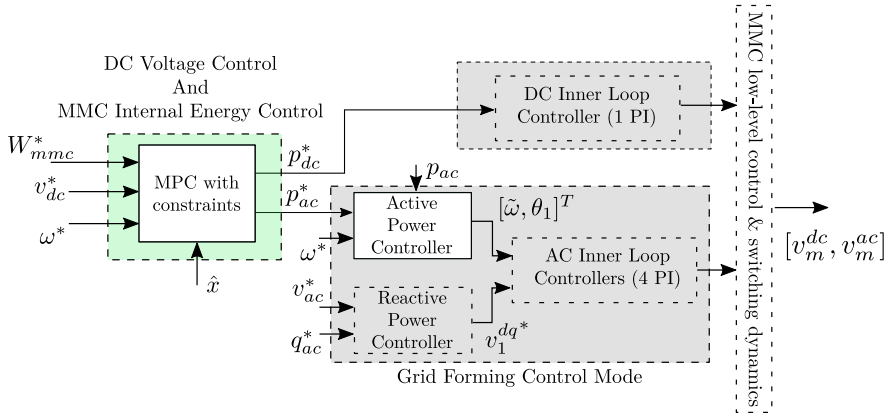

(b) New MMC control with the MPC layer as an external control loop.

Figure 5.3: General MMC high-level control structure.

5.2.1. MMC interfacing AC and DC grids

The energy exchange between AC and DC grids realized by the MMC can be illustrated by Fig. 5.1, where the MMC is modeled by an AC/DC converter, a DC/DC converter and a single capacitance representing all the submodules. $v_1 \angle \theta_1$, v_{dc} and v_{Σ} are respectively the AC voltage, the DC voltage, and the MMC submodule equivalent capacitance voltage.

The control of the internal energy of the MMC interfacing between the AC and DC grids can be seen a problem of 3 connected reservoirs, as shown in Fig. 5.2, where p^*_{dc} and p^*_{ac} are the energy exchanged with the DC and AC grids, respectively, p_L the power injection/withdrawal imposed by the DC grid, and p_M the power injection/withdrawal imposed by the AC grid. Naturally, the controller in charge of regulating the MMC internal energy can use either p^*_{dc} or p^*_{ac} or both of them as the control variables. For example, in [29], p^*_{ac} is used to regulate the MMC inernal energy, by means of a classical double PI structure shown in Fig. 5.3 (a). However, this offline choice of the control variables and the tuning of the PI controllers may turn out to be inadequate when the AC and DC grids experience drastic changes of operation conditions, such as the loss of part of the DC grid and the reduction of the inertia and frequency reserves due to high renewable energy shares.

Therefore, in this chapter, an online approach to MMC internal energy control is proposed where the AC and DC powers are optimally coordinated to enhance the system disturbance mitigation. Since the energy constraints of the system have to be taken into account, especially for the DC voltage and MMC internal energy, MPC is used. As shown in Fig. 5.3 (b), this MPC layer generates the DC and AC power references, p^*_{dc} and p^*_{ac}, to manage the DC voltage and MMC internal energy level and maintain them within acceptable limits while contributing to AC grid support. To be optimal, this implementation could require a regular update of the grid model to take into account operational changes such as power flow updates. In Continental Europe for instance, these changes occur every hour [184]. The update of the model is however not considered in this work.

5.2.2. State-space representation

Based on simplified power exchanges of an MMC which are detailed in Chapter 4, the plant in Fig. 5.2 can be modeled in per-unit system as:

$$\Sigma = \begin{cases} \dot{x}_{dc} &= \frac{2}{C_{dc}} \cdot (p_L - p_{dc}) \\ \dot{x}_{mmc} &= \frac{2}{C_{eq}} \cdot (p_{dc} - p_{ac}) \\ \dot{x}_{ac} &= f(x_{ac}, p_{ac}, p_M) \end{cases} \tag{5.1}$$

where $x_{dc} = v^2_{dc}$, $x_{mmc} = v^2_{\Sigma}$, x_{ac} is the state variable vector of the AC system, C_{eq} the equivalent MMC internal capacitance storing the total internal energy, and f describes the AC-grid dynamics. For the DC-side dynamics and the MMC internal dynamics, the simplified first-order linear models in (5.1) are considered to be known

for the MPC implementation. On the contrary , the AC model is assumed to be unknown and will be identified in Section 5.3.

5.2.3. Control structure

The general structure of the MPC with state estimation is shown in Fig. 5.4. The aim of the MPC block is to come as a hierarchical control that sends power references, p^*_{ac} and p^*_{dc} to the lower control loops. In this case, p^*_{ac} is sent to the grid-forming control whose outer loop is considered in this paper since its dynamics are slow when compared to the inner loops and the DC current controller that receives the DC power reference p^*_{dc}.

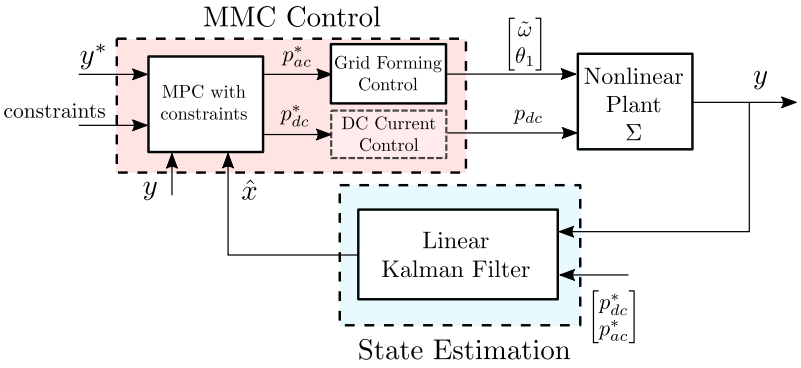

Figure 5.4: Control and state estimation general structure

For the MPC implementation, a good estimation of the nonlinear system Σ is needed in order to predict its future behavior. This estimated model, denoted by Σ_c, is obtained via a system identification method, which is detailed in Section 5.3. This model is also useful to estimate the current states of the AC/DC system that are observable but not directly measurable. Indeed, this model Σ_c is also used in the Kalman filter described in Fig. 5.4. More information about the Kalman filter is given in Section 5.4.1. In particular, as illustrated in Fig. 5.5 explaining the grid-forming control of the MMC, the block from θ_1 to ω_g and p_{ac} is unknown. As the implementation of MPC in Section 5.4 needs a linear system, we consider the equivalent linear transfer function $G(s)$, which corresponds to the linearized dynamics of the AC grid around an equilibrium state provided by a power flow computation with reference frequency ω^*:

$$\Delta\tilde{\omega}(s) = G(s) \cdot p^*_{ac}(s). \tag{5.2}$$

where we choose to consider the frequency using $\Delta\tilde{\omega} = \tilde{\omega} - \omega^*$ as the output instead of ω_g. Indeed, the former is the local estimation of the frequency deviation

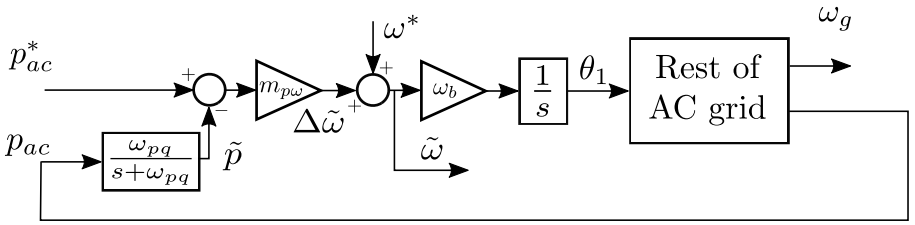

Figure 5.5: Block scheme of the AC system with the MMC in grid-forming control mode.

and is directly available while the latter, the grid frequency, is a "global" variable corresponding to the weighted sum of the frequencies measured at several distant buses of the entire system.

5.3. System identification

In this section, a method to estimate the linearized dynamics of the AC grid is proposed. To estimate $G(s)$ defined in (5.2), we choose to first estimate its discrete version, $G(z)$, which will be later converted to a continuous-time model, using a probing signal. This choice is made because the prediction error method used for identification in this chapter is said to give a more relevant identified model than the classical subspace identification for linear MPC applications [185].

Other identification techniques, such as ambient identification can be applied to AC grid parameter identification [186]. However, they are out of the scope of this chapter.

5.3.1. Identification method

The general structure of the model estimation is shown in Fig. 5.6, where $u_{id} = p^*_{ac}$ is the model input, $\hat{y}_{id} = \Delta\tilde{\omega}$ is the estimated model output, and d is the disturbance of the system, not identified here, which models the power disturbances such as p_M from (5.1). The AC grid model in Fig. 5.6 used to generate y_{id} under the excitation u_{id} is described in Section 5.5.1. $\hat{G}(z)$ is related to these variables as:

$$\hat{y}_{ac}(z) = \hat{G}(z) \cdot u_{ac}(z) + d(z) \tag{5.3}$$

To identify $\hat{G}(z)$, the nonlinear system is excited with the following multisine probing signal u_{id} and the output y_{id} is obtained:

$$u_{ac} = u_{id} = \sum_{i=0}^{N_\omega - 1} A_i \sin(\omega_i t + \phi_i) \tag{5.4}$$

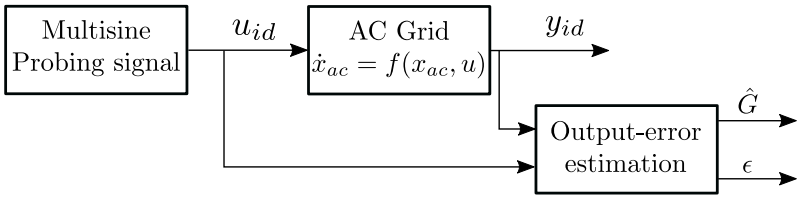

Figure 5.6: Detailed method for estimating the transfer function $\hat{G}$ with a multisine probing signal using prediction error method [187].

where $N_\omega = 1000$, $\omega_i = 0.001 \cdot (i+1)$ Hz, $A_i = 2 \times 10^{-4}$ p.u. $\forall i$, and ϕ_i is a phase shift randomly chosen. A frequency grid from 0.001 to 1 Hz is chosen to scan the AC grid, because the time constants of the frequency-related dynamics of the latter typically lie between 1s and 10s [59]. An optimization of the probing signal could be performed to minimize the energy of the whole excitation [188], but this is not the focus of the chapter. $\hat{G}(z)$ is obtained using the prediction error method [187] and assuming the output error model structure in the *System Identification toolbox* in Matlab [189]. More information about this method can be found in Appendix E.

A 4th-order model is found to match the nonlinear model dynamics with a certain accuracy, which is defined in Section 5.3.3. The parameters used for the output error function are given in Table 5.1.

Table 5.1: Parameters used in the prediction error algorithm.

Quantity	**Notation**	**Value**
Sampling time	h	0.05 s
Number of poles	n_f	4
Number of zeros	n_b	4
Experiment duration	t_{id}	50 s

5.3.2. Choice of the system order

For most of the MPC applications, the size of the computed model is a key figure since it is directly related to the computation costs of the online optimization. In this case, we try to have a proper AC grid model which captures the behavior of the real nonlinear system in the frequency range described in the previous section. In particular, the order of the identified system, characterized by the couple $\{n_f, n_b\}$ is a tunable parameter from the point of view of control. Indeed, we want to obtain a model that is small enough to lower the computation costs while accurate enough to capture the grid relevant dynamics.

With this in mind, we perform a system identification analysis based on different values of $n_t = n_f = n_b$. As a reminder, the discrete-time transfer function $\hat{G}(z)$ is defined as:

$$\hat{G}(z) = \frac{b_{n_b} z^{n_b} + b_{n_b-1} z^{n_b-1} + \ldots + b_1 z + 1}{a_{n_f} z^{n_f} + a_{n_f-1} z^{n_f-1} + \ldots + a_1 z + 1} \tag{5.5}$$

The aim of this analysis is to compare the different identified models $\hat{G}(z)$ with the exact linear transfer function G. Denote by $G_{lin}(z)$ the model obtained by exciting, with the same excitation signal, the linearized AC grid model G. This entire procedure is described in Fig. 5.7.

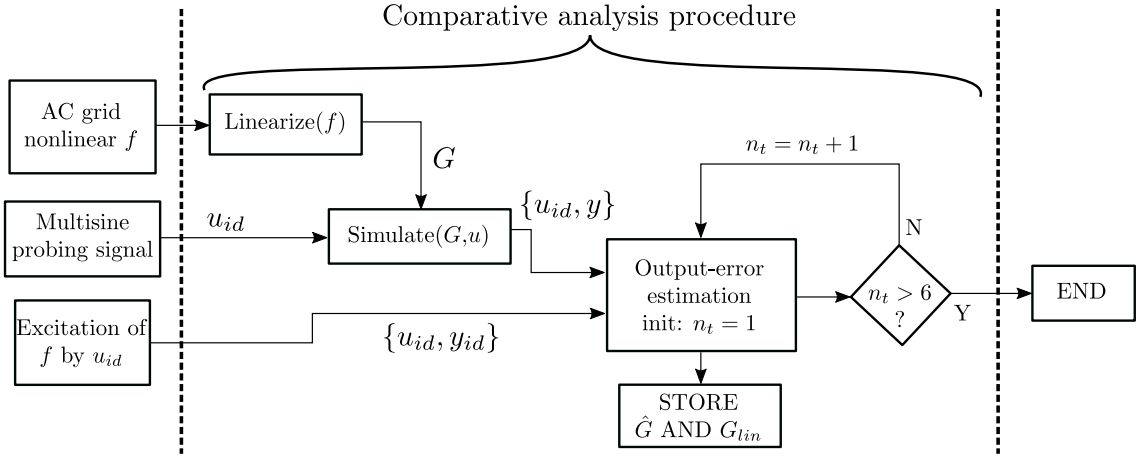

Figure 5.7: Flowchart to calculate the identified transfer functions $\hat{G}$ and G_{lin} for different model orders.

The comparison of the Bode plots of the different transfer functions is given in Fig. 5.8 for $n_t = \{1, 2, \ldots, 6\}$. In this figure, it is clear that the identified system is brought closer to the linearized model when n_t increases. However, when $n_t \geq 4$, we observe no real improvement between the identified model and the linearized one. In addition, since $\hat{G}(z)$ and $G_{lin}(z)$ have the same frequency-domain responses, it is confirmed that the output error algorithm works well when the output information is obtained using the nonlinear system. However, those results are based on noiseless measurements. In future work, it would be desired to take into account the noise of the sensor units to extend these results.

However, this procedure requires to know the linearized function $G(s)$, which can only be calculated in simulation conditions when the model is available for linearization. In real-life conditions, the AC grid is unknown, as described in Section 5.2.3. As a consequence, another method, applicable to real-life conditions, is described in the next section to validate the identified model.

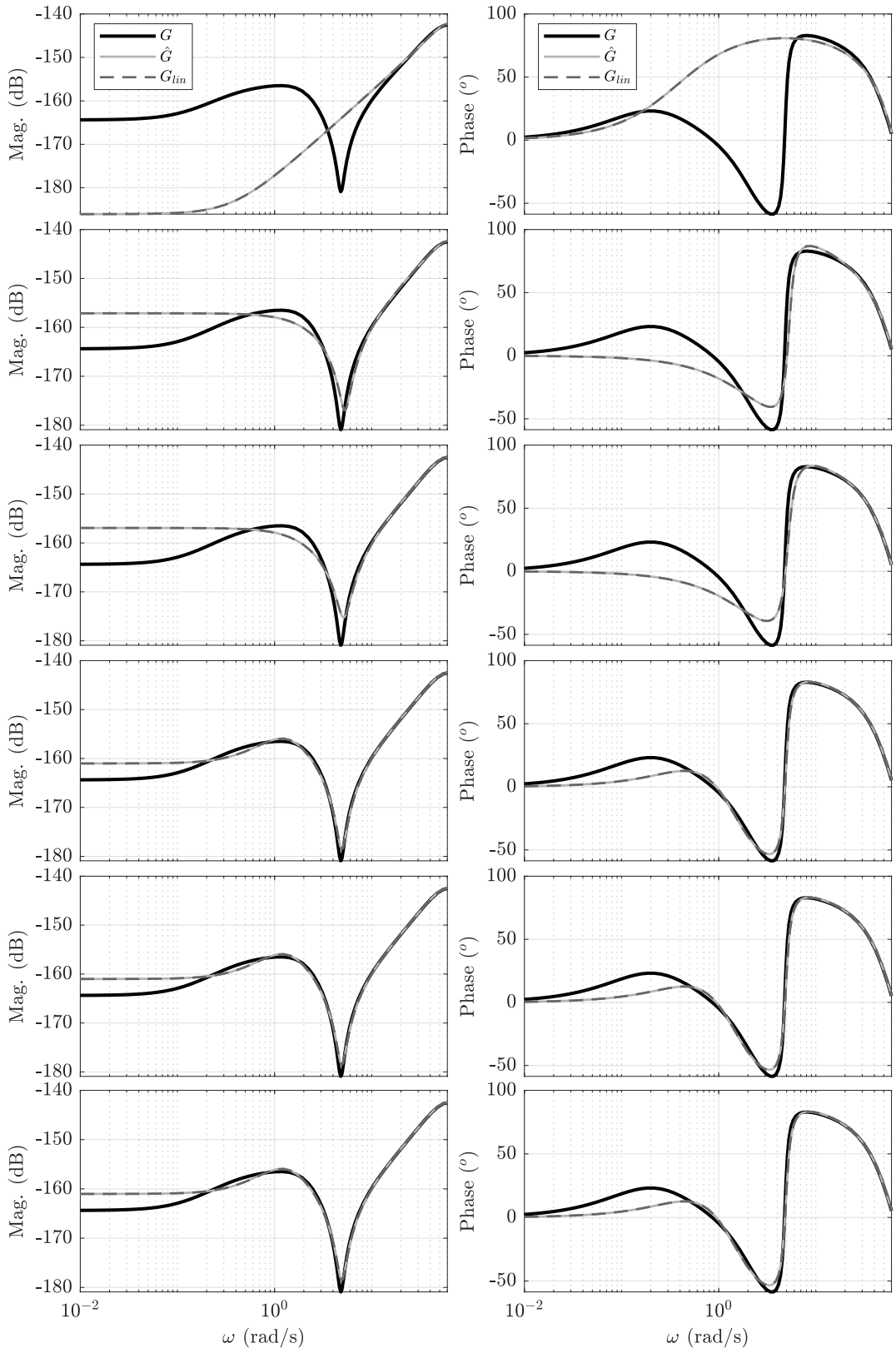

Figure 5.8: Bode plots of the linear transfer function G with respect to the identified models $\hat{G}$ and G_{lin}. The i^{th}-line gives the Bode plot (magnitude and phase) of G and the i^{th}-order identified models $\hat{G}$ and G_{lin} defined by n_t.

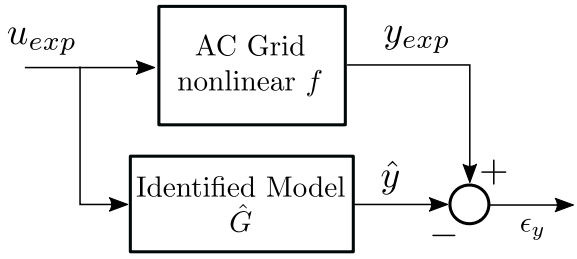

Figure 5.9: Scheme of the validation experiment to check the reliability of the identified model $\hat{G}$.

5.3.3. Validation of the identified model

In order to check the validity of our identified model $\hat{G}(z)$, we test it, as shown in Fig. 5.9, with another excitation signal u_{exp} defined as:

$$u_{ac} = u_{exp} = \sum_{i=0}^{N_\omega - 1} A_i \sin(\omega_i t + \phi_i) \neq u_{id} \tag{5.6}$$

whose only difference from u_{id} is the values of A_i, which is equal to 0 if $i/10$ is an integer and 1 otherwise. The aim of this different choice of u_{id} is to check the accuracy of $\hat{G}(z)$ in the low-frequency zone corresponding to AC frequency dynamics. The results in Fig. 5.10 give a Normalized Root Mean Square Error (NRMSE) fit $\Phi_{NRMSE} = 1 - \frac{|y-\hat{y}|}{|y-\bar{y}|} > 99.3\%$. It is also important to note that this signal is designed to have a low impact in terms of disturbances from the AC grid point of view, here with $u_{exp} < 0.005$ p.u. The identified model appears to be accurate enough for the MPC implementation.

5.3.4. Conversion of $\hat{G}(z)$ into a state-space model

Once the transfer function $\hat{G}(z)$ is obtained, we construct the continuous-time state-space model of its minimum realization, denoted by Σ_{AC}, such that:

$$\Sigma_{AC} = \begin{cases} \dot{x}_{ac} &= \hat{A} \cdot x_{ac} + \hat{B} \cdot u_{ac} \\ y_{ac} &= \hat{C} \cdot x_{ac} + \hat{D} \cdot u_{ac} \end{cases} \tag{5.7}$$

where $x_{ac} \in \mathbb{R}^4$ is the state variable vector of the AC grid, $u_{ac} = p^*_{ac}$, $y_{ac} = \Delta\tilde{\omega}$, and $(\hat{A}, \hat{B}, \hat{C}, \hat{D})$ the state-space matrices.

Based on Σ_{AC}, a 6th-order model for the whole system, denoted by Σ_c, is obtained as:

$$\Sigma_c = \begin{cases} \dot{x}_c &= A \cdot x_c + B \cdot u_c \\ y_c &= C \cdot x_c + D \cdot u_c \end{cases} \tag{5.8}$$

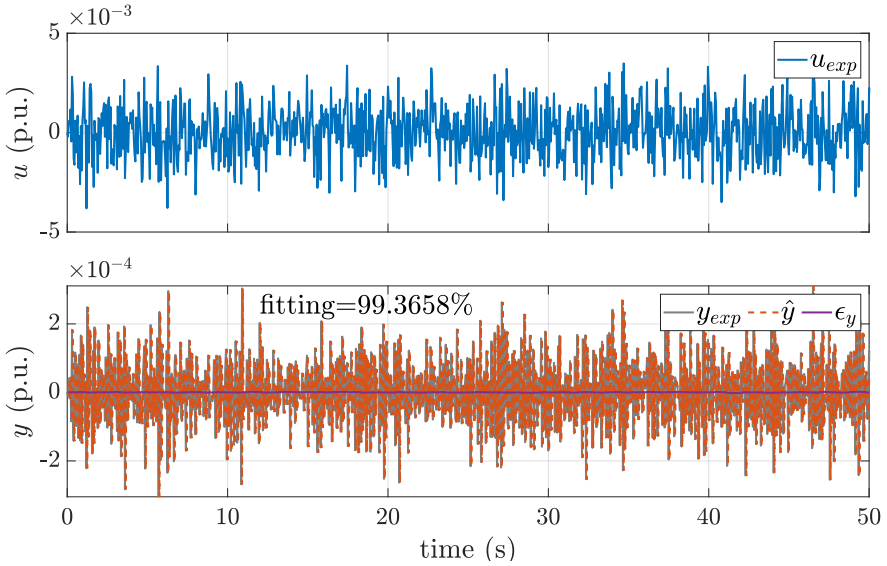

Figure 5.10: Excitation signal and output signal from the identified model and measurement collected during the validation experiment, in per unit.

where $x_c = \begin{bmatrix} \hat{x}_{dc} & \hat{x}_{mmc} & \hat{x}_{ac} \end{bmatrix}^T \in \mathbb{R}^6$, $u_c = \begin{bmatrix} p^*_{dc} & p^*_{ac} \end{bmatrix}^T \in \mathbb{R}^2$, $y_c = \begin{bmatrix} x_{dc} & x_{mmc} & \Delta\tilde{\omega} \end{bmatrix}^T \in \mathbb{R}^3$,

$$A = \begin{bmatrix} 0 & 0 \\ 0 & \hat{A} \end{bmatrix}, B = \begin{bmatrix} -\frac{2}{C_{dc}} & \frac{2}{C_{eq}} & 0 \\ 0 & -\frac{2}{C_{eq}} & \hat{B}^T \end{bmatrix}^T, C = \begin{bmatrix} I_2 & 0 \\ 0 & \hat{C} \end{bmatrix}, D = \begin{bmatrix} 0 & 0 \\ 0 & \hat{D} \end{bmatrix}. \quad (5.9)$$

5.4. MPC implementation

5.4.1. Plant model and Kalman filter tuning

To implement the MPC as given in Fig. 5.4, knowledge of all the states at each time step is also necessary, which requires the use of sensors or state observers if the variables are not measurable. For the state observation, $\hat{x}_{dc} = x_{dc}$ and $\hat{x}_{mmc} = x_{mmc}$ are considered measurable, as described in Section 5.2.2, but the AC grid states x_{ac} are not measurable, for which we use a state observer, the Kalman filter in Fig. 5.4, to obtained its estimation $\hat{x}_{ac}$. Since we obtained an identified linear state-space model for the AC grid, as described in (5.7), we can use linear state observers. However, it would be possible to extend this work to nonlinear state observers [190] but this remains out of the scope of this chapter. This Kalman filter is a continuous-time observer which uses the model Σ_{AC} that is observable. We define the process noise covariance $Q = 1$ and the sensor noise covariance $R = 0.1$ in order to correct the differences between the linear model Σ_{AC} and the nonlinear function f using the

measurements of $\Delta\tilde{\omega}$. The continuous-time Kalman filter was implemented using the function in Matlab [191].

5.4.2. Controller formulation

The system to be controlled with the MPC, Σ, is a nonlinear continuous-time 2-input/3-output MIMO system, where it is impossible to control each output *independently* with zero steady-state error [192]. To apply MPC, a discrete-time system is built using a zero-order hold with a sampling time T_s and the continuous-time linear model Σ_c. In the following, we denote by x_d the discrete state variable vector and by y the discrete output vector. The discrete-time system $\Sigma_d = \{A_d, B_d, C_d, D_d\}$ is defined such that:

$$A_d = e^{AT_s} \tag{5.10}$$

$$B_d = \left(\int_{t=0}^{T_s} e^{At} dt \right) \cdot B \tag{5.11}$$

Knowing that $C_d = C$ and assuming $D_d = 0$, the discrete-time system Σ_d can be written as:

$$x_d(k+1) = A_d \cdot x_d(k) + B_d \cdot u(k) \tag{5.12}$$

$$y(k) = C_d \cdot x_d(k) \tag{5.13}$$

To ensure zero steady-state error, the technique of constructing a state-space model with an embedded integrator. One of the advantages of this technique is that we work on the control input variation sequence $\Delta u(k) = u(k) - u(k-1)$ instead of the control signal sequence $u(k)$ itself. This makes the control design more general since it does not require any steady-state information [192]. The embedded integrator is used to find an augmented model of the system as:

$$x(k+1) = A_e \cdot x(k) + B_e \cdot \Delta u(k) \tag{5.14}$$

$$y(k) = C_e \cdot x(k) \tag{5.15}$$

with $\Delta x_d(k) = x_d(k) - x_d(k-1)$, $x(k) = \begin{bmatrix} \Delta x_d(k)^T & y(k)^T \end{bmatrix}^T \in \mathbb{R}^9$,

$$A_e = \begin{bmatrix} A_d & 0 \\ C_d A_d & I_3 \cdot \end{bmatrix}, B_e = \begin{bmatrix} B_d \\ C_d B_d \end{bmatrix}, C_e = \begin{bmatrix} 0 & 0 \\ 0 & I_3 \end{bmatrix}. \tag{5.16}$$

The MPC predicts the future states at time horizon $i = 0, 1, \ldots, N_p$:

$$x(k+(i+1)|k) = A_e \cdot x(k+i|k) + B_e \cdot \Delta u(k+i|k) \tag{5.17}$$

where N_p is the prediction horizon and N_c is the control horizon which should be chosen smaller than or equal to N_p.

The problem can be formulated in matrix form:

$$Y(k) = \begin{bmatrix} y(k+1|k) & \dots & y(k+N_p|k) \end{bmatrix}^T \in \mathbb{R}^{3N_p} \tag{5.18}$$

$$\Delta U(k) = \begin{bmatrix} \Delta u(k) & \dots & \Delta u(k+N_c-1) \end{bmatrix}^T \in \mathbb{R}^{2N_c} \tag{5.19}$$

$$\Delta Y(k) = \begin{bmatrix} \Delta y(k) & \dots & \Delta y(k+N_c-1) \end{bmatrix}^T \in \mathbb{R}^{3N_p} \tag{5.20}$$

where $Y(k)$ is the predicted augmented-system output vector at a given time $t = k$, and $\Delta u(k+i) = u(k+i) - u(k+i-1)$ and $\Delta y(k+i) = y(k+i) - y(k+i-1)$ are the difference of the control variables and outputs respectively. $Y(k)$ can be calculated using:

$$Y(k) = F \cdot x(k) + \Phi \cdot \Delta U(k) \tag{5.21}$$

where F and Φ are:

$$F = \begin{bmatrix} C_e A_e & C_e A_e^2 & \dots & C_e A_e^{N_p} \end{bmatrix}^T \tag{5.22}$$

$$\Phi = \begin{bmatrix} C_e B_e & 0 & \dots & 0 \\ C_e A_e B_e & C_e B_e & \dots & 0 \\ \vdots & \vdots & & \vdots \\ C_e A_e^{N_p-1} B_e & C_e A_e^{N_p-2} B_e & \dots & C_e A_e^{N_p-N_c} B_e \end{bmatrix} \tag{5.23}$$

The whole linear MPC function was implemented in a Matlab environment using the YALMIP toolbox [193].

5.4.3. Optimization problem and cost function

To take into account the DC voltage, the MMC internal energy and the AC grid frequency, we choose the following cost function J for the optimization problem:

$$J(k) = (\bar{R}_s - Y(k))^T \cdot \bar{Q} \cdot (\bar{R}_s - Y(k)) + \Delta U(k)^T \cdot \bar{R} \cdot \Delta U(k) + \Delta Y(k)^T \cdot \bar{P} \cdot \Delta Y(k) \tag{5.24}$$

where $\bar{R}_s \in \mathbb{R}^{3N_p}$ is the vector of the desired output setpoint in the prediction horizon N_p, and the weighting coefficients $\bar{Q} \in \mathbb{R}^{3N_p \times 3N_p}$, $\bar{R} \in \mathbb{R}^{2N_c \times 2N_c}$ and $\bar{P} \in \mathbb{R}^{3N_p \times 3N_p}$ are diagonal matrices: $\bar{Q} = \text{diag}\{\bar{q}_1, \dots, \bar{q}_{N_p}\}$, $\bar{R} = \text{diag}\{\bar{r}_1, \dots, \bar{r}_{N_c}\}$, and $\bar{P} = \text{diag}\{\bar{p}_1, \dots, \bar{p}_{N_p}\}$. The elements of $\bar{Q}$, $\bar{R}$ and $\bar{P}$ are themselves matrices

which are defined $\forall i \in [\![0, N_p]\!]$ and $\forall j \in [\![0, N_c]\!]$ as:

$$\bar{q}_i = \begin{bmatrix} q_{3i+1} & 0 & 0 \\ 0 & q_{3i+2} & 0 \\ 0 & 0 & q_{3i+3} \end{bmatrix}; \bar{r}_j = \begin{bmatrix} r_{2j+1} & 0 \\ 0 & r_{2j+2} \end{bmatrix}; \bar{p}_i = \begin{bmatrix} p_{3i+1} & 0 & 0 \\ 0 & p_{3i+2} & 0 \\ 0 & 0 & p_{3i+3} \end{bmatrix} \quad (5.25)$$

For this MPC implementation, there is no discount factor over time between the observed states/control variables and the predicted states/calculated control variables, i.e. $\bar{q}_i = \bar{q}_j, \bar{r}_i = \bar{r}_j, \bar{p}_i = \bar{p}_j, \forall i \neq j$. In addition, the magnitude of the control variable is not considered, i.e. $\bar{r}_i = 0, \forall i$. The weighting matrice $\bar{q}_i$ is defined as $\bar{q}_i = \text{diag}\{\alpha_{dc}, \alpha_{mmc}, \alpha_\omega\}$ where α_{dc}, α_{mmc} and α_ω represent respectively the weighting factors of the tracking of v_{dc}^2, v_Σ^2 and $\Delta\tilde{\omega}$. Although the tracking of the AC grid frequency is not the objective of the MPC, α_ω can be used in order to provide potential frequency support. In fact, regulating the frequency to 50 Hz following an active power disturbance would need an infinite source of energy from the DC grid, which we considered rather finite in this study. The weighting matrice $\bar{p}_i$ is defined as $\bar{p}_i = \text{diag}\{0, 0, \alpha_r\}$ where α_r represents the weighting factor for minimizing the time difference $\Delta\tilde{\omega}(k+1) - \Delta\tilde{\omega}(k)$, hence the RoCoF. The other diagonal terms in $\bar{p}_i$ are equal to 0 because we are not interested in the rate of change of the DC voltage or the internal energy.

All these control parameters will be defined in Section 5.5.1.

5.4.4. Constraints

To ensure that the levels of MMC internal energy and DC grid are kept within acceptable limits, the following constraints are considered:

$$0.8 \text{ p.u.} < y_d(1) < 1.2 \text{ p.u.} \quad (5.26)$$

$$0.8 \text{ p.u.} < y_d(2) < 1.2 \text{ p.u.} \quad (5.27)$$

$$-0.2 \text{ p.u.} < \Delta u(1) < 0.2 \text{ p.u.} \quad (5.28)$$

$$-0.05 \text{ p.u.} < \Delta u(2) < 0.05 \text{ p.u.} \quad (5.29)$$

where $\Delta u = \begin{bmatrix} \Delta p_{d,dc}^* & \Delta p_{d,ac}^* \end{bmatrix}^T$ and $y_d = \begin{bmatrix} v_{d,dc}^2 & v_{d,\Sigma}^2 \end{bmatrix}^T$.

5.5. Case study and simulation results

As presented in Fig. 5.4, the MPC presented is the last section is then tested on the case study which is described in this section.

Simulation results are carried out for different types of contingencies to show the effectiveness of the MPC. The optimization algorithm used is a the quadratic programming algorithm "quadprog" from the *Optimization toolbox* in Matlab [194].

5.5.1. System considered

We consider a two-bus system where an MMC, modeled with its outer loop control, is connected to an aggregated AC grid with the mechanical modes considered, as in [29]. The equivalent scheme of the system is given in Fig. 5.11. More information about the assumptions to build this kind of models can be found in Chapter 4. The physical parameter values are given in Table 5.2.

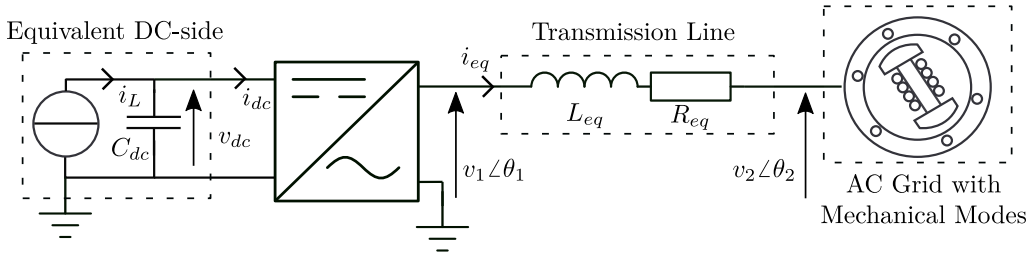

Figure 5.11: Equivalent scheme of the considered system, from [29].

Table 5.2: Parameters of the considered system.

Quantity	**Notation**	**Value**
Base frequency	ω_{base}	50 Hz
Reference frequency	ω^*	1 p.u.
AC line-to-line rated voltage	V_b^{AC}	320 kV
DC grid rated voltage	V_b^{DC}	640 kV
DC-side capacitor	C_{dc}	140 µF
MMC rated power	S_{MMC}	500 MVA
MMC submodule capacitor	C_{sub}	96 mF
# of submodules per arm	N_{arm}	400
MMC initial power reference	p^*, p^*_{dc}, p^*_{ac}	0 p.u.
AC grid rated power	S_{grid}	2000 MVA
AC grid equivalent inertia	H	2.9 s
AC grid frequency droop gain	$\hat{r}$	5 %
Transmission line reactance	x_L	0.3 Ω/km
Transmission line resistance	r_L	0.03 Ω/km
Transmission line length	d_L	100 km

We choose to consider the MMC submodules with an augmented capacity C_{sub} to have a first approximation of the behavior of MMCs with additional storage devices inside their submodules. This extra energy can be realized by oversizing the

submodules capacitors or by adding an additional Energy Storage System (ESS), as in [136, 195]. A method to calculate the needed extra energy to provide inertial support with the MMC submodules is presented in Chapter 4 and is used in this case to test the MPC solution.

The MMC control parameters are given in Table 5.3.

Table 5.3: Control parameters of the system.

Quantity	**Notation**	**Value**
Active power droop gain	$m_{p\omega}$	0.05 p.u.
LPF cutoff frequency	ω_{pq}	15.7 rad/s
Energy controller response time	T_{rwh}	250 ms
Energy reference	W^*_{mmc}	1 p.u.
DC-voltage controller response time	T_{rdc}	191 ms
DC voltage reference	v^*_{dc}	1 p.u.
Damping ratio	ζ	0.707
MPC sampling time	T_s	75 ms
MPC prediction horizon	N_p	10
MPC control horizon	N_c	8
RoCoF weighting factor	α_r	100
DC voltage weighting factor	α_{dc}	10
MMC energy weighting factor	α_{mmc}	1
AC frequency weighting factor	α_ω	0

5.5.2. Test cases

To check the efficiency of the MPC described in Section 5.4.2 in controlling the energy between the DC grid, the MMC submodules and the AC grid, two different disturbances are introduced:

- *Case 1*: a DC-side disturbance in p_L of -150MW, representing e.g. the loss of part of a wind farm.
- *Case 2*: an AC-side disturbance in p_M of -150MW, representing e.g. a load step in the AC grid.

5.5.3. Simulation results

The post-contingencies responses for the two cases are given in Fig. 5.12. They show that following the DC grid disturbance, the MPC is able to control the DC grid voltage v_{dc} as efficiently as the dedicated PI control, with no overshoot, while providing support to the AC grid frequency ω_g using the stored energy from the submodule capacitances. This support smoothens the AC power response p_{ac}.

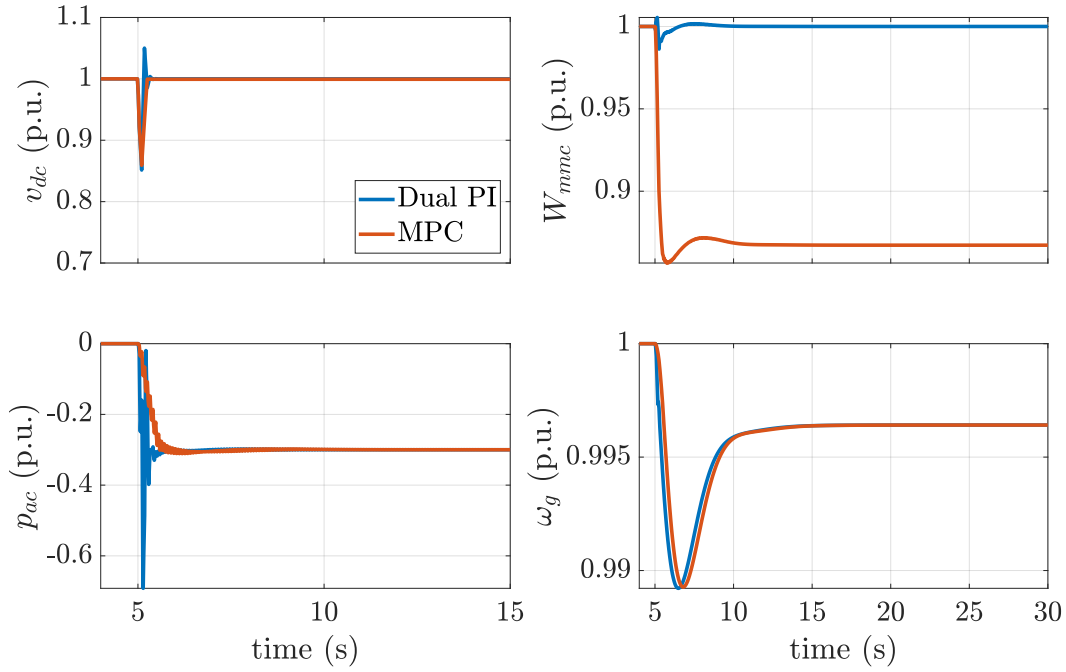

(a) Simulation results following a -0.3 p.u. DC power disturbance.

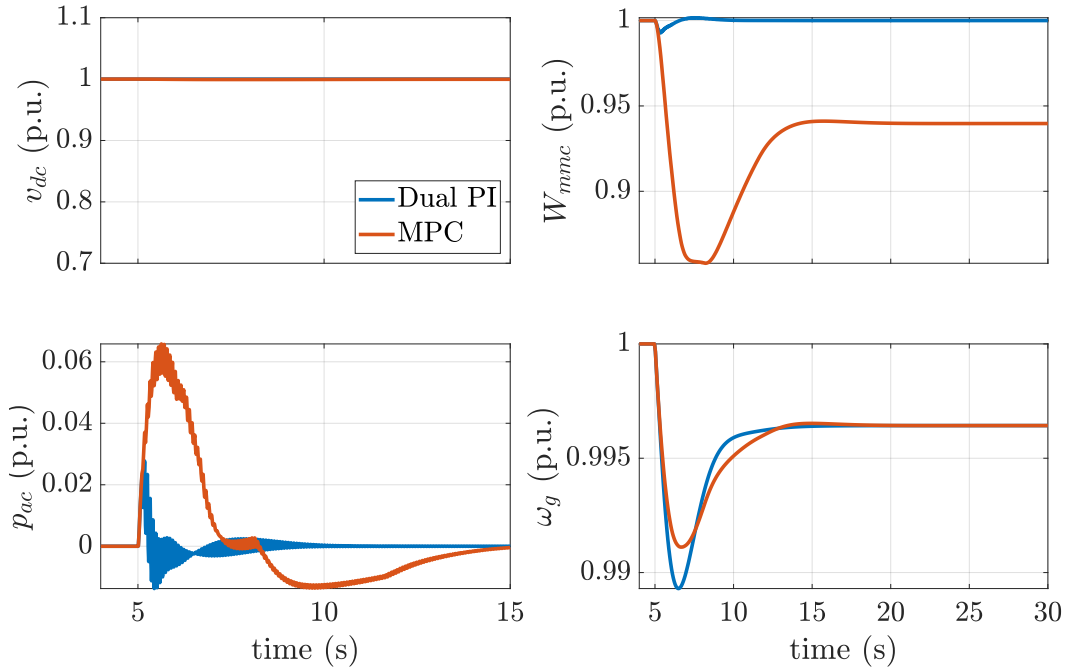

(b) Simulation results following a -0.3 p.u. AC power disturbance.

Figure 5.12: Comparison of the dual PI and MPC structures following two kinds of disturbances.

Indeed, in Fig. 5.12 (a), the AC grid frequency exhibits a better response with a smaller rate of change thanks to the weighting factor α_r. It is also interesting to note that in Fig. 5.12 (b), the MPC deploys part of the MMC internal energy reserves W_{mmc}, described in Section 5.5.1, to support the AC grid frequency ω_g and recharges them thereafter when ω_g is coming back to the steady-state value. However, since the weighting factor α_{mmc} is quite small compared to the other normalized weighting factors, the tracking of the MMC internal energy to its reference becomes less prioritized than the control of the DC voltage and the support of the RoCoF, which is desired here. Therefore, no convergence towards the reference value is observed with the dual PI solution in 5.12.

5.5.4. Influence of controller tuning and varying parameters

In the previous section, the performances of the MPC were demonstrated. However, in that case, the estimated grid model was based on the same system the control solution was tested on. In real-life conditions, the grid changes regularly, due to both planned actions (power reference dispatching, ect.) and unplanned actions (line tripping, generation loss, etc.). In consequence, it is important to check the robustness of this control solution in these conditions. This is the aim of this section. In addition, if not otherwise specified, the values of the rest of the system and control parameters are based on the nominal case whose values are given in Table 5.2 and 5.3 respectively.

5.5.4.1. Influence of MPC tuning

In control theory, the MPC response can be easily tuned by acting on:

- the horizon, defined by the prediction horizon N_p and the control horizon N_c;
- the cost function J;

In this application, the choice of the cost function J has been discussed in Section 5.4.3. We will only look at the prediction horizon in this subsection. As stated in Section 5.3.1, the AC grid frequency dynamics lie between 1-10s. In consequence, since the sampling time of the MPC is $T_s = 75$ms, we can define three different scenarii as follows:

- short-term prediction: $N_c = 4$ and $N_p = 5$;
- middle-term prediction: $N_c = 8$ and $N_p = 10$, nominal case;
- long-term prediction: $N_c = 16$ and $N_p = 20$;

The results of these different test cases are given in Fig. 5.13. These results show that for both AC and DC disturbances, the prediction horizon does have an impact on the response of the controller. In particular, the larger the prediction window is, the smaller the MMC contribution the AC grid is. On the other hand, for the *short-term prediction* case, the response is abrupt which is in accordance with the theory.

In our test cases, the MPC is used to provide support function to the AC grid inertia whose dynamics are in the timescale of 0.1-1s. The *middle-term prediction* which was considered as the nominal case in this study is in consequence the most adequate to provide this kind of support and anticipate the behavior of the grid on a relevant prediction window since $Ts \times N_c = 600$ms and $Ts \times N_p = 750$ms.

5.5.4.2. Influence of the power setpoint

From time to time, the power references sent to the HVDC station can change due to the power dispatch of the TSO, which would change the setpoint of the system [196]. In this case, we want to analyze the impacts when the identified model is not updated and thus does no longer correspond to this new power setpoint. It is then relevant to analyze the influence of this power setpoint on the accuracy and the robustness of the proposed MPC.

Three scenarii are investigated in this section:

- $p^* = 0$p.u., nominal case;
- $p^* = 0.5$p.u.;
- $p^* = 0.8$p.u.;

The simulation results are given in Fig. 5.14 for the same power disturbances that were presented in Section 5.5.2. These results show that the active power setpoint p^* appears to have almost no impact on the MPC results. Indeed, the three simulations yield similar values of the optimized cost function and the same grid responses.

These results are interesting because it confirms that the methodology developed in this chapter can be used to operate an MMC at different power setpoints without having to re-identify the AC system. However, when there is a grid change, the power flow is not the only parameter to vary. Indeed, the frequency reserves as well as the inertia of the grid can encounter massive changes. This impact can be huge, especially if the identified system does not take this into account. This is investigated in the following section.

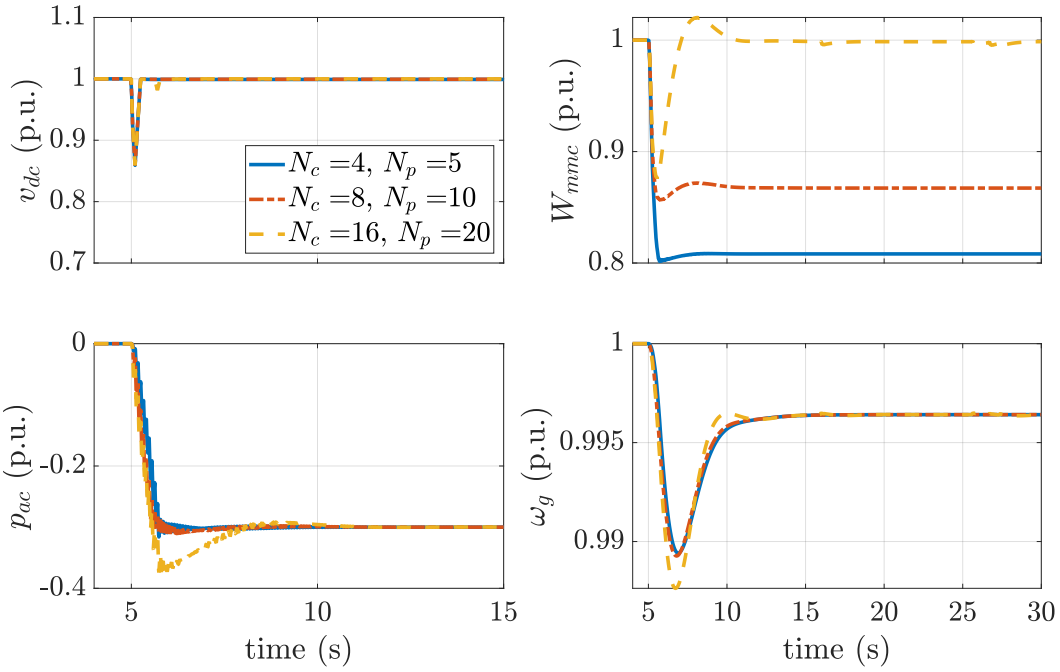

(a) Simulation results following a -0.3 p.u. DC power disturbance.

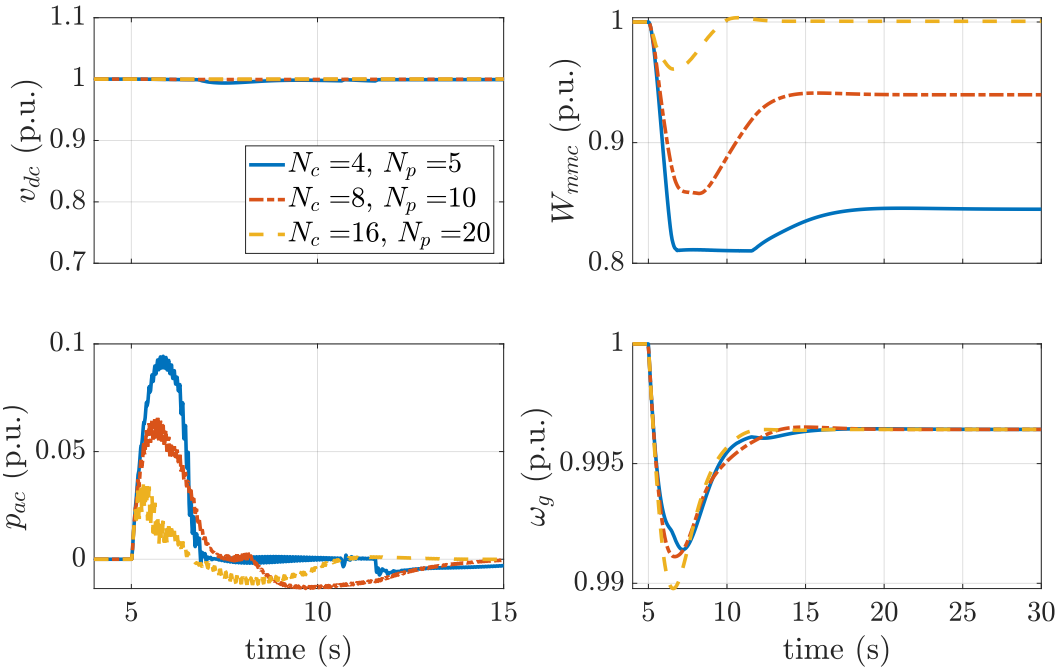

(b) Simulation results following a -0.3 p.u. AC power disturbance.

Figure 5.13: Comparison of the MPC time-domain responses for different values of the prediction horizons.

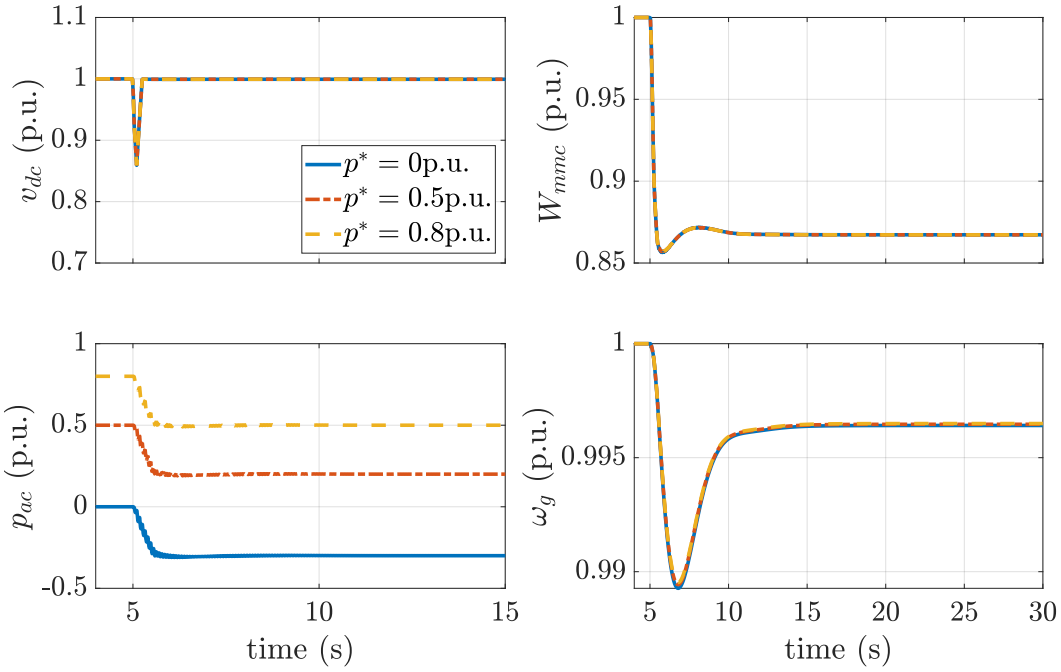

(a) Simulation results following a -0.3 p.u. DC power disturbance.

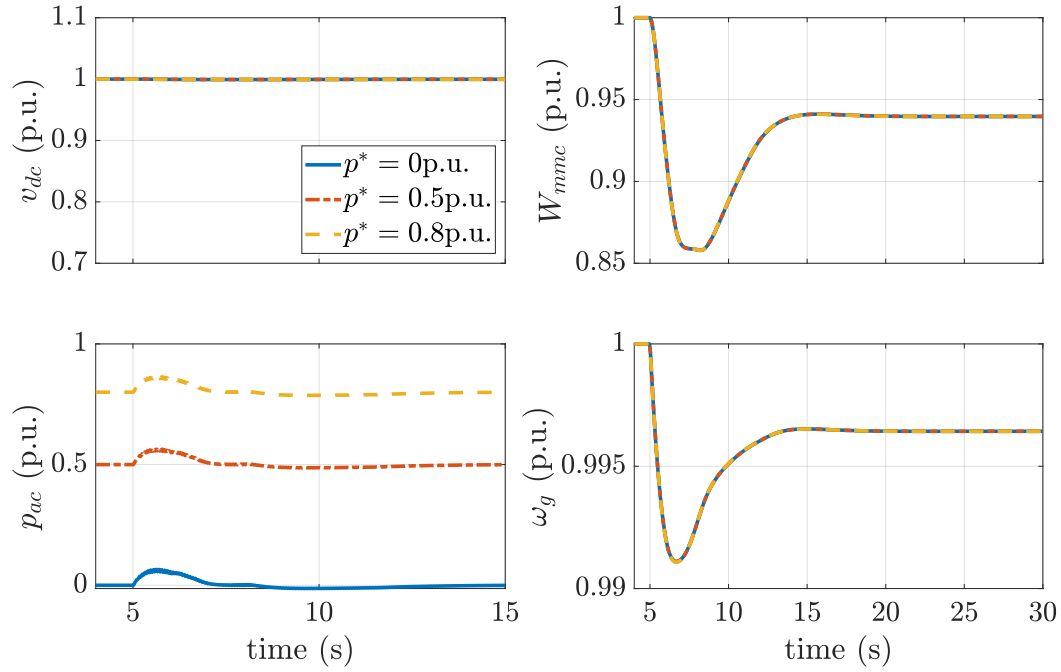

(b) Simulation results following a -0.3 p.u. AC power disturbance.

Figure 5.14: Comparison of the MPC time-domain responses for different active power reference p^* pre-disturbance values.

5.5.4.3. Influence of the model parameter changes

As stated in the previous subsection, the grid can experience drastic changes which can affect the primary frequency control and the inertial response of the grid, determined respectively by the droop $\hat{r}$ and the inertia H of the system. This can be even more problematic when the identified model used in the MPC have not been updated when those changes occured. In consequence, it is important to analyze the impact of the model parameter changes on the robustness of the control solution.

In this part, we will change some parameters of the AC/DC grid such as the inertia constant H and the frequency droop coefficient $\hat{r}$ and study in particular the impacts of decreasing H and $\hat{r}$, which is a tendency that could occur more often in future power grids with less SGs and more renewable energy sources. The results for the variation of the inertia H and frequency droop $\hat{r}$ are respectively given in Fig. 5.15 and Fig. 5.16. It is interesting to note that in the two cases, the contributions of the MMC to the DC grid are similar, meaning the change of the parameters of the AC grid does not affect the DC-grid support, which is desirable. In addition, we observe in Fig. 5.15 that the inertial contribution to the AC grid depends on its existing inertia. In particular, the MMC would provide power faster to support the grid frequency if the grid inertia is lower, which is an useful feature for grid applications. Finally, as shown in Fig. 5.16 (b), the contribution of the MMC also depends on the amount of the deployed primary reserves by the rest of the grid. In the case of $\hat{r} = 10\%$, we see that the MPC does not recharge the MMC submodules following the AC disturbance since the frequency deviation is already significant.

5.6. Conclusions

The main contributions of this chapter can be listed as follows:

- A full control solution including system identification and MPC has been proposed to control an MMC system;
- This control, as an upper layer of the existing structure, is compatible with the state-of-the-art grid-forming control of MMC;
- The use of MPC in the case of MMC with additional internal energy has shown a better response compared to the most commonly-used structure for both AC and DC grid disturbances;
- The robustness of the MPC was assessed regarding variations of the power setpoints and some AC grid parameters.

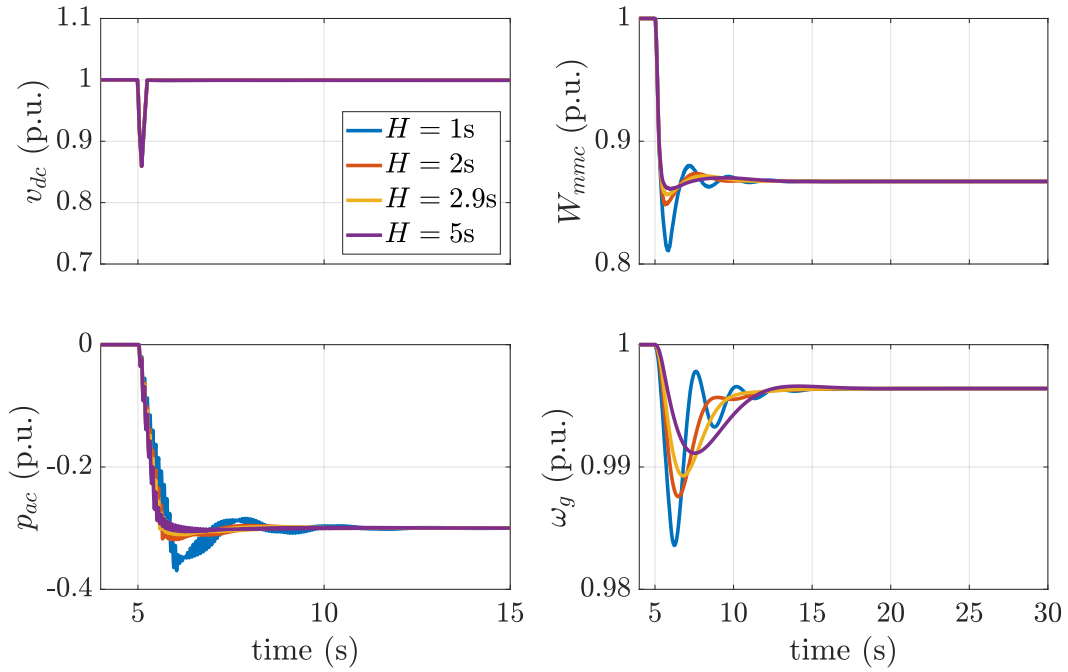

(a) Simulation results following a -0.3 p.u. DC power disturbance.

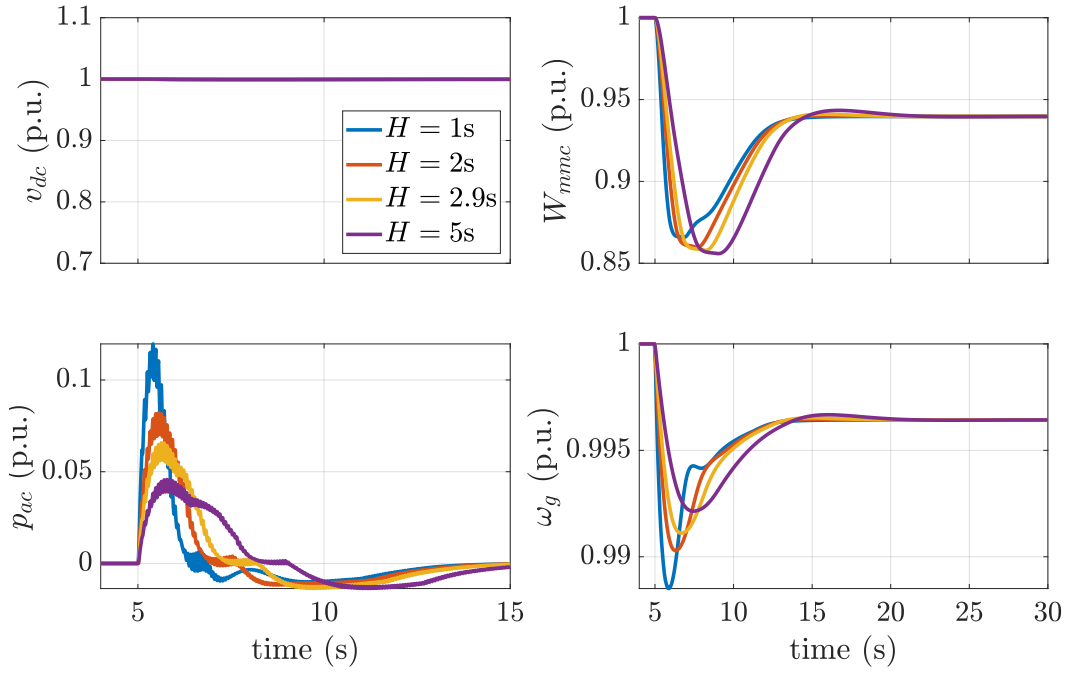

(b) Simulation results following a -0.3 p.u. AC power disturbance.

Figure 5.15: Comparison of the MPC time-domain responses for different values of the AC grid inertia constant H.

The results presented in this work are encouraging as the proposed control solution only relies on local measurements and uses an identified model to capture the

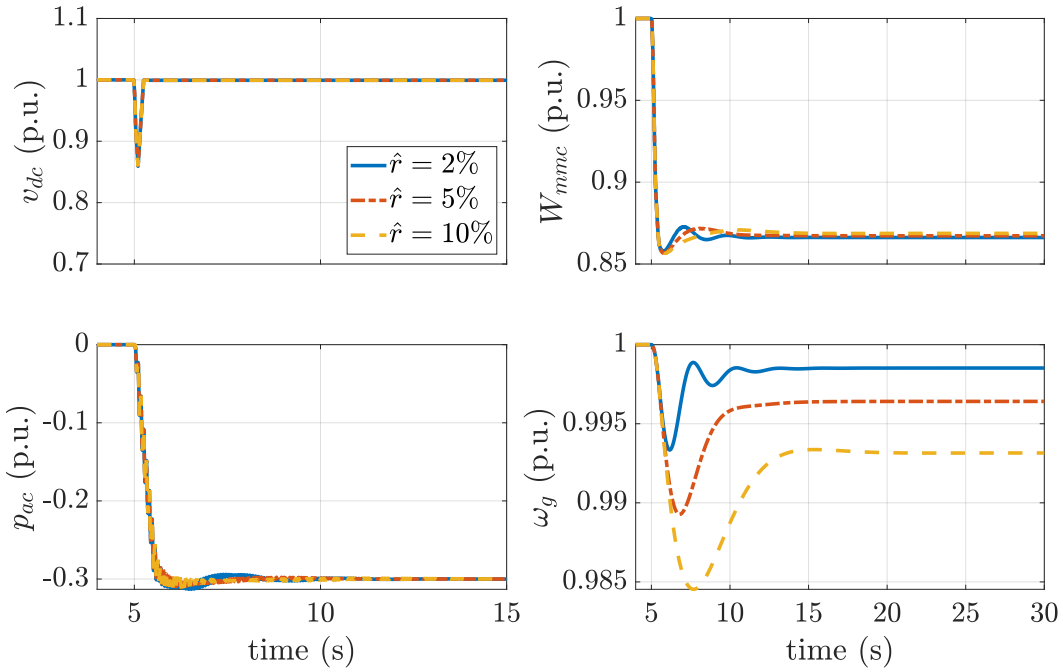

(a) Simulation results following a -0.3 p.u. DC power disturbance.

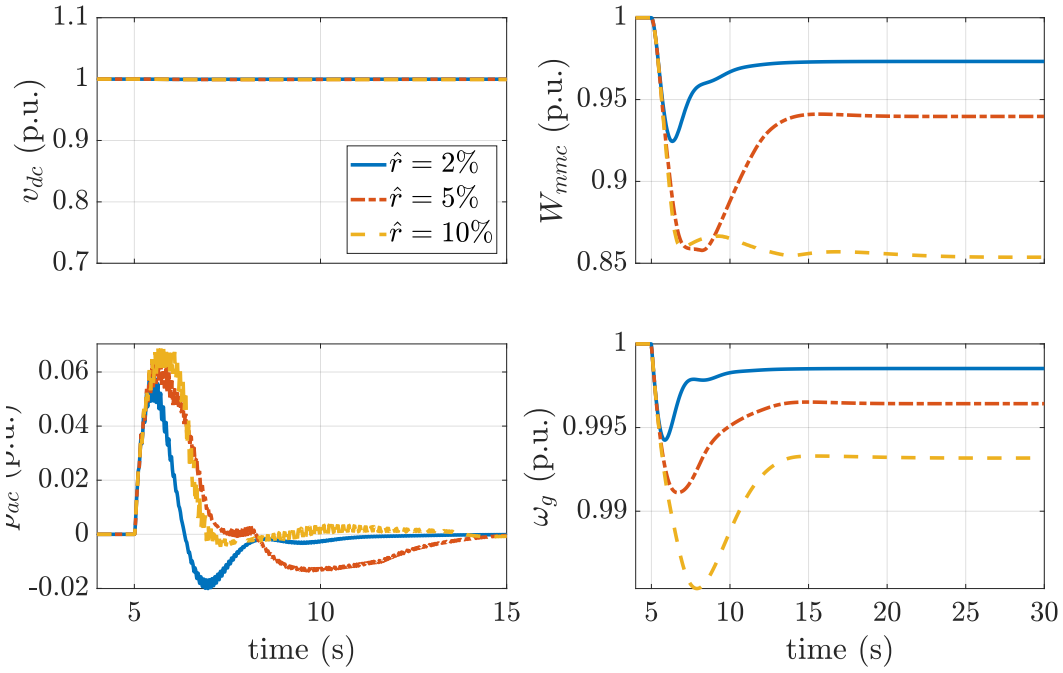

(b) Simulation results following a -0.3 p.u. AC power disturbance.

Figure 5.16: Comparison of the MPC time-domain responses for different values of the AC grid primary frequency reserves droop value $\hat{r}$.

important modes of the AC system. Using this system identification method, an MPC has been implemented to optimally generate the AC and DC power references

used in the MMC control. Indeed, in the future power systems where the traditional synchronous generators coexist with the PE-based power sources, diverse frequency control mechanisms acting jointly may induce additional power oscillations, whose modes are ever-changing with time. To identify such modes, the identification method used in this chapter can be applied, so that the converter can effectively damp power oscillations. In addition, in Section 5.5.4, we investigated the role of the controller tuning and the impacts of parameter changes on the AC grid. This study showed that the MPC tuning is adequate to our application and that it is robust to changes in the AC power setpoint, grid inertia or frequency droop values.

Based on these results, the following points could be investigated to enhance the response of the system and to prove its performance for more realistic power systems:

- A different tuning of the cost function weighting factors could enhance the dynamic response of the system;
- An identification method better adapted to the MPC application could be considered. Indeed, the identified model was found to be optimal for a one-step-ahead prediction. However, the ideal identification method should minimize the error over the prediction horizon used in the MPC in order to give even better results;
- The identification method can be also applied to the DC system and the MMC, if their parameters are not known a priori or if more complicated models are to be used;
- A real-time implementation of the proposed control could confirm the feasibility of MPC in these kinds of applications. In particular, this last item will be the topic of Chapter 6.

Chapter 6

Experimental Validation of The Online Hierarchical MPC applied to a Modular Multilevel Converter in Grid-Forming

The contents of this chapter is based on the publication ***Journal III*** *(in submission process).*

6.1. Introduction

6.1.1. Motivation and context

In Chapter 4, we studied the impacts of the grid-forming control on the MMC dynamics. In Chapter 5, we showed that applying MPC to the outer layer of the MMC control could be a promising solution to manage more efficiently the AC/DC energy exchanges. However, in these two chapters, the new concepts and methods were verified only by simulations. Moreover, the MMC model used to represent the controlled plant in Chapter 5 was an averaged one with perfect inner control and low-level control loops.

The aim of this chapter is to validate the proposed control solution developed in Chapter 5 by implementing it in a Power Hardware in the Loop (PHIL) facility based

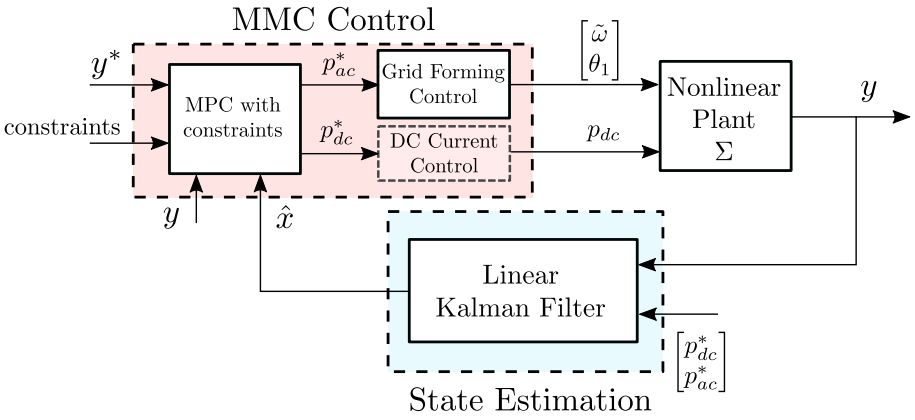

Figure 6.1: Proposed MPC for AC/DC energy management of an MMC. More details are available in Chapter 5.

on Opal-RT software and other physical devices available at SuperGrid Institute where this research work was carried out.

As a reminder, the proposed control scheme developed in Chapter 5, as recalled in Fig. 6.1, represents a MIMO-based optimal approach to control the AC and DC powers flowing through the MMC while taking into account the MMC and DC grid constraints.

6.1.2. Literature review

The main obstacle to applying MPC in power electronics and power systems is the real-life constraints (computational costs, communication delays, sensor noises, etc.). However, the evolution of hardware systems, especially their computational power, makes it possible to apply MPC to a larger field of applications [197–200]. But power electronics systems, due to their fast dynamics, are still an open field for MPC applications.

Regarding the use of real-time setups for grid-connected VSCs, there have been many works that use experimental mockups of a VSC controlled in grid-following mode [201–204]. However, the application of grid-forming to such converters is more recent and mainly concerns two-level VSCs [25, 167, 205] while operating MMC mockups in grid-forming remain marginal [166]. This makes the available setup at SuperGrid Institute [74] even more interesting for our research.

Taking into account the scarcity of such setups, little research has been conducted on implementing MPC for grid-forming controlled VSCs. There has been some recent practical implementation of MPC for VSC controlled in grid-forming mode [206]. However, this work is not about hierarchical MPC for energy management as it was

proposed in Chapter 5 but is about replacing the classical power synchronization control [79] of grid-forming by an MPC-based approach. MPC has also been applied to MMC control in experimental conditions, but the MPC layer was dedicated to cancelling circulating currents [207] and State of Charge (SOC) balancing of the MMC arms [208], and its application to MMC regarding grid-level considerations was not studied. In conclusion, there are no studies, to our best knowledge, that apply MPC to the energy management level of the MMC operated in grid-forming.

6.1.3. Chapter summary and contents

In this chapter, an experimental validation of the hierarchical MPC is proposed. This outer control layer comes as an extra control loop whose function is to ensure the AC/DC energy management of an MMC. Contrary to Chapter 5 where averaged models of the MMC were considered, in this chapter, the MPC is tested on a detailed mockup of a 6kVA MMC which contains 60 submodules and interfaces a 400V DC grid and a 120V (line to ground) three-phase AC grid. In addition, the MPC is tested with a recent grid-forming control [115] compatible with the specificities of MMCs compared to two-level VSCs. The MPC solution shows similar tracking performance with the dual PI control solution but appears to have a better disturbance rejection when compared to this dual PI.

The structure of this chapter is as follows: in Section 6.2, the procedure of experimental verification is presented, including a workflow to test the controllers in real-time conditions and the mockup used for the experimental validation. In Section 6.3, we present how the GFC was implemented on this existing structure. In Section 6.4, the hierarchical MPC implementation is detailed. In Section 6.5, the results obtained in PHIL are presented and compared to the dual PI solution and Section 6.6 finally concludes.

6.2. Procedure of experimental validation

This part presents the methodology used to test our controller in real-time conditions.

6.2.1. Presentation of the mockup

The setup we will be using is presented in [74,164,209]. This experimental benchmark has been developed over years at SuperGrid Institute and relies on Opal RT solution

Table 6.1: Parameters of the mockup

Quantity	**Notation**	**Value**
MMC rated power	S_b	6 kVA
AC base voltage (line-ground)	V_b^{ac}	120 V
DC base voltage	V_b^{dc}	400 V
number of SM per arm	N_{arm}	10
SM capacitance	C_{sub}	4.92 mF
AC filter inductance	L_{eq}	0.5 mH
AC filter resistance	R_{eq}	26 mΩ
MMC arm inductance	L_{arm}	6 mH
MMC arm resistance	R_{arm}	35.3 mΩ
DC grid capacitance	C_{dc}	6 mF

for the MMC mockup [210] as well as for the harware embedding the controllers and the measurement units. This benchmark makes it possible to test our developed control solutions, compiled from a Matlab/Simulink file into C-code, as further detailed in Section 6.2.2. This compiled code is then built on a hardware system and interfaced with Opal RT software RT-lab [211] to have a real-time display of the results and interact with the target during the experiment. The full experimental setup is given in Fig. 6.2. The MMC with its 60 submodules is at the center. At the top, there is the Opal RT 4510 (OP4510) hardware that contains the controller and sends the gate signals to the MMC. At the edges of the photograph, there are the AC and DC amplifiers, which emulate respectively a voltage source and a current source. There are both connected to the OP4510.

The electrical equivalent scheme of this setup is given in Fig. 6.2 (b). It is important to note that in addition to the different components presented above, there are also some passive components to recreate the transmission grid conditions.

In particular, there is a physical inductance L_{eq} between the MMC and the AC power amplifier which represents the inductive effect of a power transformer between the AC grid and the MMC. In addition, there is a physical DC capacitance C_{dc} between the MMC and the DC power amplifier that represents the equivalent DC grid inertia of this system. The numerical values of the mockup are given in Table 6.1.

Also, it is important to note that with this kind of setup it is possible to consider simulated AC/DC grids in real time instead of perfect sources [167, 177]. However, since this work focuses on the synthesis of an online MPC dedicated to the converter real-time control, we will only consider the system described in Fig. 6.2

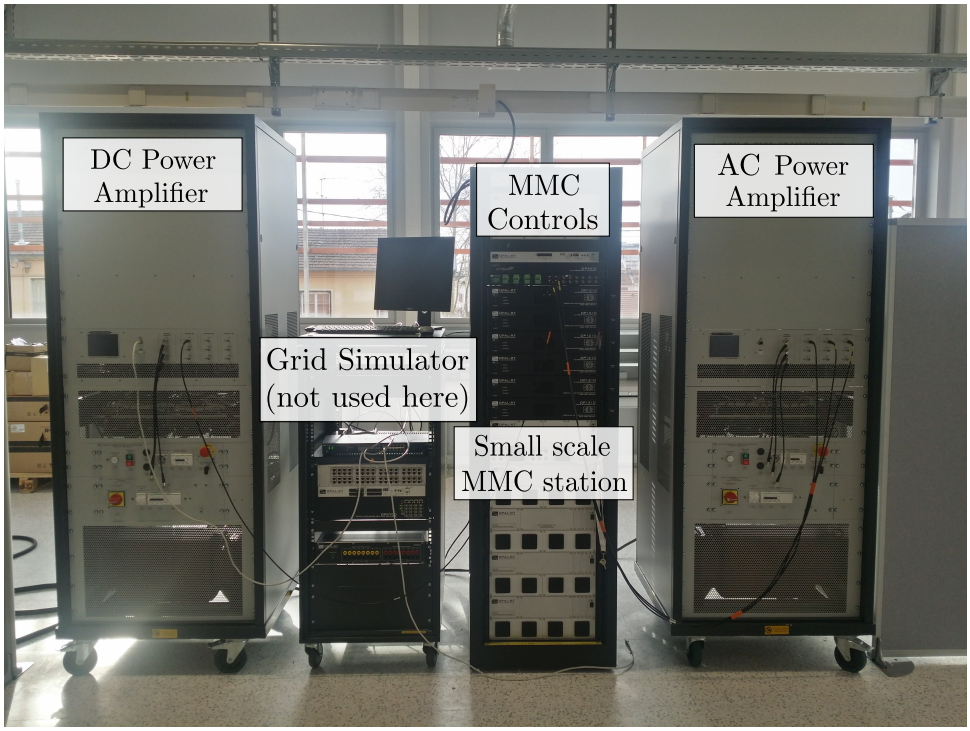

(a) Photograph of the mock-up.

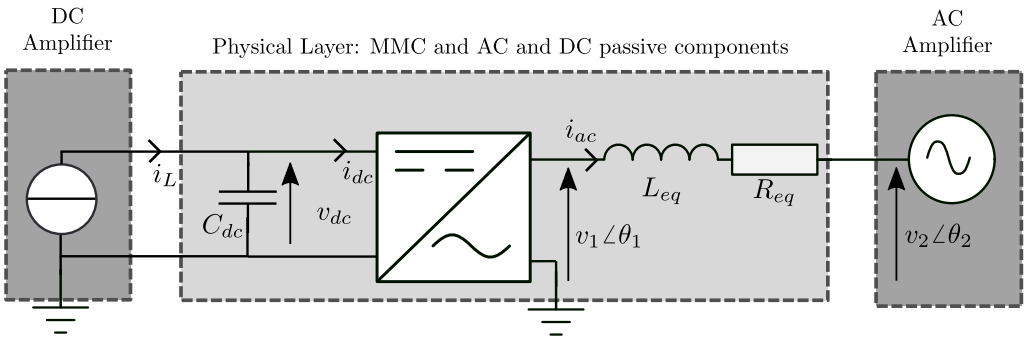

(b) Electrical scheme of the MMC mock-up with its AC and DC power amplifiers.

Figure 6.2: Power-Hardware-In-the-Loop (PHIL) experimental setup at SuperGrid Institute in Villeurbanne, France.

(b). Nevertheless, simulating more complex AC/DC systems would be a promising way of extending these results and will be discussed in the conclusions.

6.2.2. Existing controls and required changes

The control structure that had already been implemented before we started the project is given in Fig. 6.3. It is based on previous work at SuperGrid Institute [74,164] and is implemented in Matlab/Simulink environment which is then compiled on the target using RT-lab as presented in Section 6.2.1. This MMC control is

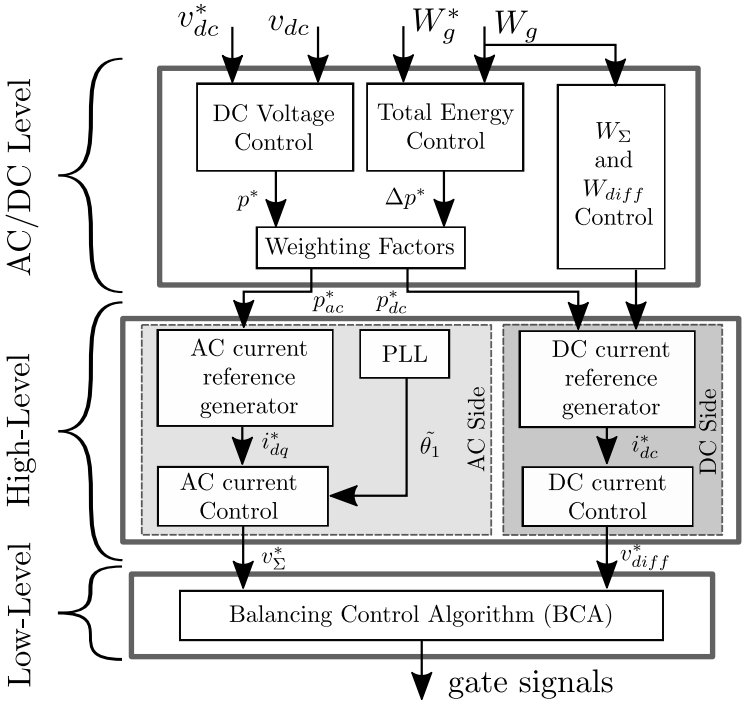

Figure 6.3: Existing MMC control with the PHIL setup before starting the project [74,164].

complex and can be divided into three categories, corresponding to the three control layers:

- *AC/DC level*: This control layer corresponds to the management of the AC/DC interface and the MMC energy. Since the DC grid is a current source, the MMC, as in Chapter 4 and Chapter 5, has to control the DC voltage. At the same time, the controller must ensure that the internal energy of the MMC, denoted by W_g, is well controlled to make sure that the MMC submodules are operable. These two controllers are coupled using a weighting factor block that was introduced in Chapter 4. In addition to these two controllers, there are also the energy sum (W_Σ) and energy difference (W_{diff}) controllers which ensure that the energy is well balanced between the phases and the arms. These controllers were not considered in Chapter 4 and Chapter 5 because the MMC internal energy was modeled using an average model.
- *High level*: This control layer corresponds to the AC and DC power and current controls of the MMC. In Fig. 6.3, the two controls are divided in AC and DC sides because the MMC is capable of controlling them independently. For the AC side, this control structure is the most commonly used grid-following control, which uses a PLL to synchronize with the grid, and where the AC current control generates the voltage reference v_Σ^* sent to the low-level control.

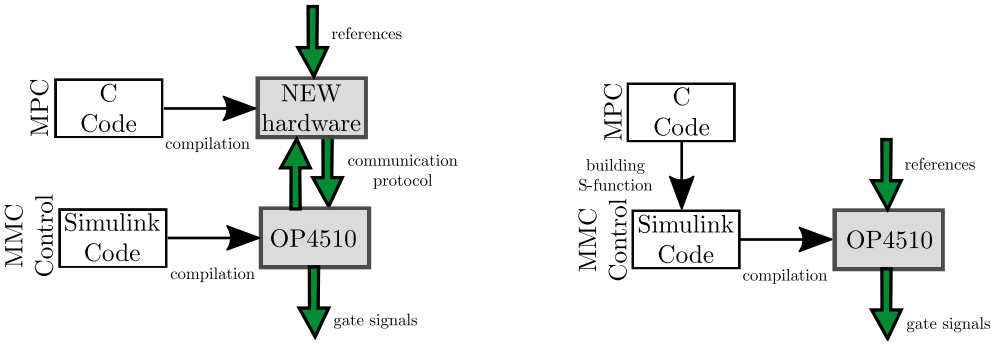

(a) Two hardware systems (b) Single hardware system

Figure 6.4: Considered hardware configurations to implement the control solution.

For the DC side, the DC current control similarly generates a voltage reference v^*_{diff} sent to the low-level control.

- *Low level*: This control layer corresponds to the activation and deactivation of the submodules to generate the desired voltage waveform. A Balancing Control Algorithm (BCA) is implemented to specify which submodules to be inserted. This BCA uses measurements of the submodules voltages and activates or desactivates the submodules so that their voltages converge to their mean value.

In our case, we want to implement the grid-forming control (GFC) and the MPC similarly to the control structure presented in Chapter 5. This requires to make changes in the AC/DC-level control and the High-level control.

6.2.3. Choice of hardware configuration

The two hardware configurations considered are given in Fig. 6.4. In Fig. 6.4 (a), the configuration consists in compiling the MPC layer in a different hardware ship than the OP4510 where the main MMC control is compiled. This makes the solution more modular but requires to establish communication protocols between the two chips since they need to communicate with each other in real time. In Fig. 6.4 (b), the solution implements the MPC coded in C in an S-function so that all the MMC control is in Matlab/Simulink and is then compiled in a single chip. One of the main advantages of the latter hardware configuration is that it does not require any communication protocol. Furthermore, since the MPC layer remains a 100% local controller dedicated to the converter control, it makes sense to compile all the MMC control into a single hardware system. However, for controls dedicated to the operation of AC/DC systems as a whole and to provide support to the AC grid

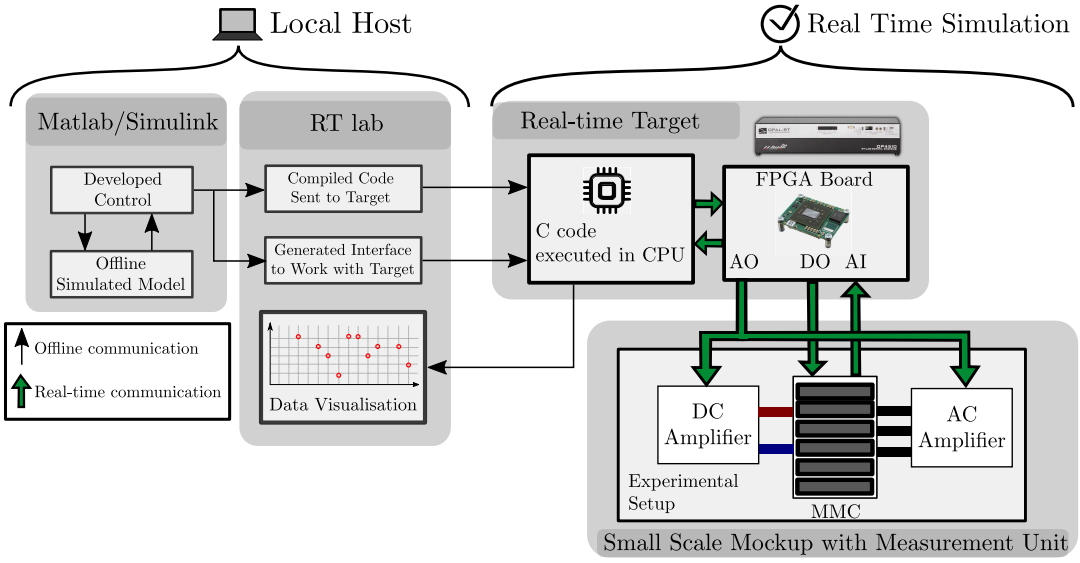

Figure 6.5: Power Hardware-In-the-Loop experimental setup and workflow.

by coordinating the response of an HVDC system [127, 181], other configurations should be investigated.

In the rest of this chapter, the single hardware configuration described in Fig. 6.4 (b) is considered.

6.2.4. Controller validation workflow

The proposed setup and workflow to demonstrate the feasability of the control using MPC technique is given in Fig. 6.5. As discussed in Section 6.2.3, all the MMC control is compiled on a single hardware system, which is the OP4510 (real-time target in Fig. 6.5). This system includes

- a CPU that executes the code in real time;
- an FPGA board that sends the control inputs (the gate signals) to the MMC and converts the console signals to analog outputs sent to the AC and DC amplifiers. The FPGA board also collects the analog inputs from the mockup which are then sent to the CPU of the OP4510.

This workflow is separated into two parts:

- *"Local Host" part*: it includes all the tasks that are executed on the local host, i.e. the physical computer, and are not executed in real time. This is where the control is developed in the Matlab/Simulink environment, compiled and sent to the target using RT-lab. As specified in the scheme, the control can be implemented and debugged directly in Matlab/Simulink without the need

to pass by RT-lab. In addition, the local host acts as the console which makes it possible to send reference changes or new setpoints to the mockup and to display the measurements online.

- *"Real-Time Simulation" part*: it includes all the operations executed in real time, such as the interface between the FPGA of the OP4510 and the mockup and between the CPU of the OP4510, where the control is compiled, and its FPGA. Also this is where the MMC control is tested in real time since the MMC mockup and the AC/DC amplifiers directly receive orders from the FGPA board of the OP4510.

This setup makes it possible to test any MMC control developed in Matlab/Simulink. As detailed in Section 6.2.3, since all the tested controls will be sent to the OP4510 target, this setup will be considered in the rest of this chapter.

6.3. Grid-Forming Control (GFC) implementation

This grid-forming control is implemented taking into account the complexity of existing MMC control detailed in Fig. 6.3. The whole MMC control structure with the grid-forming control is updated as described in Fig. 6.7, which is known as the direct voltage control. The outer loop corresponds to the classical outer loop control used in the previous chapters. For the inner loop, there is a saturation block "SAT" which is used to saturate the filtered measure of the dq-current (i_g^{dq}), denoted by $i_g^{dq^*}$. The damping resistor term R_a is used to damp the variations in i_g^{dq}. The decoupling term $j\omega L$ is used to compensate for the physical inductance in the MMC and thus to control the voltage at the PCC instead of the voltage at the MMC terminals. However, in our case, since an infinite bus is connected to the PCC, as described in Fig. 6.2 (b), it is not possible to control the PCC voltage, thus $j\omega L = 0$.

The above structure is based on recent works on grid-forming control where there is no inner voltage loop [115,212]. Indeed, because of the physical LC filter, this type of cascaded control, presented in Chapter 2, is better suited for two-level VSCs than for MMCs [167]. However, there has been no consensus yet in the literature to define a control structure of the MMC in grid-forming mode and some recent works still use the cascaded structure when considering the capacitive effects of the AC grid to design the inner voltage loop [77, 166].

The parameter values considered for this control are given in Table 6.2. In order to validate the GFC in Fig. 6.6, we investigate the activation of this control when the MMC is operating in a steady state in grid-following mode. To achieve such a steady

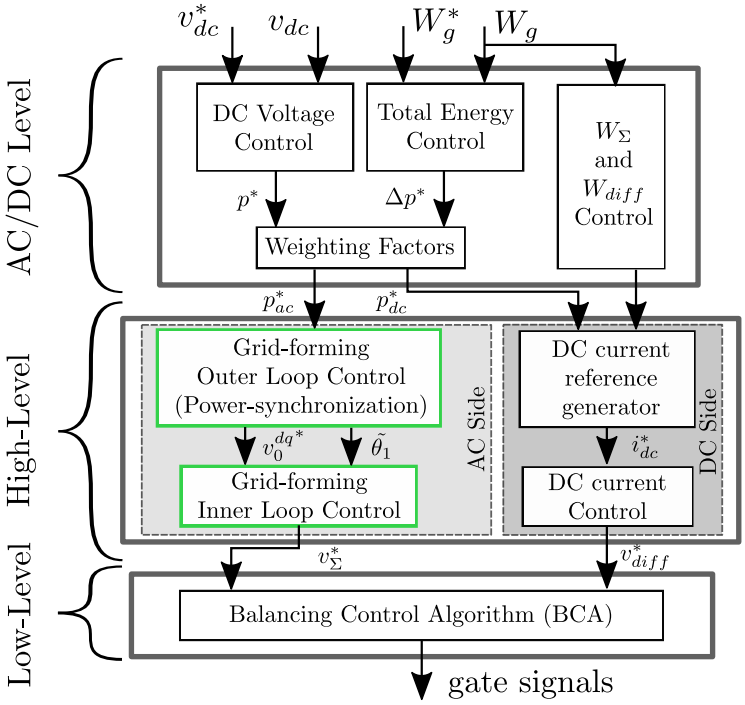

Figure 6.6: Modified MMC control to integrate the grid-forming control in the high-level layer: dual-PI control structure.

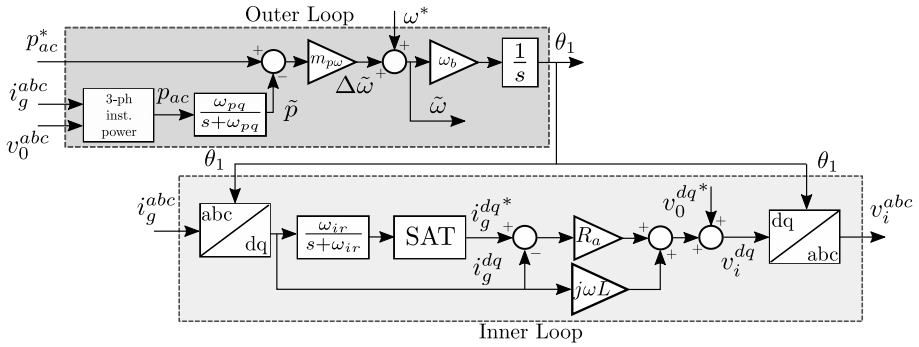

Figure 6.7: Implemented grid forming control. Scheme based on [115,212].

state, we first carry out the start-up sequence where the MMC submodules and the DC grid are energized by the AC grid. Indeed, since the grid-forming control relies on the synchronization based on the variations of active power, it has to start from an equilibrium point so that it remains synchronized. In consequence, we keep the startup sequence developed in [209] in grid-following mode and switch to the grid-forming mode when $v_{dc} = v_{dc}^*$ and $W_g = W_g^*$. In order to smoothen the transients caused by the switching, we use the estimated angle from the PLL to initialize the three GFC integrators, contained in the low-pass filters and in the outer loop as described in Fig. 6.6.

Table 6.2: Control parameters of the MMC control.

Quantity	**Notation**	**Value**
Active power droop gain	$m_{p\omega}$	0.05 p.u.
Reactive power droop gain	m_{qv}	0 p.u.
Outer loop filter cut-off frequency	ω_{pq}	62.8 rad/s
Inner loop filter cut-off frequency	ω_{ir}	314 rad/s
Damping resistance	R_a	0.2 p.u.
Inductance compensation	L	0 p.u.
Energy control response time	τ_{rwh}	0.5 s
W_Σ control response time	τ_{W_Σ}	1 s
W_{diff} control response time	$\tau_{W_{diff}}$	1 s
Energy reference	W_g^*	1 p.u.
DC voltage reference	v_{dc}^*	1 p.u.
Energy distribution coefficient	α	1
DC-voltage control response time	τ_{rdc}	0.15 s
DC-current control response time	τ_{idc}	0.003 s
AC-current control response time	τ_{iac}	0.005 s
Damping ratio of all control loops	ζ	0.707

We performed two types of experiments: *i*) switching from grid-following to grid-forming when $i_L = 0$; *ii*) switching from grid-following to grid-forming when $i_L = 0.3$ p.u. The results given in Fig. 6.8 and Fig. 6.9 show that in both cases, the MMC manages to synchronize with the grid thanks to the power synchonization loop. However, even though the GFC activation does not affect the DC voltage and DC current, we observe a larger MMC internal energy transient when $i_L = 0.3$ p.u. Also, we see that in this case the MMC aborbs some reactive power from the AC grid when the GFC is activated. This is because the converter, now controlled as a voltage source, adjusts its reactive power injection or absorption in order to regulate the AC voltage.

To summarize, these results are really encouraging because they demonstrate that we are capable of activating a grid-forming control of a physical mockup in real-time conditions.

6.4. MPC implementation

6.4.1. Choice of the software solution

The MPC was implemented in Chapter 5 using the Matlab-based tool YALMIP [193] which exclusively works in a Matlab environment. In this chapter, we implement the MPC in C which, as a programming language close to the machine target

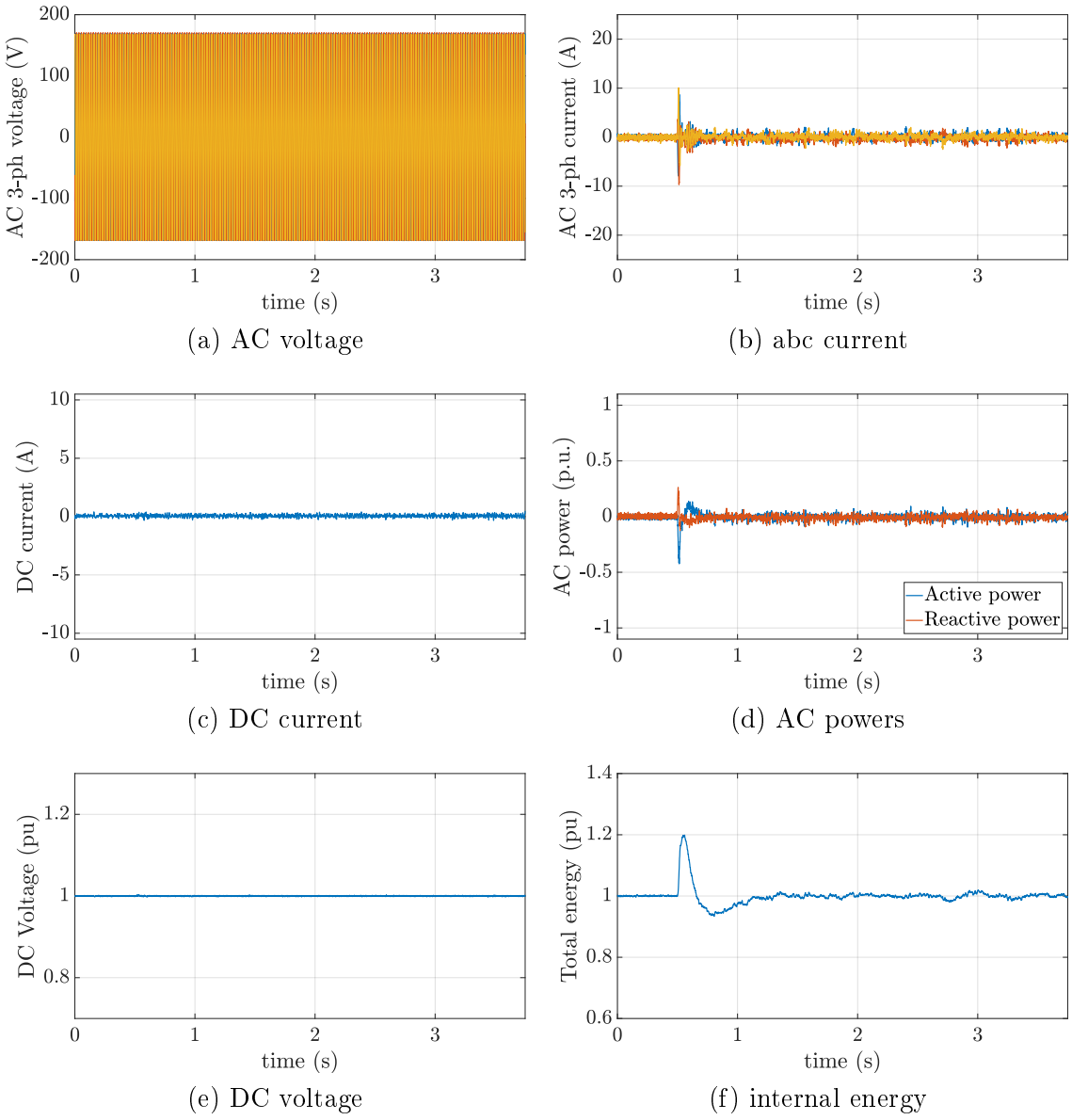

(a) AC voltage (b) abc current

(c) DC current (d) AC powers

(e) DC voltage (f) internal energy

Figure 6.8: GFC activation off-load, when $i_L = 0$ p.u.

language, can be easily complied into industrial systems. In consequence, we need to find another software solution. In order for the solution to be compatible with different hardware systems, we consider the solutions based on C code exclusively. In fact, there are several free software solutions [213, 214] to generate C-based linear MPC. There has been also some academic work to compare different linear MPC implementations in C for industrial processes [215]. In our case, we decided to use the μao-MPC solution [214] because, as a solution initially designed for microcontroller, it is highly portable and is an open-source software.

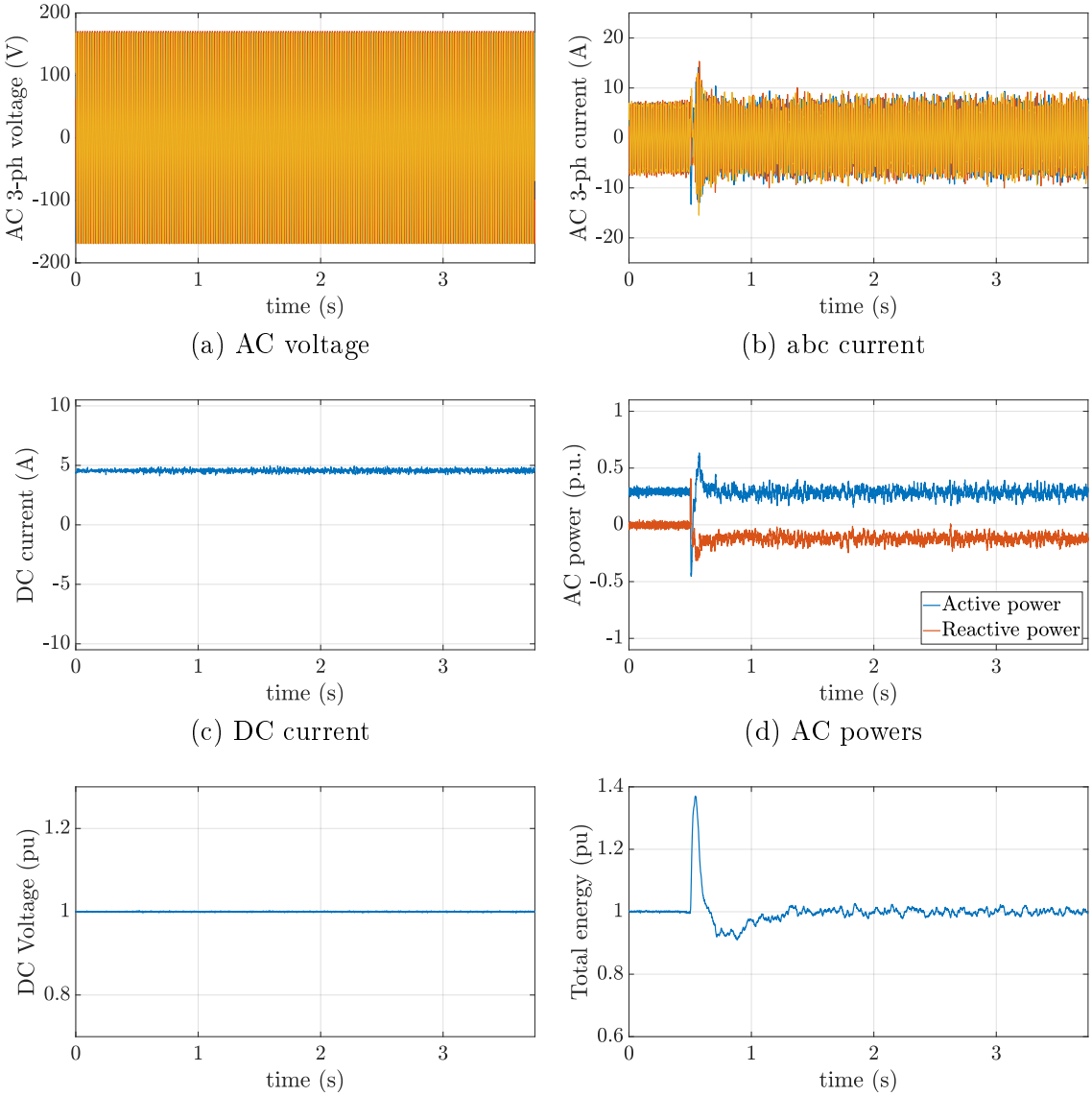

(a) AC voltage (b) abc current

(c) DC current (d) AC powers

(e) DC voltage (f) internal energy

Figure 6.9: GFC activation on-load, when $i_L = 0.3$ p.u.

6.4.2. μao-MPC embedded QP solver

This section presents the embedded QP solver of μao-MPC. In the literature, most of the solvers use condensed forms of the Quadratic Problem (QP) to solve it more efficiently [216]. This condensed form of the cost function, denoted by J_{QP}, can be expressed as:

$$J_{QP}(\theta, x) = \frac{1}{2}\theta^T H \theta + h(x)^T \theta \tag{6.1}$$

The aim of the QP solver is to minimize this cost function:

$$\min_{\theta \in \Theta} J_{QP}(\theta, x) \tag{6.2}$$

$$\text{subject to } \underline{z}(x) \leq E\theta \leq \bar{z}(x) \tag{6.3}$$

where θ is the control input vector, x is the state variable vector, H is the Hessian matrix of the function describing the evolution of the state variables θ, h is the gradient vector, E is a constant matrix to express the state constraints, $\underline{z}(x)$ and $\bar{z}(x)$ are respectively the state minimum and maximum constraints and

$$\Theta = \{\theta | \underline{\theta} \leq \theta \leq \bar{\theta}\} \tag{6.4}$$

where $\underline{\theta}$ and $\bar{\theta}$ are respectively the control input minimum and maximum constraints. In order for the problem (6.2) to have a global minimum, the problem must be convex, i.e. the Hessian matrix must be positive-definite. In the case of μao-MPC, the solver was designed to only rely on simple mathematical operations to solve the QP problem defined in (6.2) and (6.3).This feature makes it compatible with most of the microcontrollers and hardware systems used for real-time controllers. This solver uses the augmented Lagrangian method and Nesterov's fast gradient method [214], which are presented respectively in this part.

6.4.2.1. Augmented Lagrangian Method (ALM)

This method is used to convert the constrained problem into a serie of unconstrained optimization problems that are much simpler to solve:

$$\min_{\theta \in \Theta} J_u(\theta, \lambda^*, x) \tag{6.5}$$

where J_u, called the condensed cost function, is the equivalent unconstrainted cost function of the optimization under constraints problem (6.2) – (6.3) such that:

$$J_u(\theta, \lambda, x) = \frac{1}{2}\theta^T H \theta + h^T \theta + T(\theta, \lambda, x) \tag{6.6}$$

where T is defined as:

$$T(\theta, \lambda, x) = \min_s \lambda^T s + \frac{\mu}{2}\|s\|_2^2 \tag{6.7}$$

$$\text{subject to } \underline{z}(x) \leq E\theta + s \leq \bar{z}(x) \tag{6.8}$$

where μ is the penalty parameter of the augmented Lagrangian method. Let λ^* be a Lagrange multiplier that minimizes the condensed cost function J_u. The augmented Lagrangian method is used to estimate this λ^* by successive iterations.

$$\lambda^{i+1} = S(\theta^{*i}, \lambda^i, x) \tag{6.9}$$

where θ^{*i} is the solution minimizing (6.5) but with λ^* replaced by λ^i and i is the iteration index:

$$\theta^{*i} = \arg\min_{\theta \in \Theta} J_u(\theta, \lambda^i, x) \tag{6.10}$$

and

$$S(\theta, \lambda, x) = \min(\underline{\lambda}(\theta, \lambda, x), 0) + \min(\bar{\lambda}(\theta, \lambda, x), 0) \tag{6.11}$$

where

$$\underline{\lambda}(\theta, \lambda, x) = \lambda + \mu \times (E\theta - \underline{z}(x)) \tag{6.12}$$

$$\bar{\lambda}(\theta, \lambda, x) = \lambda + \mu \times (E\theta - \bar{z}(x)) \tag{6.13}$$

In order to take into account the constraints in (6.3) represented by the term $T(\theta, \lambda, x)$, we need to estimate λ^{i+1}, and in consequence, to have a good estimation of the optimal control input θ^{*i}. This estimation is obtained by using the Fast Gradient Method (FGM) described in the next subsection.

6.4.2.2. Fast Gradient Method (FGM)

The fast gradient method is a technique to estimate the local minimum of a convex function based on the observation of its gradient. In our case, we assume that J_u is a convex function, so we can apply the FGM. The gradient step projected onto the set Θ can then be calculated as:

$$G_\Theta(w, \lambda^i, x) = P_\Theta(w - \frac{1}{L} \nabla J_u(w, \lambda^i, x)) \tag{6.14}$$

where, knowing that $\underline{\theta}$ and $\bar{\theta}$ are respectively the control input minimum and maximum constraints:

$$P_\Theta(\alpha) = \max(\underline{\theta}, \min(\bar{\theta}, \alpha)), \tag{6.15}$$

and $L = \|H + \mu E^T E\|$ is assumed to be the Lipschitz constant for ∇J_u ,the gradient of J_u. More details about these assumptions can be found in [214]. We can then calculate the approximation of the optimum θ^{j+1} and compute the extra step w used for the iterative loop:

$$\theta^{j+1} = G_\Theta(w, \lambda^i, x) \tag{6.16}$$

$$w = \theta^{j+1} + \nu \times (\theta^{j+1} - \theta^j) \tag{6.17}$$

where ν is the extra-step constant defined as:

$$\nu = (\sqrt{L} - \sqrt{\phi})(\sqrt{L} + \sqrt{\phi})^{-1}, \tag{6.18}$$

where ϕ is a strong convexity parameter for J_u given by the smallest eigenvalue of H (the Hessian of the QP problem) [214]. As a reminder, a function f is said to be "strongly convex" with respect to a parameter m if and only if the function g, defined such that

$$g : x \mapsto f(x) - \frac{m}{2}\|x\|^2 \tag{6.19}$$

is convex. More information about this definition can be found in [217].

Finally, it is possible to calculate u^{j+1} which can then be used in the ALM described in Section 6.4.2.1.

6.4.2.3. Structure and tuning of the solver

The global structure of the solver combines the ALM and the FGM, and is described in Fig. 6.10. There are three tuning parameters for this solver:

- ex_{iter}: the number of external interations, which corresponds to the number of times the ALM algorithm is called per MPC step;
- in_{iter}: the number of internal interations, which corresponds to the number of times the FGM algorithm is called per ALM step;
- μ: the penalty parameter of the augmented Lagrangian method, defined in (6.7), which corresponds to the weight put on the state constraints defined in the QP optimization problem (6.2) – (6.3). In practice, the developers of µao-MPC have set the software so that it finds an appropriate value of μ depending on the MPC problem.

The solver must do at least one external iteration and one internal iteration. However, since the ALM is used to make the unconstrained problem converge, while taking into account the term $T(\theta, \lambda, x)$, the number of external iterations ex_{iter} is only useful when we consider state constraints, which is our case for the application the MMC control presented in Chapter 5.

6.4.3. Validation of µao-MPC solution

In this section, we try to validate µao-MPC before its implementation on the mockup. We decided to implement the linear MPC using the C-based µao-MPC [214] and a Matlab/Simulink S-function to compare the controller performances with the well-known Matlab-based YALMIP [193]:

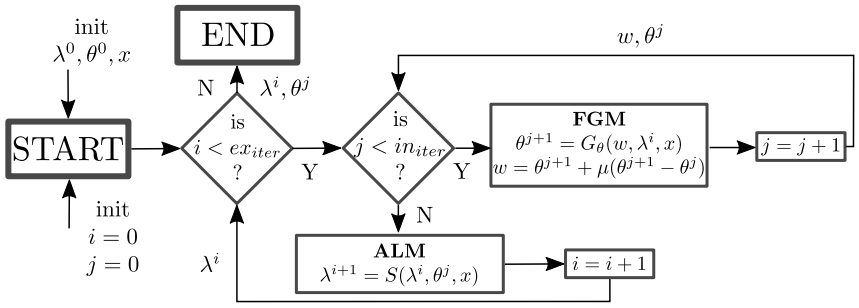

Figure 6.10: Flowchart of the used embedded QP solver. Scheme based on [214].

- For the YALMIP solution, it was already implemented in the Simulink examples available online [218]. This solution relies on the Matlab interpreted function block [219] that forces the function to be computed exclusively in Matlab. In consequence, it is impossible to use it for real-time applications.
- For the μao-MPC solution, we generated the C-code of the control offline and then embedded it in an S-function [220], which makes it possible to compile C-code in a Matlab/Simulink environment.

The two tools use different solvers to calculate the optimal control solution. In YALMIP, we use Matlab's "quadprog" algorithm [194] introduced in Chapter 5 whereas for μao-MPC, there is an dedicated C-coded solver that "relies only on matrix-vector operations". This latter solver is based on the augmented Lagrangian method (also called method of multipliers) and Nesterov's fast gradient method [214] presented in Fig. 6.10, with $in_{iter} = 5$ and $ex_{iter} = 1$.

The test system under consideration [218] is:

$$\Sigma_{example} = \begin{cases} \dot{x} = & Ax + Bu \\ y = & Cx + Du \end{cases} \tag{6.20}$$

where:

$$A = \begin{bmatrix} 0 & 0 \\ 1 & 0 \end{bmatrix}, B = \begin{bmatrix} 1 & 0 \end{bmatrix}, C = \begin{bmatrix} 0 & 1 \end{bmatrix}, D = 0. \tag{6.21}$$

And the cost function J is defined as:

$$J = (y^* - y)^T \cdot Q \cdot (y^* - y) + u^T \cdot R \cdot u \tag{6.22}$$

with

$$R = \begin{bmatrix} 0.1 & 0 \\ 0 & 0.1 \end{bmatrix}, Q = \begin{bmatrix} 10 & 0 \\ 0 & 10 \end{bmatrix} \tag{6.23}$$

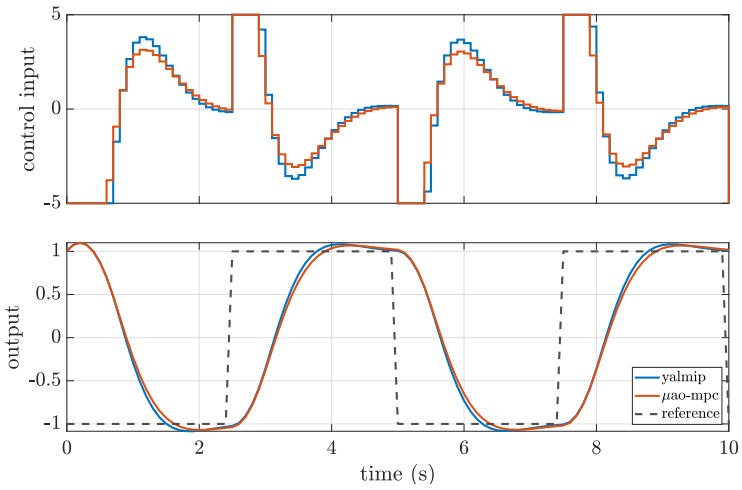

(a) Similar MPC implementations

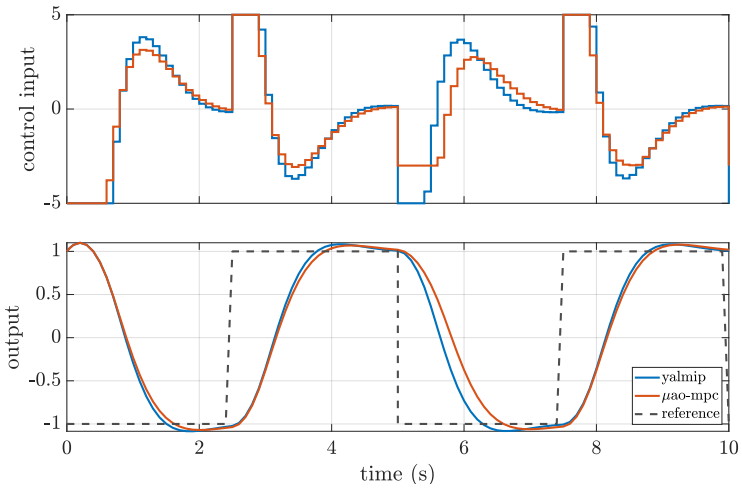

(b) Change in u_{min} in μao-MPC from -5 to -3 at $t = 5$s.

Figure 6.11: Comparison of similar MPC implementations using two different tools: YALMIP [193] versus μao-MPC [214].

The optimal control input is calculated based on minimizing J such that:

$$\frac{\partial J}{\partial u} = 0 \tag{6.24}$$

$$\text{subject to } -5 \leq u \leq 5 \tag{6.25}$$

The results following the change of the reference y using a step function are given in Fig. 6.11. In Fig. 6.11 (a), the two MPCs have similar parameters and are supposed to give similar results. This is confirmed by the simulation results where only slight differences between the two implementations are observed. These differences are mainly due to the difference of QP solvers.

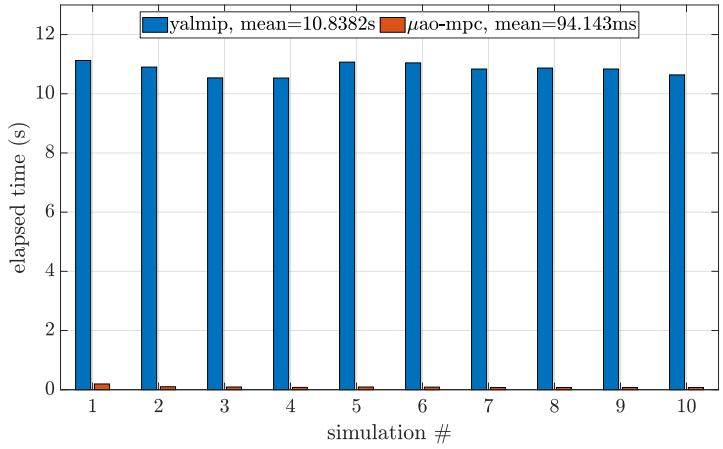

Figure 6.12: Comparison of the elapsed time of the two control implementations in a Matlab/Simulink environment with the standard tuning parameters of the solver.

In Fig. 6.11 (b), we analyzed the efficiency of online updates of the input constraints of the μao-MPC solution. The minimum value of the input u, denoted by u_{min}, is changed from -5 to -3 at $t = 5$s. We observe that the MPC does consider this change in this figure, and that in consequence the tracking of the output reference is worse than the nominal solution.

The μao-MPC appears to offer similar performances as YALMIP in terms of synthetizing a linear MPC for linear systems. To compare the computation costs between the two options, we performed 10 consecutive simulations of this example for each solution. The respective elapsed times are given in Fig. 6.12. It is clear that the MPC implemented in C is much more efficient in terms of computational costs, up to 100 times faster, than the YALMIP option. This is an interesting feature since the computation cost of the algorithm will be critical for the implementation on a real hardware system.

The C-based μao-MPC solution appears to have sufficient performances to be used for our MPC implementation.

6.4.4. Practical implementation of the MPC in real-time target

To implement the hierarchical MPC in the MMC mockup, we desired to keep the workflow defined in [209] and described in Section 6.2 that uses RT-lab to generate a C-code from a Matlab/Simulink controller that is then compiled in the Opal-RT 4510 target. The modified MMC control structure, integrating the MPC, is given in

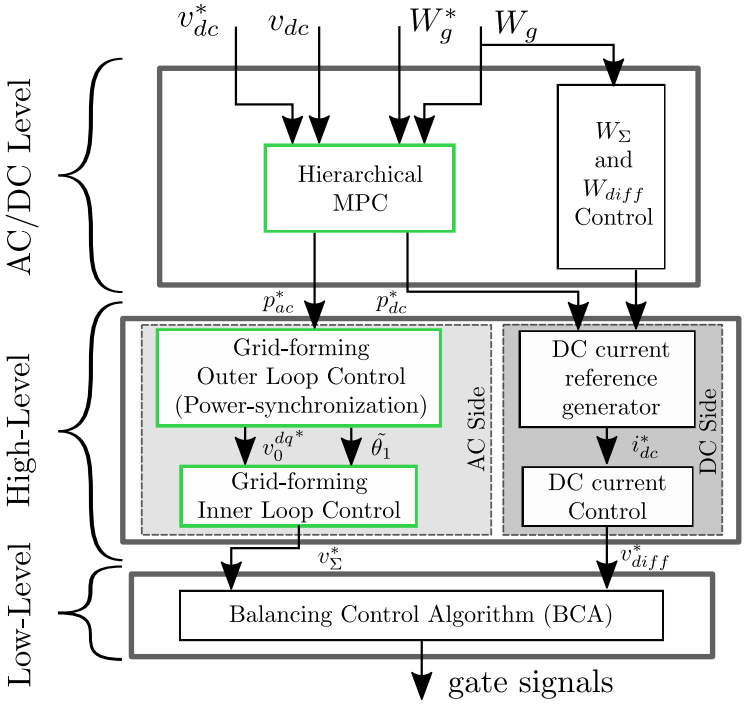

Figure 6.13: Modified MMC control to integrate the grid-forming control in the high-level layer and the MPC in the AC/DC-level layer: MPC control structure.

Fig. 6.13. Here, the two PI controllers presented in Figs. 6.3 and 6.6 are replaced by a MIMO-based MPC that would be handling the control of the internal energy of the MMC as well as the DC voltage. This control generates AC and DC power references in real time, while taking into account the constraints on W_g and v_{dc}. In order to implement this control, the MPC must be compiled in Matlab/Simulink so that the workflow is kept as usual. The different steps to generate the MPC for the real-time target is given below:

1. Define the MPC parameters (prediction horizon, sampling time, state-space system, etc.) in Matlab;
2. Generate C-code for the MPC using μao-MPC software;
3. Embed the C-code files in an S-function in the MMC control in Matlab/Simulink;
4. Generate the C-code for the MMC control using RT-lab software and Simulink Coder.

The equations of the MPC must be of low order in order to be compatible with the real-time constraints. In Chapter 5, we had a 6^{th}-order model where 4 states were used to capture the AC grid dynamics. In this chapter, since the AC grid is modeled as a perfect voltage source, these dynamics are neglected, which means

that the MPC can use a second order model as:

$$\Sigma_c = \begin{cases} \dot{x}_c &= Ax_c + Bu_c \\ y_c &= Cx_c + Du_c \end{cases} \tag{6.26}$$

where $x_c = \begin{bmatrix} x_{dc} & x_\Sigma \end{bmatrix}^T \in \mathbb{R}^2$, $u_c = \begin{bmatrix} p^*_{dc} & p^*_{ac} \end{bmatrix}^T \in \mathbb{R}^2$, $y_c = x_c$, $x_{dc} = v^2_{dc}$, $x_\Sigma = v^2_\Sigma$ (v_Σ being the average of the six arm voltages of the MMC),

$$A = \begin{bmatrix} 0 & 0 \\ 0 & 0 \end{bmatrix}, B = \begin{bmatrix} -\frac{2}{C_{dc}} & 0 \\ \frac{2}{C_{eq}} & -\frac{2}{C_{eq}} \end{bmatrix}, C = I_2, D = 0. \tag{6.27}$$

This system is discretized to be implemented in the MPC. The sampling time is $T_s = 0.015$s and the prediction horizon is $N = 6$. The MPC takes also into account the following state and control input constraints:

$$0.8 \text{ p.u.} < v^2_{dc} < 1.2 \text{ p.u.} \tag{6.28}$$

$$0.8 \text{ p.u.} < W_g < 1.2 \text{ p.u.} \tag{6.29}$$

$$-0.3 \text{ p.u.} < \Delta p^*_{dc} < 0.3 \text{ p.u.} \tag{6.30}$$

$$-0.3 \text{ p.u.} < \Delta p^*_{ac} < 0.3 \text{ p.u.} \tag{6.31}$$

The cost function J that is considered is defined as:

$$J = \sum_{i=0}^{N} (y^* - y(k|k+i))^T \cdot Q \cdot (y^* - y(k|k+i)) + \Delta y(k|k+i)^T \cdot S \cdot \Delta y(k|k+i) \tag{6.32}$$

with the normalized weighting factor matrices Q and T being:

$$Q = \begin{bmatrix} 1 & 0 \\ 0 & 10 \end{bmatrix}, S = \begin{bmatrix} 0.1 & 0 \\ 0 & 0 \end{bmatrix} \tag{6.33}$$

In practice, the technique of the embedded integrator is used to build the augmented model of the system that is compiled into the target [192]. For the solver, it appears that the higher ex_{iter} and in_{iter}, the better its performances. However, because of computational burden, we had to limit the maximum number of iterations, which of course also depends on the prediction horizon N and the time step T_s. For such configuration, we found that $in_{iter} = 6$ and $ex_{iter} = 4$ yield the best compromise.

6.5. Experimental results and discussions

Case #	Feature	Description
Case 1	DC-voltage tracking	Reference step from 1 p.u. to 0.95 p.u. in v_{dc}^*
Case 2	internal energy tracking	Reference step from 1 p.u. to 0.9 p.u. in W_g^*
Case 3	DC-side disturbance	DC current step from 0 p.u. to 0.1 p.u. in i_L
Case 4	AC-side disturbance	AC voltage step from 1 p.u. to 0.9 p.u. in v_2
Case 5	AC-side disturbance	AC angle step from 0^o to 10^o in θ_2

Table 6.3: Case studies for the PHIL experimental validation.

6.5.1. Test cases

The aim of this section is to discuss the interest of replacing the dual PI controllers by a MPC when operating the MMC in grid-forming. Indeed, even if the MPC-based solution in Chapter 5 exhibited better performances, this type of solutions are still marginal for industrial power electronics systems. This subsection introduces the test cases we considered to compare the two control solutions in PHIL.

The idea is to compare the two controllers in terms of tracking and disturbance rejection from either the AC or the DC grid. The different test cases that are considered are presented in Table 6.3. For the tracking cases (Case 1 and Case 2), we want to assess the performances of the MPC. Also, in order to validate the control executed with the MMC mockup, a similar experiment is simulated using a Software-in-Loop (SIL) system, where the embedded code is compiled on an Opal RT 5700 target (OP5700). Contrary to the workflow presented in Fig. 6.5 for the PHIL experiment, SIL relies on two cores of the OP5700 system to simulate the experiment in real time. One core is dedicated to simulate a detailed model of the mockup and another core is used to execute the same control that is embedded in the OP4510 system in PHIL. More information about the detailed model of the mockup and its validation can be found in [209].

For the AC and DC disturbances, we define them as follows:

- Case 3 is a DC power step which can represent the loss of parts of the generation from the DC grid or a DC load step;
- Case 4 is a negative step in the voltage magnitude which can represent a voltage sag or a short-circuit happening somewhere in the grid;
- Case 5 is a phase jump that can be used to model grid disturbances such as a line tripping. This type of disturbance is also used to characterize voltage sags in some works [221, 222].

The rest of this section compares the two control solutions with the PHIL experiment.

6.5.2. Results regarding tracking

The results regarding the capability of both the dual PI and the MPC to control the internal energy W_g and the DC voltage v_{dc} are given in Fig. 6.14. First, we note that there is a small static error in PHIL between the reference of MMC internal energy W_g^* and the measurement of W_g, which is not observed with the dual PI. In addition, the MMC control is exactly the same between the SIL and the PHIL experiments, whereas this static error is only observed for the PHIL case. This error is difficult to interpret:

- it does not seem to be related to an error in the MPC code itself since it is the same code that is compiled into the OP5700 for the SIL experiment and into the OP4510 for the PHIL experiment. Yet, there is no steady-state error in SIL whereas there is a less than 1% error in PHIL;
- it cannot be caused by an offset or noise of the mockup sensors because the dual PI control solution in the PHIL experiment does not have any static error while it uses the same measurements for the control.

Despite the static error of less than 1%, the two sets of results are still quite similar, which means we can argue that the PHIL setup is valid against the SIL results. This offset could be caused by the numerical error of the QP solver combined with the sensor noise of the mockup. Correcting this offset will be one of the future tasks in the development of this PHIL setup.

Also, it is important to note that there is a small difference between the DC voltage dynamic response of the SIL and the PHIL experiments. In both Figs. 6.14 (a) and 6.14 (e), the DC voltage response with the MPC exhibits an overshoot but the time response is slightly slower in the SIL experiment. On the other hand, the response of the dual PI in PHIL and SIL appear to be similar. For the energy tracking however, the dynamic response of the MPC in SIL (Fig. 6.14 (d)) and in PHIL (Fig. 6.14 (h)) are almost identical, except the static error.

Additional experimental data obtained with the PHIL setup for Case 1 and Case 2 are given in Fig. 6.15 and Fig. 6.16 respectively. We observe that the AC power and the DC current are well controlled. Also, the capacitor voltages of the MMC submodules are within a $\pm 5\%$ envelop around the nominal setpoint. It is important to note though that this distribution is the result of the BCA in the low-level control,

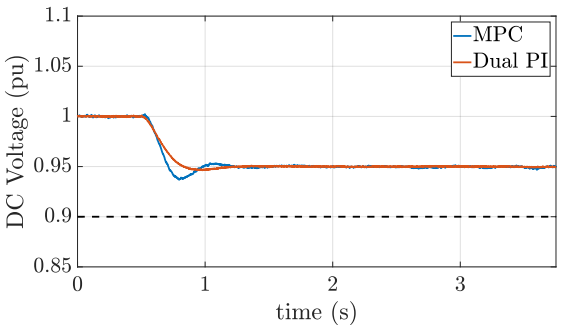

(a) Case 1: DC voltage in SIL

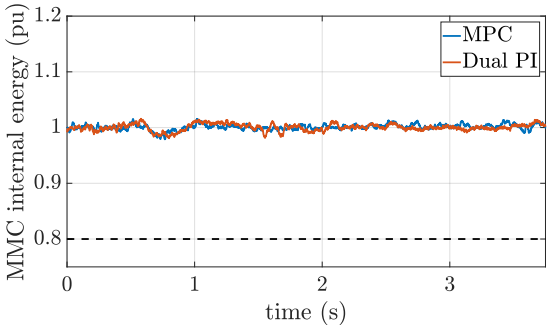

(b) Case 1: MMC internal energy in SIL

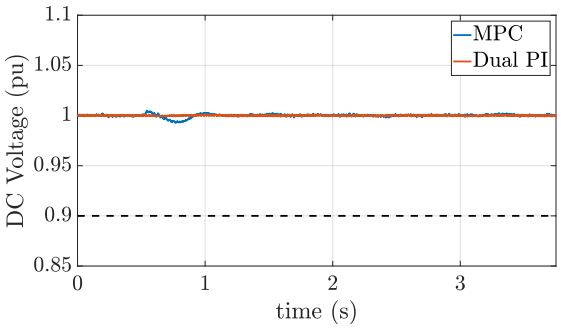

(c) Case 2: DC voltage in SIL

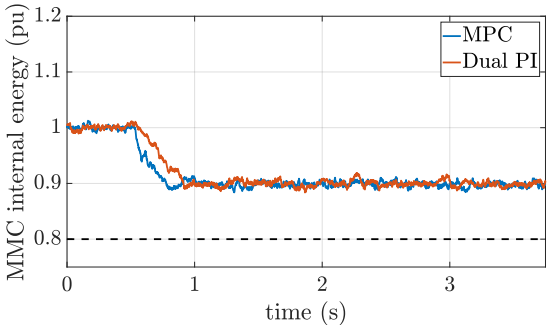

(d) Case 2: MMC internal energy in SIL

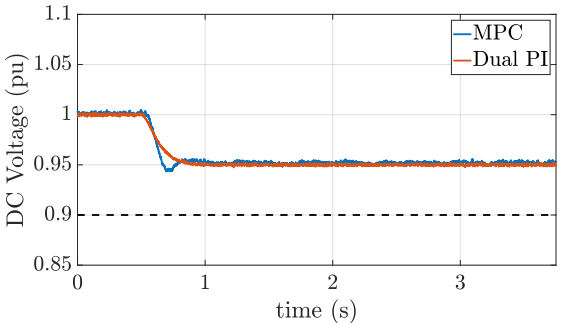

(e) Case 1: DC voltage in PHIL

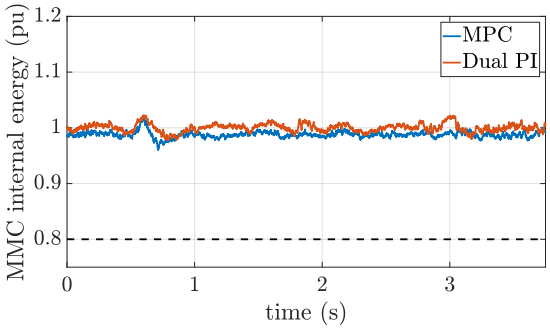

(f) Case 1: MMC internal energy in PHIL

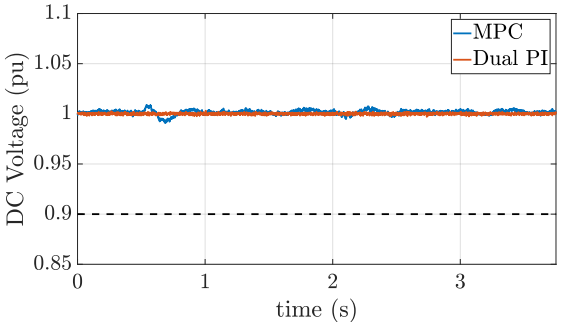

(g) Case 2: DC voltage in PHIL

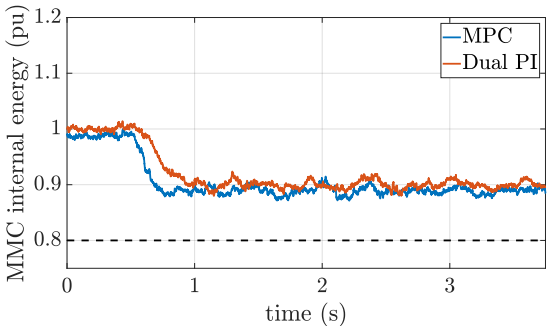

(h) Case 2: MMC internal energy in PHIL

Figure 6.14: Comparison of the tracking performances of the MPC and dual PI solutions in SIL and PHIL experiments.

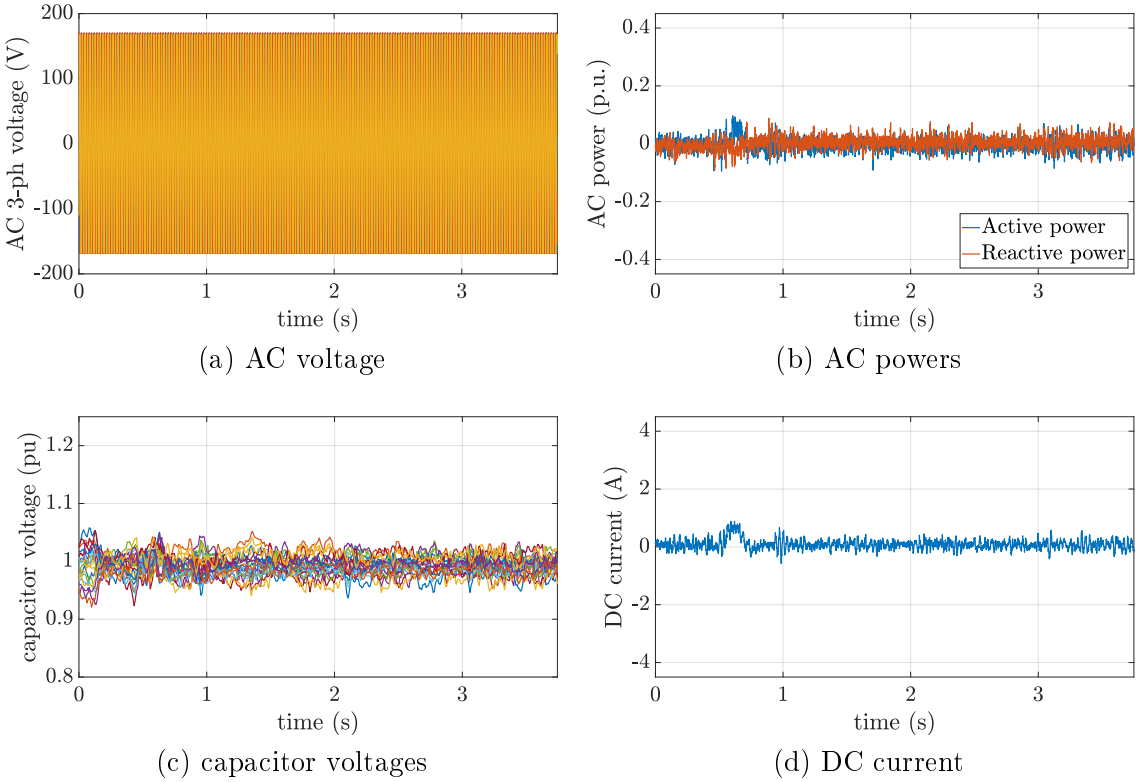

(a) AC voltage (b) AC powers

(c) capacitor voltages (d) DC current

Figure 6.15: PHIL mockup data: MPC and Case 1

since the MPC is only responsible for controlling the internal energy stored in the converter. This means that the total control structure is efficient because all the measurements reach acceptable values.

6.5.3. Results regarding disturbance rejection

Now that the MMC control given in Fig. 6.13 has been validated with a SIL simulation, we compare in this part the two controllers in terms of disturbance rejection, in PHIL only. The results for the disturbance rejection cases (Case 3 to Case 5) are given in Fig. 6.17. For Case 3 with the DC current disturbance, the MPC and the dual PI solutions give comparable results, even though the dual PI appears to have a smoother transient regarding the DC voltage. For the voltage magnitude negative step (Case 4), we see that MPC and dual PI give similar responses, as shown in Figs. 6.17 (c) and 6.17 (d), but the energy level does not come back to its pre-disturbance state with the MPC. On the other hand, for the angle step (Case 5), the results are drastically different between MPC and dual PI because the dual PI solution is unstable: the breakers of the mockup open due to the DC voltage fall, whereas the system is maintained stable with the MPC.

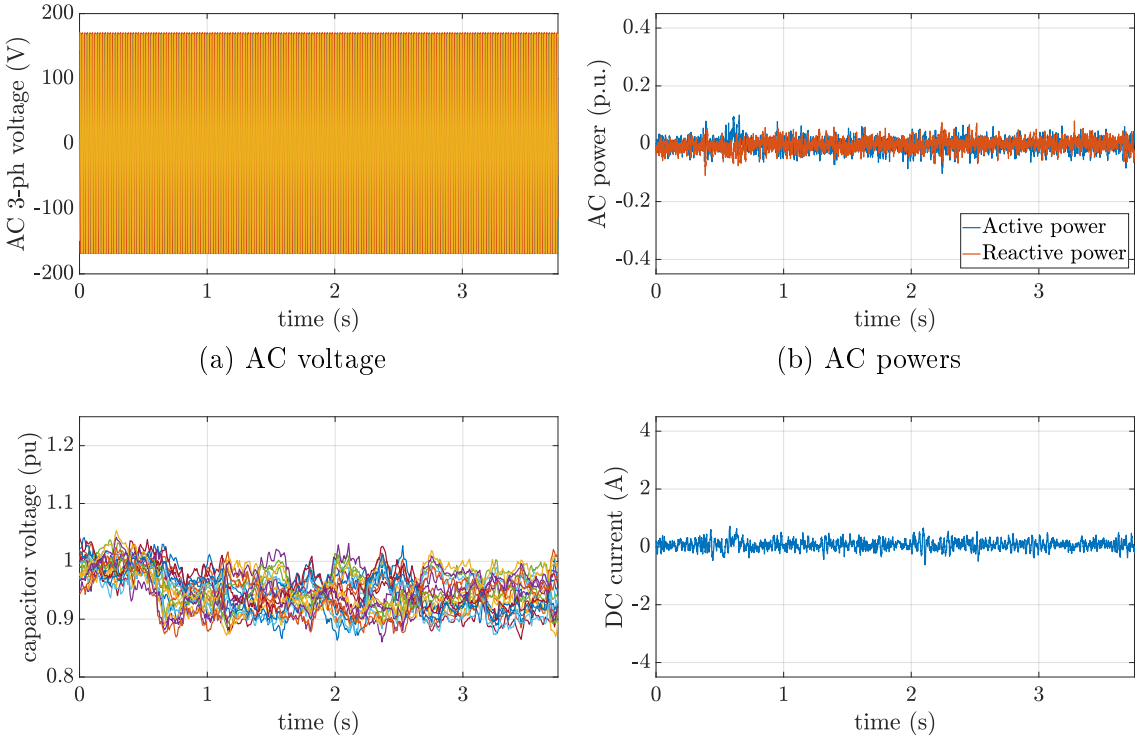

(a) AC voltage (b) AC powers

(c) capacitor voltages (d) DC current

Figure 6.16: PHIL mockup data: MPC and Case 2

To summarize, the results presented in Fig. 6.17 show that on the one hand, the MPC does not let v_{dc} and W_g track exactly their references but these variables respect the acceptable limits. On the other hand, MPC shows better performances regarding disturbance rejection. This tendency is really encouraging and justifies the use of MPC-based solutions for the MMC control since in real-life conditions the AC/DC system encounters that will probably be handled by the MMC in the future.

The state variable responses with the MPC for Cases 3 to 5 are described in Figs. 6.18, 6.19 and 6.20 respectively. It is interesting to note that since the MMC is operated in grid-forming mode, the first two disturbances generate some reactive power absorption/injection so that the MMC output voltage is maintained at 1 p.u. Regarding Case 5, we observe active and reactive power transient oscillations with abnormally large amplitudes but the system comes back to a normal state in less than 500 ms.

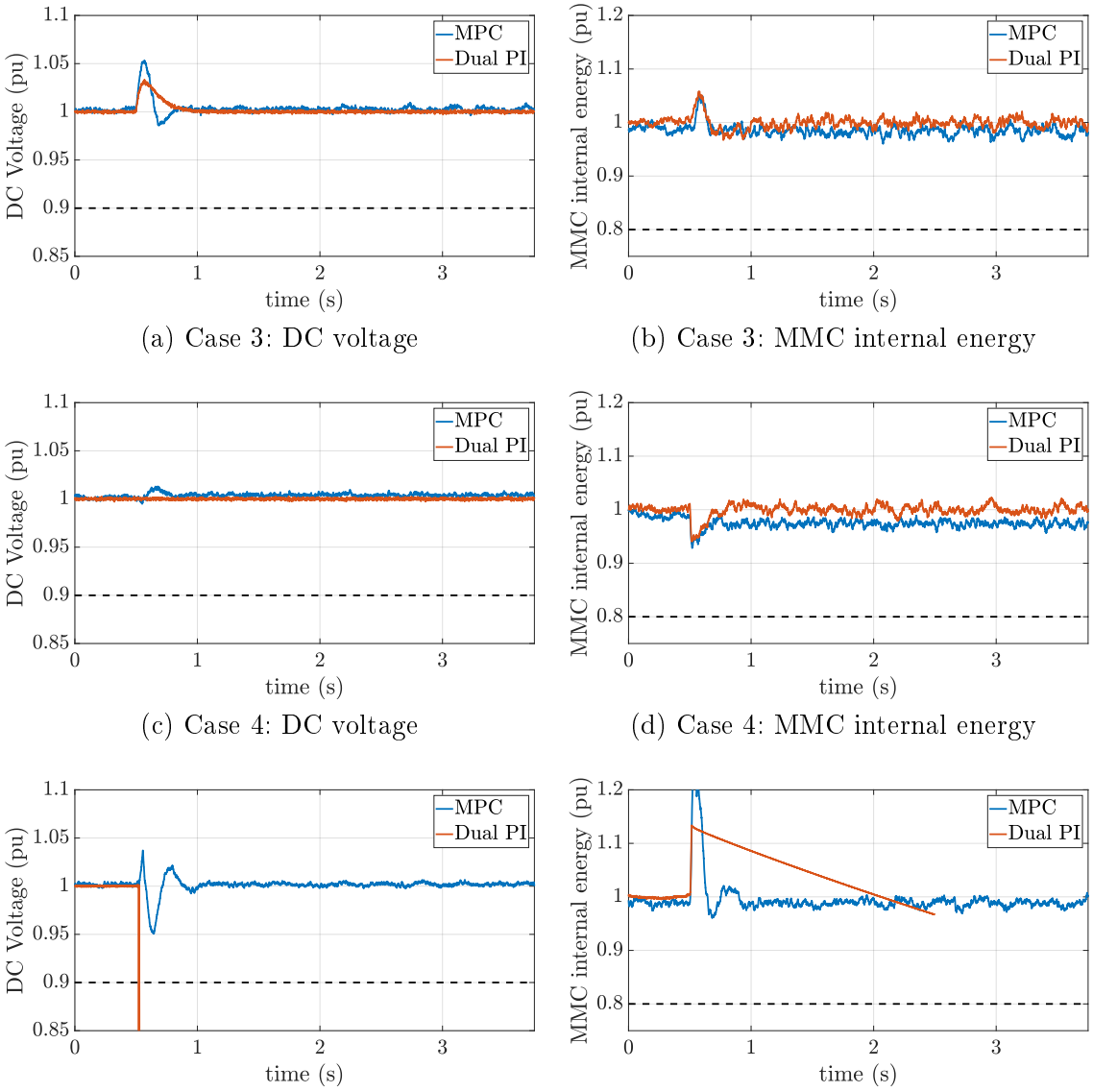

(a) Case 3: DC voltage

(b) Case 3: MMC internal energy

(c) Case 4: DC voltage

(d) Case 4: MMC internal energy

(e) Case 5: DC voltage

(f) Case 5: MMC internal energy

Figure 6.17: Comparison of the dual PI and MPC solutions in PHIL following DC and AC grid disturbances (Case 3 to Case 5).

6.6. Conclusions

In this chapter, we presented an experimental validation of an MMC control based on the implementation of a linear MPC in real time. The control was tested using an OP4510 from Opal-RT and applied to a real MMC mockup of 6 kVA operated in grid-forming mode. In order to have a linear MPC compatible with real-time constraints, we used the C-based μao-mpc solution to generate the C files compiled in the target. The control solution was compared to the state-of-the-art dual PI

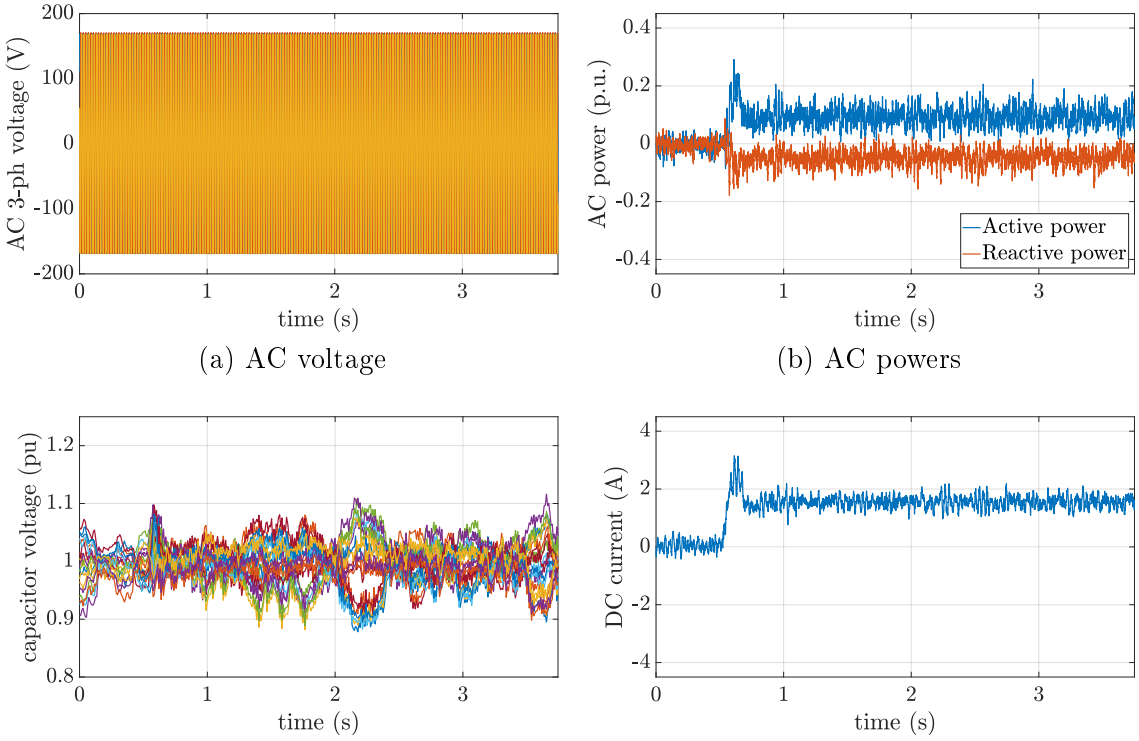

(a) AC voltage (b) AC powers

(c) capacitor voltages (d) DC current

Figure 6.18: PHIL mockup data: MPC and Case 3

control structure and showed similar tracking performances but a better disturbance rejection capability.

The main contributions of this chapter can be listed as follows:

- implementation of a recent grid-forming control [115,212] to operate the MMC as a voltage source in grid-connected mode;
- demonstration of the feasibility of the MPC layer to control a power converter operated in grid-forming in real time;
- use of an averaged model of the MMC, presented in Chapter 5, in the MPC algorithm to generate the optimal control inputs sent to a real mockup of an MMC with its complete set of controls.
- the experimental validation of the better performance of MPC regarding disturbance rejection than the state-of-the-art dual PI solution.

However, the MPC solution could still be enhanced by acting on the solver of the optimization, which must be embedded in the target as well, since the current solver shows some limits when we tried to enhance its accuracy. In future work, the following items could be investigated in order to strengthen the obtained results:

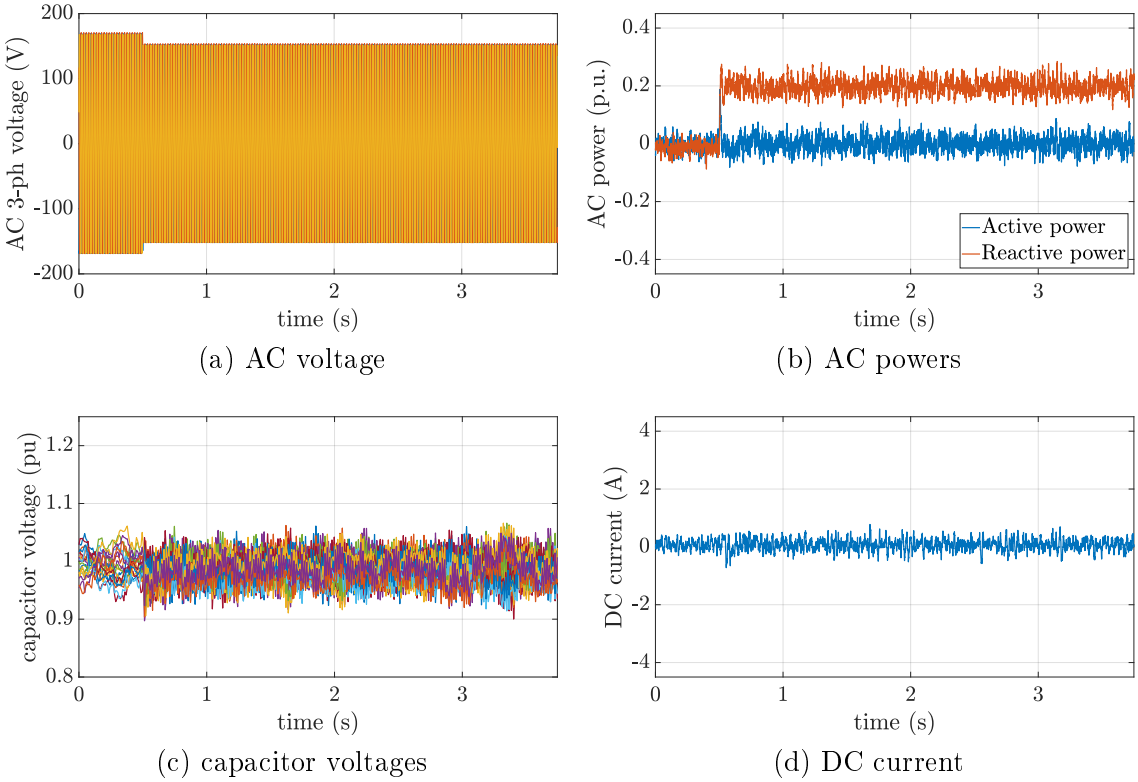

(a) AC voltage (b) AC powers

(c) capacitor voltages (d) DC current

Figure 6.19: PHIL mockup data: MPC and Case 4

- In its current form, the MPC only considers constant constraints, as detailed in (6.29). However, recent works suggested that the limits of the MMC internal energy depend on the system setpoints and the energy levels of each arm. These limits can be calculated using analytical expressions [223] and could be integrated in the MPC and would be an added value in the choice of MPC-based control versus classical PI solutions;
- In this chapter, the model of the DC grid and the MMC internal energy is based on averaged models. However, the dynamics of the MMC are more complex and a better knowledge of these dynamics could enhance the performances of the MPC. In consequence, it would be interesting to investigate the use of system identification techniques to identify an equivalent model of the MMC which will then be used by the MPC;
- As stated in Section 6.2.1, the AC and DC amplifiers of the mockup were operated as perfect sources in this setup. However, it is possible to emulate multi-machine AC grids [167] or multi-terminal DC grids [177] using more complex models. This requires additional work to interface the amplifiers with the real-time simulation software so that the simulation takes into account the actual measurements from the mockup and vice-versa. Nevertheless, this

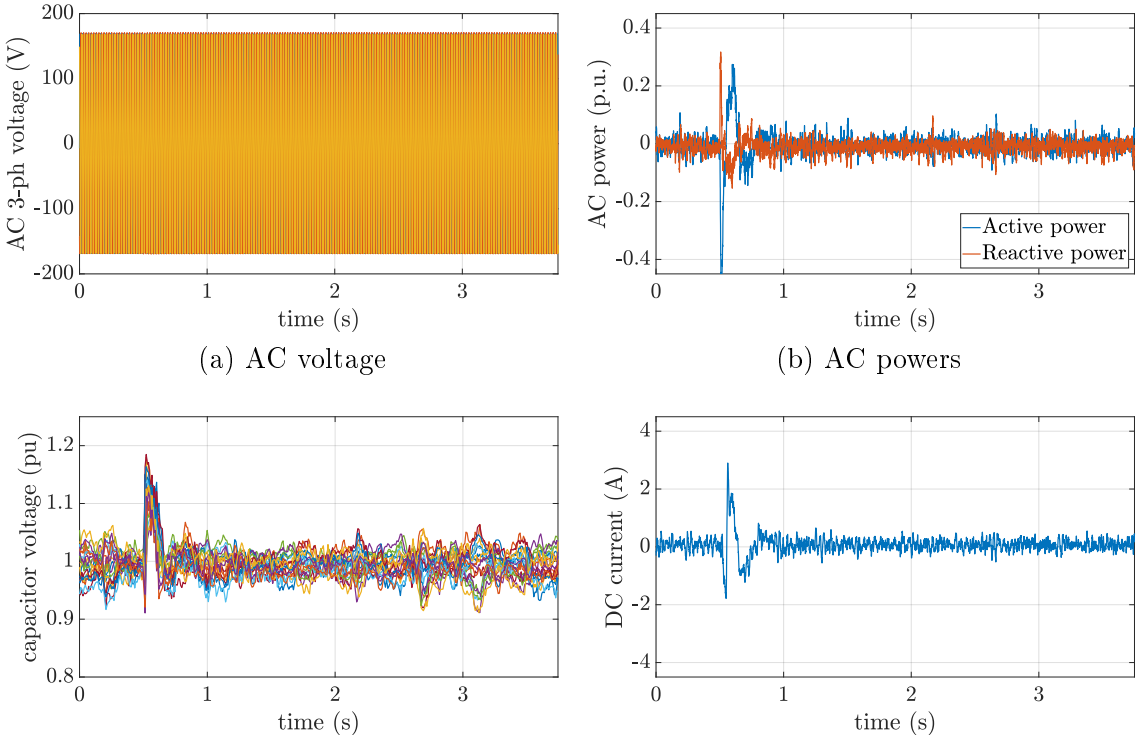

(a) AC voltage (b) AC powers

(c) capacitor voltages (d) DC current

Figure 6.20: PHIL mockup data: MPC and Case 5

would make it possible to study the impact of the proposed MMC control in even more realistic conditions;

- The MPC-based MMC control proposed in this PhD thesis was also quite suited for providing inertial support the AC grid, as shown in Chapter 5. However, since the current MMC mockup represents a standard MMC, it was not possible to analyze how its internal energy could support the AC grid frequency. In a long-term range, we could consider to apply this controller to an MMC with a Large Buffer Storage (LBS) that is designed for AC grid related ancillary services [224].

CHAPTER 7

Conclusions and perspectives

7.1. General conclusions

7.1.1. Conclusions per chapter

With the ongoing changes in the electricity production, transmission and distribution, power systems are expected to endure drastic changes in their operation and control. The increasing share of renewable energy worldwide drives towards PE-dominated grids where converters are expected to play a major role at the distribution and transmission levels. To ensure the stability and reliability of such grids, these PE interfaces must provide support functions to the system as synchronous generators do. These expectations also apply to HVDC systems and in particular MMCs which are expected to play a growing role in the operation of large power corridors and in the interconnection of offshore wind farms.

This thesis focused on the application of grid-forming concept to VSCs and in particular MMCs in the context of power systems with high penetration of renewables, which are low inertia and weak grid systems. The conclusions of each chapter of the thesis is recalled in the next paragraphs.

In Chapter 2, a compehensive overview of the recent control strategies to operate a VSC are presented. In particular, the so-called *grid-following* and *grid-forming* controls are compared in terms of their behavior from the converter and the grid perspectives. The definition of these two controls as well as their contributions to grid services from the literature are assessed and discussed in this chapter.

In Chapter 3, the main VSC control strategies, namely grid-following/grid-feeding, grid-supporting and grid-forming, are compared using an elementary benchmark that models a hybrid grid with a VSC, an SG and a load, interconnected by a variable AC transmission line. Using modal analysis tools, the maximum allowable penetration limit of power electronics is assessed in the different cases and shows the advantage of grid-forming control for introducing more power electronics in the grid. However, because of its SG-like behavior, some interactions between the generator's AVR and the grid-forming control are expected and should be taken care of.

In Chapter 4, the grid-forming control is applied to HVDC systems and more specifically to onshore MMCs in the case of offshore wind farm interconnection. After having highlighted the stability issues due to the interactions between the DC voltage and the grid-forming controls, we propose a methodology to determine the energy of the MMC submodules to support the AC grid inertia. The associated control, named *virtual rotor control*, is proposed, and its tuning and the application to multi-machine systems are discussed. While the compatibility of this contro with grid-forming controlled MMC and neighboring SGs is proved, the problems related to the inter-area oscillations and to the support of the DC grid voltage remain an open topic.

In Chapter 5, a Multi-Input Multi-Output (MIMO) approach is proposed to support the AC and DC grids of the MMC using an MPC solution to replace the DC voltage and the MMC internal energy control loops. The MPC is implemented using an averaged model of the MMC, a simplified model of the DC grid and an identified model of the AC grid. This control solution provides better disturbance rejection and a better handling of the MMC internal energy than the classical dual PI control structure. Also, its robustness regarding setpoint changes as well as parameter uncertainties is verified with different test cases. Nevertheless, the applicability of such advanced control techniques to detailed models of MMCs as well as its compatibility with real-life hardware systems still requires further investigation.

In Chapter 6, the linear MPC, as presented in Chapter 5, is applied to a physical mockup of an MMC. This experimental validation is performed using a Power Hardware-in-the-Loop (P-HIL) benchmark to prove the industrial feasibility of such concept. The MPC is implemented in C-code and coupled with the rest of the MMC grid-forming control implemented in Matlab/Simulink. All the control is compiled using Opal-RT software onto an OP4510 hardware system to control an MMC

mockup of 6kVA and 60 submodules connected to AC and DC power amplifiers. The proposed control shows similar tracking performances when compared to the dual PI structure but a better disturbance rejection. This confirms the interest of MPC-based techniques for MMC operation in the future.

7.1.2. Concluding remarks

To synthetize the main conclusions of this PhD thesis, the present work has proven the interest to have more grid-connected VSCs operated in grid-forming mode. Indeed, this grid-forming feature avoids weak grid problems and can even support islanding from the grid. However, the main function of a converter is to inject power to the grid and this control brings several problems such as: DC voltage mitigation, internal energy control, AC/DC interactions, etc. due to the relatively slow dynamics of the control and its poor power tracking. After having discussed the need of slowing down the DC-voltage controller to solve this problem, this PhD thesis investigated the application of grid-forming to MMCs and developed a methodology based on MPC to solve the problem. The application of MPC to the MMC-level control was demonstrated with a physical MMC mockup which makes a contribution towards applying this kind of advanced control solutions in industrial power electronics systems. In the case of the MPC proposed in this thesis, this control could be apply to real-life MMCs regardless of their converter control modes.

7.1.3. Scientific contributions

The scientific contributions of this dissertation can be summarized as follows:

- Chapter 2
  - Overview of the existing VSC control strategies to support the AC grid.
  - Comparative analysis of the behavior of the grid-following and grid-following VSC controls from the converter and the grid perspectives.
- Chapter 3
  - Development of an elementary benchmark to study the impacts of the power ratio (the ratio of the VSC rated power to the rating of the whole system), the electrical distance and the control mode in the stability limits of a system comprising a VSC and an SG.
  - Modal analysis showing the importance of grid-forming control to allow more power electronics to be integrated in the grid.

  - Validation of the conclusions using time-domain simulations in a multi-machine system.
- Chapter 4
  - Analysis of the impacts of the grid-forming control upon the control of the MMC internal energy and the DC voltage.
  - Proposition of a methodology with its associated control design to calculate the amount of energy from the MMC submodules to provide inertia-like response to the AC grid.
  - Validation of the method and control using time-domain simulations in a modified version of the Nordic 44 system that includes 80 SGs.
- Chapter 5
  - Proposition of a MIMO-based MPC to replace the MMC internal energy and DC voltage controllers.
  - Identification of the AC grid model from the MMC perspective using system identification methods.
  - Validation of the proposed MPC when compared to the classical dual PI control.
  - Analysis of the robustness of the proposed control in terms of setpoint changes and parameter uncertainties.
- Chapter 6
  - Practical implementation of grid-forming control using recent controls from the literature.
  - Implementation of the MPC in C to make it compatible with hardware systems.
  - Validation of the MPC proposed in Chapter 4 in P-HIL using a 6kVA mockup of an MMC and two AC and DC power amplifiers.

7.2. Perspectives

7.2.1. Integration of the DC source dynamics

In the first chapters of this work, the DC side was considered as an ideal voltage source. This is a well-known assumption to study the interactions between a VSC controlled in grid-forming and the AC grid but it cannot integrate all the constraints of future AC/DC grids, as shown in the later chapters of this thesis. In particular, in these chapters, the DC grid was modeled as a constant power source and a DC capacitance which takes into account the DC-voltage dynamics. However, it does

not integrate all the dynamics of a realistic HVDC grid and its associated sources and loads. Indeed, if the DC grid is powered by a renewable energy source [225], its response to AC grid disturbances would depend on the dynamics of wind [226, 227] and solar PV [228] systems, including the dynamics of the power source itself and their associated controls. Moreover, if the DC grid is powered by a storage system such as a lithium/ion battery [135] or supercapacitors [172], its response would depend on the state of the charge of this system as well. In the future, such constraints should in consequence also be taken into account in the control and simulation of power electronics converters.

7.2.2. Artificial Intelligence (AI) techniques for MPC

In Chapter 6, the solution of embedding an online optimal control in a real-time hardware system was studied by using µao-mpc code generation [214]. However, the computational limits of the CPU impose constraints on the solver number of iterations, causing potential convergence problems as well as small offsets in the results obtained with the mockup when compared to the simulation data. With the growing role of artificial intelligence (AI) based techniques in the domain of power electronics [229, 230], it would be possible in our case to use machine learning techniques to determine an offline optimal solution of the MPC optimization problem. This solution would be possible by compiling data from the simulation file and using regression techniques [231]. This approach could be much lighter in terms of online computational burden for the controller than the solution with the embedded solver in real time.

7.2.3. Transient stability analysis of MMCs

In Chapter 3, we performed a small-signal stability analysis of a hybrid system with a VSC and an SG. The conclusions of this analysis only stand for small disturbances and do not consider large ones, such as short circuits or generator loss for instance. In these cases, it is worth investigating the transient stability of the system. Contrary to SGs whose electrical angle is a physical variable linked to the rotor speed, the VSC synchronizing capability depends on the calculation of the electrical angle, which is given by a PLL or the power controller depending on the control mode. The VSC has a better capacity than SGs to remain synchronized with the grid because the angle is a digital figure that is not directly coupled to the physical conversion devices [232]. However, it is still possible to observe a Loss of Synchronism (LoS) in the case of large faults in grid-following as well as in grid-forming [25]. While there have been

some works on the transient stability enhancement of two-level VSCs [117], the transient stability of an MMC still needs to be assessed. In particular, the absence of LC filter makes the current limitation algorithm, necessary in order to control the transient states of the MMC, more challenging. There are some recent works in developing current limitation controls for MMCs [167, 233] but their role in the transient stability analysis of hybrid grids still needs to be assessed.

7.2.4. Coordinated control of multiple converters

In this PhD thesis, we focused on the converter control of a VSC in a hybrid grid but without considering the opportunity of coordinating these different PE-based interfaces at a system level. Indeed, with the high controllability of these devices and adequate communication tools, it is possible to coordinate the action of several converters with various and decoupled DC sources [87], or from a multi-terminal DC (MTDC) grid embedded in an AC grid [129] connected to a single synchronous AC grid. It is also possible to coordinate the support action of the different converters in the case of an MTDC interfacing several AC grids [177, 234] to provide a more adapted system-level response to the AC and DC grid disturbances. This aspect represents one of the main advantages of the PE-based sources compared to the SG-based systems and requires grid-level analysis of the contributions of the converters.

Bibliography

[1] European Routes of Industrial Heritage (ERIH), "Industrial History of European Countries," 2021. [Online]. Available: https://www.erih.net/how-it-started/industrial-history-of-european-countries

[2] S. Akkari, "Control of a multi-terminal HVDC (MTDC) system and study of the interactions between the MTDC and the AC grids." PhD Dissertation, Université Paris Saclay, Oct. 2016.

[3] IPCC, "Global Warming of 1.5°C. An IPCC Special Report on the impacts of global warming of 1.5°C above pre-industrial levels and related global greenhouse gas emission pathways, in the context of strengthening the global response to the threat of climate change, sustainable development, and efforts to eradicate poverty," *Summary for Policymakers*, 2018.

[4] H. Fountain, "Climate Change Affected Australia's Wildfires, Scientists Confirm," *NY Times*, Mar. 2020. [Online]. Available: https://www.nytimes.com/2020/03/04/climate/australia-wildfires-climate-change.html

[5] The Economist explains, "Why is Texas experiencing a winter freeze?" *the Economist*, Feb. 2021. [Online]. Available: https://www.economist.com/the-economist-explains/2021/02/17/why-is-texas-experiencing-a-winter-freeze

[6] J. Cohen, X. Zhang, J. Francis, T. Jung, R. Kwok, J. Overland, T. Ballinger, U. Bhatt, H. Chen, D. Coumou *et al.*, "Divergent consensuses on arctic amplification influence on midlatitude severe winter weather," *Nature Climate Change*, vol. 10, no. 1, pp. 20–29, 2020.

[7] F. Dottori, W. Szewczyk, J.-C. Ciscar, F. Zhao, L. Alfieri, Y. Hirabayashi, A. Bianchi, I. Mongelli, K. Frieler, R. A. Betts *et al.*, "Increased human and economic losses from river flooding with anthropogenic warming," *Nature Climate Change*, vol. 8, no. 9, pp. 781–786, 2018.

[8] D. Tong, Q. Zhang, Y. Zheng, K. Caldeira, C. Shearer, C. Hong, Y. Qin, and S. Davis, "Committed emissions from existing energy infrastructure jeopardize 1.5 °C climate target," *Nature*, vol. 572, pp. 373–377, Aug. 2019.

[9] United Nations, "Adoption of the Paris Agreement," 2015. [Online]. Available: https://unfccc.int/process-and-meetings/the-paris-agreement/the-paris-agreement

[10] Y. Kanazawa and M. Kamitani, "Rare earth minerals and resources in the world," *Journal of Alloys and Compounds*, p. 5, 2006.

[11] G. S. Seck, E. Hache, C. Bonnet, M. Simoen, and S. Carcanague, "Copper at the crossroads_ Assessment of the interactions between low-carbon energy transition and supply limitations," *Resources, Conservation & Recycling*, p. 21, Jul. 2020.

[12] Victoria State Government, "The Victorian Big Battery," Apr. 2021. [Online]. Available: https://www.energy.vic.gov.au/renewable-energy/the-victorian-big-battery

[13] U.S. Geological Survey, "Lithium Data Sheet," *Mineral Commodity Summaries 2020*, 2020.

[14] T. Riofrancos, "The rush to go electric comes with a hidden cost: destructive lithium mining," *The Guardian*, Jun. 2021. [Online]. Available: https://www.theguardian.com/commentisfree/2021/jun/14/electric-cost-lithium-mining-decarbonasation-salt-flats-chile

[15] B. Faessler, "Stationary, Second Use Battery Energy Storage Systems and Their Applications: A Research Review," *Energies*, vol. 14, no. 8, Apr. 2021.

[16] J. Ambrose, "Farmers swap crops for energy as east of england solar farm proposals double," *The Guardian*, Jun. 2021. [Online]. Available: https://www.theguardian.com/business/2021/jun/28/solar-farm-proposals-for-east-of-england-more-than-double

[17] European Commission, "EU Reference Scenario 2016 - Energy, transport and GHG emissions Trends to 2050," institutional website, Jul. 2016. [Online]. Available: https://ec.europa.eu/energy

[18] I. Oleinikova and E. Hillberg, "micro vs mega: trends influencing the development of the power system," *ISGAN*, 2020.

[19] B. A. Martinez-Trevino, A. E. Aroudi, A. Cid-Pastor, G. Garcia, and L. Martinez-Salamero, "Synthesis of Constant Power Loads Using Switching Converters Under Sliding-Mode Control," *IEEE Transactions on Circuits and Systems I: Regular Papers*, vol. 68, no. 1, pp. 524–535, Jan. 2021.

[20] A. Nishioka, F. Alvarez, and T. Omori, "Global rise of hvdc and its background," *Hitachi ABB HVDC Technologies Global Innovation Report*, 2020.

[21] D. Obradovic, M. Dijokas, A. Tosatto, T. Van Cutsem, R. Eriksson, and M. Ghandhari, "Assessment of HVDC Frequency Control Methods in the Nordic Test System," in *2020 CIGRE*. Paris, France: CIGRE, 2020.

[22] GE Grid Solutions, "Flexible AC Transmission Systems (FACTS)," 2021. [Online]. Available: https://www.gegridsolutions.com/facts.htm

[23] J. Rocabert, A. Luna, F. Blaabjerg, and P. Rodríguez, "Control of power converters in AC microgrids," *IEEE Transactions on Power Electronics*, vol. 27, no. 11, pp. 4734–4749, Nov. 2012.

[24] MIGRATE, "Deliverable 1.1: Current and arising issues caused by increasing power electronics penetration," May 2017.

[25] M. G. Taul, X. Wang, P. Davari, and F. Blaabjerg, "An Overview of Assessment Methods for Synchronization Stability of Grid-Connected Converters Under Severe Symmetrical Grid Faults," *IEEE Transactions on Power Electronics*, vol. 34, no. 10, pp. 9655–9670, Oct. 2019.

[26] R. Mourouvin, J. C. Gonzalez-Torres, J. Dai, A. Benchaib, D. Georges, and S. Bacha, "Understanding the role of VSC control strategies in the limits of power electronics integration in AC grids using modal analysis," *Electric Power Systems Research*, p. 106930, Nov. 2020.

[27] R. Mourouvin, J. Dai, S. Bacha, D. Georges, and A. Benchaib, "An Overview on the Recent Advances of the Voltage Source Converter Control Modes in Terms of their Roles in Transmission Grid Ancillary Services," *preprint*, 2021.

[28] R. Mourouvin, L. Filliot, A. Ghyselinck, J. Dai, S. Bacha, D. Georges, and A. Benchaib, "An Online Hierarchical MPC applied to an MMC in Grid-Forming Mode: Practical Implementation and Hardware-in-the-Loop Validation," *preprint*.

[29] R. Mourouvin, K. Shinoda, J. Dai, A. Benchaib, S. Bacha, and D. Georges, "AC/DC Dynamic Interactions of MMC-HVDC in Grid-Forming for Wind-Farm Integration in AC Systems," in *2020 22nd European Conference on Power Electronics and Applications (EPE'20 ECCE Europe)*. Lyon, France: IEEE, Sep. 2020.

[30] R. Mourouvin, J. Dai, S. Boersma, S. Bacha, D. Georges, and A. Benchaib, "Model Predictive Control for AC/DC Energy Management of a Modular Multilevel Converter Operated in Grid-Forming Mode," in *2021 European Control Conference (ECC)*, Rotterdam, Netherlands, Jun. 2021, p. 6.

[31] R. Mourouvin, J. Dai, S. Bacha, A. Benchaib, and D. Georges, "Energy Requirements of Modular Multilevel Converter Submodules and High-level Control Design for Synthetic Inertia Function," in *2021 23rd European Conference on Power Electronics and Applications (EPE'21 ECCE Europe)*. Ghent, Belgium: IEEE, Sep. 2021.

[32] J. C. Gonzalez-Torres, R. Mourouvin, K. Shinoda, A. Zama, and A. Benchaib, "A Simplified Approach to Model Grid-Forming Controlled MMCs in Power System Stability Studies," in *2021 IEEE PES Innovative Smart Grid Technologies Europe (ISGT-Europe)*. Espoo, Finland: IEEE, Oct. 2021.

[33] J. Glasdam, J. Hjerrild, L. H. Kocewiak, and C. L. Bak, "Review on multi-level voltage source converter based HVDC technologies for grid connection of large offshore wind farms," in *2012 IEEE International Conference on Power System Technology (POWERCON)*. IEEE, Oct. 2012.

[34] F. Blaabjerg, Z. Chen, and S. Kjaer, "Power Electronics as Efficient Interface in Dispersed Power Generation Systems," *IEEE Transactions on Power Electronics*, vol. 19, no. 5, pp. 1184–1194, Sep. 2004.

[35] R. Venkatesh, P. Sharma, H. Siguerdidjane, D. Kumar, and H. D. Mathur, "Frequency Excursion Mitigation in a Multi-source Islanded Energy System Using Meta-Heuristic Optimization Strategies," in *2020 IEEE 8th International Conference on Smart Energy Grid Engineering (SEGE)*. Oshawa, ON, Canada: IEEE, Aug. 2020, pp. 148–152.

[36] ENTSO-E, "High Penetration of Power Electronic Interfaced Power Sources and the Potential Contribution of Grid Forming Converters," ENTSO-E, Brussels, BE, Technical Report, 2020.

[37] B. Kroposki, "Can smarter solar inverters save the grid?" *IEEE Spectrum*, Oct. 2016. [Online]. Available: https://spectrum.ieee.org/energy/renewables/can-smarter-solar-inverters-save-the-grid

[38] J. Ambrose, "Solar farms can keep UK's lights on even at night," *The Guardian*, Nov. 2019. [Online]. Available: https://www.theguardian.com/environment/2019/nov/24/solar-farms-keep-uk-lights-on-at-night

[39] Y. G. Rebours, D. S. Kirschen, M. Trotignon, and S. Rossignol, "A survey of frequency and voltage control ancillary services—part i: Technical features," *IEEE Transactions on Power Systems*, vol. 22, no. 1, pp. 350–357, Feb. 2007.

[40] ——, "A survey of frequency and voltage control ancillary services—part II: Economic features," *IEEE Transactions on Power Systems*, vol. 22, no. 1, pp. 358–366, Feb. 2007.

[41] P. Pinson, "Ancillary services and regulation markets," in *Lecture at DTU*. Technical University of Denmark - Center for Electric Power and Energy: DTU, Feb. 2018.

[42] R. Ramachandran, S. Poullain, A. Benchaib, S. Bacha, and B. Francois, "AC grid forming by coordinated control of offshore wind farm connected to diode rectifier based HVDC link - review and assessment of solutions," in *2018 20th European Conference on Power Electronics and Applications (EPE'18 ECCE Europe)*. IEEE, Sep. 2018.

[43] M. Yu, A. Dysko, C. D. Booth, A. J. Roscoe, and J. Zhu, "A review of control methods for providing frequency response in VSC-HVDC transmission systems," in *2014 49th International Universities Power Engineering Conference (UPEC)*. IEEE, Sep. 2014.

[44] B. Luscan, S. Bacha, A. Benchaib, A. Bertinato, L. Chedot, J. Gonzalez-Torres, S. Poullain, M. Romero-Rodriguez, and K. Shinoda, "A vision of HVDC key role towards fault-tolerant and stable AC/DC grids," *IEEE Journal of Emerging and Selected Topics in Power Electronics*, 2020.

[45] IEEE and CIGRE, "Definition and Classification of Power System Stability IEEE/CIGRE Joint Task Force on Stability Terms and Definitions," *IEEE Transactions on Power Systems*, vol. 19, no. 3, pp. 1387–1401, Aug. 2004.

[46] Power System Dynamic Performance Committee Task Force on Stability definitions and characterization of dynamic behavior in systems with high

penetration of power electronic interfaced technologies, "Stability definitions and characterization of dynamic behavior in systems with high penetration of power electronic interfaced technologies," IEEE Power & Energy Society, Technical Report 77, Apr. 2020.

[47] Q. Peng, Q. Jiang, Y. Yang, T. Liu, H. Wang, and F. Blaabjerg, "On the stability of power electronics-dominated systems: Challenges and potential solutions," *IEEE Transactions on Industry Applications*, vol. 55, no. 6, pp. 7657–7670, Nov. 2019.

[48] A. Tayyebi, D. Gross, A. Anta, F. Kupzog, and F. Dorfler, "Frequency Stability of Synchronous Machines and Grid-Forming Power Converters," *IEEE Journal of Emerging and Selected Topics in Power Electronics*, vol. 8, no. 2, pp. 1004–1018, Jun. 2020.

[49] A. Crivellaro, A. Tayyebi, C. Gavriluta, D. Gross, A. Anta, F. Kupzog, and F. Dorfler, "Beyond low-inertia systems: Massive integration of grid-forming power converters in transmission grids," in *2020 IEEE Power & Energy Society General Meeting (PESGM)*. Montreal, QC, Canada: IEEE, Aug. 2020.

[50] P. Unruh, M. Nuschke, P. Strauß, and F. Welck, "Overview on Grid-Forming Inverter Control Methods," *Energies*, vol. 13, no. 10, p. 2589, May 2020.

[51] K. M. Cheema, "A comprehensive review of virtual synchronous generator," p. 10, 2020.

[52] B. Hartmann, I. Vokony, and I. Táczi, "Effects of decreasing synchronous inertia on power system dynamics—overview of recent experiences and marketisation of services," *International Transactions on Electrical Energy Systems*, vol. 29, no. 12, Dec. 2019.

[53] X. Zhao, L. Chang, R. Shao, and K. Spence, "Power system support functions provided by smart inverters—a review," *CPSS Transactions on Power Electronics and Applications*, vol. 3, no. 1, pp. 25–35, Mar. 2018.

[54] J. Fang, H. Li, Y. Tang, and F. Blaabjerg, "On the Inertia of Future More-Electronics Power Systems," *IEEE Journal of Emerging and Selected Topics in Power Electronics*, vol. 7, no. 4, pp. 2130–2146, Dec. 2019.

[55] J. Jia, G. Yang, and A. H. Nielsen, "A review on grid-connected converter control for short-circuit power provision under grid unbalanced faults," *IEEE Transactions on Power Delivery*, vol. 33, no. 2, pp. 649–661, Apr. 2018.

[56] Y. Han, H. Li, P. Shen, E. A. A. Coelho, and J. M. Guerrero, "Review of active and reactive power sharing strategies in hierarchical controlled microgrids," *IEEE Transactions on Power Electronics*, vol. 32, no. 3, pp. 2427–2451, Mar. 2017.

[57] T. Jouini, U. Markovic, and D. Groß, "New options for existing system services and needs for new system services," p. 105, Dec. 2018.

[58] M. M. Siraj Khan, Y. Lin, B. Johnson, M. Sinha, and S. Dhople, "Stability Assessment of a System Comprising a Single Machine and a Virtual Oscillator Controlled Inverter with Scalable Ratings," in *IECON 2018 - 44th Annual Conference of the IEEE Industrial Electronics Society*. D.C., DC, USA: IEEE, Oct. 2018, pp. 4057–4062.

[59] U. Markovic, O. Stanojev, E. Vrettos, P. Aristidou, and G. Hug, "Understanding stability of low-inertia systems," *arXiv*, 2019.

[60] P. Kundur, *Power System Stability and Control*, Electric Power Research Institute ed., ser. 1. McGraw-Hill, 1994.

[61] X.-F. Wang, Y.-H. Song, and M. Irving, *Modern Power Systems Analysis*. Springer, 2008.

[62] K. L. Anaya and M. G. Pollitt, "Reactive Power Management and Procurement Mechanisms: Lessons for the Power Potential Project," National Grid ESO, Technical Report, 2018.

[63] Elia, "Overview of ancillary services for the power grid," Belgian High Voltage Grid Operator, Brussels, BE, Review report, Jan. 2008.

[64] J. Machowski, J. W. Bialek, and J. R. Bumby, *Power System Dynamics*, wiley ed., Chichesgter, West Sussex, UK, 2008.

[65] N. Xu, C. Yu, and F. Wen, "Valuation of reactive power support services based on sensitivity and risk analysis," *Electric Power Systems Research*, vol. 77, no. 5-6, pp. 646–651, Apr. 2007. [Online]. Available: https://linkinghub.elsevier.com/retrieve/pii/S0378779606001350

[66] National Grid, "2016 System Operability Framework," National Grid ESO, Warwick, UK, SOF, 2016.

[67] NERC, "Short-circuit modeling and system strength," Feb. 2018.

[68] Joint Working Group C4/C6.35, *Modelling of inverter-based Generation For Power System Dynamic Studies*. CIGRE/CIRED, May 2018.

[69] C. Liu, R. Yokoyama, K. Koyanagi, and K. Y. Lee, "PSS design for damping of inter-area power oscillations by coherency-based equivalent model," *International Journal of Electrical Power & Energy Systems*, vol. 26, no. 7, pp. 535–544, Sep. 2004.

[70] ENTSO-E, "Oscillation Event 03.12.2017," ENTSO-E, Brussels, BE, Tech. Rep., Mar. 2018.

[71] F. Milano, F. Dörfler, G. Hug, D. J. Hill, and G. Verbic, "Foundations and challenges of low-inertia systems (invited paper)," in *Power Systems Computation Conference (PSCC)*, Jul. 2018.

[72] J. Li, C. Liu, P. Zhang, Y. Wang, and J. Rong, "Difference between grid connections of large-scale wind power and conventional synchronous generation," *Global Energy Interconnection*, vol. 3, no. 5, pp. 486–493, Oct. 2020.

[73] M.-S. Debry, G. Denis, T. Prevost, F. Xavier, and A. Menze, "Maximizing the penetration of inverter-based generation on large transmission systems: the MIGRATE project," in *6th Solar Integration Workshop*, 2016.

[74] A. Zama, A. Benchaib, S. Bacha, D. Frey, S. Silvant, and D. Georges, "Linear feedback Dead-Beat Control for Modular Multilevel Converters: Validation under Faults Grid Operation mode," *IEEE Transactions on Industrial Electronics*, 2020.

[75] Y. Lin, B. Johnson, V. Gevorgian, V. Purba, and S. Dhople, "Stability assessment of a system comprising a single machine and inverter with scalable ratings," in *2017 North American Power Symposium (NAPS)*. Morgantown, WV: IEEE, Sep. 2017, pp. 1–6.

[76] U. Markovic, J. Vorwerk, P. Aristidou, and G. Hug, "Stability Analysis of Converter Control Modes in Low-Inertia Power Systems," in *2018 IEEE PES Innovative Smart Grid Technologies Conference Europe (ISGT-Europe)*. Sarajevo, Bosnia and Herzegovina: IEEE, Oct. 2018.

[77] E. Sanchez-Sanchez, E. Prieto-Araujo, and O. Gomis-Bellmunt, "The role of the internal energy in MMCs operating in grid-forming mode," *IEEE Journal of Emerging and Selected Topics in Power Electronics*, 2020.

[78] G. Denis, "From grid-following to grid-forming: The new strategy to build 100 % power-electronics interfaced transmission system with enhanced transient behavior," PhD Dissertation, Ecole Centrale Lille, Nov. 2017.

[79] L. Zhang, L. Harnefors, and H.-P. Nee, "Power-synchronization control of grid-connected voltage-source converters," *IEEE Transactions on Power Systems*, vol. 25, no. 2, pp. 809–820, May 2010.

[80] J. W. Simpson-Porco, F. Dörfler, and F. Bullo, "Synchronization and power sharing for droop-controlled inverters in islanded microgrids," *Automatica*, vol. 49, no. 9, pp. 2603–2611, Sep. 2013.

[81] T. Qoria, F. Gruson, F. Colas, G. Denis, T. Prevost, and X. Guillaud, "Inertia effect and load sharing capability of grid forming converters connected to a transmission grid," in *15th IET International Conference on AC and DC Power Transmission (ACDC 2019)*. Institution of Engineering and Technology, 2019.

[82] Q.-C. Zhong and G. Weiss, "Synchronverters: Inverters that mimic synchronous generators," *IEEE Transactions on Industrial Electronics*, vol. 58, no. 4, pp. 1259–1267, Apr. 2011.

[83] S. D'Arco, J. A. Suul, and O. B. Fosso, "Control system tuning and stability analysis of virtual synchronous machines," in *2013 IEEE Energy Conversion Congress and Exposition*. IEEE, Sep. 2013, pp. 2664–2671.

[84] M. Guan, W. Pan, J. Zhang, Q. Hao, J. Cheng, and X. Zheng, "Synchronous generator emulation control strategy for voltage source converter (VSC) stations," *IEEE Transactions on Power Systems*, vol. 30, no. 6, pp. 3093–3101, Nov. 2015.

[85] Q. Cossart, F. Colas, and X. Kestelyn, "Model reduction of converters for the analysis of 100% power electronics transmission systems," in *2018 IEEE International Conference on Industrial Technology (ICIT)*. IEEE, Feb. 2018, pp. 1254–1259.

[86] J. Roldan-Perez, A. Gonzalez-Cajigas, A. Rodriguez-Cabero, M. Prodanovic, and P. Zumel, "Design and analysis of a current-controlled virtual synchronous machine for weak grids," in *2019 IEEE Applied Power Electronics Conference and Exposition (APEC)*. IEEE, Mar. 2019, pp. 1459–1465.

[87] U. Markovic, Z. Chu, P. Aristidou, and G. Hug-Glanzmann, "LQR-based adaptive virtual synchronous machine for power systems with high inverter penetration," *IEEE Transactions on Sustainable Energy*, vol. 10, no. 3, pp. 1501–1512, 2019.

[88] D. Groß, M. Colombino, J.-S. Brouillon, and F. Dörfler, "The effect of transmission-line dynamics on grid-forming dispatchable virtual oscillator control," *IEEE Transactions on Control of Network Systems*, vol. 6, no. 3, pp. 1148–1160, Sep. 2018.

[89] C. Arghir, T. Jouini, and F. Dörfler, "Grid-forming control for power converters based on matching of synchronous machines," *Automatica*, vol. 95, pp. 273–282, Sep. 2018.

[90] B. Johnson, M. Rodriguez, M. Sinha, and S. Dhople, "Comparison of virtual oscillator and droop control," in *2017 IEEE 18th Workshop on Control and Modeling for Power Electronics (COMPEL)*. Stanford, CA, USA: IEEE, Jul. 2017, pp. 1–6.

[91] R. Ofir, U. Markovic, P. Aristidou, and G. Hug, "Droop vs. virtual inertia: Comparison from the perspective of converter operation mode," in *2018 IEEE International Energy Conference (ENERGYCON)*. IEEE, Jun. 2018, pp. 1–6.

[92] A. Tayyebi, D. Groß, A. Anta, F. Kupzog, and F. Dörfler, "Interactions of grid-forming power converters and synchronous machines – a comparative study," *arXiv*, 2019.

[93] H. Yu, M. A. Awal, H. Tu, I. Husain, and S. Lukic, "Comparative Transient Stability Assessment of Droop and Dispatchable Virtual Oscillator Controlled Grid-Connected Inverters," *IEEE Transactions on Power Electronics*, vol. 36, no. 2, pp. 2119–2130, Feb. 2021.

[94] E. Rokrok, T. Qoria, A. Bruyere, B. Francois, and X. Guillaud, "Classification and dynamic assessment of droop-based grid-forming control schemes: Application in HVDC systems," *Electric Power Systems Research*, vol. 189, Dec. 2020.

[95] M. Molinas, J. Suul, S. D'Arco, and P. Rodriguez, "Extended stability range of weak grids with voltage source converters through impedance-conditioned grid synchronization," in *11th IET International Conference on AC and DC Power Transmission*. Institution of Engineering and Technology, 2015.

[96] S. Akkari, M. Petit, J. Dai, and X. Guillaud, "Interaction between the voltage-droop and the frequency-droop control for multi-terminal HVDC systems," in *11th IET International Conference on AC and DC Power Transmission*. IET, 2015.

[97] C. Collados-Rodriguez, M. Cheah-Mane, E. Prieto-Araujo, and O. Gomis-Bellmunt, "Stability analysis of systems with high VSC penetration: Where is the limit?" *IEEE Transactions on Power Delivery*, Dec. 2019.

[98] J. Fradley, R. Preece, and M. Barnes, "Adaptive fast frequency response for power electronic connected energy sources," in *2019 IEEE Milan PowerTech*. IEEE, Jun. 2019.

[99] G. S. Misyris, J. Mermet-Guyennet, S. Chatzivasileiadis, and T. Weckesser, "Grid Supporting VSCs in Power Systems with Varying Inertia and Short-Circuit Capacity," in *2019 IEEE PES Power Tech*. Milano, Italy: IEEE, 2019.

[100] D. Duckwitz and B. Fischer, "Modeling and design of df/dt-based inertia control for power converters," *IEEE Journal of Emerging and Selected Topics in Power Electronics*, vol. 5, no. 4, pp. 1553–1564, Dec. 2017.

[101] B. K. Poolla, D. Gros, and F. Dorfler, "Placement and implementation of grid-forming and grid-following virtual inertia and fast frequency response," *IEEE Transactions on Power Systems*, vol. 34, no. 4, pp. 3035–3046, Jul. 2019.

[102] C. Rahmann and A. Castillo, "Fast frequency response capability of photovoltaic power plants: The necessity of new grid requirements and definitions," *Energies*, vol. 7, no. 10, pp. 6306–6322, Sep. 2014.

[103] Q. Hong, M. Nedd, S. Norris, I. Abdulhadi, M. Karimi, V. Terzija, B. Marshall, K. Bell, and C. Booth, "Fast frequency response for effective frequency control in power systems with low inertia," *The Journal of Engineering*, no. 16, pp. 1696–1702, Mar. 2019.

[104] National Grid ESO, "Enhanced frequency response FAQs," Mar. 2016.

[105] Y. Zuo, M. Paolone, and F. Sossan, "Effect of voltage source converters with electrochemical storage systems on dynamics of reduced-inertia bulk power grids," in *Power Systems Computation Conference (PSCC)*. IEEE, Jun. 2020.

[106] E. Rokrok, T. Qoria, A. Bruyere, B. Francois, and X. Guillaud, "Effect of using PLL-based grid-forming control on active power dynamics under various SCR," in *IECON 2019 - 45th Annual Conference of the IEEE Industrial Electronics Society*. IEEE, Oct. 2019, pp. 4799–4804.

[107] A. Narula, M. Bongiorno, M. Beza, J. R. Svensson, X. Guillaud, and L. Harnefors, "Impact of steady-state grid-frequency deviations on the performance of grid-forming converter control strategies," in *2020 22nd European Conference on Power Electronics and Applications (EPE'20 ECCE Europe)*. Lyon, France: IEEE, Sep. 2020.

[108] ENTSO-E, "Static Synchronous Compensation (STATCOM)." [Online]. Available: https://www.entsoe.eu/Technopedia/techsheets/static-synchronous-compensation-statcom

[109] S. Kovacevic, D. Jovcic, S. S. Aphale, P. Rault, and O. Despouys, "Analysis of potential low frequency resonance between a 1GW MMC HVDC and a nearby nuclear generator," *Electric Power Systems Research*, vol. 187, p. 106491, Oct. 2020.

[110] J. Z. Zhou, H. Ding, S. Fan, Y. Zhang, and A. M. Gole, "Impact of Short-Circuit Ratio and Phase-Locked-Loop Parameters on the Small-Signal Behavior of a VSC-HVDC Converter," *IEEE Transactions on Power Delivery*, vol. 29, no. 5, pp. 2287–2296, Oct. 2014.

[111] J. Matevosyan, "Experience in Texas with declining inertia," in *IEA - Technical secure integration of large shares of converter based power sources*. Paris, France: ERCOT, Mar. 2020.

[112] E. Marrazi, G. Yang, and P. Weinreich-Jensen, "Allocation of synchronous condensers for restoration of system short-circuit power," *Journal of Modern Power Systems and Clean Energy*, vol. 6, no. 1, pp. 17–26, Jan. 2018.

[113] Phi-Long Nguyen, Q.-C. Zhong, F. Blaabjerg, and J. M. Guerrero, "Synchronverter-based operation of STATCOM to mimic synchronous condensers," in *2012 7th IEEE Conference on Industrial Electronics and Applications (ICIEA)*. IEEE, Jul. 2012, pp. 942–947.

[114] A. A. A. Radwan and Y. A.-R. I. Mohamed, "Improved vector control strategy for current-source converters connected to very weak grids," *IEEE Transactions on Power Systems*, vol. 31, no. 4, pp. 3238–3248, Jul. 2016.

[115] L. Harnefors, F. M. M. Rahman, M. Hinkkanen, and M. Routimo, "Reference-feedforward power-synchronization control," *IEEE Transactions on Power Electronics*, 2020.

[116] L. Díez-Maroto, L. Rouco, and F. Fernandez-Bernal, "Fault ride through capability of round rotor synchronous generators: Review, analysis and discussion of European grid code requirements," *Electric Power Systems Research*, p. 10, 2016.

[117] X. Wang, M. G. Taul, H. Wu, Y. Liao, F. Blaabjerg, and L. Harnefors, "Grid-Synchronization Stability of Converter-Based Resources An Overview," *IEEE Open Journal of Industry Applications*, 2020.

[118] J. Keller and B. Kroposki, *Understanding Fault Characteristics of Inverter-Based Distributed Energy Resources*, nrel ed., Jan. 2010.

[119] J. Jia, G. Yang, A. H. Nielsen, E. Muljadi, P. Weinreich-Jensen, and V. Gevorgian, "Synchronous condenser allocation for improving system short circuit ratio," in *2018 5th International Conference on Electric Power and Energy Conversion Systems (EPECS)*. IEEE, Apr. 2018, pp. 1–5.

[120] G. Denis, T. Prevost, M.-S. Debry, F. Xavier, X. Guillaud, and A. Menze, "The Migrate project: the challenges of operating a transmission grid with only inverter-based generation. A grid-forming control improvement with transient current-limiting control," *IET Renewable Power Generation*, vol. 12, no. 5, pp. 523–529, Apr. 2018.

[121] T. Qoria, F. Gruson, F. Colas, G. Denis, T. Prevost, and X. Guillaud, "Critical clearing time determination and enhancement of grid-forming converters embedding virtual impedance as current limitation algorithm," *IEEE Journal of Emerging and Selected Topics in Power Electronics*, 2019.

[122] H. Biellmann, M. Buquet, P. Chay, A. Schwery, V. Costan, J. Drommi, and G. Prime, "The benefits of implementing Synchronous Compensators in grids with high penetration of Renewables," in *2020 CIGRE Session*. Paris: CIGRE, 2020.

[123] M. Paolone, A. Monti, T. Gaunt, T. Van Cutsem, X. Guillaud, V. Vittal, M. Liserre, C. Vournas, and S. Meliopoulos, "Fundamentals of Power Systems Modelling in the Presence of Converter-Interfaced Generation," in *2020 Power*

Systems Computation Conference (PSCC). Porto, Portugal: IEEE, 2020, p. 35.

[124] R. Eriksson, "Coordinated control of multiterminal DC grid power injections for improved rotor-angle stability based on lyapunov theory," *IEEE Transactions on Power Delivery*, vol. 29, no. 4, pp. 1789–1797, Aug. 2014.

[125] J. Renedo, A. Garcia-Cerrada, and L. Rouco, "Active power control strategies for transient stability enhancement of AC/DC grids with VSC-HVDC multiterminal systems," *IEEE Transactions on Power Systems*, vol. 31, no. 6, pp. 4595–4604, Nov. 2016.

[126] O. Kotb, M. Ghandhari, J. Renedo, L. Rouco, and R. Eriksson, "On the design and placement of a supplementary damping controller in an embedded VSC-MTDC network," in *2017 IEEE PES Innovative Smart Grid Technologies Conference Europe (ISGT-Europe)*. IEEE, Sep. 2017.

[127] J. C. Gonzalez-Torres, G. Damm, V. Costan, A. Benchaib, and F. Lamnabhi-Lagarrigue, "Transient stability of power systems with embedded VSC-HVDC links: stability margins analysis and control," *IET Generation, Transmission & Distribution*, vol. 14, no. 17, pp. 3377–3388, Sep. 2020.

[128] J. Renedo, L. Rouco, A. García-Cerrada, and L. Sigrist, "A communication-free reactive-power control strategy in VSC-HVDC multi-terminal systems to improve transient stability," *Electric Power Systems Research*, vol. 174, Sep. 2019.

[129] J. C. Gonzalez-Torres, G. Damm, V. Costan, A. Benchaib, and F. Lamnabhi-Lagarrigue, "A novel distributed supplementary control of multi-terminal vsc-hvdc grids for rotor angle stability enhancement of ac/dc systems," *IEEE Transactions on Power Systems*, 2020.

[130] P. Rodriguez Cortes, J. I. Candela Garcia, J. Rocabert Delgado, and R. Teodorescu, "Virtual Controller of Electromechanical Characteristics for Static Power Converters," Spain Patent WO 2012/117 132, 2012.

[131] G. N. Baltas, N. B. Lai, L. Marin, A. Tarraso, and P. Rodriguez, "Grid-Forming Power Converters Tuned through Artificial Intelligence to Damp Subsynchronous Interactions in Electrical Grids," *IEEE Access*, 2020.

[132] H. A. Pereira, V. F. Mendes, L. Harnefors, and R. Teodorescu, "Comparison of 2l-VSC and MMC-based HVDC converters: Grid frequency support considering reduced wind power plants models," *Electric Power Components and Systems*, vol. 45, no. 18, pp. 2007–2016, Nov. 2017.

[133] H. T. Nguyen, G. Yang, A. H. Nielsen, and P. H. Jensen, "Combination of synchronous condenser and synthetic inertia for frequency stability enhancement in low inertia systems," *IEEE Transactions on Sustainable Energy*, 2018.

[134] C. R. Shapiro, J. Meyers, C. Meneveau, and D. F. Gayme, "Wind farms providing secondary frequency regulation: evaluating the performance of model-based receding horizon control," *Wind Energy Science*, vol. 3, no. 1, pp. 11–24, Jan. 2018.

[135] U. Markovic, V. Haberle, D. Shchetinin, G. Hug, D. Callaway, and E. Vrettos, "Optimal sizing and tuning of storage capacity for fast frequency control in low-inertia systems," in *2019 International Conference on Smart Energy Systems and Technologies (SEST)*. IEEE, Sep. 2019.

[136] F. Errigo, P. Venet, L. Chedot, and A. Sari, "Optimal supercapacitor pack sizing for modular multilevel converter with integrated energy storage system," in *2018 IEEE International Conference on Industrial Technology (ICIT)*. Lyon: IEEE, Feb. 2018, pp. 1760–1766.

[137] L. Zhang, L. Harnefors, and H.-P. Nee, "Interconnection of two very weak AC systems by VSC-HVDC links using power-synchronization control," *IEEE Transactions on Power Systems*, vol. 26, no. 1, pp. 344–355.

[138] J. Gleadow, G. Love, H. Saad, T. Rauhaia, C. Barker, A. Canelhas, M. Barnes, G. Denis, S. Bartlett, E. Prieto-Araujo, X. Chen, S. Iftekharul, V. Pathirana, K. Schonleber, J. Rittinger, K. Koreman, J. Paquin, and J. Sakamuri, "AC fault response options for VSC HVDC converters," *CIGRE Science & Engineering*, vol. 15, pp. 105 – 110, Oct. 2019.

[139] N. Modi, B. Badrzadeh, A. Halley, A. Louis, and A. Jalali, "Operational manifestation of low system strength conditions – Australian experience," in *2020 CIGRE*, ser. C2. Paris, France: CIGRE, Aug. 2020, p. 11.

[140] RTE. (2018) Electricity report 2018. [Online]. Available: https://bilan-electrique-2018.rte-france.com/?lang=en#

[141] G. S. Pereira, V. Costan, A. Bruyère, and X. Guillaud, "Impact of synchronous machine dynamics on the stability of a power grid with high penetration of Variable Renewable Energies," in *15th IET International Conference on AC and DC Power Transmission (ACDC 2019)*. Coventry, UK: IET, Feb. 2019.

[142] ——, "Synchronous machine representations for stability studies of power systems with inverters," in *2019 IEEE PES Power Tech*, 2019.

[143] L. R. Castillo and D. A. Roscoe, "Experimental stability assessment of converter-dominated electrical grids," in *16th Wind Integration Workshop*, Oct. 2017.

[144] C. Albea Sanchez, O. Lopez Santos, D. A. Zambrano Prada, F. Gordillo, and G. Garcia, "On the Practical Stability of Hybrid Control Algorithm With Minimum Dwell Time for a DC–AC Converter," *IEEE Transactions on Control Systems Technology*, vol. 27, no. 6, pp. 2581–2588, Nov. 2019.

[145] S. Bacha, I. Munteanu, and A. I. Bratcu, *Power Electronic Converters Modeling and Control with Case Studies*, advanced textbooks in control and signal processing ed. Springer, 2013.

[146] A. Manoloiu, H. A. Pereira, R. Teodorescu, M. Bongiorno, M. Eremia, and S. R. Silva, "Comparison of PI and PR current controllers applied on two-level VSC-HVDC transmission system," in *2015 IEEE Eindhoven PowerTech*. Eindhoven, Netherlands: IEEE, Jun. 2015, pp. 1–5.

[147] A. A. Nazeri, P. Zacharias, F. M. Ibanez, and S. Somkun, "Design of Proportional-Resonant Controller with Zero Steady-State Error for a Single-Phase Grid-Connected Voltage Source Inverter with an LCL Output Filter," in *2019 IEEE Milan PowerTech*. Milan, Italy: IEEE, Jun. 2019, pp. 1–6.

[148] J. Vorwerk, "Small-signal analysis of power systems with low rotational inertia," Semester Thesis, ETH Zürich, May 2018.

[149] N. Grid, "Impacts of Declining Short-Circuit Levels," National Grid ESO, Tech. Rep., Dec. 2018.

[150] J. Hou, Z. Liu, S. Wang, and Z. Chen, "Modeling and HIL Test of a D-PMSG Connected to Power System with Damping Control for Real Time Studies," in *2021 3rd Asia Energy and Electrical Engineering Symposium (AEEES)*. Chengdu, China: IEEE, Mar. 2021, pp. 644–649.

[151] L. Fan and Z. Miao, "Wind in Weak Grids: 4 Hz or 30 Hz Oscillations?" *IEEE Transactions on Power Systems*, vol. 33, no. 5, pp. 5803–5804, Sep. 2018.

[152] T. Midtsund, J. A. Suul, and T. Undeland, "Evaluation of current controller performance and stability for voltage source converters connected to a weak grid," in *The 2nd International Symposium on Power Electronics for Distributed Generation Systems*. Hefei, China: IEEE, Jun. 2010, pp. 382–388.

[153] G. S. Pereira, V. Costan, A. Bruyére, and X. Guillaud, "Simplified approach for frequency dynamics assessment of 100% power electronics-based systems," *Electric Power Systems Research*, vol. 188, Nov. 2020.

[154] L. Vanfretti, T. Rabuzin, M. Baudette, and M. Murad, "iTesla Power Systems Library (iPSL): A Modelica library for phasor time-domain simulations," *SoftwareX*, vol. 5, pp. 84–88, 2016.

[155] Q. Hu, L. Fu, F. Ma, and F. Ji, "Large Signal Synchronizing Instability of PLL-Based VSC Connected to Weak AC Grid," *IEEE Transactions on Power Systems*, vol. 34, no. 4, pp. 3220–3229, Jul. 2019.

[156] National Grid, "Regional Trends and Insights," National Grid ESO, Tech. Rep., Jun. 2018. [Online]. Available: https://www.nationalgrideso.com/sites/eso/files/documents/SOF%20Report-%20Regional%20Trends%20and%20Insights.pdf

[157] H. Liu and Z. Chen, "Contribution of VSC-HVDC to Frequency Regulation of Power Systems With Offshore Wind Generation," *IEEE Transactions on Energy Conversion*, vol. 30, no. 3, pp. 918–926, Sep. 2015.

[158] K. Shinoda, A. Benchaib, J. Dai, and X. Guillaud, "DC voltage control of MMC-based HVDC grid with virtual capacitor control," in *2017 19th European Conference on Power Electronics and Applications (EPE'17 ECCE Europe)*. IEEE, Sep. 2017.

[159] J. Freytes, S. Akkari, J. Dai, F. Gruson, P. Rault, and X. Guillaud, "Small-signal state-space modeling of an HVDC link with modular multilevel converters," in *2016 IEEE 17th Workshop on Control and Modeling for Power Electronics (COMPEL)*. Trondheim, Norway: IEEE, Jun. 2016.

[160] C. Spallarossa, M. Merlin, and T. Green, "Augmented inertial response of multi-level converters using internal energy storage," in *2016 IEEE International Energy Conference (ENERGYCON)*. IEEE, Apr. 2016, pp. 1–6.

[161] H. Kim, J. Kang, J. W. Shim, J. Beerten, D. Van Hertem, H.-J. Jung, C.-K. Kim, and A. Kyeon Hur, "Exploiting redundant energy of MMC-HVDC to enhance frequency response of low inertia AC grid," *IEEE Access*, vol. 7, pp. 138 485 – 138 494, 2019.

[162] P. Favre-Perrod, F. Krismer, S. Milovanovic, M. Paolone, F. Rachidi, R. Razzaghi, T. Schultz, G. Tsolaridis, M. Utvic, Z. Wang, J. Biela, M. Carpita, A. Christe, P. Czyz, D. Dujic, C. Franck, T. Guillod, and J. Kolar, "Swiss competence center on energy research FURIES - Overview and contributions in the area of power electronics and SmartGrids," in *2019 21st European Conference on Power Electronics and Applications (EPE '19 ECCE Europe)*. Genova, Italy: IEEE, Sep. 2019, pp. 1–10.

[163] K. Shinoda, A. Benchaib, J. Dai, and X. Guillaud, "Virtual Capacitor Control: Mitigation of DC Voltage Fluctuations in MMC-Based HVdc Systems," *IEEE Transactions on Power Delivery*, vol. 33, no. 1, pp. 455–465, Feb. 2018.

[164] A. Zama, A. Benchaib, S. Bacha, D. Frey, and S. Silvant, "High Dynamics Control for MMC Based on Exact Discrete-Time Model With Experimental Validation," *IEEE Transactions on Power Delivery*, vol. 33, no. 1, pp. 477–488, Feb. 2018.

[165] F. Deng and Z. Chen, "Voltage-Balancing Method for Modular Multilevel Converters Switched at Grid Frequency," *IEEE Transactions on Industrial Electronics*, vol. 62, no. 5, pp. 2835–2847, May 2015.

[166] S. D Arco, G. Guidi, and J. A. Suul, "Operation of a Modular Multilevel Converter Controlled as a Virtual Synchronous Machine," in *2018 International Power Electronics Conference (IPEC-Niigata 2018 -ECCE Asia)*. Niigata: IEEE, May 2018, pp. 782–789.

[167] T. Qoria, "Grid-forming control to achieve a 100% power electronics interfaced power transmission systems," PhD thesis, HESAM Universite, Lille, France, Nov. 2020.

[168] H. Ramadan, H. Siguerdidjane, M. Petit, and R. Kaczmarek, "Performance enhancement and robustness assessment of VSC–HVDC transmission systems

controllers under uncertainties," *International Journal of Electrical Power & Energy Systems*, vol. 35, no. 1, pp. 34–46, Feb. 2012.

[169] E. Sanchez-Sanchez, D. Gross, E. Prieto-Araujo, F. Dorfler, and O. Gomis-Bellmunt, "Optimal multivariable MMC energy-based control for DC voltage regulation in HVDC applications," *IEEE Transactions on Power Delivery*, 2019.

[170] National Grid, "UK Grid Code," Mar. 2017.

[171] ——, "Historic Frequency Data," Nov. 2020. [Online]. Available: https://www.nationalgrideso.com/balancing-services/frequency-response-services/historic-frequency-data

[172] F. Errigo, L. Chedot, F. Morel, P. Venet, A. Sari, A. Hijazi, and R. A. Pena, "Assessment of Aging and Performance Degradation of Supercapacitors Integrated into a Modular Multilevel Converter," in *2020 22nd European Conference on Power Electronics and Applications (EPE'20 ECCE Europe)*. Lyon, France: IEEE, Sep. 2020.

[173] S. H. Jakobsen, L. Kalemba, and E. H. Solvang, "The Nordic 44 test network," *Online: https://figshare. com/projects/Nordic_44/57905*, 2018.

[174] C. Karawita and U. Annakkage, "A hybrid network model for small signal stability analysis of power systems," *IEEE Transactions on power systems*, vol. 25, no. 1, pp. 443–451, 2009.

[175] Dassault Systems, "DYMOLA Systems Engineering," Jul. 2021. [Online]. Available: https://www.3ds.com/products-services/catia/products/dymola/

[176] J. Fradley, R. Preece, and M. Barnes, "Assessment of the impact of MMC-VSC intrinsic energy on power system stability," *The Journal of Engineering*, vol. 2019, no. 17, pp. 4012–4016, Jul. 2019.

[177] A. Taffese, A. G. Endegnanew, S. D Arco, and E. Tedeschi, "Power oscillation damping with virtual capacitance support from modular multilevel converters," *IET Renewable Power Generation*, Sep. 2019.

[178] P. D. Judge and T. C. Green, "Modular Multilevel Converter With Partially Rated Integrated Energy Storage Suitable for Frequency Support and Ancillary Service Provision," *IEEE Transactions on Power Delivery*, vol. 34, no. 1, pp. 208–219, Feb. 2019.

[179] E. F. Camacho and C. Bordons, *Model Predictive Control*. London: Springer, 1998.

[180] J. Zárate Flórez, J. Martinez, G. Besançon, and D. Faille, "Decentralized-coordinated model predictive control for a hydro-power valley," *Mathematics and Computers in Simulation*, vol. 91, pp. 108–118, May 2013.

[181] J. C. Sánchez, O. Marjanovic, M. Barnes, and P. R. Green, "Secondary Model Predictive Control Architecture for VSC-HVDC Networks Interfacing Wind Power," *IEEE Transactions on Power Delivery*, vol. 35, no. 5, 2020.

[182] E. Thau, E. Kamal, B. Marinescu, and G. Denis, "Model Predictive Control of VSC-HVDC Embedded into AC Grid Subject to State and Control Constraints," in *2019 IEEE Milan PowerTech*. Milan, Italy: IEEE, Jun. 2019.

[183] O. Stanojev, U. Markovic, P. Aristidou, G. Hug, D. Callaway, and E. Vrettos, "MPC-Based Fast Frequency Control of Voltage Source Converters in Low-Inertia Power Systems," *arXiv:2004.02442 [cs, eess]*, Apr. 2020. [Online]. Available: http://arxiv.org/abs/2004.02442

[184] ENTSO-E, "ENTSO-E Transparency Plateform," Mar. 2021. [Online]. Available: https://transparency.entsoe.eu/

[185] J. B. Jorgensen and S. B. Jorgensen, "Continuous-discrete time prediction-error identification relevant for linear model predictive control," in *2007 European Control Conference (ECC)*. Kos, Greece: IEEE, Jul. 2007, pp. 4752–4758.

[186] B. Wang, D. Yang, G. Cai, J. Ma, Z. Chen, and L. Wang, "Online Inertia Estimation Using Electromechanical Oscillation Modal Extracted from Synchronized Ambient Data," *Journal Of Modern Power Systems and Clean Energy*, Oct. 2020.

[187] L. Ljung, *System Identification: Theory for the User*, ser. Information and system sciences series. Prentice Hall PTR, 1999.

[188] S. Boersma, X. Bombois, L. Vanfretti, J. C. Gonzalez-Torres, and A. Benchaib, "Probing Signal Design for Enhanced Damping Estimation in Power Networks," *Preprint*, Jul. 2020.

[189] Mathworks, "System identification toolbox," Apr. 2021. [Online]. Available: https://fr.mathworks.com/products/sysid.html

[190] G. Besançon, Ed., *Nonlinear observers and applications*, ser. Lecture notes in control and information sciences. Berlin Heidelberg: Springer, 2007, no. 363.

[191] Mathworks, "Kalman filtering," Apr. 2021. [Online]. Available: https://fr.mathworks.com/help/control/ug/kalman-filtering.html

[192] L. Wang, *Model Predictive Control System Design and Implementation Using MATLAB®*, ser. Advances in Industrial Control. London: Springer London, 2009.

[193] J. Lofberg, "YALMIP : a toolbox for modeling and optimization in MATLAB," in *2004 IEEE International Conference on Robotics and Automation (IEEE Cat. No.04CH37508)*. Taipei, Taiwan: IEEE, 2004, pp. 284–289.

[194] Mathworks, "Quadratic programming (quadprog)," Apr. 2021. [Online]. Available: https://fr.mathworks.com/help/optim/ug/quadprog.html

[195] A. F. Cupertino, W. C. S. Amorim, H. A. Pereira, S. I. Seleme Junior, S. K. Chaudhary, and R. Teodorescu, "High Performance Simulation Models for ES-STATCOM Based on Modular Multilevel Converters," *IEEE Transactions on Energy Conversion*, vol. 35, no. 1, pp. 474–483, Mar. 2020.

[196] N. Gionfra, G. Sandou, H. Siguerdidjane, P. Loevenbruck, and D. Faille, "A novel distributed particle swarm optimization algorithm for the optimal power flow problem," in *2017 IEEE Conference on Control Technology and Applications (CCTA)*. Mauna Lani Resort, HI, USA: IEEE, Aug. 2017, pp. 656–661.

[197] J. P. Koeln, H. C. Pangborn, M. A. Williams, M. L. Kawamura, and A. G. Alleyne, "Hierarchical Control of Aircraft Electro-Thermal Systems," *IEEE Transactions on Control Systems Technology*, vol. 28, no. 4, pp. 1218–1232, Jul. 2020.

[198] P. Simon Berner and M. Monnigmann, "A Complexity Analysis of Event-Triggered Model Predictive Control on Industrial Hardware," *IEEE Transactions on Control Systems Technology*, vol. 28, no. 6, pp. 2625–2632, Nov. 2020.

[199] Z. Karami, Q. Shafiee, Y. Khayat, M. Yaribeygi, T. Dragicevic, and H. Bevrani, "Decentralized Model Predictive Control of DC Microgrids With Constant Power Load," *IEEE Journal of Emerging and Selected Topics in Power Electronics*, vol. 9, no. 1, pp. 451–460, Feb. 2021.

[200] S. Cheng, L. Li, H.-Q. Guo, Z.-G. Chen, and P. Song, "Longitudinal Collision Avoidance and Lateral Stability Adaptive Control System Based on MPC of Autonomous Vehicles," *IEEE Transactions on Intelligent Transportation Systems*, vol. 21, no. 6, pp. 2376–2385, Jun. 2020.

[201] R. N. Beres, X. Wang, F. Blaabjerg, M. Liserre, and C. L. Bak, "Optimal Design of High-Order Passive-Damped Filters for Grid-Connected Applications," *IEEE Transactions on Power Electronics*, vol. 31, no. 3, pp. 2083–2098, Mar. 2016.

[202] E. T. Louokdom, D. Siemaszko, S. Gavin, D. Leu, P. Favre-Perrod, and M. Carpita, "Use of Modular Multilevel Converter in multi-terminal DC transmission network: Reduced scale set-up and experimental results," in *2017 19th European Conference on Power Electronics and Applications (EPE'17 ECCE Europe)*. Warsaw: IEEE, Sep. 2017, pp. P.1–P.9.

[203] J. Fang, P. Lin, H. Li, Y. Yang, and Y. Tang, "An Improved Virtual Inertia Control for Three-Phase Voltage Source Converters Connected to a Weak Grid," *IEEE Transactions on Power Electronics*, 2018.

[204] M. Schiesser, S. Wasterlain, M. Marchesoni, and M. Carpita, "A Simplified Design Strategy for Multi-Resonant Current Control of a Grid-Connected Voltage Source Inverter with an LCL Filter," *Energies*, vol. 11, no. 3, p. 609, Mar. 2018.

[205] V. Pirsto, J. Kukkola, and M. Hinkkanen, "Multifunctional Cascade Control of Voltage-Source Converters Equipped With an LC Filter," *IEEE Transactions on Industrial Electronics*, 2021.

[206] A. Labella, F. Filipovic, M. Petronijevic, A. Bonfiglio, and R. Procopio, "An MPC Approach for Grid-Forming Inverters: Theory and Experiment," *Energies*, vol. 13, no. 9, p. 2270, May 2020.

[207] J. Bocker, B. Freudenberg, A. The, and S. Dieckerhoff, "Experimental Comparison of Model Predictive Control and Cascaded Control of the Modular

Multilevel Converter," *IEEE Transactions on Power Electronics*, vol. 30, no. 1, pp. 422–430, Jan. 2015.

[208] Q. Yuan, F. Yang, A. Li, and T. Ma, "A Novel Hybrid Control Strategy for the Energy Storage Modular Multilevel Converters," *IEEE Access*, vol. 9, pp. 59 466–59 474, 2021.

[209] A. Zama, "Modeling and Control of Modular Multilevel Converters (MMCs) for HVDC applications," PhD thesis, Universite Grenoble Alpes, Grenoble, France, Oct. 2017.

[210] Opal RT, "Modular Multilevel Converters," Jun. 2021. [Online]. Available: https://www.opal-rt.com/modular-multilevel-converter/

[211] ——, "Software simulation, Real Time applications: RT-lab," Jun. 2021. [Online]. Available: https://www.opal-rt.com/software-rt-lab-2/

[212] L. Harnefors, J. Kukkola, M. Routimo, M. Hinkkanen, and X. Wang, "A Universal Controller for Grid-Connected Voltage-Source Converters," *IEEE Journal of Emerging and Selected Topics in Power Electronics*, pp. 1–1, 2020.

[213] J. Mattingley and S. Boyd, "CVXGEN: a code generator for embedded convex optimization," *Optimization and Engineering*, vol. 13, no. 1, pp. 1–27, Mar. 2012.

[214] P. Zometa, M. Kogel, and R. Findeisen, "µAO-MPC: a Free Code Generation Tool for Embedded Real-Time Linear Model Predictive Control," in *2013 American Control Conference (ACC)*, Washington DC, USA, Jun. 2013, p. 6.

[215] C. Ibanez, "Implementation of optimization-based controllers for industrial processes," Master's thesis, CSIC-UPC, Barcelona, Spain, Jun. 2017.

[216] J. L. Jerez, E. C. Kerrigan, and G. A. Constantinides, "A Condensed and Sparse QP Formulation for Predictive Control," in *2013 IEEE 54th Annual Conference on Decision and Control (CDC)*. Washington DC, USA: IEEE, Jun. 2013, p. 6.

[217] V. M. Veliov and P. T. Vuong, "Gradient Methods on Strongly Convex Feasible Sets and Optimal Control of Affine Systems," *Applied Mathematics & Optimization*, vol. 81, no. 3, pp. 1021–1054, Jun. 2020.

[218] J. Lofberg, "Simulink models with yalmip components," 2021. [Online]. Available: https://yalmip.github.io/example/simulink/

[219] Mathworks, "Interpreted MATLAB Function," 2021. [Online]. Available: https://fr.mathworks.com/help/simulink/slref/interpretedmatlabfunction.html?s_tid=doc_ta

[220] ——, "S-function examples," 2021. [Online]. Available: https://fr.mathworks.com/help/simulink/sfg/s-function-examples.html

[221] M. Bollen and R. de Graaff, "Behavior of AC and DC drives during voltage sags with phase-angle jump and three-phase unbalance," in *IEEE Power Engineering Society. 1999 Winter Meeting (Cat. No.99CH36233)*. New York, NY, USA: IEEE, 1999, pp. 1225–1230 vol.2.

[222] D. S. d. S. Andrade, Y. N. Batista, F. A. S. Neves, and H. E. P. de Souza, "Fast Phase Angle Jump Estimation to Improve the Convergence Time of the GDSC-PLL," *IEEE Transactions on Industrial Electronics*, vol. 67, no. 4, pp. 2852–2862, Apr. 2020.

[223] K. Shinoda, A. Benchaib, J. Dai, and X. Guillaud, "Analysis of the Lower Limit of Allowable Energy in Modular Multilevel Converters," in *2018 20th European Conference on Power Electronics and Applications (EPE'18 ECCE Europe)*. Riga, Latvia: IEEE, Sep. 2018.

[224] F. Errigo, "Power converters with integrated energy storage systems for high voltage direct current systems," PhD thesis, INSA Lyon, Villeurbanne, France, Oct. 2020.

[225] C. García-Ceballos, S. Pérez-Londoño, and J. Mora-Flórez, "Integration of distributed energy resource models in the vsc control for microgrid applications," *Electric Power Systems Research*, vol. 196, p. 107278, 2021.

[226] B. Boukhezzar and H. Siguerdidjane, "Nonlinear Control of a Variable-Speed Wind Turbine Using a Two-Mass Model," *IEEE Transactions on Energy Conversion*, vol. 26, no. 1, pp. 149–162, Mar. 2011.

[227] J. Sandoval-Moreno, G. Besancon, and J. J. Martinez, "Observer-based maximum power tracking in wind turbines with only generator speed measurement," in *2013 European Control Conference (ECC)*. Zurich: IEEE, Jul. 2013, pp. 478–483.

[228] O. Lopez-Santos, L. Martinez-Salamero, G. Garcia, and H. Valderrama-Blavi, "Sliding-mode control of a transformer-less dual-stage grid-connected

photovoltaic micro-inverter," in *10th International Multi-Conferences on Systems, Signals & Devices 2013 (SSD13)*. Hammamet, Tunisia: IEEE, Mar. 2013, pp. 1–6.

[229] D. Cao, W. Hu, J. Zhao, G. Zhang, B. Zhang, Z. Liu, Z. Chen, and F. Blaabjerg, "Reinforcement Learning and Its Applications in Modern Power and Energy Systems: A Review," *Journal of Modern Power Systems and Clean Energy*, vol. 8, no. 6, pp. 1029–1042, 2020.

[230] S. Zhao, F. Blaabjerg, and H. Wang, "An Overview of Artificial Intelligence Applications for Power Electronics," *IEEE Transactions on Power Electronics*, vol. 36, no. 4, pp. 4633–4658, Apr. 2021.

[231] D. Georges, "A Simple Machine Learning Technique for Model Predictive Control," in *2019 27th Mediterranean Conference on Control and Automation (MED)*. Akko, Israel: IEEE, Jul. 2019, pp. 69–74.

[232] H. N. V. Pico and B. B. Johnson, "Transient Stability Assessment of Multi-Machine Multi-Converter Power Systems," *IEEE Transactions on Power Systems*, vol. 34, no. 5, pp. 3504–3514, Sep. 2019.

[233] J. Freytes, J. Li, G. De-Preville, and M. Thouvenin, "Grid-Forming Control with Current Limitation for MMC under Unbalanced Fault Ride-Through," *IEEE Transactions on Power Delivery*, 2021.

[234] A. Rodriguez-Cabero, J. Roldan-Perez, M. Prodanovic, J. A. Suul, and S. D'Arco, "Virtual Friction for Oscillation Damping and Inertia Sharing from Multi-Terminal VSC-HVDC Grids," in *2020 IEEE Energy Conversion Congress and Exposition (ECCE)*. Detroit, MI, USA: IEEE, Oct. 2020, pp. 4891–4896.

[235] Mathworks, "State space, part 2: Pole placement," Nov. 2021. [Online]. Available: https://ch.mathworks.com/fr/videos/state-space-part-2-pole-placement-1547198830727.html

[236] E. Tohme, "Initialization of Output Error Identification Algorithms," PhD thesis, Université Poitiers, Poitiers, France, Feb. 2008.

[237] D. Eckhard, A. S. Bazanella, C. R. Rojas, and H. Hjalmarsson, "Cost function shaping of the output error criterion," *Automatica*, vol. 76, pp. 53–60, Feb. 2017.

[238] D. Alazard, "Introduction to Kalman filtering," in *Course key notes*. Toulouse, France: ISAE Supaero, Dec. 2011.

APPENDIX A

SG MODELING

In the following, the differential equations are presented in the dq-frame with the q-axis aligned with the rotor.

Voltage dynamics

The SG is supposed to regulate its voltage v_g at its reference v^* at the connection point. This function is realized by the AVR, which is composed of a lead-lag filter controller and an AC exciter model, as:

$$T_c \cdot \Delta\dot{v} + \Delta v = T_b \cdot \dot{v}_c + v_c \tag{A.1}$$

$$T_a \cdot \dot{v}_{fd} + v_{fd} = k_a \cdot v_c \tag{A.2}$$

where $\Delta v = v^* - \|v_g\|_2$, T_b and T_c are the time constants of the lead-lag filter, T_a the exciter time constant, k_a the exciter gain and v_{fd} the field excitation voltage. It is important to note that the dynamics of PSS (Power System Stabilizers) could also have been taken into account, as in [59]. But, since the PSS enhances the system stability and does not reflect the behavior of standard SG with classical AVR schemes, it is not included in our study.

To excite the machine, the AVR uses the field excitation voltage, v_{fd}. The dynamics are modeled as:

$$\dot{\lambda}_{fd} = \omega_{base} \cdot (v_{fd} - r_{fd} \cdot i_{fd}) \tag{A.3}$$

$$L_{fdfd} \cdot i_{fd} = \lambda_{fd} + L_{afd} \cdot i_g^d \tag{A.4}$$

where r_{fd} is the rotor winding resistance, i_{fd} the field current, λ_{fd} the field flux, L_{fdfd} and L_{afd} are respectively the self and mutual inductances of the rotor and ω_{base} the system fundamental angular frequency. Using the magnetic couplings between the

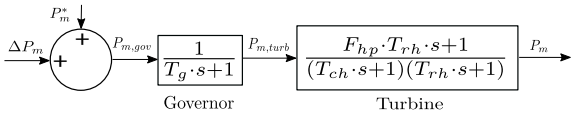

Figure A.1: Transfer function of the governor and turbine model from [75].

rotor and the stator, the field current i_{fd} is related to the stator armature current i_g^{dq}, via the stator flux λ^{dq} as:

$$\lambda^d = -L_d \cdot i_g^d + L_{afd} \cdot i_{fd} \tag{A.5}$$

$$\lambda^q = -L_q \cdot i_g^q \tag{A.6}$$

The relationship between the stator flux and the terminal voltage v_g^{dq}, as described in [61], with the copper losses, modeled with the resistance r_a is given as:

$$v_g^d = -\lambda^q - r_a \cdot i_g^d \tag{A.7}$$

$$v_g^q = \lambda^d - r_a \cdot i_g^q \tag{A.8}$$

The electrical power is given by $P_e = \lambda^d \cdot i^q - \lambda^q \cdot i^d$, which neglects the copper losses in the stator.

Frequency dynamics

The swing equation is related to the dynamics of the rotor speed and thus of the grid frequency, ω_g. The rotor angle, denoted by δ, corresponds to the integral of the frequency:

$$2 \cdot H \cdot \Delta\dot{\omega}_g + D \cdot \Delta\omega_g = P_m - P_e \tag{A.9}$$

$$\dot{\delta} = \omega_{base} \cdot (\omega_{ref} + \Delta\omega_g) \tag{A.10}$$

where ω_{ref} is the grid reference frequency in per unit. The primary frequency control of the machine is realized by a droop controller as:

$$P_{m,gov} = P_m^* - \frac{1}{r_d} \cdot \Delta\omega_g = P_m^* + \Delta P_m \tag{A.11}$$

where $P_{m,gov}$ is the mechanical power at the governor input. The SG mechanical dynamics, which include the governor and turbine dynamics, are given in Fig. A.1, with $P_{m,turb}$ being the mechanical power at the turbine input.

APPENDIX B

PI Controller Tuning using Pole Placement Method

The aim of this appendix is to present the *pole placement method* [2] that is used in the power system community to tune the gains of PI controllers.

B.1. Theory

First, the classical structure of the PI controller is recalled in Fig. B.1, integrated in a feedback loop to regulate the plant output y to its desired reference y^*. The plant is described by a continuous-time transfer function $G(s)$.

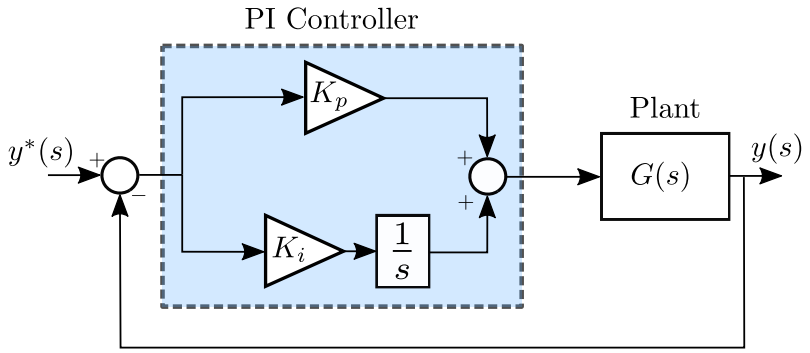

Figure B.1: Closed-loop system with a PI controller and a linear plant.

In this case, the PI controller's transfer function, denoted by C_{PI}, can be defined as:

$$C_{PI}(s) = K_p + \frac{K_i}{s} \tag{B.1}$$

where K_p and K_i are respectively the proportional and integral gains of the controller.

And the closed-loop transfer function, denoted by G_F, is:

$$G_F(s) = \frac{C_{PI}(s)G(s)}{1 + C_{PI}(s)G(s)} \tag{B.2}$$

The modes of the closed-loop system correspond to the poles of the transfer function $G_F(s)$. Applying a pole placement method here means that we choose adequate values of the PI gains, K_p and K_i, to "shape" the denominator of $G_F(s)$.

However, because the PI has only two parameters, it is not possible to place the poles of a closed-loop system with an order superior or equal to 3. But, in the case of VSC control, the cascaded control structure [78], which is one of the most commonly-used control structures for the VSC, makes it possible to decouple the dynamics of the VSC, thus reducing the plant dynamics to a low order model.

B.2. Example with a simple system

In order to illustrate the pole placement method presented in the above section, we apply this methodology to a simple linear first-order system representing an RL circuit and described in Fig. B.2.

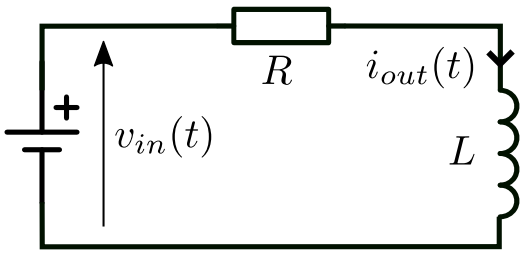

Figure B.2: RL electrical circuit with a DC voltage source v_{in} considered as control input.

The control input of this plant is the DC voltage $u = v_{in}$ and the plant output is $y = i_{out}$. Thanks to the Kirchhoff's law, we obtain the following equation:

$$v_{in}(t) = Ri_{out}(t) + L\frac{di_{out}(t)}{dt} \tag{B.3}$$

which is, in the frequency domain:

$$v_{in}(s) = Ri_{out}(s) + sLi_{out}(s) \tag{B.4}$$

And the corresponding transfer function $G(s)$ can be calculated as:

$$G(s) = \frac{i_{out}(s)}{v_{in}(s)} = \frac{1}{R + Ls} = \frac{K_s}{1 + \tau s} \tag{B.5}$$

where $K_s = 1/R$ and $\tau = L/R$.

The dynamic response of this first-order system is given in Fig. B.3, where the role of the plant's time constant, here denoted by τ, is shown in the time response of the output.

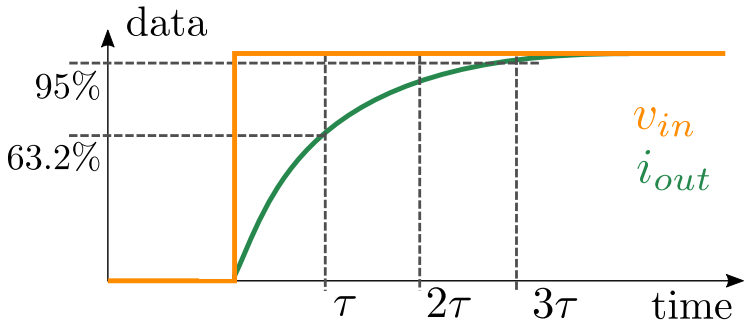

Figure B.3: Illustrative dynamic response of the branch current i_{out} following a DC voltage (v_{in}) step.

In order to control this system and track the reference $y^* = i^*_{out}$, we need to add a controller before the control input of the plant (v_{in}) as in Fig. B.1. To illustrate the pole placement method, we choose a PI controller whose gains will be tuned in order to design the denominator of the closed-loop transfer function $G_F(s)$. This transfer function is equivalent to:

$$G_F(s) = \frac{i_{out}}{i^*_{out}} = \frac{C_{PI}(s)G(s)}{1 + C_{PI}(s)G(s)} = \frac{s\frac{K_p}{L} + \frac{K_i}{L}}{s^2 + s\frac{(R+K_p)}{L} + \frac{K_i}{L}} \tag{B.6}$$

As we added one order to the system when we introduce the PI controller dynamics, the closed-loop system is of second order. Then it is possible to choose the gains of the PI to obtain the transfer function of a typical second-order system:

$$H(s) = \frac{\omega_n^2}{s^2 + 2\xi\omega_n s + \omega_n^2} \tag{B.7}$$

where ω_n is the undamped natural frequency and ξ the damping ratio.

To make these two $G_F(s)$ and $H(s)$ match, we compare their charactistic polynomial:

$$s^2 + s\frac{(R+K_p)}{L} + \frac{K_i}{L} = s^2 + 2\xi\omega_n s + \omega_n^2 \tag{B.8}$$

And if we choose ω_n and ξ properly we can then determine the values of K_p and K_i. A common choice is:

$$\omega_n = \frac{3}{t_{r,5\%}}, \xi = 0.707 \tag{B.9}$$

where $t_{r,5\%}$ is the desired settling time to reach the steady-state value in a $\pm 5\%$ bandwidth.

In addition, it is possible to add a zero-compensation term in the PI structure, which can be used to make $H(s)$ and $G_F(s)$ match perfectly.

B.3. Main applications and differences from state-feedback pole placement method

It is important to note that the vector control, in the dq-frame, makes it possible to have time-invariant variables for the AC currents and voltages instead of sine waveforms [2]. In consequence, the tuning presented in this appendix can be used to tune the controller in the dq frame.

Moreover, in the control systems community, the pole placement method refers to a technique that uses state feedback action to place the poles of the whole closed-loop system [235]. While in the case presented in the appendix, a PI controller can only place the poles of a second-order closed-loop system, this state-feedback pole placement method is more general. However, it requires an accurate model of the system to be controlled, which is in practice uncommon. On the other hand, with the PI controller, the structure of a control system is such that the controller received the control error between an output (the variable to be controlled) and its setpoint. It is then possible to place the poles of a simplified first-order plant model where the PI controller regulates the single state variable. With the time-scale separation in any system, we can design the whole control structure as a cascaded structure with cascaded loops, where we use the dynamic decoupling between different variables with different time scales. In such cascaded structure, each loop can use a PI controller to form the whole control system. Because of the inherent time-scale separation in power systems [59], among other reasons, this type of control structure is a common practice in the field of VSC control.

APPENDIX

Parameter values of the test system

The parameter values of the test-system from in Section 3.2 are given in Table C.1.

Table C.1: Parameter values of the system for the simulations.

SG		**VSC**	
T_c	1 s	$K_{p\omega}$	50 p.u.
T_b	12 s	K_{qv}	0.2 p.u.
T_a	0.04 s	p_{ref}	0.7 p.u.
k_a	0.0745 p.u.	q_{ref}	variable
r_{fd}	0.0006 p.u.	v_{ref}	1 p.u.
L_{afd}	1.66 p.u.	k_{ip}	20 rad/s
L_{fdfd}	1.825 p.u.	$\omega_{c,power}$	31.42 rad/s
L_d	1.81 p.u.	$m_{p\omega}$	2%
L_q	1.76 p.u.	H_c	795.8 ms
r_a	0.003 p.u.	D_c	50 p.u.
H	2.9 s	m_{qv}	0.1%
D	1 p.u.	c_f	0.066 p.u.
r_d	5%	l_f	0.15 p.u.
T_g	0.2 s	r_f	0.005 p.u.
F_{hp}	0.3 p.u.	k_{iv}	2.1008 rad/s
T_{rh}	7 s	k_{pv}	0.0294 p.u.
T_{ch}	0.3 s	k_{ii}	477.5 rad/s
v^*	1 p.u.	k_{pi}	0.6635 p.u.
P_m^*	variable	$k_{i,pll}$	-3603.6 rad/s
ω_{base}	314.16 rad/s	$k_{p,pll}$	-120 p.u.
ω_{ref}	1 p.u.	$\omega_{c,pll}$	200 rad/s
Line		**Load**	
X/R	10	P_{load}	385 MW
U_{base}	24 kVLL	Q_{load}	50 MVAR
S_{base}	550 MVA		

APPENDIX D

Simulation conditions of the Kundur 4-machine, 2-area system

The initial power flow is given below in the base system where U_{base} = 400kV, S_{base} = 100MVA and f_{base} = 60Hz. The inertia constants are $H_{g_1} = H_{g_2} = 6.5$s and $H_{g_3} = H_{g_4} = 6.175$s. More details about the simulation parameters can be found in [60]. The synchronous generator model is based on a round rotor model from the iPSL library [154]. The AVR is modeled with an excitation system SEXS and coupled with a type II PSS. The governor is a G1 type model.

Table D.1: Power Flow data of the Kundur 4-machine, 2-area system

bus #	**1**	**2**	**3**	**4**	**5**	**6**	**7**	**8**	**9**	**10**	**11**
v (p.u.)	1.03	1.01	1.03	1.01	1.007	0.98	0.96	0.95	0.97	0.98	1.009
$\theta(^o)$	20.27	10.51	-6.8	-17.0	13.8	3.71	-4.69	-18.5	-32.15	-23.7	-13.4
P(MW)	700	700	719.1	700	0	0	-967	0	-1767	0	0
Q(MVAR)	185.0	234.6	176.0	202.1	0	0	+84.7	0	+230.2	0	0

APPENDIX E

Definition of system identification tools

Error structures

In this appendix, we present the different types of error structures used in the field of system identification. More information can be found in the following PhD thesis [236].

We consider the following simple system, defined as:

$$y = \frac{B(s)}{A(s)}u \tag{E.1}$$

System identification techniques rely on the minimization of a certain error. There are two main error structures in the literature, namely Output Error (OE) and Equation Error (EE) structures [236], respectively denoted by ϵ_{OE} and ϵ_{EE} and defined for the simple system (E.1) as:

$$\epsilon_{OE} = y - \hat{y} = y - \frac{\hat{B}(s)}{\hat{A}(s)}u \tag{E.2}$$

$$\epsilon_{EE} = \hat{a}y - \hat{B}(s)u = \hat{A}(s)\epsilon_{OE} \tag{E.3}$$

where $\hat{B}(s)$ and $\hat{A}(s)$ are respectively the estimations of $B(s)$ and $A(s)$ defined in (E.1). In this study, the identification method relies on the output error structure given in (E.2). This means that the identified model will be obtained by minimizing the error between the measured output y and the estimated model output $\hat{y}$.

Prediction error method

This section presents the system identification method named "prediction error method" and is based on [187, 236, 237].

First, we consider a single-input/single-output discrete-time system:

$$y(k) = G(q)u(k) + v(k) \tag{E.4}$$

where q is the forward shift operator, $u(k)$ and $y(k)$ are respectively the system inputs and outputs, v a white noise measurement noise and G the transfer function of the system.

Then, the corresponding identified transfer function $\hat{G}$, that we want to match the response of G, is:

$$\hat{y}(k,\theta) = \hat{G}(q,\theta)u(k) + \nu(k) \tag{E.5}$$

where $\nu(k)$ is supposed to be white noise and θ is the set of parameters that will be determined by the identification method.

The prediction error using the output-error structure (E.2) is here denoted as $\epsilon(k,\theta) = y_F - \hat{y}_F$, where $y_F(k) = L(q)y(k)$ and $\hat{y}_F(t,\theta) = L(q)\hat{y}(k,\theta)$ are respectively the filtered system output and optimal one-step-ahead predicted output calculated using (E.5).

The prediction error method is based on finding an optimal set of parameters $\hat{\theta}_N$ which minimizes the error over an N-long selected set of data Z^N, defined such that:

$$Z^N = \begin{Bmatrix} u(k=1) & u(k=2) & \cdots & u(k=N) \\ y(k=1) & y(k=2) & \cdots & y(k=N) \end{Bmatrix} \tag{E.6}$$

The algorithm minimizes the quadratic function V_N:

$$V_N(\theta, Z^N) = \frac{1}{N}\sum_{k=1}^{N} \epsilon_F^2(k,\theta) \tag{E.7}$$

And by using this method, we obtain a set of parameters $\hat{\theta}_N$ of $\hat{G}$ that minimizes this criterion:

$$\hat{\theta}_N = \arg\min(V_N(\theta, Z^N)) \tag{E.8}$$

This set of parameters should converge to a solution θ_0 such that $\lim_{N\to+\infty} \hat{\theta}_N = \theta_0$.

APPENDIX F

KALMAN FILTERING

A Kalman filter is a tool that belongs to the family of state estimators. Its main function is to estimate the non-measurable but observable states of a given system by using an estimated model of the real system and available measurements. The details about the implementation in Matlab can be found in [191].

The classical implementation of the continuous-time Kalman filter can be found below and is based on the control theory course given at ISAE-Supaero [238].

First, we consider the following continuous-time linear state-space system:

$$\dot{x}(t) = Ax(t) + Bu(t) + M\omega(t) \tag{F.1}$$

$$y(t) = Cx(t) + Du(t) + v(t) \tag{F.2}$$

where v and w are the Gaussian noises on the input and the measurement respectively. The objective of the Kalman filter is to obtain an estimated state vector $\hat{x}(t)$ close enough to $x(t)$. The following assumptions are also made:

- the pair (A,C) is supposed to be detectable. This means that all unobservable states are stable in the model;
- $\omega(t)$ and $v(t)$ are centered gaussian white noises, defined by their covariances $E[\omega(t), \omega(t)^T] = Q$ and $E[v(t), v(t)^T] = R$. The two matrices Q and R are respectively the process noise and the sensor noise covariances.
- R is invertible.

Then the state space realization of the Kalman filter is defined as:

$$\dot{\hat{x}}(t) = A_F\hat{x}(t) + \begin{bmatrix} B_F & K_F \end{bmatrix} \begin{bmatrix} u(t) \\ y(t) \end{bmatrix} \tag{F.3}$$

$$= A_F\hat{x}(t) + B_F u(t) + K_F y(t) \tag{F.4}$$

where K_F is the Kalman filter gain and A_F and B_F are the Kalman filter matrices. We can then define the state estimation error $\epsilon(t) = x(t) - \hat{x}(t)$ and then derive $\dot{\epsilon} = \dot{x}(t) - \dot{\hat{x}}(t)$ based on (F.1) and (F.4). Since we want to design the Kalman filter to converge to the real state variables in steady state, i.e. $E[\epsilon(t \to \infty)] = 0$, which is only possible if and only if:

$$A_F = A - K_F C; \qquad B_F = B - K_F D \tag{F.5}$$

Then, by replacing (F.5) in (F.4), we obtain:

$$\dot{\hat{x}} = (A\hat{x} + Bu) + K_F(y - C\hat{x} - Du) \tag{F.6}$$

This equation corresponds to the Kalman filter realization (F.4) and shows how the filter works:

- the first part $(A\hat{x} + Bu)$ corresponds to the estimation of the future state based on the knowledge of the process;
- the second part corresponds to the corrective action based on the difference between the process $\hat{y} = C\hat{x} - Du$ and the measurement y.

In consequence, the value of K_F will depend on the confidence we put in the model. We can choose an arbitrary value or we can calculate it using an optimization method. It is this second option that is implemented in Matlab, where K_F is "chosen to minimize the steady-state covariance of the estimation error" [191].

The value of K_F can be determined by minimizing the cost function $J_K(t)$ defined as:

$$J_K(t) = E[\epsilon^T(t)\epsilon(t)] = \text{trace}(P(t)) \tag{F.7}$$

where $P(t) = E[(x(t) - \hat{x}(t))(x(t) - \hat{x}(t))^T]$. To minimize $J_K(t)$ we can calculate $\frac{\partial(trace(P(t))}{\partial K_F}$ which gives in steady state, i.e. for $\dot{P}(t) = 0$, a stationary value of K_F. This value corresponds to the steady-state covariance of the estimation error such that:

$$K_F = PC^T R^{-1} \tag{F.8}$$

The details to obtain (F.8) using (F.7) can be found in [238].

To conclude, the user can play on the two covariance matrices Q and R to change the Kalman filter performances, which respectively represent the confidence of the user in the state estimation and the measurement. In addition to these two parameters, it is also possible to act on the confidence of the state estimation initialization, which is not detailed here. More information about the confidence in the state estimation initialization can be found in [238].